University of Cambridge
Department of Chemistry

The Structure, Thermodynamics and Dynamics of Atomic Clusters

A dissertation submitted to the University of Cambridge in partial fulfilment of the requirements for the degree of Doctor of Philosophy.

Jonathan Peter Kelway Doye
Gonville & Caius College

September 1996

Declaration

The work described in this dissertation was carried out by the author in the department of Theoretical Chemistry at the Univerisity of Cambridge from October 1993 to September 1996. The contents are the original work of the author except where indicated otherwise and have not been previously submitted for any other degree or qualification at any academic institution.

Acknowledgements

I would like to thank my supervisor, Dr David Wales, for his help and encouragement, and the Engineering and Physical Sciences Research Council and Gonville & Caius College for financial support. I would also like to thank Professor Stephen Berry and Dr Ralph Kunz for helpful discussions.

To
'David'

Abstract

The potential energy surface determines the structure, thermodynamics and dynamics of a cluster. In this thesis, I investigate for simple atomic clusters both the nature of this relationship, and how the form of the potential affects the potential energy surface and consequently the behaviour of the cluster.

The solid-like structure of a cluster is given by the global minimum on the potential energy surface. Using a Morse potential to describe the interatomic forces, I have investigated how the structure depends upon the range of attraction of the potential. This model exhibits a diverse range of structural behaviour, which is relevant to a wide variety of systems from sodium and rare gas clusters, to clusters of C_{60} molecules. A short-ranged potential favours face-centred-cubic and decahedral structures, as opposed to those based upon the icosahedron.

The melting of clusters is associated with a transition from the low potential energy solid-like minima to the numerous high potential energy liquid-like minima. Here, I have developed a method to accurately describe the thermodynamics of this transition using a representative sample of minima on the potential energy surface.

By investigating the dependence of the topography of the potential energy surface on the range of the potential for both clusters and bulk, I have provided a microscopic explanation of the destabilization of the liquid phase that occurs for short-ranged potentials. Furthermore, this study shows that clusters can develop bulk-like liquid structure at small sizes, and also provides an explanation of the transition from electronic to geometric magic numbers that is seen in mass spectroscopic studies of sodium clusters.

If all the minima and transition states on the potential energy surface are known, the dynamics of a system can be obtained by solving a master equation. This method is applied to model potential energy surfaces to investigate the factors affecting relaxation to the global minimum. The results are not only relevant to clusters, but also to disciplines such as protein folding and glass formation. Finally, I investigate some ways of characterizing cluster potential energy surfaces which can give insight into their dynamics.

Contents

List of Abbreviations

DSD	diamond-square-diamond
fcc	face-centred cubic
hcp	hexagonal close-packed
LJ	Lennard-Jones
M	Morse
MC	Monte Carlo
MD	molecular dynamics
PES	potential energy surface
PG	point group
RRKM	Rice-Ramsperger-Kassel-Marcus
STA	short time averaged

Chapter 1
Introduction

1.1 The Evolution of Cluster Science

In the last thirty years, cluster science has become a rapidly expanding field of interdisciplinary study as experimental and theoretical techniques have advanced and computational power has increased. Clusters are finite aggregates of atoms or molecules that are bound by forces which may be metallic, covalent, ionic, hydrogen-bonded or Van der Waals in character and can contain from a few to tens of thousands of atoms.

Clusters can be prepared in a number of ways. A large proportion of experimental studies are now performed on clusters that are produced in molecular beams by free-jet expansion. The discovery of this technique was one of the most important factors in the growth of cluster studies. The resulting clusters can then be mass-selected and subjected to many types of high-resolution spectroscopies. However, although this technique allows very detailed and sensitive studies to be performed, it is not so suitable for producing large quantities of (size-selected) clusters—a likely requirement for industrial applications—and it is hard to make direct measurements of structure. One alternative that circumvents the latter problem is to deposit the clusters on a surface, where their structure can then be probed by techniques such as high resolution electron microscopy[1], and scanning tunneling microscopy[2,3]. However, the effects of the surface on the cluster have then to be taken into account.

The oldest route for the preparation of clusters is by colloidal chemistry: back in 1856 Faraday famously investigated the optical properties of gold colloids[4]. Typically, clusters produced by this method are stabilized by the addition of a passivating layer, as compared to the naked clusters produced in molecular beams. One of the main advantages of this method is that large quantities of clusters can be produced. Furthermore, significant advances have now been made in controlling the size, shape and structure of these particles[5–7].

But why are so many people interested in studying clusters? If you look back into the early cluster literature three motivations are particularly common. Firstly, clusters provide a bridge between the limits of isolated atoms and molecules and bulk matter, and so much interest has focussed on the evolution of properties with size[8], particularly those, such as phase transitions, which have no counterpart in atomic physics, and which must therefore emerge as collective behaviour becomes possible. The hope is that such knowledge will provide a new perspective on and an increased understanding of the behaviour that occurs at the more familiar limits. This motivation is still a fundamental driving force for cluster science and this thesis will touch upon some aspects of the size evolution of cluster properties.

A second motivation to study clusters, particularly from the theoretical viewpoint, is to try to understand nucleation at an atomistic level, rather than by the continuum theories of classical nucleation theory[9]. Whenever a new phase is forming the initial nuclei will be within the cluster regime. Much of the early work on the thermodynamics of clusters had this as its goal[10–12]. However, these ambitions have never been fully realized; this task is a far more difficult problem than perhaps was originally conceived. Most of the current work in this area is now no longer directed at clusters as as a model of a (critical) nucleus, but instead at clusters as an environment in which nucleation can occur on fast time scales[13] and for which only a single nucleation event is required to transform the cluster[14].

Thirdly, much work has been, and still is, driven by the prospect that a fundamental understanding of the properties, particularly the chemical reactivity, of metal clusters could have far-reaching consequences for catalysis. Small metal particles and clusters (supported, for instance, within a zeolite) could provide both a large surface area to volume ration and properties, such as activity and selectivity, that have been tailored to catalyse a specific reaction[15,16].

In recent years, though, the ambitions and breadth of cluster science have expanded greatly as the numbers of types of clusters that have been studied has grown, and as it has been realized that clusters can provide a new environment to study many of the phenomena of chemical physics. Here, we just provide some illustrative examples of the range of the recent work.

Insights into the nature of hydrogen bonding have been obtained from water clusters by the coupling of high-resolution laser spectroscopy with theoretical calculations[17] to identify in detail the structure of the clusters[18] and the rearrangement dynamics of the hydrogen-bond network[19]. By studying heteroclusters detailed microscopic information on the nature of solvation can be obtained[20], such as the number of species required for the formation of a complete solvent shell[21], and the effects of this solvent shell on the chemical reactions dynamics[22–24]. Helium, because of its superfluid properties, can be a particular gentle solvent. Consequently, helium clusters probably a suitable environment for ultra-cold high-resolution spectroscopy of Van der Waals complexes[25,26].

The collision of clusters with solid surfaces at high speeds can give rise to short-lived, but particularly extreme conditions of temperature and pressure[27]. It has been shown that these impact-heated clusters provide an environment in which chemical reactions can be induced[28]—it has even been suggested that they could lead to the burning of 'air' (binary N_2 and O_2 clusters)[29]. Energetic cluster impact also has the potential for technological application in the formation of particularly dense and coherent metal[30,31] and semiconductor[32] thin films. However, if clusters instead collide with surfaces covered by liquid layers, the clusters can be 'soft landed' onto the surface[33].

These latter examples touch on one of the more recent reasons for the increased interest in clusters: nanotechnology—the fabrication of structures and devices on the nanometer scale. In this regard, semiconductor clusters have been the focus of particular attention since size control could provide a means of tailoring their electronic and optical properties to a particular application[34,35]. One of the dreams of researchers is to produce quantum dot lasers whose frequency can be fine-tuned by variation of the cluster size[32]. Such hopes have led to a major efforts to improve fabrication techniques and methods are now available for making structurally well-defined monodisperse passivated clusters which can then be formed into orientationally-ordered superlattices[7,36]. Assemblies of nanoparticles have even been constructed using the base pairings of DNA as connections[37,38].

1.2 Thesis Overview

The work described in this thesis is theoretical and its aim is to help provide a fundamental understanding of three of the most important properties of clusters, their structure, thermodynamics, and dynamics. Rather than attempting to model accurately a specific substance, I choose to study homogeneous atomic clusters for which the interactions are described by simple potentials. Only with this simplicity does the main theme of the thesis—the relationship between the form of the potential and the behaviour of the cluster—become tractable. To attempt this task I focus on the potential energy surface (PES), because it allows the elucidation of this relationship to be broken down into two steps: firstly, how the potential determines the topographical features of the PES, and then how these in turn determine the behaviour of the cluster. In the analyses of the PES performed here, the stationary points (at which $\nabla V = 0$ where V is the potential energy) will be particularly important, since the minima on the PES represent locally stable structures, and the transition states characterize the possible rearrangement paths between minima.

The thesis progresses in the following way. In Chapter 2, I show how the range of attraction of the potential affects the structures of the global minima. In Chapter 3, I extend a statistical method to incorporate anharmonicity so that the thermodynamic properties of clusters can be accurately calculated from a representative sample of minima. In Chapter 4, I attempt to provide a microscopic explanation of the range-dependence of the stability of the liquid phase. In Chapter 5, by examining model PES's I seek to elucidate the topographical features which significantly affect relaxation to the global minimum. In Chapter 6, I outline and apply methods by which to characterize the topology of the PES, particularly the network of connections between the minima, in order to provide insights into the dynamics. Finally, in the conclusion I attempt to summarize the achievements of the work described in this thesis, and suggest some possible future directions. Comprehensive introductions into each area will be given at the beginning of each chapter.

As I hope the interdependence of the chapters in this thesis will illustrate, structure, thermodynamics and dynamics are intimately connected. For example, only once liquid structure is characterized can the range-dependence of the liquid phase thermodynamics be explained. Furthermore, to be able to predict whether a cluster is likely to adopt the structure of the global minimum, one must first know whether the minimum is kinetically accessible, which in turn depends on whether there are free energy barriers to this relaxation process.

Although the approach of this work is unashamedly fundamental, throughout the thesis I shall attempt to relate the findings to experiment and other more specific theoretical calculations. Indeed, the hope is that the results for these simple systems can begin to provide a framework for understanding the diverse behaviour of real clusters.

Chapter 2
The Structure of Clusters

2.1 Introduction

Structure has a central role in cluster science and is a prerequisite for elucidating many of the properties of clusters. As a consequence, much experimental and theoretical effort has been expended in order to characterize cluster structure. Indeed, many of the experimental methods for obtaining structural information take advantage of the sensitive dependence of cluster properties, such as chemical reactivity[39] and magnetism[40], on cluster structure.

One of the most interesting aspects of cluster structure is the possibility of non-crystallographic symmetry which arises from the absence of translational periodicity. In particular, many clusters are found to have fivefold axes of symmetry. The three main types of ordered structure that simple atomic clusters adopt are close-packed, decahedral and icosahedral. Examples of each are given in Figure 2.1. The decahedral structures have a single fivefold axis of symmetry and are based on pentagonal bipyramids, and the icosahedral structures have six fivefold axes of symmetry.

Icosahedral structures were first discovered in investigations of clusters bound by the Lennard-Jones (LJ) potential[41]. Although early theoretical studies considered structures that were fragments of a crystalline lattice, it soon became clear that the lowest energy structures were based on Mackay icosahedra[42]. The LJ potential provides a reasonable description of the interaction between rare gas atoms, and it has been confirmed by electron diffraction[43–46] and mass spectroscopy[47–49] that rare gas clusters are icosahedral for sizes up to at least 750 atoms. Furthermore, the detailed intensity variations in the mass spectra show very good agreement with those expected from the icosahedral growth sequence of LJ clusters[50]. Icosahedral structures have since been found for many other gas phase clusters, in-

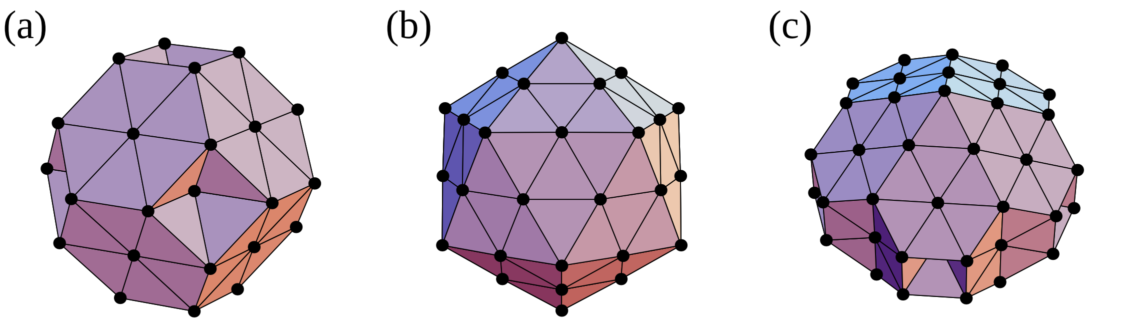

FIGURE 2.1: Three examples of the structures clusters can adopt: (a) a 38-atom truncated octahedron, (b) a 55-atom Mackay icosahedron, and (c) a 75-atom Marks' decahedron. These clusters have the optimal shape for the three main types of ordered packing seen in clusters: face-centred cubic (fcc), icosahedral and decahedral, respectively. The latter two structural types cannot be extended to bulk because of the presence of five-fold axes of symmetry.

cluding metals[51–56], and molecular clusters[57,58]. Icosahedral and decahedral structures are also commonly observed for metal clusters supported on surfaces[1]. At sufficiently large sizes, though, there must be a crossover to the bulk limit where crystalline structures have the lowest energy.

The focus of this chapter is to elucidate the relationship between the form of the interatomic potential and the structure of clusters. Many studies have concentrated on the structures of clusters exhibited by a specific functional form, including model potentials such as the LJ potential and those designed for a particular material. Fewer studies have examined the general structural effects of the different contributions to the potential. For this purpose, it is useful to consider a potential which is simple enough that the effects of any changes made to its form can be understood and that these changes can be made by varying a single parameter. This method has been used to investigate the effect of the range[59–61] and anisotropy[62,63] of the potential on the structure and phase behaviour of small clusters.

In this chapter we further investigate the effects of the range of the potential. Previous studies have found that as the range is increased the number of minima and saddle points on the PES decreases; the PES becomes smoother and simpler[59,64,65]. Furthermore, Bytheway and Kepert noted that, for a sufficiently long-ranged potential, structures based on icosahedral packings become less favoured energetically than structures with even higher coordination[60]. Little, however, has been discovered about the structures associated with shorter-ranged potentials, and the effects of the range and size on the competition among icosahedral, decahedral and close-packed structures. Here we address these issues by examining clusters of atoms bound by the Morse potential. We consider all clusters containing up to 80 atoms, and in particular we attempt to find the global minimum as a function of the range and size.

Such a study provides the most comprehensive model of cluster structure in the literature, having a wider range of applicability and exhibiting a much greater diversity of structural behaviour than observed for LJ clusters, the most well-studied cluster system. The structural catalogue provided by this study will be useful for experimentalists, as they can only obtain indirect structural information which, in order to be assigned, must be compared to that expected for model structures. This is particularly so for chemical probe studies which can obtain detailed information about individual sizes[66–68]. This structural database also provides a useful test of global optimization methods, and would represent a much tougher and more general examination than that provided by LJ clusters which are commonly used as a test system.

The known behaviour of LJ clusters provides a useful starting point for our study. For the majority of small sizes, icosahedral clusters are the lowest in energy. Northby has conducted a systematic survey for $13 \leq N \leq 147$ to find the lowest energy minima based on icosahedral structures[50]. Some of his results have since been superseded[69–73]. Of particular interest are the few sizes at which the lowest energy structures are not icosahedral, but instead decahedral or fcc[70–72]. For larger systems sequences of clusters with the optimal shape for the different morphologies have been compared[74–76]. In these comparisons, the energy is interpolated between the values of N for each cluster of the sequence. The values of N at which the lowest energy lines cross are indicators of the size for which a structural transition is likely to occur. These studies have shown that a decahedral sequence becomes most stable at $N \approx 1600$ and an fcc sequence[76] at $N \approx 10^5$.

2.2 Methods

2.2.1 The potential

The Morse potential[77] may be written as

$$V_M = \epsilon \sum_{i<j} e^{\rho_0(1-r_{ij}/r_0)}\left(e^{\rho_0(1-r_{ij}/r_0)} - 2\right), \tag{2.1}$$

where ϵ is the pair well depth and r_0 the equilibrium pair separation. In reduced units ($\epsilon = 1$ and $r_0 = 1$) the potential has a single adjustable parameter, ρ_0, which

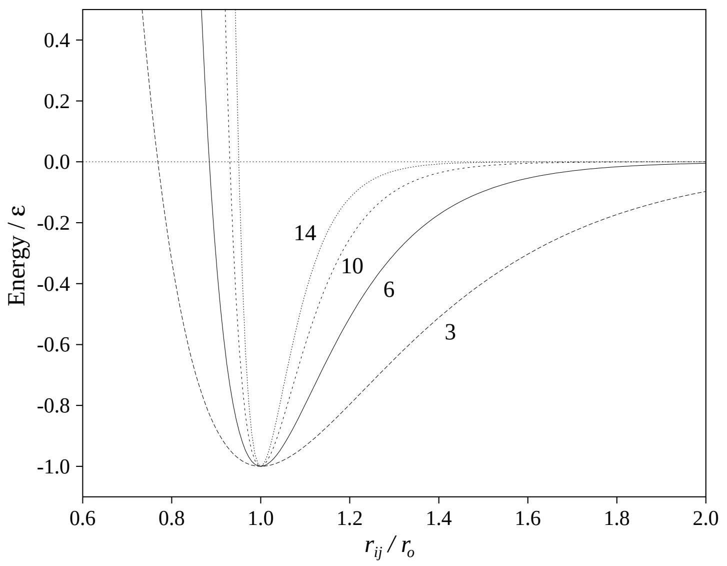

FIGURE 2.2: The Morse potential for different values of the range parameter ρ_0 as marked.

determines the range of the interparticle forces. Figure 2.2 shows that decreasing ρ_0 increases the range of the attractive part of the potential and softens the repulsive wall, thus widening the potential well. Values of ρ_0 appropriate to a wide range of materials have been catalogued elsewhere[78]. Here, we give some representative examples. The LJ potential, which provides a reasonable description of the rare gases, has the same curvature at the bottom of the well as the Morse potential when $\rho_0 = 6$. Girifalco has obtained an intermolecular potential for C_{60} molecules[79] which is isotropic and short-ranged relative to the equilibrium pair separation, with an effective value[80] of $\rho_0 = 13.62$. This potential was designed to describe the room temperature fcc solid phase in which the C_{60} molecules are able to rotate freely. The alkali metals have long-ranged interactions, for example ρ_0=3.15 has been suggested for sodium[81]. Fitting to bulk data gives a value of ρ_0=3.96 of nickel[82].

The structure of a cluster is given by the structure(s) associated with the global free energy minimum. At zero temperature, the structure with the lowest free energy is simply the global minimum of the PES. At higher temperatures, entropic factors must also be considered. Although we only perform a comprehensive survey of the zero Kelvin structure, some examples of the structural effects of temperature are discussed in §2.4.

To understand what factors cause a structure to have low potential energy and how these change with the value of the range parameter, ρ_0, it is instructive to look more closely at the form of the potential. The energy can be partitioned into three contributions as follows,

$$V_M = -n_{nn}\epsilon + E_{\text{strain}} + E_{nnn}. \tag{2.2}$$

The number of nearest-neighbour contacts, n_{nn}, the strain energy, E_{strain}, and the contribution to the energy from non-nearest neighbours, E_{nnn}, are given by

$$\begin{aligned} n_{nn} &= \sum_{i<j, x_{ij}<x_0} 1, \\ E_{\text{strain}} &= \epsilon \sum_{i<j, x_{ij}<x_0} (e^{-\rho_0 x_{ij}} - 1)^2, \\ E_{nnn} &= \epsilon \sum_{i<j, x_{ij}>x_0} e^{-\rho_0 x_{ij}}(e^{-\rho_0 x_{ij}} - 2), \end{aligned} \tag{2.3}$$

where $x_{ij} = r_{ij}/r_0 - 1$, and x_0 is a nearest-neighbour criterion. x_{ij} is the strain in the contact between atoms i and j.

The dominant term in the energy comes from n_{nn}. E_{nnn} is a smaller term and its value varies in a similar manner to n_{nn}. It is only likely to be important in determining the lowest energy structures when other factors are equal. For example, bulk fcc and hexagonal close-packed (hcp) lattices both have twelve nearest neighbours per atom. Next-nearest neighbour interactions are the cause of the lower energy of the hcp crystal when a pair potential such as the LJ form is used[83,84]. Non-nearest neighbour interactions also cause the contraction of nearest neighbour distances from the equilibrium pair value and this contraction increases with the range of the potential[41].

E_{strain}, which measures the energetic penalty for the deviation of a nearest-neighbour distance from the equilibrium pair distance, is a key quantity in this analysis. It should not be confused with strain due to an applied external force. For a given geometry, E_{strain} grows rapidly with increasing ρ_0 because the potential well narrows. This can be seen by taking a Taylor expansion of E_{strain} about $x_{ij} = 0$:

$$E_{\text{strain}} \approx \sum_{i<j, x_{ij}<x_0} \rho_0^2 x_{ij}^2 - \rho_0^3 x_{ij}^3 + 7\rho_0^4 x_{ij}^4/12 + \ldots \tag{2.4}$$

This expansion is valid when $\rho_0 x_{ij}$ is small. To a first approximation the strain energy grows quadratically with ρ_0. Thus decreasing the range destabilizes strained structures.

From this analysis we can see that minimization of the potential energy involves a balance between maximizing n_{nn}, and minimizing E_{strain}. The interior atoms of the three morphologies (Figure 2.1) all have twelve nearest neighbours, and so

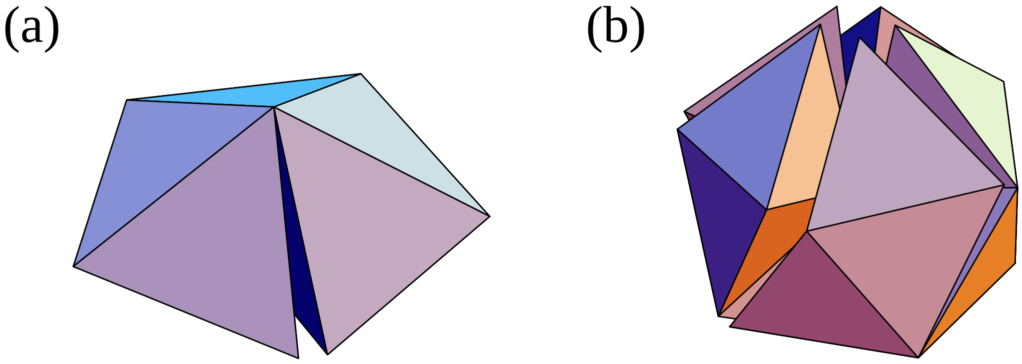

FIGURE 2.3: Examples of the strain involved in packing tetrahedra. (a) Five regular tetrahedra around a common edge. The angle of the gap is 7.36°. (b) Twenty regular tetrahedra about a common vertex. The gaps amount to 1.54 steradians.

differences in n_{nn} arise from surface effects. The optimal shape for each morphology results from the balance between maximizing the proportion of {111} faces (an atom on a {111} face is 9-coordinate, but on a {100} face only 8-coordinate) and minimizing the fraction of atoms in the surface layer. As Mackay icosahedra (Figure 2.1b) have only {111} faces and are approximately spherical, the icosahedral structures have the largest n_{nn}. Complete Mackay icosahedra occur at $N = 13, 55, 147, \ldots$ A pentagonal bipyramid has all {111} faces, but as it is not very spherical more stable decahedral forms are obtained by truncating the structure parallel to the five-fold axis to reveal five {100} faces and then introducing re-entrant {111} faces between adjacent {100} faces. The resulting structure is called a Marks' decahedron (Figure 2.1c) and was first predicted by the use of a modified Wulff construction[85]. The decahedral structures have lower values of n_{nn} than icosahedral structures because of the presence of the {100} faces. The tetrahedron and octahedron are fcc structures that have only {111} faces but they are not very spherical. The optimal fcc structure is the truncated octahedron with regular hexagonal faces (Figure 2.1a). At larger sizes than those considered in this study, the optimal structure involves further facetting, so that it more closely approximates the Wulff polyhedron[86]. Of the three morphologies fcc structures have the lowest values of n_{nn}.

However, icosahedral structures involve the most strain of the three structural types. The Mackay icosahedra can be considered to be made of twenty fcc tetrahedra which share a common vertex. As we see from Figure 2.3b, when twenty regular tetrahedra are packed around a common vertex large gaps remain. To bridge these gaps the tetrahedra have to be distorted, thus introducing strain into the structure. The distance between adjacent vertices of the icosahedron is 5% longer than the distance between a vertex and the centre. Similarly, a pentagonal bipyramid can be considered to be made up of five fcc tetrahedra sharing a common edge. Again, a gap remains if regular tetrahedra are used (Figure 2.3a) and consequently decahedral structures are necessarily strained, although to a lesser extent than icosahedral structures. By contrast, close-packed structures can be unstrained.

Having deduced the relative values of n_{nn} and E_{strain} for icosahedral, decahedral and fcc structures, we can predict the effect of the range on the competition between the three morphologies. For a moderately long-ranged potential, the strain associated with the icosahedral structures can be accommodated without too large an energetic penalty and so they are the most stable. As the range of the potential is decreased, the strain energy associated with the icosahedral structures increases rapidly, and there comes a point where decahedral structures become more stable. Similarly, for a sufficiently short-ranged potential fcc structures become more stable than decahedral structures.

The decomposition of the potential energy also helps us to understand the effect of size on the energetic competition between the three morphologies. The differences in n_{nn} between the morphologies, which arise from their different surface structures, are approximately proportional to the surface area ($\propto N^{2/3}$). The strain energies, though, are proportional to the volume ($\propto N$). Therefore, the differences in E_{strain} increase more rapidly with size than the differences in n_{nn}, thus explaining the changes in the most stable morphology from icosahedral to decahedral to fcc with increasing size. The effect of increasing the size is similar to the effect of decreasing the range of the potential: both destabilize strained structures. The most favourable morphology varies with both the size of the cluster and the range of the potential.

2.2.2 Searching the potential energy surface

The main method that we have used to generate candidate structures for the global minima makes use of the physical insight gained from the last section. We have simply attempted to construct those structures that maximize n_{nn} for the three ordered morphologies. The resulting geometries were then minimized by either the conjugate gradient[87] or eigenvector-following[88] methods. A similar approach was

Table 2.1: Number of known stationary points on the PES of M_{13} as a function of ρ_0. The number of stationary points that have not been found as a fraction of the total number is likely to be larger for transition states than minima, and to increase with ρ_0.

	$\rho_0 = 3$	$\rho_0 = 4$	$\rho_0 = 6$	$\rho_0 = 10$	$\rho_0 = 14$
minima	9	159	1441	9290	12717
transition states	27	687	8380	37499	54444

successfully used by Northby to generate low energy icosahedral structures for LJ clusters[50]. The effectiveness of this method is reflected by how few of Northby's lowest energy structures have been superseded and by the length of time that it has taken to find these exceptions[69–73]. As we will show in §2.4, some of the global minima that we have found by this method may be extremely difficult to find by an '*ab initio*' global optimization method. This method, though, does depend on the imagination of the practitioner to conceive of all the possible ways that a structure with a large value of n_{nn} could be obtained. Furthermore, the method will always fail to find the global minima if the latter is not based on one of the ordered types of cluster structure, as is the case for the larger clusters we have considered at low values of ρ_0.

Therefore, complementary to the above method, a number of global optimization techniques were used to try to find structures that might have been missed. First, we used molecular dynamics to explore the PES and generate configurations for minimization. Using high energy runs large regions of the PES are sampled, whereas low energy runs allow a more detailed search of a local region of the PES. Secondly, we used a method in which eigenvector-following is employed to take steps directly between minima on the PES[89]. If low temperature Metropolis Monte Carlo is used in this space of minima, the system will walk down to the bottom of a basin containing many minima. This technique avoids the difficulties associated with trapping in local minima that can occur for methods which take steps directly in configuration space. It is outlined further in Chapter 6. Thirdly, we used a global optimization method developed by David Wales which employs a 'basin hopping' technique.

The above three global optimization methods are least successful for short-ranged potentials. This is because the PES become more rugged as the range is decreased. As illustrated in Table 2.1 for M_{13}, the number of minima and transition

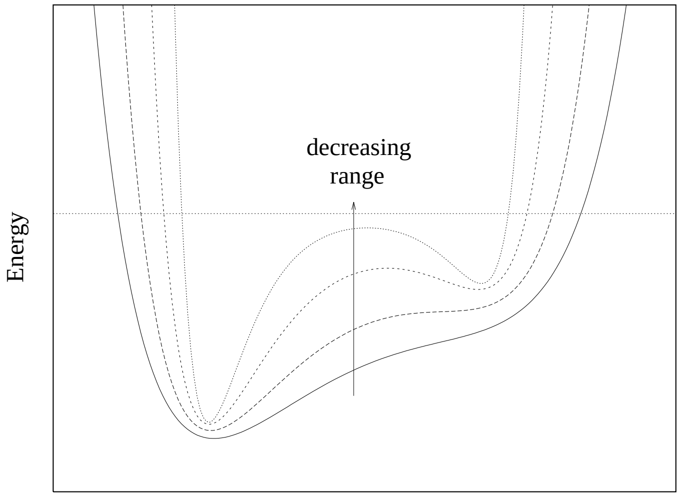

Figure 2.4: Schematic diagram to show how a higher energy minimum can be 'swallowed up' by a lower energy minimum as the range of the potential increases.

states on the PES increases with ρ_0. The physical reason for the larger number of minima at short range is the loss of accessible configuration space as the potential wells become narrower, thus producing barriers where there are none at long range. This effect is shown schematically in Figure 2.4.

Barrier heights are also likely to become higher and rearrangements more localized for a shorter-ranged potential. These trends have been observed in comparisons of the rearrangements of 55-particle C_{60} and LJ clusters[90]. Other effects are noted in a detailed analysis of the topography of the M_{13} PES in §6.3. These changes imply that the range of the potential is likely to have a significant effect on the dynamics, making escape from local minima much more difficult. This has been illustrated by Rose and Berry who have shown that the rate at which the ground state structure of a potassium chloride cluster is found upon cooling can be significantly decreased by using a shielded Coulomb potential to reduce the range of the interactions[91]. Similarly, Stillinger and Stillinger[92] and Bytheway and Kepert[60] both found that minimizations performed from random starting configurations are much more likely to find the global minimum for a long-ranged potential.

Finding the global minimum at short range can also be harder for a more subtle reason. Fcc and decahedral minima have a smaller degree of structural similarity with the large number of minima typical of the liquid-like state than the icosahedral structures. Therefore, the paths from the liquid-like state to the decahedral structures are likely to be fewer and longer than those to the icosahedral structures. This effect will be considered in more depth later in the thesis.

It must be emphasized, though, that none of these methods are guaranteed to find the global minimum. Finding the global minima for a PES with so many degrees of freedom is an NP-hard problem[93]. Morse clusters, however, provide an ideal system to compare different global optimization methods both because the complexity of the PES can be systematically varied by changing a single parameter and because this study provides a comprehensive catalogue of likely global minima.

2.3 Results

All the global minima that we have found are catalogued in Table 2.2 along with their energies, point groups, number of nearest neighbours, strain energies and the range of ρ_0 for which they are the lowest in energy. These minima are illustrated in the figures that appear throughout this chapter.

The results are summarized in Figure 2.5 which provides a zero temperature 'phase diagram', showing how the global minimum depends upon N and ρ_0. The structural behaviour of Morse clusters with less than eight atoms is rather uninteresting because the global minimum is independent of ρ_0. For all $N \geq 8$, however, the global minimum changes at least once as a function of ρ_0. For $N \geq 13$, icosahedral, decahedral and fcc structures all exist, and the form of the phase diagram is in very good agreement with the predictions made in §2.2.1. For most sizes the structure changes from icosahedral to decahedral to close-packed as the range of the potential is decreased. For $N < 23$, however, the transition from decahedral to close-packed occurs at larger values than we consider in this study. There are also a number of sizes (N=38–40, 52, 53, 59 and 61) at which there is a transition directly from an icosahedral to a close-packed structure; this occurs when n_{nn} for the lowest energy close-packed structure is greater than or equal to that for the lowest energy decahedral structure. It can be confirmed by examining Table 2.2 that the causes of these transitions are the relative values of n_{nn} and E_{strain}, as we suggested in §2.2.1.

The boundaries between the different morphologies are sensitive functions of N. Such size-dependence is observed for many properties of clusters, and gradually lessens as the size increases (because the addition of a single atom becomes a smaller perturbation) until the bulk limit is reached where properties are continuous functions of N. The decahedral to close-packed boundary is particularly

Table 2.2: Candidate global minima for $N \leq 80$. Energies are given in bold if the structure is the global minimum at that value of ρ_0. ρ_{min} and ρ_{max} give the range of ρ_0 for which the structure is the global minimum. E_{strain} has been calculated at ρ_0=10. If a structure is not stable at ρ_0=10 no value of E_{strain} is given. All energies are given in ϵ.

	PG	n_{nn}	E_{strain}	$\rho_0 = 3$	$\rho_0 = 6$	$\rho_0 = 10$	$\rho_0 = 14$	ρ_{min}	ρ_{max}
5A	D_{3h}	9	0.000	**-9.2995**	**-9.0449**	**-9.0036**	**-9.0003**		
6A	O_h	12	0.000	**-13.5442**	**-12.4878**	**-12.0949**	**-12.0182**		
7A	D_{5h}	16	0.062	**-17.5530**	**-16.2076**	**-15.9565**	**-15.8831**		
8A	D_{2d}	18	0.006	**-22.0429**	-19.1619	-18.2751	-18.0762		5.28
8B	C_s	19	0.062		**-19.3274**	**-18.9646**	**-18.8837**	5.28	
9A	D_{3h}	21	0.002	**-26.7784**	-22.3308	-21.2135	-21.0380		3.42
9B	C_{2v}	23	0.186	-26.6077	**-23.4172**	**-22.8508**	**-22.6449**	3.42	
10A	D_{4d}	24	0.002	-31.5198	-25.5039	-24.2050	-24.0320		2.28
10B	C_{3v}	27	0.694	**-31.8886**	**-27.4733**	**-26.5839**	**-26.1327**	2.28	
11A	D_{4d}	34	10.374	**-37.9308**	-28.7952	-23.6661			3.40
11B	C_{2v}	32		-37.8917				3.40	3.67
11C	C_{2v}	31	0.792		**-31.5219**	**-30.2652**	-29.5881	3.67	13.57
11D	C_s	30					**-29.5961**	13.57	15.29
11E	C_2	30	0.248	-36.6132	-30.6989	-29.8090	-29.5244	15.29	20.60
11F	C_{2v}	29	0.001	-36.6978	-30.4317	-29.2155	-29.0379	20.60	
12A	C_{2v}	38		-43.9713	-35.1999				2.63
12B	C_{5v}	36	1.704	**-44.0979**	**-36.4003**	**-34.3668**	-33.1159	2.63	12.15
12C	C_s	34					-33.1995	12.15	13.03
12D	D_{2d}	34	0.346	-41.8164	-34.8388	-33.7242	**-33.3323**	13.03	17.08
12E	D_{3h}	33	0.001	-42.1214	-34.5680	-33.2223	-33.0383	17.08	
13A	I_h	42	2.425	**-51.7370**	**-42.4399**	**-39.6630**	**-37.2589**		14.76
13B	D_{5h}	37	0.141	-49.9981	-39.3607	-37.2080	-36.7905	14.76	
14A	C_{2v}	46	4.373	**-56.7547**	-44.8275	-41.7170			3.23
14B	C_{3v}	45	2.425	-56.6605	**-45.6193**	**-42.6752**	-40.2598	3.23	13.06
14C	C_{2v}	41	0.141	-55.9716	-43.6340	-41.2493	**-40.7983**	13.06	
15A	D_{6d}	50	9.527	**-63.1621**	-47.5706	-40.5692	-35.7589		3.72
15B	C_{2v}	49	2.573	-62.5939	**-49.7484**	**-46.5414**	-44.0866	3.72	12.71
15C	C_{2v}	45	0.141	-62.6314	-47.9526	-45.2938	**-44.8064**	12.71	
16A	D_{3h}	54	11.222	**-69.1406**	-50.8342	-42.8876			3.39
16B	C_s	53	2.868	-68.7572	**-53.8458**	**-50.2619**	-47.8320	3.39	11.99
16C	C_{2v}	49	0.142	-68.5757	-52.2653	-49.3382	**-48.8145**	11.99	
17A	D_{3h}	58		**-75.6624**	-53.1560				3.42
17B	C_{3v}	57	3.372	-75.1474	-57.8845	-53.7722	-51.3296	3.42	4.88
17C	C_s	57	3.281	-75.0914	-57.9130	-53.8620	-51.4406	4.88	4.91
17D	C_2	57	3.163	-75.0054	**-57.9414**	**-53.9836**		4.91	11.30
17E	C_{2v}	53	0.142	-74.8689	-56.5736	-53.3823	**-52.8226**	11.30	
18A	C_2	65		**-82.5793**	-59.8814			2.14	3.03
18B	C_{5v}	62	4.500	-82.5489	**-62.6892**	**-57.6571**	-54.0597	3.03	10.35
18C	D_{5h}	57	0.142	-81.4902	-60.9265	-57.4297	**-56.8309**	10.35	

TABLE 2.2: continued.

	PG	n_{nn}	E_{strain}	$\rho_0 = 3$	$\rho_0 = 6$	$\rho_0 = 10$	$\rho_0 = 14$	ρ_{min}	ρ_{max}
19A	D_{5h}	68	6.001	**-90.6475**	**-68.4923**	**-62.1668**	-56.6767		10.70
19B	C_{2v}	61	0.151	-87.4857	-65.0648	-61.4271	**-60.8124**	10.70	
20A	C_{2v}	72	6.507	**-97.4174**	**-72.5078**	**-65.6791**	-61.3272	2.02	10.24
20B	C_{2v}	65	0.162	-94.2224	-69.2027	-65.4237	**-64.7920**	10.24	
21A	C_{2v}	76	7.133	**-104.337**	-76.4873	-69.0687	-65.1796		5.40
21B	C_1	76	6.922	-104.004	**-76.5291**	-69.2763	-65.7789	5.40	9.84
21C	C_s	69	0.169		-73.5770	**-69.4499**	**-68.7836**	9.84	
22A	C_s	81	8.198	**-112.041**	**-81.1367**	-73.0143	-68.5809		9.58
22B	C_1	73	0.169		-77.8879	**-73.4943**	**-72.7917**	9.58	
23A	D_{3h}	87	10.597	**-120.787**	**-86.7355**	-76.6306	-70.8161		8.35
23B	D_{3h}	84	6.097	-116.279	-84.9406	-78.1439	-74.4424	8.35	9.71
23C	C_s	78	0.433		-83.5049	**-78.3254**	**-77.3025**	9.71	22.45
23D	C_1	76	0.007		-82.2527	-76.8988	-76.1575	22.45	
24A	C_s	91	10.947	**-127.885**	**-90.6854**	-80.2955	-74.6137	2.79	8.55
24B	C_1	82	0.434		-87.8204	**-82.3702**	**-81.3095**	8.55	15.34
24C	C_{2v}	81	0.007		-87.6268	-81.9414	-81.1642	15.34	
25A	C_s	96	12.090	**-136.073**	**-95.1279**	-84.1688		2.62	7.76
25B	C_{3v}	87	0.893		-93.3428	**-86.9897**	**-85.4774**	7.76	15.40
25C	C_s	85	0.010		-92.2415	-86.0154	-85.1768	15.40	
26A	T_d	102	15.393	**-145.322**	**-100.550**	-86.8823			7.89
26B	C_{2v}	91	0.491	-138.941	-97.3632	**-91.3703**	**-90.2108**	7.89	14.20
26C	D_{3h}	90	0.008		-97.6487	-91.0851	-90.1893	14.20	
27A	C_s	106		**-152.514**	-104.489				4.72
27B	C_{2v}	106		-151.735	**-104.745**			4.72	7.71
27C	C_s	97	3.076		-102.750	-94.7362	-91.2366	7.71	8.53
27D	C_s	95	0.491	-146.171	-101.723	**-95.4195**	**-94.2198**	8.53	14.22
27E	C_s	94	0.008		-101.920	-95.1213	-94.1956	14.22	
28A	C_s	111		**-160.773**	-108.855				4.82
28B	C_s	111		-160.385	**-108.998**			4.82	6.70
28C	C_{3v}	102	3.369		-108.186	-99.5240	-95.6921	6.70	8.88
28D	C_s	100	0.983		-107.214	**-100.008**	**-98.3317**	8.88	14.57
28E	C_{2v}	98	0.008		-106.239	-99.1611	-98.2021	14.57	
29A	D_{3h}	117		**-170.116**	**-114.146**				6.90
29B	C_1	106	3.370		-112.656	-103.586	-99.7027	6.90	8.95
29C	C_1	104	0.988		-111.544	**-104.051**	-102.333	8.95	11.07
29D	C_{2v}	103	0.246		-111.509	-103.946	-102.744	11.07	11.17
29E	D_{5h}	103	0.225	-164.721	-111.354	-103.927	**-102.775**	11.17	21.90
29F	C_{3v}	102	0.010		-111.135	-103.299	-102.227	21.90	
30A	C_{2v}	121		**-177.579**	-118.116				4.47
30B	C_{2v}	121	8.279	-176.941	**-118.433**	-103.408		4.47	6.86
30C	C_{2v}	109	1.538		-117.011	**-108.571**	-106.426	6.86	12.61
30D	C_s	107	0.238		-115.941	-107.985	**-106.765**	12.61	21.33
30E	C_s	106	0.012		-115.625	-107.368	-106.239	21.33	

Table 2.2: continued.

	PG	n_{nn}	E_{strain}	$\rho_0 = 3$	$\rho_0 = 6$	$\rho_0 = 10$	$\rho_0 = 14$	ρ_{min}	ρ_{max}
31A	C_1	126		**-185.984**	-122.440				4.60
31B	C_s	126		-185.299	**-122.858**			4.60	6.35
31C	C_s	115	3.490		-122.342	-112.543	-108.723	6.35	8.95
31D	C_s	112	0.276		-121.535	**-113.057**	-111.711	8.95	10.42
31E	C_{2v}	112	0.246	-181.901	-121.367	-113.048	**-111.761**	10.42	20.90
31F	C_s	111	0.011		-120.805	-112.376	-111.240	20.90	
32A	C_{2v}	132		**-195.468**	-127.644				5.93
32B	C_{2v}	120	3.83		**-127.771**	**-117.284**		5.93	10.27
32C	C_s	116	0.269		-125.954	-117.117	-115.733	10.27	11.33
32D	C_1	116	0.260		-125.950	-117.106	**-115.748**	11.33	20.32
32E	C_s	115	0.011		-125.126	-116.416	-115.246	20.32	
33A	C_s	137		**-204.209**	-131.704				5.35
33B	C_{5v}	137		-203.575	-131.774			5.35	5.74
33C	C_s	124	3.832		**-132.287**	-121.352		5.74	8.46
33D	C_{2v}	121	0.313		-131.556	-122.160	-120.666	8.46	9.71
33E	C_{2v}	121	0.269		-131.379	**-122.167**	**-120.741**	9.71	19.88
33F	C_s	120	0.011		-130.467	-121.455	-120.253	19.88	
34A	D_{5h}	143		**-214.068**	-136.468				5.87
34B	C_{2v}	128	3.832	-209.947	**-136.798**	-125.420		5.87	8.52
34C	C_s	125	0.313		-135.989	-126.212	-124.675	8.52	9.79
34D	C_s	125	0.293		-135.973	**-126.214**	**-124.711**	9.79	19.06
34E	C_{4v}	124	0.013		-135.486	-125.616	-124.282	19.06	
35A	C_s	147		**-221.771**	-140.503				4.05
35B	C_{3v}	147		-221.294	-141.106			4.05	5.62
35C	C_1	133	3.975		**-141.957**	-130.282	-126.120	5.62	8.08
35D	C_{2v}	130	0.304		-141.403	**-131.274**	**-129.700**	8.08	18.65
35E	C_{3v}	129	0.011		-140.132	-130.533	-129.265	18.65	
36A	C_s	152		**-230.508**	-144.827				4.68
36B	C_1	152		-229.689	-145.274			4.68	5.07
36C	C_s	138	4.35		**-147.382**	-134.989		5.07	9.51
36D	C_1	134	0.334		-145.985	**-135.313**	-133.656	9.51	10.50
36E	C_s	134	0.314		-145.748	-135.305	**-133.691**	10.50	18.42
36F	C_s	133	0.013		-145.279	-134.701	-133.296	18.42	
37A	C_s	158		**-240.008**	-149.766				5.25
37B	C_1	142	4.35		**-151.891**	-139.056	-134.765	5.25	7.62
37C	C_{2v}	139	0.357		-151.436	**-140.360**	-138.622	7.62	10.57
37D	C_s	139	0.318		-151.078	-140.343	**-138.690**	10.57	18.29
37E	C_s	138	0.014		-150.885	-139.776	-138.308	18.29	
38A	D_2	164	30.138	**-249.159**	-153.209	-134.320			3.15
38B	C_1	163	27.962	-249.088	-154.165	-135.519	-129.339	3.15	4.70
38C	C_s	163		-248.600	-154.042			4.70	4.76
38D	O_h	144	0.013	-246.415	-157.407	**-145.850**	**-144.321**	4.76	5.40
								6.95	
38E	C_{5v}	147	3.714		**-157.477**	-144.756		5.40	6.95

Table 2.2: continued.

	PG	n_{nn}	E_{strain}	$\rho_0 = 3$	$\rho_0 = 6$	$\rho_0 = 10$	$\rho_0 = 14$	ρ_{min}	ρ_{max}
39A	C_{2v}	169		**-258.945**	-158.266				4.48
39B	C_{5v}	153	5.039		**-163.482**	-149.456		4.48	9.46
39C	C_{4v}	148	0.014		-161.702	**-149.887**	**-148.327**	9.46	
40A	C_s	174		**-268.395**	-163.957				4.51
40B	C_s	157	5.040	-263.925	**-167.993**	-153.524	-148.493	4.51	9.51
40C	D_{4h}	152	0.014	-261.116	-165.996	**-153.925**	**-152.334**	9.51	
41A	C_{2v}	180		**-278.406**					4.60
41B	C_s	161	5.040	-273.700	**-172.527**	-157.593		4.60	8.75
41C	C_{2v}	157	0.435		-171.125	-158.506	-156.512	8.75	9.60
41D	C_s	157	0.368	-269.035	-170.808	**-158.521**	-156.631	9.60	11.06
41E	C_{2v}	157	0.366	-267.688	-170.759	-158.518	**-156.633**	11.06	16.83
41F	C_{3v}	156	0.015		-170.898	-158.063	-156.359	16.83	
42A	C_{3v}	186		**-288.335**	-172.252				4.54
42B	C_s	166	5.275	-282.296	**-177.680**	-162.366	-157.125	4.54	9.77
42C	C_s	161	0.368		-175.184	**-162.566**	-160.638	9.77	11.10
42D	C_s	161	0.367		-175.136	-162.564	**-160.641**	11.10	16.82
42E	C_s	160	0.017		-175.405	-162.134	-160.371	16.82	
43A	C_{2v}	192		**-298.172**	-175.540				4.40
43B	C_s	171		-290.632	**-183.093**			4.40	9.34
43C	C_{2v}	166	0.443		-180.838	-167.586	-165.511	9.34	9.57
43D	C_{2v}	166	0.374	-288.302	-180.515	**-167.603**	**-165.635**	9.57	16.67
43E	C_s	165	0.016	-289.533	-180.590	-167.142	-165.371	16.67	
44A	C_{5v}	198		**-308.277**	-179.032				4.38
44B	C_1	175	5.722	-302.004	**-187.626**	-171.071	-165.690	4.38	9.38
44C	C_s	170	0.443		-185.214	-171.631	-169.519	9.38	9.65
44D	C_s	170	0.374	-300.114	-184.841	**-171.645**	**-169.642**	9.65	16.67
44E	C_1	169	0.016		-184.937	-171.182	-169.378	16.67	
45A	I_h	204		**-318.661**	-182.301				4.24
45B	C_1	180	5.965	-310.750	**-192.955**	-175.389	-169.713	4.24	8.75
45C	C_{2v}	175	0.452		-190.548	**-176.666**	-174.510	8.75	11.79
45D	C_{2v}	175	0.451	-303.604	-190.500	-176.663	**-174.512**	11.79	15.10
45E	C_s	174	0.016		-190.275	-176.222	-174.384	15.10	
46A	C_s	207		**-327.033**					3.96
46B	C_{2v}	186	6.646	-320.119	**-199.178**	**-181.236**	-174.605	3.96	10.46
46C	C_s	179	0.452		-194.924	-180.711	-178.518	10.46	11.79
46D	C_s	179	0.451		-194.877	-180.709	**-178.519**	11.79	15.11
46E	C_s	178	0.016		-194.622	-180.262	-178.391	15.11	
47A	C_3	210	40.212	**-336.666**	-194.242	-170.368			4.03
47B	C_1	190	6.648	-331.591	**-203.704**	-185.302	-178.621	4.03	9.60
47C	C_{2v}	184	0.461	-323.011	-200.257	**-185.746**	**-183.508**	9.60	14.94
47D	C_{3v}	183	0.016		-199.964	-185.302	-183.397	14.94	

Table 2.2: continued.

	PG	n_{nn}	E_{strain}	$\rho_0 = 3$	$\rho_0 = 6$	$\rho_0 = 10$	$\rho_0 = 14$	ρ_{min}	ρ_{max}
48A	C_{2v}	213		**-346.663**					4.01
48B	C_s	195	7.464	-340.396	**-209.044**	-189.557	-182.618	4.01	9.81
48C	C_s	188	0.461		-204.632	**-189.791**	**-187.516**	9.81	14.72
48D	C_s	187	0.020		-205.419	-189.535	-187.440	14.72	
49A	C_s	219		**-356.413**					3.91
49B	C_{3v}	201	7.770	-350.540	**-215.254**	**-195.275**	-187.212	3.91	10.32
49C	D_{5h}	193	0.471	-337.433	-210.010	-194.828	**-192.504**	10.32	21.18
49D	C_s	191	0.023		-210.023	-193.595	-191.449	21.18	
50A	C_{5v}	224		**-366.636**					4.04
50B	C_s	205	7.770		**-219.820**	**-199.345**	-191.240	4.04	10.12
50C	C_s	197	0.455		-216.105	-199.188	**-196.612**	10.12	15.27
50D	C_1	196	0.023		-215.519	-198.666	-196.462	15.27	
51A	C_2	232		**-376.673**	-217.628				3.74
51B	C_{2v}	210	9.360	-373.933	**-225.391**	-202.912		3.74	9.46
51C	C_s	202	0.863		-221.114	**-203.757**	-200.829	9.46	10.17
51D	C_s	201	0.022		-220.986	-203.737	**-201.474**	10.17	
52A	C_s	238		**-387.587**					3.71
52B	C_{3v}	216	9.618	-384.521	**-231.615**	-208.673	-199.353	3.71	9.36
52C	D_{2h}	207	0.021		-227.346	**-209.769**	**-207.479**	9.36	
53A	D_{6d}	244		**-398.783**					3.70
53B	C_{2v}	222	9.902	-395.150	**-237.835**	**-214.410**	-203.181	3.70	10.32
53C	C_s	211	0.021		-231.694	-213.809	**-211.486**	10.32	
54A	C_s	248		**-407.966**	-232.987				3.41
54B	C_{5v}	228	10.215	-405.832	**-244.058**	**-220.119**	-208.330	3.41	10.32
54C	C_{2v}	217	0.465		-238.115	-219.427	**-216.637**	10.32	15.17
54D	C_{2v}	216	0.021		-237.038	-218.849	-216.492	15.17	
55A	C_1	252		**-417.919**					3.25
55B	I_h	234	10.543	-416.626	**-250.287**	**-225.814**	-213.524	3.25	11.15
55C	C_{2v}	221	0.465		-242.622	-223.482	**-220.646**	11.15	15.18
55D	C_s	220	0.021		-241.385	-222.889	-220.498	15.18	
56A	C_s	258		**-428.611**					3.60
56B	C_{3v}	237	10.545	-425.709	**-253.923**	**-228.900**	-216.538	3.60	10.18
56C	C_{2v}	226	0.481		-248.168	-228.553	-225.633	10.18	11.38
56D	C_s	226	0.465		-248.051	-228.534	**-225.655**	11.38	15.20
56E	D_{2h}	225	0.021	-410.499	-246.729	-227.929	-225.505	15.20	
57A	D_{3h}	264		**-439.960**					4.13
57B	C_s	241	10.563	-436.125	**-258.042**	-232.878	-220.503	4.13	9.61
57C	C_{2v}	231	0.465	-426.762	-253.482	**-233.586**	**-230.664**	9.61	21.83
57D	C_s	229	0.028		-252.749	-232.227	-229.557	21.83	
58A	C_s	267		**-449.432**	-253.759				4.05
58B	C_{3v}	246	10.585	-442.501	**-263.411**	**-237.898**	-225.469	4.05	10.13
58C	C_s	235	0.481		-258.106	-237.660	-234.652	10.13	11.76
58D	C_s	235	0.476		-258.102	-237.649	-234.661	11.76	11.85
58E	C_1	235	0.465		-257.876	-237.631	**-234.671**	11.85	14.94
58F	C_{3v}	234	0.027		-258.241	-237.298	-234.570	14.94	

Table 2.2: continued.

	PG	n_{nn}	E_{strain}	$\rho_0 = 3$	$\rho_0 = 6$	$\rho_0 = 10$	$\rho_0 = 14$	ρ_{min}	ρ_{max}
59A	C_{3v}	267		**-459.509**	-260.795				3.77
59B	C_{2v}	272		-459.250	-261.475			3.77	4.26
59C	C_1	250	10.832		-267.858	-241.706	-229.054	4.26	4.86
								7.93	9.09
59D	C_{2v}	250	10.939	-453.110	**-267.945**	-241.627	-228.849	4.86	7.93
59E	T_d	240	0.027		-264.710	**-243.331**	**-240.572**	9.09	
60A	C_s	278		**-470.448**					4.51
60B	C_s	255	11.042		**-273.341**	-246.579	-233.702	4.51	9.34
60C	C_s	245	0.540		-269.408	**-247.786**	-244.566	9.34	11.00
60D	C_{2v}	245	0.536		-269.292	-247.782	-244.572	11.00	13.95
60E	C_s	244	0.027		-269.050	-247.371	**-244.579**	13.95	
61A	T_d	284		**-482.026**	-271.693				4.65
61B	C_{2v}	260	11.174		**-278.727**	-251.502	-238.499	4.65	9.54
61C	C_{3v}	249	0.027		-274.135	**-252.397**	**-249.587**	9.54	
62A	C_s	293		**-491.052**	-272.268				4.00
62B	C_s	264	11.707	-485.426	**-283.183**	-255.038	-241.549	4.00	6.33
62C	C_{2v}	264	11.174		-283.103	-255.559	-242.510	6.33	9.24
62D	C_1	254	0.623		-279.852	-256.900	-253.442	9.24	9.78
62E	C_s	254	0.560		-279.460	**-256.908**	-253.555	9.78	10.47
62F	C_1	254	0.526		-279.358	-256.897	**-253.613**	10.47	14.15
62G	C_1	253	0.027	-476.610	-278.482	-256.437	-253.593	14.15	
63A	C_s	301		**-501.732**					3.83
63B	C_1	269	11.880	-497.182	**-288.561**	-259.921	-246.279	3.83	8.87
63C	C_s	259	0.533	495.357	-285.142	**-262.030**	**-258.621**	8.87	14.16
63D	C_s	258	0.027		-283.826	-261.477	-258.600	14.16	
64A	D_{3d}	307		**-512.832**					3.85
64B	C_s	274	12.066	-503.235	**-293.932**	-264.790	-250.989	3.85	8.22
64C	C_{2v}	265	0.552	-501.818	-291.412	**-268.024**	**-264.587**	8.22	24.31
64D	C_s	262	0.031		-289.324	-265.715	-262.643	24.31	
65A	C_s	310		**-523.446**					3.86
65B	C_1	278	12.494		-298.322	-268.407	-254.407	3.86	4.74
65C	C_2	278	12.574	-515.415	**-298.392**	-268.352	-254.301	4.74	6.32
65D	C_1	278	12.081		-298.318	-268.837	-254.984	6.32	8.12
65E	C_{2v}	269	0.603		-296.318	**-272.099**	-268.514	8.12	10.53
65F	C_1	269	0.565		-296.028	-272.084	-268.578	10.53	11.30
65G	C_1	269	0.552		-295.807	-272.070	**-268.595**	11.30	19.72
65H	C_s	267	0.027		-293.515	-270.557	-267.613	19.72	
66A	C_s	314		**-534.464**					3.82
66B	C_1	284	15.128	-530.517	-303.513	-271.712	-256.391	3.82	4.83
66C	C_1	283	12.758	-528.937	**-303.763**	-273.223	-259.079	4.83	7.83
66D	C_s	274	0.640		-301.866	-277.135	-273.454	7.83	9.74
66E	C_s	274	0.573		-301.465	**-277.145**	-273.574	9.74	11.50
66F	C_s	274	0.552		-301.193	-277.116	**-273.602**	11.50	24.31
66G	C_s	271	0.033		-299.454	-274.861	-271.668	24.31	

TABLE 2.2: continued.

	PG	n_{nn}	E_{strain}	$\rho_0 = 3$	$\rho_0 = 6$	$\rho_0 = 10$	$\rho_0 = 14$	ρ_{min}	ρ_{max}
67A	C_s	318		**-544.754**	-297.548				3.80
67B	C_s	289	15.345	-539.667	-308.980	-276.565		3.80	5.46
67C	C_2	288	12.945	-538.179	**-309.130**	-278.090	-263.853	5.46	7.72
67D	C_{2v}	279	0.677		-307.349	**-282.172**	-278.396	7.72	11.36
67E	C_{2v}	279	0.674		-307.234	-282.166	**-278.401**	11.36	21.85
67F	C_{3v}	276	0.032		-304.942	-279.933	-276.681	21.85	
68A	C_s	324		**-555.582**					3.68
68B	C_1	294	15.980	-551.451	**-314.375**	-281.011	-265.754	3.68	7.29
68C	C_s	293	12.938	-549.986	-314.147	-281.905	-267.101	7.29	7.78
68D	C_1	283	0.666		-311.913	-286.250	-282.430	7.78	9.67
68E	C_{2v}	283	0.597		-311.516	**-286.263**	-282.554	9.67	11.24
68F	C_s	283	0.573		-311.247	-286.237	-282.588	11.24	11.51
68G	C_{2v}	283	0.552		-310.974	-286.208	-282.618	11.51	13.47
68H	C_{3v}	282	0.031		-311.260	-285.949	**-282.682**	13.47	
69A	C_1	329		**-566.364**	-307.246				3.65
69B	C_1	308		-560.639	-318.206			3.65	4.22
69C	C_{5v}	298	14.909	-559.783	-319.688	-286.265		4.22	5.22
69D	C_s	299	16.223		**-319.820**	-285.837		5.22	7.64
69E	C_s	288	0.705		-317.396	-291.284	-287.367	7.64	9.66
69F	C_1	288	0.653		-317.293	**-291.294**	**-287.462**	9.66	18.06
69G	C_1	286	0.033		-315.850	-290.023	-286.694	18.06	
70A	C_{2v}	335		**-577.740**					3.22
70B	C_1	332		-577.287	-313.363			3.22	3.67
70C	C_5	314		-571.815	-324.212			3.67	4.16
70D	C_{5v}	304	15.324	-570.747	**-325.888**	-291.872		4.16	7.89
70E	C_s	293	0.676		-323.082	**-296.412**	**-292.439**	7.89	17.69
70F	C_s	291	0.035		-321.460	-295.097	-291.707	17.69	
71A	C_1	330		**-588.397**	-316.491				3.42
71B	C_5	320		-583.203	-330.363			3.42	4.28
71C	C_{5v}	310	17.608	-581.945	**-331.589**	-295.612		4.28	7.29
71D	C_{2v}	299	0.695		-329.356	**-302.405**	**-298.405**	7.29	21.50
71E	C_{2v}	296	0.034	-575.523	-326.901	-300.164	-296.719	21.50	
72A	C_1	335		**-599.690**	-320.666				3.40
72B	C_1	314	17.960	-595.065	-335.877	-299.301	-283.195	3.40	4.77
72C	C_s	313	16.818	-592.641	**-336.122**	-299.750	-283.664	4.77	7.29
72D	C_1	303	0.713		-333.968	**-306.460**	-302.387	7.29	10.53
72E	C_1	303	0.695		-333.804	-306.454	**-302.413**	10.53	21.49
72F	C_s	300	0.037		-331.605	-304.245	-300.732	21.49	
73A	C_3	339		**-610.937**	-324.743				3.50
73B	C_s	319	18.316	-603.874	**-341.266**	-304.027	-287.806	3.50	6.97
73C	C_s	318	16.192	-602.727	-340.979	-305.190	-289.451	6.97	7.03
73D	C_s	308	0.725		-339.405	**-311.518**	-307.374	7.03	10.72
73E	C_s	308	0.695		-339.242	-311.503	**-307.421**	10.72	21.49
73F	C_s	305	0.037	-597.775	-336.825	-309.251	-305.732	21.49	

Table 2.2: continued.

	PG	n_{nn}	E_{strain}	$\rho_0 = 3$	$\rho_0 = 6$	$\rho_0 = 10$	$\rho_0 = 14$	ρ_{min}	ρ_{max}
74A	C_{3v}	357		**-622.680**					3.92
74B	C_s	324	18.513	-614.020	**-346.611**	-308.886		3.92	6.83
74C	C_{5v}	313	0.699	-610.492	-345.200	**-316.651**	**-312.441**	6.83	21.38
74D	C_s	310	0.035		-342.317	-314.324	-310.745	21.38	
75A	C_s	364		**-633.513**					3.70
75B	C_1	328	18.559	-630.521	-351.177	-312.987	-296.599	3.70	5.81
75C	D_{5h}	319	0.718		**-351.472**	**-322.644**	**-318.407**	5.81	21.14
75D	C_{4v}	316	0.035		-348.841	-320.398	-316.758	21.14	
76A	C_s	370		**-644.952**					3.56
76B	C_1	334	21.847	-642.129	-355.971	-315.525	-298.049	3.56	4.16
76C	C_1	333	19.297	-641.559	**-356.250**	-317.225	-300.489	4.16	6.10
76D	C_s	323	0.737		-356.085	**-326.697**	-322.387	6.10	10.93
76E	C_{2v}	323	0.718		-355.772	-326.683	**-322.414**	10.93	21.14
76F	C_s	320	0.035		-353.246	-324.440	-320.764	21.14	
77A	C_1	368		**-656.080**	-349.696				3.68
77B	C_s	339	22.562	-650.116	-361.293	-319.898		3.68	5.01
77C	C_1	339	22.076		-361.416	-320.372	-302.897	5.01	5.24
77D	C_s	338	19.503	-647.494	**-361.591**	-322.075		5.24	6.04
77E	C_{2v}	328	0.749		-361.521	**-331.754**	**-327.372**	6.04	20.66
77F	C_s	325	0.035		-358.645	-329.483	-325.771	20.66	
78A	C_3	384		**-667.576**					3.54
78B	C_1	344	22.724	-664.006	-366.727	-324.815	-307.287	3.54	5.18
78C	C_1	344	22.651		**-366.761**	-324.883	-307.076	5.18	6.04
78D	C_s	338	11.849		-366.723	-330.163	-315.401	6.04	6.53
78E	C_1	332	0.769		-366.132	**-335.807**	-331.349	6.53	10.71
78F	C_s	332	0.749	-650.436	-365.872	-335.796	**-331.379**	10.71	16.80
78G	C_s	330	0.036		-364.252	-334.558	-330.784	16.80	
79A	C_1	385		**-678.940**	-358.580				3.59
79B	C_{2v}	348	19.381	-673.565	**-372.832**	-332.365		3.59	6.53
79C	C_{2v}	343	11.973		-372.466	-335.139	-320.223	6.53	6.67
79D	C_{2v}	337	0.783	-663.444	-371.568	**-340.862**	-336.332	6.67	11.06
79E	C_s	337	0.752	-659.186	-371.199	-340.834	-336.380	11.06	11.55
79F	O_h	336	0.036		-370.784	-340.632	**-336.796**	11.55	
80A	C_3	387		**-690.578**					3.53
80B	C_s	354	21.858	-683.221	**-378.333**	-335.898		3.53	6.36
80C	C_1	348	12.120		-377.972	-340.072	-324.944	6.36	7.34
80D	C_1	341	0.806	-674.292	-376.176	**-344.911**	-340.304	7.34	10.44
80E	C_s	341	0.783		-375.919	-344.904	-340.340	10.44	11.02
80F	C_s	341	0.752	-668.582	-375.572	-344.878	-340.387	11.02	11.57
80G	C_{4v}	340	0.036		-375.075	-344.669	**-340.803**	11.57	

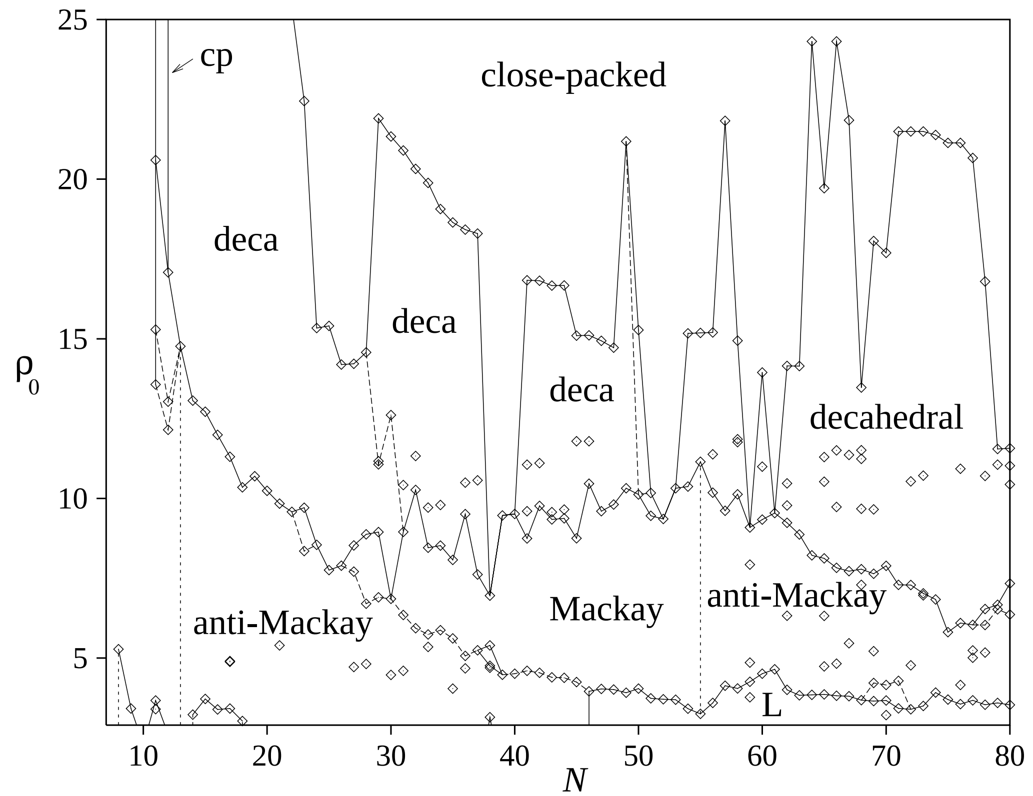

FIGURE 2.5: Zero temperature 'phase diagram' showing the variation of the lowest energy structure with N and ρ_0. The data points are the values of ρ_0 at which the global minimum changes. The lines joining the data points divide the phase diagram into regions where the global minima have similar structures. The solid lines denote the boundaries between the four main structural types—icosahedral, decahedral, close-packed and those associated with low ρ_0 (L)—and the dashed lines internal boundaries within a structural type, e.g. between icosahedral structures with Mackay and anti-Mackay overlayers, or between decahedral structures with different length decahedral axes.

sensitive, because the range of ρ_0 for which the decahedral structure is most stable changes dramatically even when the difference in n_{nn} between the decahedral and close-packed structures changes by one.

Sizes for which a morphology is the lowest in energy for a particularly large range of ρ_0 indicate that the structure is especially stable. The optimal structures shown in Figure 2.1 are particularly good examples of this. Another indicator of sizes of especial stability is provided by $\Delta_2 E(N) = E(N+1) + E(N-1) - 2E(N)$. Peaks in $\Delta_2 E$ have been found to correlate well with the magic numbers (sizes at which clusters are particularly abundant) observed in mass spectroscopic studies of clusters formed in molecular beams[94]. Plots of $\Delta_2 E$ are shown in Figure 2.6 for a number of values of ρ_0. Unsurprisingly, the plot for ρ_0=6 is very similar to that

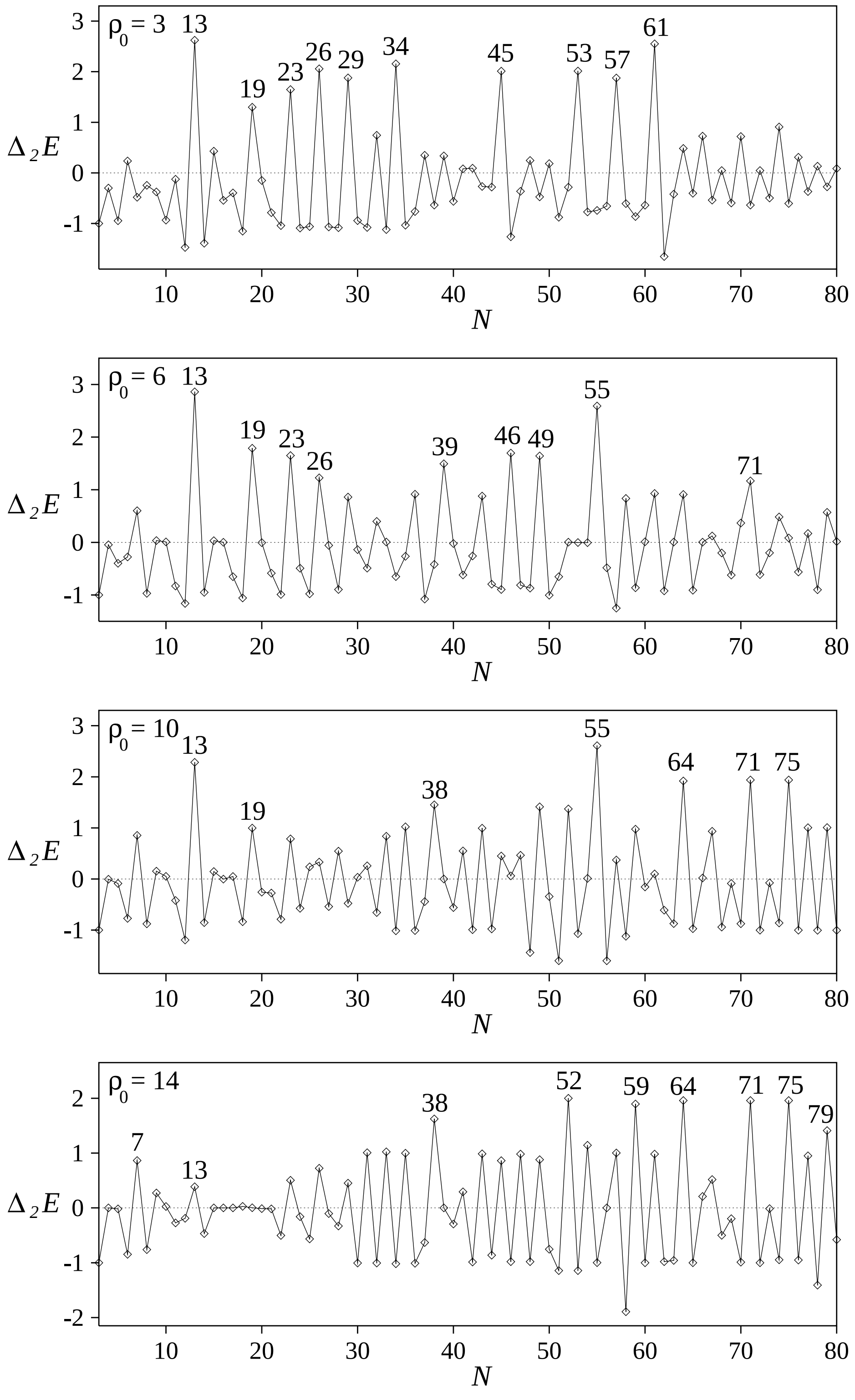

FIGURE 2.6: Plots of $\Delta_2 E$ as a function of N for ρ_0=3, 6, 10 and 14 as marked.

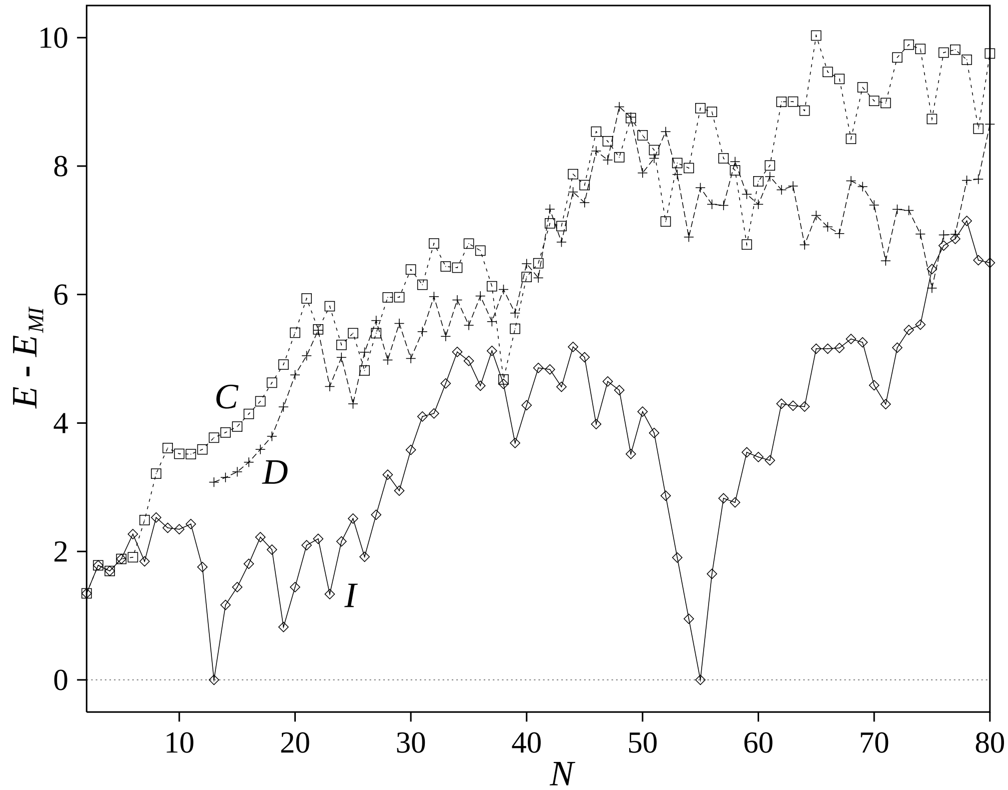

FIGURE 2.7: Comparison of the energies of icosahedral (solid line with diamonds), decahedral (dashed line with crosses) and close-packed (dotted line with squares) M_N clusters at ρ_0=6. The energy zero is E_{MI}, the interpolated energy of Mackay icosahedra. $E_{MI} = -3.0354 + 0.2624N^{1/3} + 8.8400N^{2/3} - 6.8381N$ and was obtained by fitting to the first four Mackay icosahedra (N=13, 55, 147 and 309).

for LJ clusters with peaks due to especially stable icosahedral clusters. At higher values of ρ_0 peaks corresponding to especially stable close-packed and decahedral clusters begin to occur. The plot at ρ_0=14 is very similar to that recently obtained for C_{60} clusters using the Girifalco potential[95]. Similarly, if the energy is normalized by subtracting a suitable function of N, again particularly stable sizes stand out (Figure 2.7).

In the following subsections we will look at the growth sequences for each structural class in more detail. As well as the three ordered morphologies, we also examine the unusual structures that occur for the larger clusters at low ρ_0, which, as we will see, involve a mixture of order and disorder.

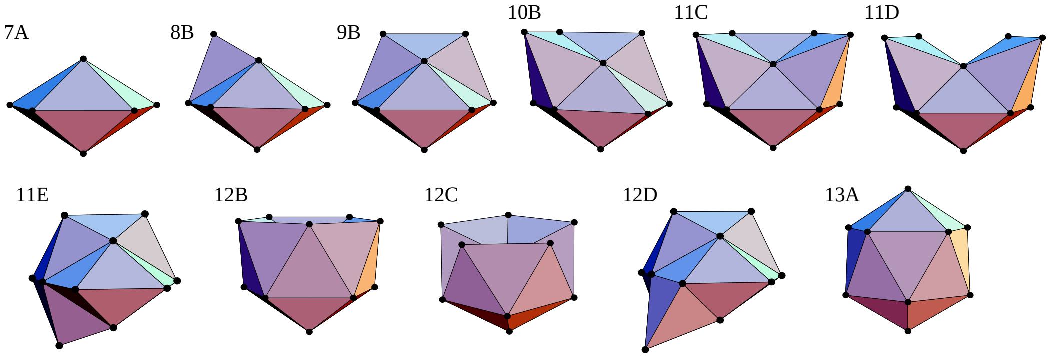

FIGURE 2.8: Global minima for $N \leq 13$ which are formed by growth on the 7-atom pentagonal bipyramid and which lead to the 13-atom icosahedron.

2.3.1 Icosahedral clusters

The growth sequence that leads from the 7-atom pentagonal bipyramid to the 13-atom icosahedron is shown in Figure 2.8. The growth occurs by the capping of the faces on one half of the bipyramid. For M_{11} and M_{12}, related structures become the global minimum at short range. Firstly, a symmetry breaking of structures 11C and 12B occurs. This results in the loss of one (11D) or two (12C) nearest-neighbour bonds, but also allows the other nearest-neighbour contacts to relax closer to the pair equilibrium distance. At still larger ρ_0, structures 11E and 12D, which involve capping of the faces on both sides of the pentagonal bipyramid, become lowest in energy. These structures have fewer nearest neighbours, but they are also less strained. All the structures shown in Figure 2.8 are polytetrahedral, in the sense that the whole of the cluster can be divided into tetrahedra with atoms at the vertices.

Addition of atoms to the 13-atom icosahedron can occur in two ways. The two types of overlayer that result are illustrated in Figure 2.9. One growth mode continues the fcc packing of the twenty strained tetrahedra making up the icosahedron, and leads to the 55-atom Mackay icosahedron (Figure 2.1b). This growth mode introduces octahedral interstices, and so the resulting structures are no longer polytetrahedral. The other growth mode involves sites which are hcp with respect to the tetrahedra, and has been termed the anti-Mackay overlayer. For growth on the 13-atom icosahedron, this overlayer preserves polytetrahedral character. Each of the vertices of the original icosahedron becomes icosahedrally coordinated, and the structure that results from the completion of this overlayer, 45A, is a rhombic tricontahedron; it is an icosahedron of interpenetrating icosahedra. Interestingly, the rhombic tricontahedron is the face-dual of the truncated icosahedron

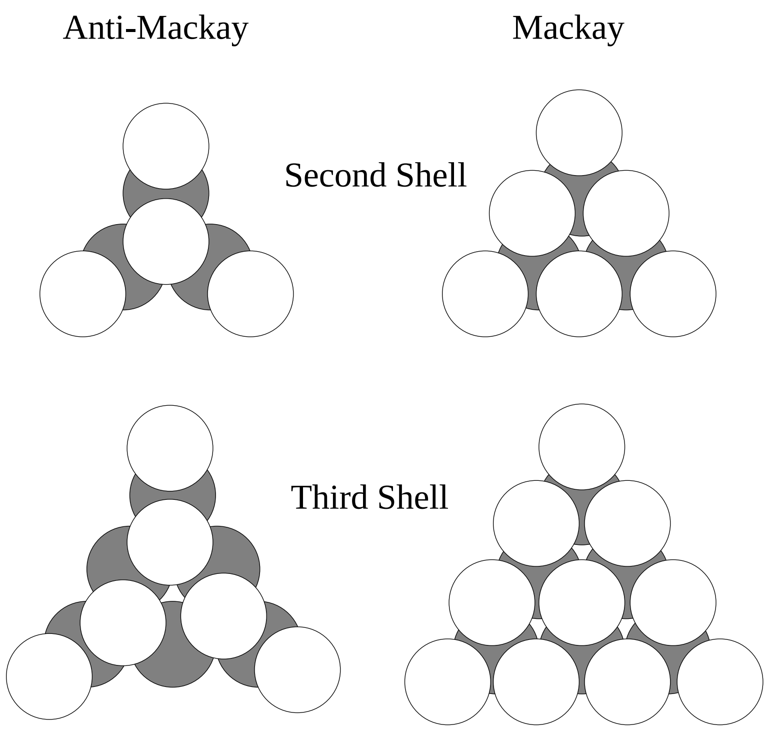

FIGURE 2.9: Atomic positions for the two possible overlayers of the icosahedron, anti-Mackay (left) and Mackay (right). These are shown for a single face of the icosahedron.

made famous by C_{60}; indeed, it is even a particularly stable shell for the coverage of a C_{60} molecule by alkaline earth metal atoms[96]. In previous studies, the anti-Mackay overlayer has been referred to as the polyicosahedral[43–45] or the face-capping overlayer[50]. Such names are reasonable for growth on the 13-atom icosahedron, but are confusing for growth on larger Mackay icosahedra.

The icosahedral structures with an anti-Mackay overlayer are illustrated in Figure 2.10 and those with an Mackay overlayer in Figure 2.11. Growth from the 13-atom icosahedron begins in the anti-Mackay positions, because these do not include any low-coordinate edge sites, thus giving the structures a larger n_{nn}. However, at some critical size the Mackay overlayer becomes lower in energy, because of the larger strain energies associated with the anti-Mackay overlayer. Further growth then leads to the next Mackay icosahedron. The size at which this change occurs depends on the range of the potential; it is given by the dashed line of negative slope that divides the icosahedral region of the phase diagram (Figure 2.5). The crossover size increases with the range of the potential; a long-ranged potential can accommodate the greater strain associated with the anti-Mackay overlayer more easily.

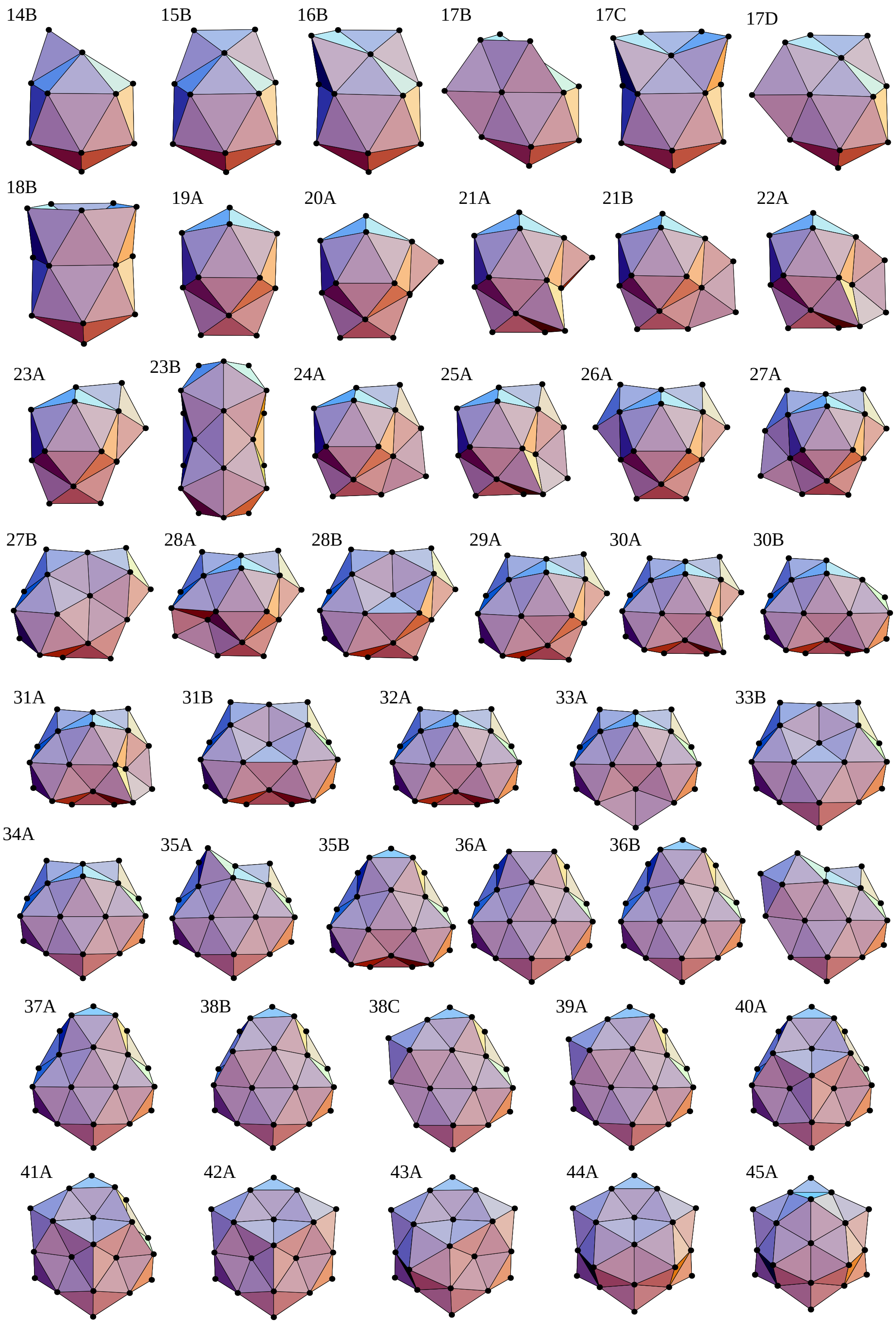

FIGURE 2.10: Icosahedral global minima formed by growth of an anti-Mackay overlayer on the 13-atom icosahedron, except structure 23B which is composed of two face-sharing icosahedra.

At $\rho_0 = 6$ the Mackay overlayer is occupied for $N \geq 32$. This compares to $N \geq 31$ for LJ clusters; as expected the results are very similar. In *ab initio* molecular dynamics calculations for lithium clusters[97], the anti-Mackay overlayer is lowest in energy up to $N = 45$. Similarly, polytetrahedral structures were observed in a tight-binding study of sodium clusters up to the largest size considered N=34 (for which 34A was the most stable structure)[98]. These effects are nicely explained by the long range of alkali metal potentials.

Especially stable structures with an anti-Mackay overlayer occur when the icosahedral coordination of a vertex atom is complete. These structures give rise to the peaks in $\Delta_2 E$ at N=19, 23 26, 29, 34 and 45 for ρ_0=3; only the first four of these peaks are seen at ρ_0=6, and only the first at ρ_0=10 (Figure 2.6). Some of these magic numbers have been observed in mass spectroscopic studies of rare gases[47,48] and even barium[99]. The centres of the icosahedra in these structure form a dimer for 19A, an equilateral triangle for 23A, a tetrahedron for 26A, a trigonal bipyramid for 29A, a pentagonal bipyramid for 34A, and an icosahedron for 45A. At a number of sizes there is more than one global minimum with an anti-Mackay overlayer. The transitions between these structures are related to slight differences in the value of E_{strain}. Also illustrated in Figure 2.10 is structure 23B, which is made up of two face-sharing icosahedra. It can be formed from structure 17B by the addition of six atoms not to the icosahedron but to the atoms which are part of the overlayer.

The first global minimum with a Mackay overlayer occurs at N=27. Especially stable structures occur at those sizes for which complete faces of the 55-atom Mackay icosahedra are missing. These structures give rise to the peaks at N=39, 46 and 49 for ρ_0=6 and correspond to 5, 2 and 1 missing faces, respectively. Again, these magic numbers have been seen in mass spectra of rare gases[48].

Structure 38E has an atom missing from a vertex of the original 13-atom icosahedron to allow the overlayer to complete a particularly stable form. This structure was not found in Northby's study of icosahedral LJ clusters, even though it is the lowest energy LJ icosahedral cluster[73].

The icosahedral global minima with more than 55 atoms are shown in Figure 2.12. As for the 13-atom icosahedron, growth initially occurs at the anti-Mackay sites, because this results in structures with larger n_{nn}. Completion of this overlayer occurs for a cluster with 127 atoms. The vertex atoms of the 55-atom Mackay icosahedron become icosahedrally coordinated, but the edge atoms have a decahedral (13B) coordination shell (this is clearly visible for 59C) leading to the half

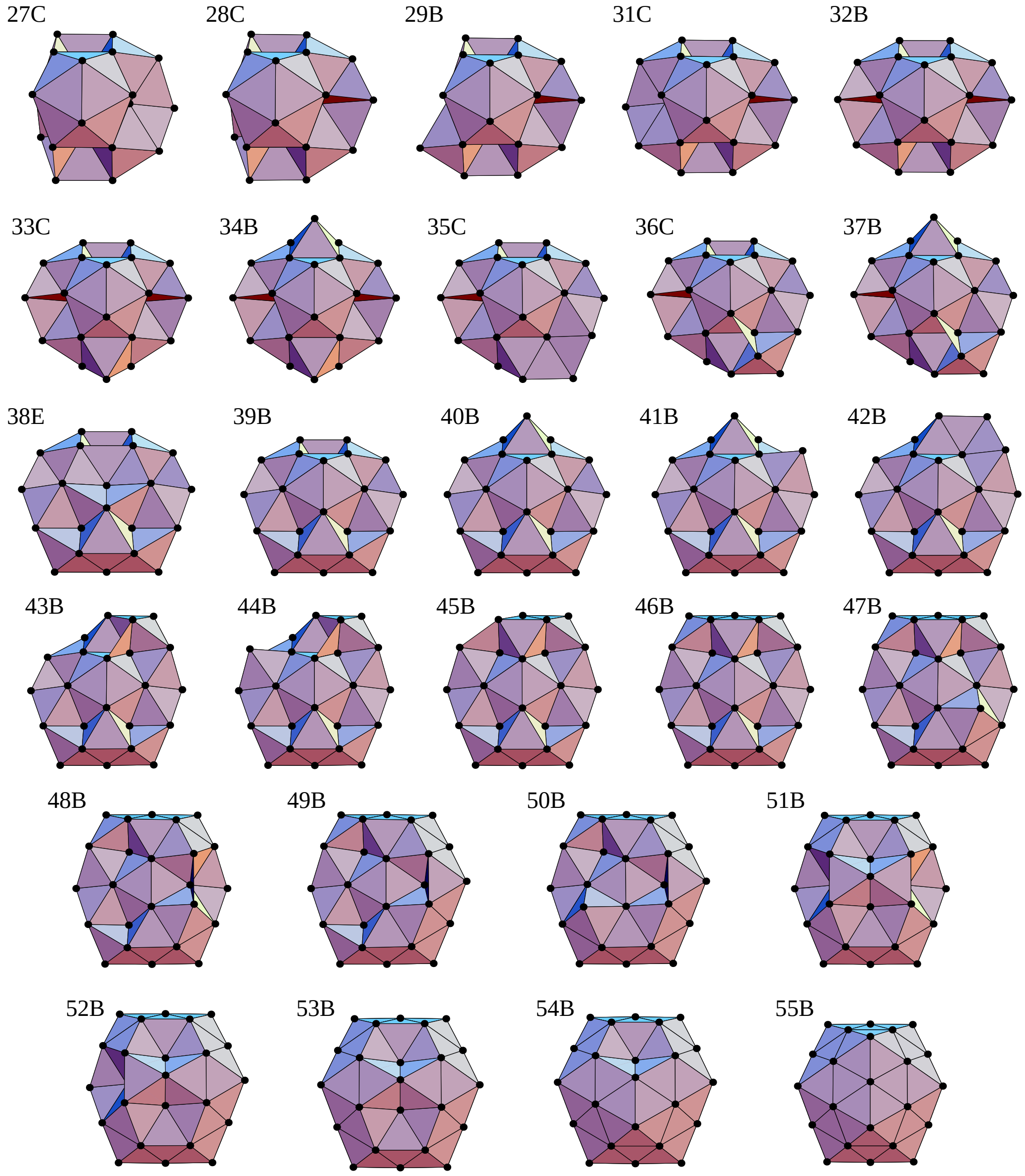

FIGURE 2.11: Icosahedral global minima formed by growth of an Mackay overlayer on the 13-atom icosahedron.

octahedra that are visible in the surface layers of the anti-Mackay clusters. The most prominent peak in $\Delta_2 E$ due to an anti-Mackay structure occurs at N=71 for ρ_0=6. This corresponds to an overlayer which completely covers the five faces surrounding a vertex of the underlying icosahedron. There are smaller peaks at N=58, 61, and 64, which correspond to complete coverage of one, two and three faces, respectively.

Similar to 38E, structure 69C has a vertex atom missing from the underlying Mackay icosahedra. There are also structures (62C, 65D, 72C and 75B) where an atom is added to the surface of the overlayer rather than to the Mackay icosahedra.

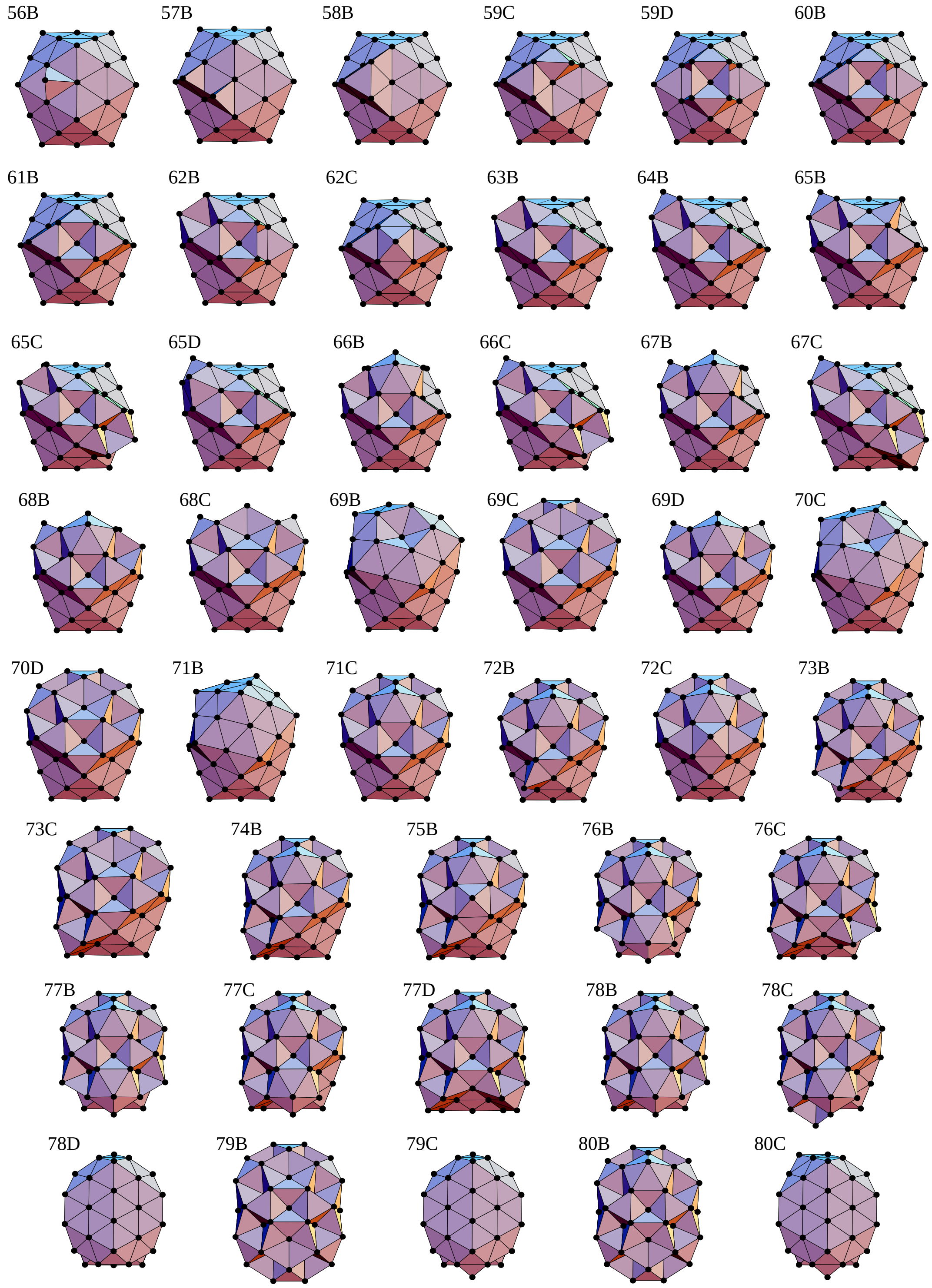

FIGURE 2.12: Icosahedral global minima formed by growth from the 55-atom Mackay icosahedron.

The first structure in this size range with a Mackay overlayer is 78D. It is expected that the size at which the crossover from an anti-Mackay to a Mackay overlayer again increases with the range of the potential, but to confirm this prediction the study would need to be extended to larger sizes. There are also three icosahedral global minimum, 69B, 70C and 71B, which do not fit neatly into either the Mackay or anti-Mackay category. The surface layer has a Mackay-like character, but it is not in correct alignment with the underlying icosahedron. The overlayer has been given a twist about one of the fivefold axis in order to collapse some of the half octahedra at the edge of the overlayer into trigonal bipyramids in a multiple diamond-square-diamond (DSD) process[100]. In fact for M_{71} at ρ_0=5, the lowest energy Mackay structure is a transition state which mediates a multiple DSD rearrangement between two permutational isomers of 71B.

Figure 2.7 provides an illuminating illustration of the variation of the icosahedral energies with size. The complete Mackay icosahedra represent narrow minima, which are separated by broad maxima corresponding to structures with an incomplete outer shell. At ρ_0=6 it is only near the top of these maxima that fcc and decahedral structures begin to have similar energies, such as at N=38 and 75.

2.3.2 Decahedral clusters

The decahedral global minima are shown in Figures 2.13–2.15. The structures have been grouped by the number of the atoms along the fivefold axis of the pentagonal bipyramid upon which they are based.

The growth sequence for the decahedral clusters is quite simple; they grow by capping exposed {100} faces and by filling in the grooves produced by the re-entrant {111} faces. As this process progresses the structure changes from prolate to approximately spherical to oblate. This cycle begins again when a prolate cluster with a longer decahedral axis becomes lower in energy than the oblate cluster (e.g. at $N \approx 30$ and 50). For the clusters based upon a pentagonal bipyramid with 5 atoms along the fivefold axis ($N \geq 50$), the growth proceeds asymmetrically—the decahedral axis does not always pass through the center of the cluster. For example, for 54C the surface structure of the 75-atom Marks' decahedron is completed on one side of the cluster before atoms are added to the other.

Deviations from this basic growth scheme occur for N=21–30 (Figure 2.13) and 51C. These structures are formed by addition of atoms to the {111} faces

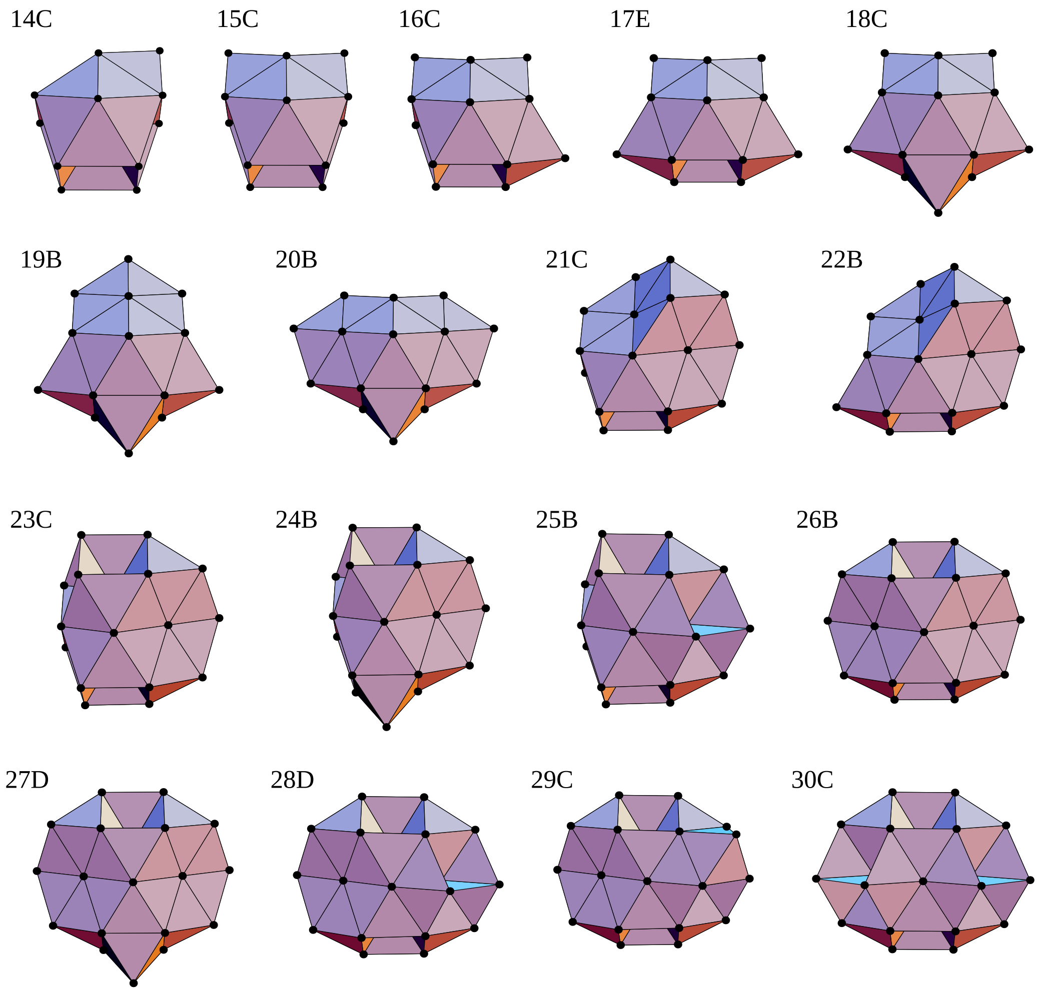

Figure 2.13: Global minima based upon a decahedron with three atoms along the fivefold axis.

surrounding the fivefold axis in the hcp sites with respect to the five fcc tetrahedra that make up the decahedral structures. These structures are more favourable even though they are more strained than the usual decahedral structures, because they have a larger n_{nn}. For N=21–30 these structures are actually fragments of the 55-atom Mackay icosahedron. The difference from the icosahedral structures is that the growth occurs from the five tetrahedra at the bottom of the Mackay icosahedron, rather than the centre.

As we mentioned in §2.2.1 the complete Marks' decahehedron, 75C, is particularly stable. The value of ρ_0 at which it becomes the global minimum (5.81) is the lowest of any of the decahedral structures. It is also the global minimum[71] for LJ_{75}. This stability is also indicated by the large peak in $\Delta_2 E$ for ρ_0=10 and 14. Other particular stable structures occur at N=64 and 71; these are fragments of 75C with 3 and 4 $\{100\}$ faces of the Marks' decahedron complete.

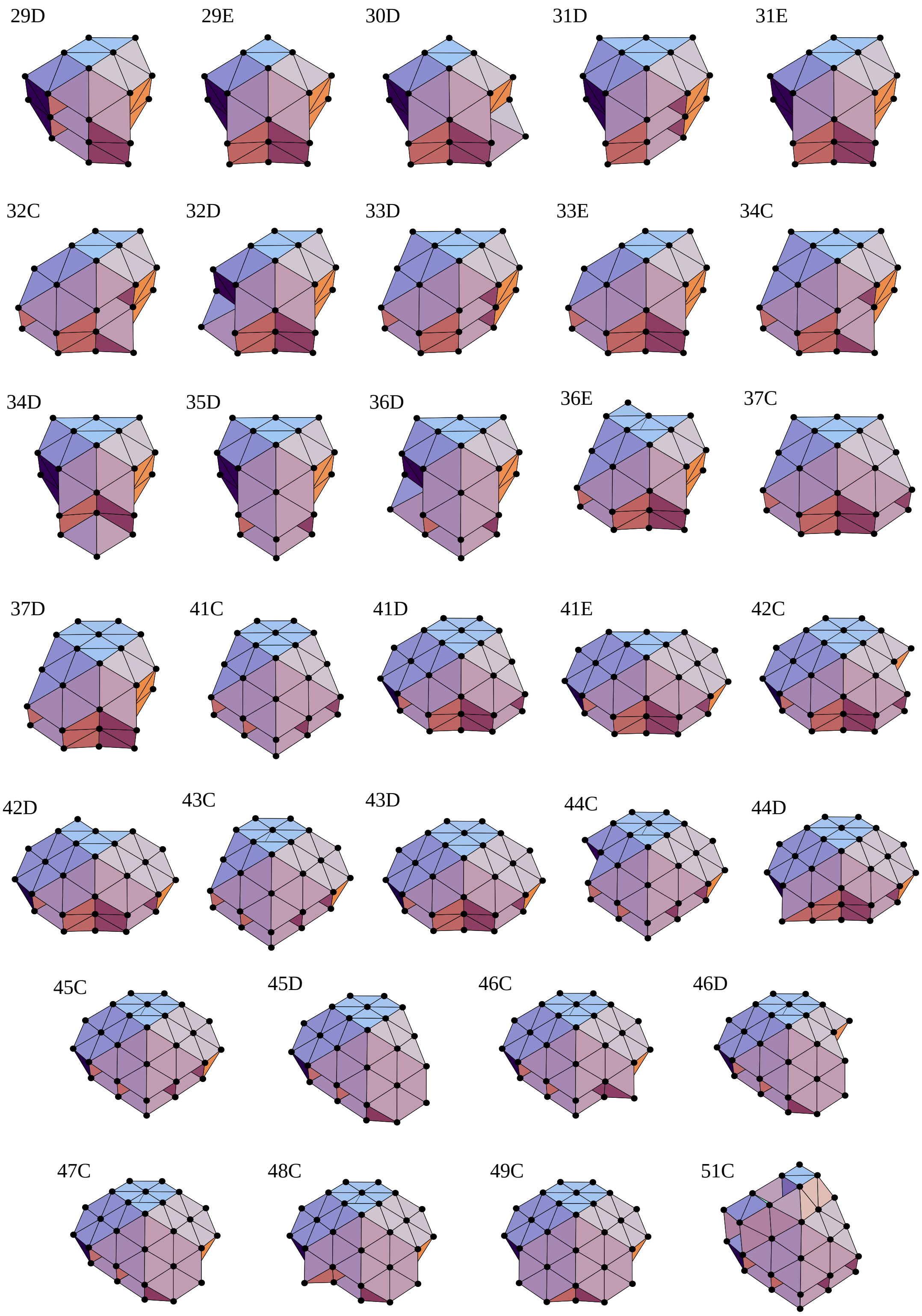

Figure 2.14: Global minima based upon a decahedron with four atoms along the fivefold axis.

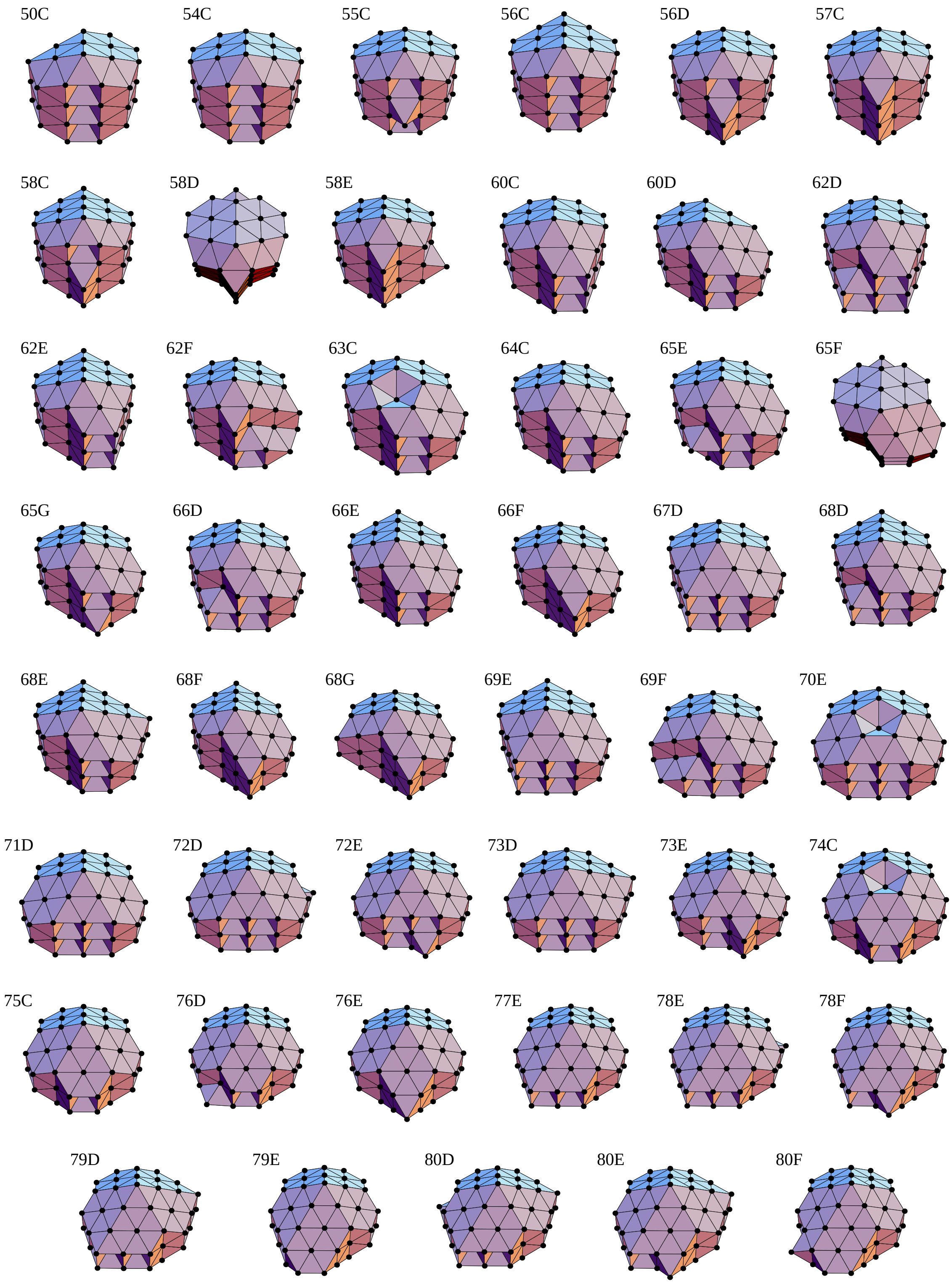

Figure 2.15: Global minima based upon a decahedron with five atoms along the fivefold axis.

2.3.3 Close-packed clusters

The close-packed global minima are illustrated in Figure 2.16. They have a diverse range of structures: there are 30 minima that are pure fcc, 10 that are pure hcp and 20 that involve a mixture of stacking sequences and twin planes. The global minima are broadly based on four structures: the hcp 26C, the two truncated octahedra, 38D and 79F; and the tetrahedral 59D,

The 38-atom truncated octahedron is the most stable fcc cluster in the size range we consider. It becomes the global minimum at the lowest value of ρ_0 (4.76) of any of the close-packed structures. Curiously, there are two ranges of ρ_0 for which it is the global minimum. At long range, E_{nnn} represents a significant part of the total energy. The truncated octahedron is most stable for $4.76 < \rho_0 < 5.40$ because it is approximately spherical and so has a larger value of E_{nnn} than the more oblate icosahedral structure 38E. For shorter-ranged potentials, the contribution of E_{nnn} diminishes and so 38E becomes the global minimum for $5.40 < \rho_0 < 6.95$ because it has a larger n_{nn}. Then for $\rho_0 > 6.95$ the truncated octahedron again becomes the global minimum because it has a lower strain energy than 38E. There is a growing body of experimental evidence for the importance of truncated octahedra. EXAFS (extended x-ray absorption fine structure) spectra of small gold clusters suggest that truncated octahedral clusters are present, particularly the 38-atom truncated octahedron[101]. Gold clusters passivated by alkylthiolate molecules selectively form truncated octahedra, which can even be isolated and formed into superlattices[7]. The structure is also observed for ligated 38-atom platinum clusters[5].

Most of the structures with between 38 and 79 atoms are broadly based on a growth sequence that goes between the two truncated octahedra. It proceeds by addition of overlayers to four of the {111} faces and by capping any new (2×2) {100} faces created. For example, there is a peak in $\Delta_2 E$ at $\rho_0 = 14$ that is caused by the low energy of 52C; this structure is formed by the addition of complete overlayers to two faces of 38D. For a number of sizes, the structures that result from adding the overlayers in fcc or hcp sites with respect to {111} faces have the same n_{nn}. For these cases the structures with the hcp overlayers are often lower in energy because they have a larger value of E_{nnn}—some of the third nearest neighbours are at 1.63 rather than 1.73 times the equilibrium pair separation. Examples include 41F, 42C, 64D, 66G, 67F, 68H, 69G, 70F and 72F.

The exceptions to the above growth sequence are those structures—49D, 50D, 51D, 57D, 58F and 60E—that are based on structure 59D. This structure is a 31-

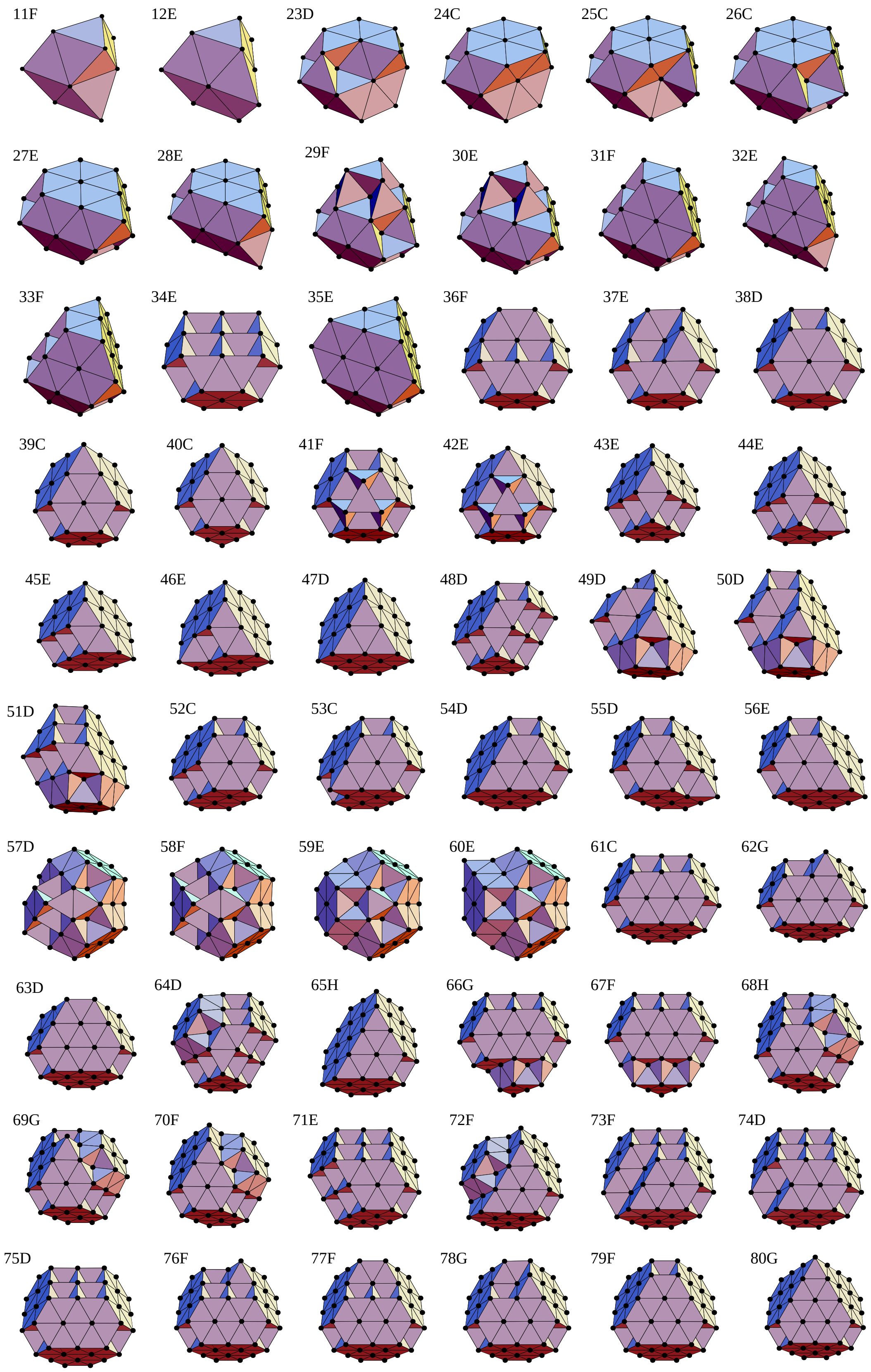

Figure 2.16: Global minima based on close-packing.

atom truncated tetrahedron with the faces covered by four seven-atom hexagonal overlayers occupying hcp sites with respect to the underlying tetrahedron. The smaller of those structures based on 59D have no overlayer on one face of the underlying tetrahedron. The stability of 59D comes from the combination of its high proportion of {111} faces and spherical shape. Interestingly, if atoms are added to one of the grooves in the structure a decahedral-like axis results, suggesting a possible transformation route between decahedral and closed-packed clusters.

It is worth noting that the cuboctahedron is not the lowest energy close-packed structure for N=55. In fact, it has five fewer nearest neighbours than structure 55D. Consequently, one has interpret with caution those studies in which cuboctahedra have been compared with Mackay icosahedra[75,102–104]; the cuboctahedra are likely to be suboptimal fcc structures, thus making the comparison unfair.

2.3.4 Structures at long range

In this subsection, we consider those structures which become the global minimum only at low values of ρ_0. We have restricted our study to those clusters with $\rho_0 \geq 3$, since we know of no cluster system for which longer-ranged potentials are of relevance. It may well be that further changes in the global minima occur[60] at lower ρ_0. The low ρ_0 structures that we have found separate into two size ranges, those with N close to N=13 and those with $N > 45$; they are shown in Figures 2.17 and 2.18, respectively.

The group of structures associated with low ρ_0 are close to spherical in shape and in the main are highly strained in order to maximize n_{nn}. The exceptions are 8A, 9A and 10A (Figure 2.17). These clusters have smaller values of n_{nn} than the other low energy minima (Figure 2.8), but are more stable because of a larger contribution from E_{nnn}; the next-nearest neighbour shell is significantly closer than for the incomplete icosahedra. In each case the structures are roughly spherical but do not have an atom in the centre of the cluster.

The majority of the other structures are polytetrahedral, that is the whole volume of the cluster can be divided into tetrahedra with atoms at the vertices. As we noted in §2.3.1, the 13-atom icosahedron is polytetrahedral. In this structure, each nearest-neighbour bond between the centre and a vertex is the common edge of five tetrahedra. This is also true of all the nearest-neighbour bonds of the rhombic tricontahedron (45A) which do not lie on the surface. Nearest-neighbour bonds which are surrounded by a different number of tetrahedra are said to have

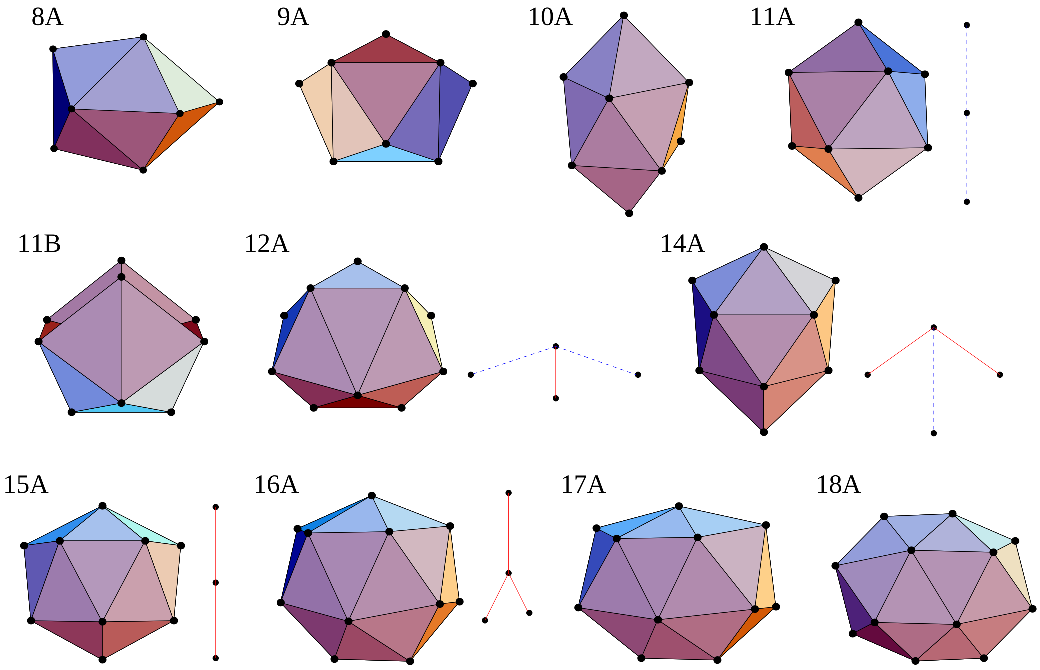

FIGURE 2.17: Global minima for small clusters at low values of ρ_0. If appropriate, the disclination network is displayed next to each structure. $-72°$ disclinations are represented by red lines, and $+72°$ disclinations by blue lines.

defects called disclination lines running along the bond. Those bonds with more than five tetrahedra are termed negative disclinations (if there are six it is a $-72°$ disclination, if there are seven a $-144°$ disclination, ...) and those with fewer than five tetrahedra are positive disclinations (if there are four it is a $+72°$ disclination and if there are three a $+144°$ disclination). Most of the structures associated with low ρ_0 are polytetrahedral structures that involve disclinations. Although packing five tetrahedra around a nearest-neighbour bond involves some strain, the strain energy associated with packing more or less tetrahedra around a bond is greater. Therefore, structures involving disclinations are only likely to be lowest in energy for long-ranged potentials for which the associated strain can be most easily accommodated, and only if the structures have a larger n_{nn} than disclination-free structures. A $-72°$ disclination line involves less strain than a $+72°$ disclination line as can be deduced from the gap that remains when five regular tetrahedra share a common edge (Figure 2.3a). Consequently, structures which involve only negative disclinations, or an excess of them, are more common amongst the low ρ_0 global minima.

To calculate the network of disclination lines in a structure, one must first partition space according to the Voronoi procedure, in which each point in space is assigned to the Voronoi polyhedron of the atom to which it is closest. This allows nearest neighbours to be defined as those atoms whose Voronoi polyhedra share a face. The Delaunay network that results from joining all such nearest neighbours is the dual of the Voronoi construction and divides all space into tetrahedra. This definition of a nearest neighbour has been termed geometric, rather than physical (e.g. using a cutoff distance), and the division of space into tetrahedra that this method achieves is artificial in the sense that it is independent of whether a polytetrahedral description is appropriate. In practice we determined the Voronoi polyhedra by using the fact that a set of four atoms constitutes a Delaunay tetrahedron if the sphere that touches all four atoms contains no other atoms[105]. The centre of this sphere is then a vertex of the Voronoi polyhedron of each atom. As the number of tetrahedra around a nearest-neighbour bond is the same as the number of sides on the face common to the Voronoi polyhedra of both nearest neighbours, disclination lines can then be assigned. However, problems can occur in assigning the Delaunay network if there are more than four atoms exactly on the surface of the sphere. Such a degeneracy, which only occurs as a result of symmetry, renders the analysis non-unique. This is the case for the 55-atom Mackay icosahedra and for bulk close-packed solids because of the presence of octahedra, but is not a problem here since we only apply the method to clusters that are polytetrahedral in character. One further consideration is that the analysis should not be applied to nearest-neighbour bonds between the surface atoms of a cluster.

The smallest global minimum that involves a disclination line is 11A. It involves a central atom surrounded by a 10-atom coordination shell, which has the structure of the hollow cluster 10A. The encapsulation of the central atom gives the structure a larger n_{nn} than the incomplete icosahedron 11B, but results in a larger strain energy (Table 2.2); the surface is in tension. The structure involves a single positive disclination line running through the centre of the cluster. Similarly, for N=12 and 14-16 structures with a single coordination shell become lower in energy than structures based on the icosahedron at long range. For those with $N > 13$ the surface is in compression. As we shall see in §4.4, structures 11A, 12A, 14A, 15A and 16A correspond to Kasper polyhedra. Of these structures 15A is the most stable as measured by the range of ρ_0 for which it is the global minimum. For 17A, the surface has the same structure as 16A, but there are two atoms in the centre of the cluster. The second lowest energy structure of M_{17} at $\rho_0 = 3$ has a 16-coordinate central atom, which is the node for a tetrahedral array of disclinations. Structures with a more highly coordinated central atom involve increasingly large

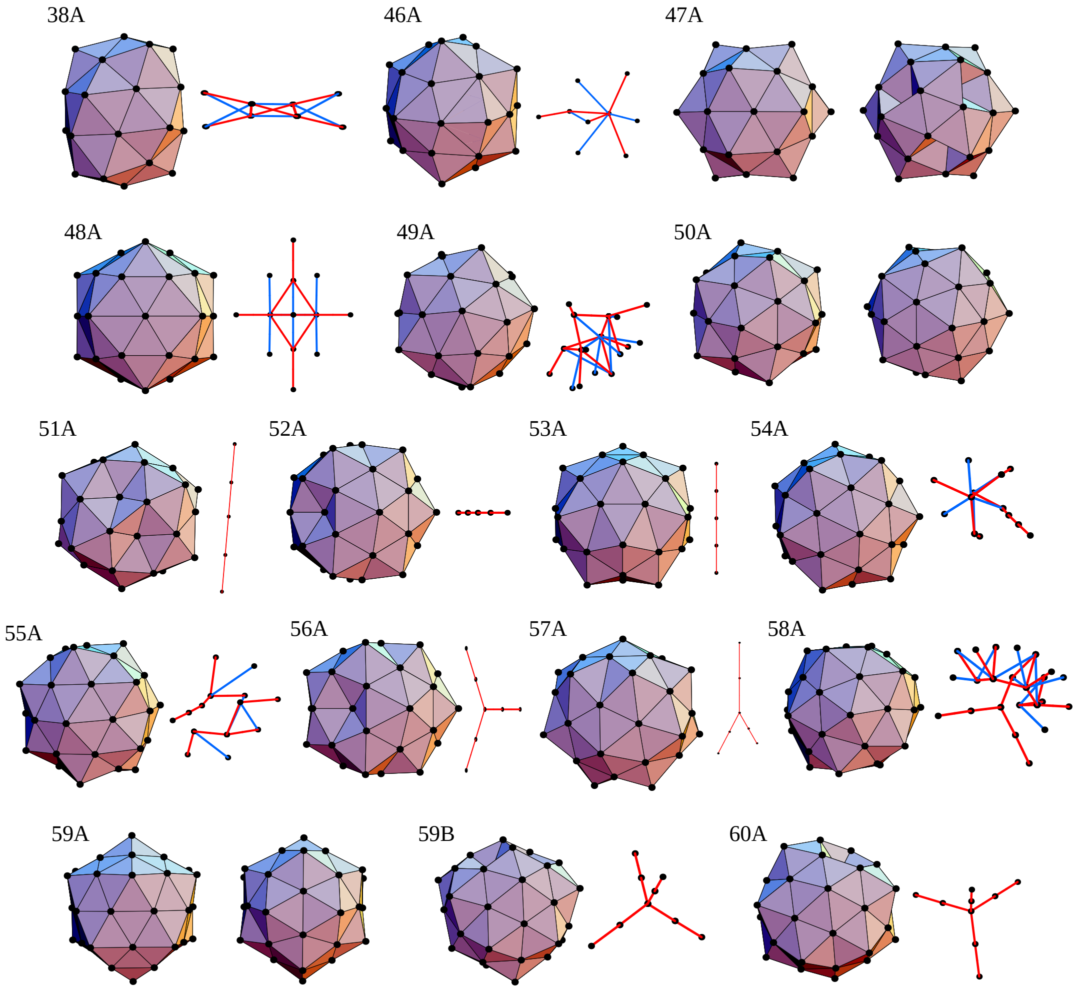

FIGURE 2.18: Global minima at low values of ρ_0 for $N \geq 38$. If appropriate, the disclination network is displayed next to each structure. -72° disclinations are represented by red lines, and $+72^\circ$ disclinations by blue lines. -144° disclinations by green lines, and $+144^\circ$ disclinations by yellow lines.

strains, and for M_{18}, say, would only have the same n_{nn} as the icosahedral 18B.

The structures 11A, 12A, 14A, 15A and 16A are all deltahedral, and so growth can occur on these structures in 'anti-Mackay' or 'Mackay' sites (Figure 2.9), in the same way as for the icosahedron 13A. However, if one considers the addition of a hexagonal pyramidal cap to the most stable of the Kasper polyhedra, 15A, the result is a D_{6h} structure with a positive disclination running the length of the symmetry axis (a disclinated equivalent of the double icosahedron 19A) that has only the same n_{nn} as the icosahedral structure 22A. Disclinated polytetrahedral structures cannot compete with the disclination-free polytetrahedral structures produced by the anti-Mackay overlayer to the icosahedron. Only once this growth sequence is completed at N=45 are structures with disclinations again global min-

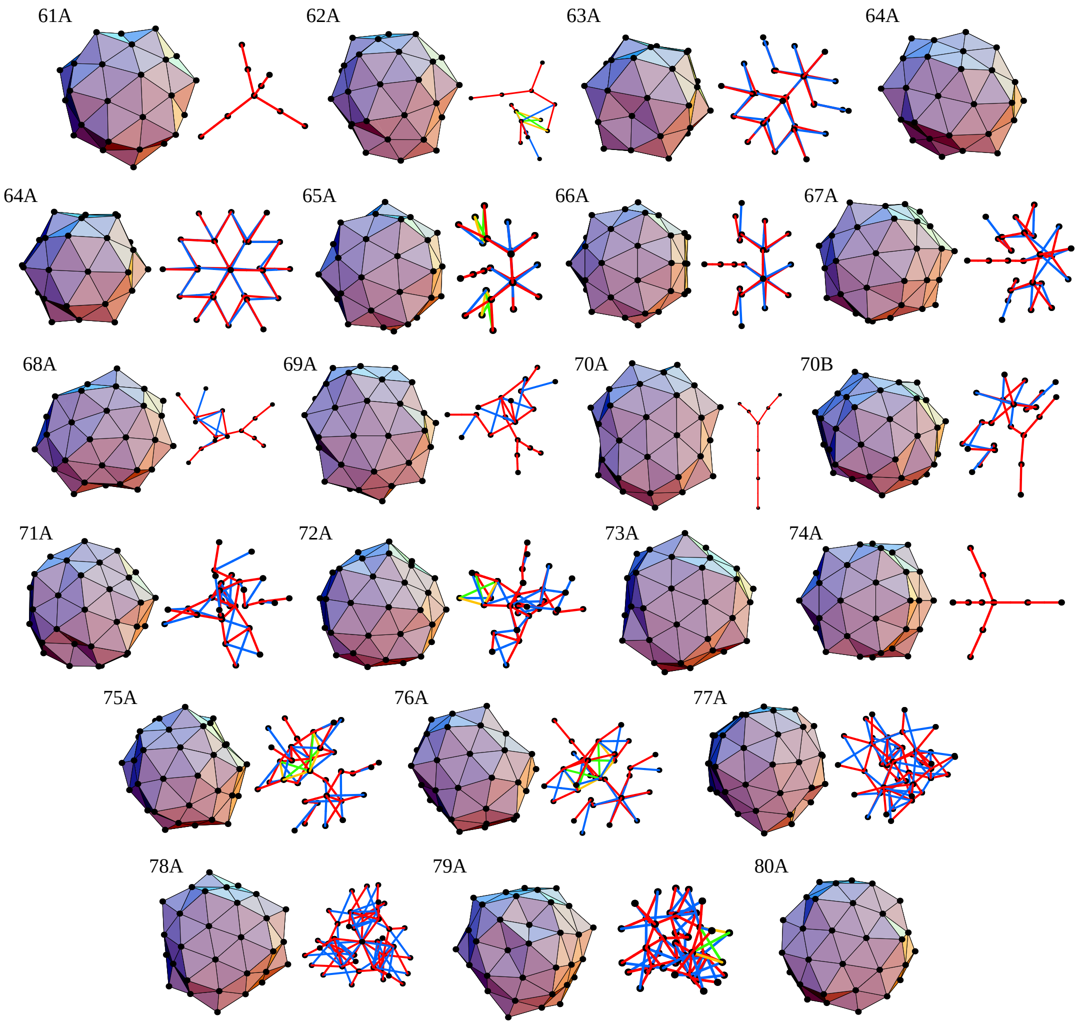

Figure 2.18: continued.

ima (Figure 2.18). The one exception is structure 38A, which is similar to the icosahedral structures 38B and 38C, but has two positive disclinations running through the structure in a strange double helical twist.

The most stable disclinated polytetrahedral structures occur at N=53, 57, and 61 (Figure 2.6). These are the sizes for which 'anti-Mackay' overlayers of 15A, 16A and the 17-atom structure involving a tetrahedral arrangement of disclinations are completed. In these structures, those interior atoms not lying on a disclination line are icosahedrally coordinated. Many other minima are related to these stable structures: 51A and 52A are based on 53A but with missing vertex atoms; similarly, 59B and 60A are based on 61A; and 70A and 74A are based on 57A and 61A, respectively, but with an additional 13-atom cap which extends one of the 'arms' of the disclination network. Furthermore, many of the other structures include parts of the disclination networks of 53A, 57A and 61A, but combined with a more disordered array of disclinations in another part of the cluster.

Other interesting structures are also seen. 47A, 50A and 59A seem to have a mixture of Mackay and anti-Mackay overlayers present. 64A is formed from the rhombic tricontahedron 45A by the extension of the structure along a three-fold axis and the addition of a ring of atoms in the centre of the cluster. However, for the larger clusters it becomes harder to recognize any motifs in the structures, and some just seem to be disordered tangles of disclinations. Disordered polytetrahedral structures involving a network of disclination lines will be considered further when the structure of liquids is discussed in detail in §4.4. It suffices to note here that the nearest-neighbour peak in the radial distribution function of these structures is broader than for the ordered structures considered in the preceding sections, and that, furthermore, these clusters when reoptimized to larger values of ρ_0 correlate with structures that are in the lower energy range of the band of minima associated with the liquid-like state of clusters. It is interesting that theoretical studies of sodium clusters have shown that amorphous structures are lower in energy than regular structures up to at least 340 atoms, the largest size considered in that study[106]. The present results allow us to identify the cause of these disordered structures as the relatively long range of the sodium potential.

Since most minima in this structural class do not have a common lattice, or packing scheme, it is difficult to predict the low energy structures, and so most have been found by one of the global optimization methods mentioned in §2.2.2. Fortunately, these methods are most likely to succeed at long range because the PES is smoother and has fewer minima than at shorter ranges. Another consequence of the lack of lattice structure is that the differentiation between nearest neighbours and next-nearest neighbours becomes ambiguous and the decomposition of equation 2.2 more arbitrary. For these clusters, we choose to define n_{nn} using a cutoff at ρ_0=4 which corresponds to the distance at which the pair energy is $0.6\,\epsilon$.

2.4 Discussion

In this chapter we have attempted to find the global minimum for Morse clusters as a function of ρ_0 and the number of atoms. The global minimum represents the equilibrium structure at zero Kelvin. However, we need to consider how important the global minimum is in determining the structure at finite temperature. To answer this question we have to examine the effects of other local minima on the

TABLE 2.3: The ten lowest energy decahedral and icosahedral minima found for M_{75} at $\rho_0 = 6$.

decahedral			icosahedral		
Energy/ϵ	Point Group	n_{nn}	Energy/ϵ	Point Group	n_{nn}
-351.472365	D_{5h}	319	-351.177041	C_1	328
-349.500086	C_1	317	-351.139799	C_1	328
-349.498552	C_1	317	-351.135122	C_s	328
-349.498393	C_1	317	-350.984741	C_1	328
-349.496058	C_1	317	-350.912649	C_1	328
-349.489864	C_1	317	-350.890122	C_1	328
-349.275647	C_1	317	-350.874153	C_1	328
-348.606586	C_1	316	-350.686821	C_1	327
-348.332763	C_1	316	-350.612539	C_s	329
-347.636104	C_1	315	-350.464407	C_1	327

PES. The thermodynamic properties of a collection of minima can be approximated by superposition of the density of states from each minimum, as described in detail in Chapter 3.

Here we apply this method to M_{75} at $\rho_0 = 6$ to illustrate the limitations of finite temperature structural predictions based on knowledge of the global minimum alone. Sets of low energy decahedral and icosahedral minima were obtained by performing minimizations from configurations generated by low energy MD runs starting from icosahedral and decahedral regions of configuration space. The ten lowest energy minima of each sample are given in Table 2.3. For M_{75}, the Marks' decahedron, 75C, is the most stable cluster at $\rho_0 = 6$. There is an energy gap of 2ϵ to the next lowest energy decahedral isomer (Table 2.3). At this value of ρ_0 the lowest energy icosahedral structure is only 0.3ϵ higher in energy than 75C and there are many icosahedral isomers of similar energy (Table 2.3). In fact we found 31 icosahedral isomers which were of lower energy than the second lowest energy decahedral isomer. From this it might be expected that as the energy is increased the density of states of the icosahedral isomers would become larger than the decahedral isomers, and so the structure would change from decahedral to icosahedral with increasing energy or temperature.

We calculated within the harmonic approximation the equilibrium probabilities that the structure would be icosahedral or decahedral as a function of the microcanonical total energy. The results are given in Figure 2.19. From this it can be

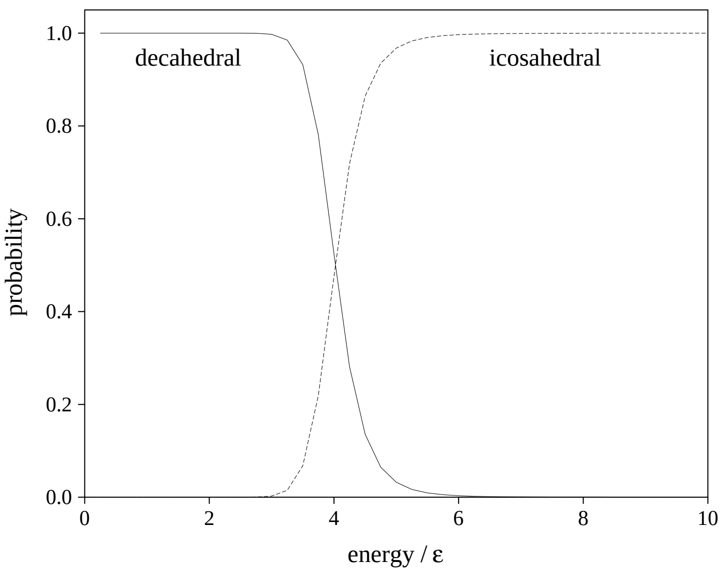

FIGURE 2.19: Calculated equilibrium values for the microcanonical probability that an M_{75} cluster at $\rho_0 = 6$ has an icosahedral or a decahedral structure as a function of the total energy. The energy is measured with respect to the bottom of the well of the Marks' decahedron, 75C.

seen that the equilibrium structure changes from decahedral to icosahedral when the total energy is only $4\,\epsilon$ above the bottom of the lowest well, which corresponds to a reduced temperature of $0.018\,\epsilon\,k^{-1}$. It is likely that such a transition would not be observed until higher energies because of the free energy barrier involved. In fact we once observed this transition in an MD run started from structure 75C. The run was 1×10^6 time steps long and at a total energy of 74ϵ above the lowest well.

This calculation also helps to explain why 75C has not been previously reported as the lowest energy structure for the much-studied LJ potential. Global optimization algorithms are often based upon tracking the free energy global minimum as the temperature is decreased. This is the principle behind the widely-used simulated annealing method[107]. However, such methods will not find the global minimum if a change in the free energy global minimum occurs at a temperature where the rate of isomerization is so low that a transition to the new structure cannot occur on the time scale of the simulation.

We should not conclude from the above calculation, though, that the global minimum is not important in understanding cluster structures. This example is probably an exception rather than the rule. Such a transition is only likely to occur for values of ρ_0 near to where the global minimum changes and in the above example the cause is clearly the differences in the energy spectrum of minima for the two morphologies. In general, then, the global minimum provides a reasonable guide to the finite temperature structural properties of a cluster, which can be usefully supplemented by a knowledge of other low energy minima on the PES.

If there is a unique low energy global minimum separated by a large energy gap from higher energy structures it is appropriate to associate the solid-like structure of the cluster with this single minimum. This would be the case, for example, for the icosahedron 55B at intermediate ranges of the potential. For the LJ potential, microcanonical simulations have shown that the 55-atom cluster resides only in the icosahedral potential well up to an energy of 40ϵ (measured with respect to the bottom of the icosahedral well) above which the formation of surface defects is observed and then complete melting[108–112]. However, when there is a set of low energy minima with very similar energies, at all but very low temperatures an equilibrium ensemble of clusters will contain a mixture of these isomers. It is therefore more appropriate to associate the 'structure' with this set of minima rather than the global minimum alone. For example, this would be the case for 55C, which has three other low energy isomers with the same n_{nn}.

In the above discussion we have been considering the equilibrium structural properties. However, we also need to consider the question of kinetic versus thermodynamic products. How important are the low potential energy structures in practice? When will they actually be found in an experiment? Van de Waal has suggested that kinetic factors could be essential in the growth of fcc rare-gas clusters and the nucleation of fcc solid from the LJ liquid[113,114]. Indeed an extremely good fit is obtained to electron diffraction results for argon clusters from non-optimal structures that involve cross-twinning to allow rapid growth[115,116]. As we noted earlier, the effect of increasing the size and decreasing the range of the potential is to increase the complexity of the PES. Therefore, as the range of the potential decreases the formation of glassy or amorphous clusters, rather than the lowest energy structure, becomes more likely. Whether this is the case for the larger clusters we have studied when the potential is short-ranged would require further investigation. The results for bulk C_{60} may also provide some insight into this question. When formed by vapour phase deposition C_{60} gives an amorphous soot[117], and only forms the crystalline phase on recrystallization from benzene.

In this chapter we have been considering the effect of the range of attraction of pair interactions on cluster structure. As rare gas clusters and clusters of C_{60} molecules can be reasonably modelled by pair potentials we would expect the structures we have found at the appropriate ρ_0 to be very similar to the actual structures of these clusters. Interestingly, the results lead us to predict that neutral clusters of C_{60} molecules exhibit decahedral and fcc structures at small sizes because of the short range of the intermolecular potential. This basic conclusion has been confirmed in studies using more realistic potentials[95,118]. However, this prediction for neutral cluster differs from experimental results[58] for charged clusters for which icosahedral structures are observed up to 55 molecules for $(C_{60})_N^+$ and 147 molecules for $(C_{60})_N^{++}$. Given the exceptionally large polarizability of C_{60}, though, it is not unreasonable that the introduction of a long range Coulomic term would significantly affect the energetic competition between morphologies. Therefore, it would be very interesting if this dramatic difference in structure between charged and neutral clusters could be observed experimentally, say by electron diffraction.

In contrast, making predictions for metal clusters from our results is much more difficult because the range of the potential is only one factor influencing structure. In particular, many-body terms may also be important[62,63]. These terms may affect the relative surface energies of {111} and {100} faces, and so alter the energetic competition between icosahedral, decahedral and fcc structures[102]. For example, in a study of lead clusters cuboctahedra are always found to be lower in energy than icosahedra because the surface energies of {111} and {100} faces are nearly equal[104]. The value of our results is in providing candidate structures for comparison with the increasingly detailed structural information being provided by experiments, such as chemical probe studies[66–68], and for theoretical studies with more realistic, but also more computationally expensive, descriptions of the interactions.

Our results also allow us to comment on a global optimization method proposed by Stillinger and Stillinger in which the PES is deformed by increasing the range[92]. We have to echo Chang and Berry's caution[119] that although increasing the range of a potential does lead to a simplification of the PES it can also cause large changes in the relative stability of different minima. The global minimum when a potential is long-ranged may be very different from the global minimum at the conditions of interest.

For mixtures of spherical colloidal particles and non-adsorbing polymer, the range of the attractive interaction between the colloidal particles can be systematically varied by changing the size of the polymer[120]. This effect has been used to study experimentally the phase diagram for such colloidal systems as a function of the range of the interaction[121–123]. We know of no physically realizable system for clusters where the range of the potential could be similarly varied to cause range-induced transitions in cluster structure. However, it remains an intriguing possibility.

Chapter 3
Thermodynamics of Small Lennard-Jones Clusters

3.1 Introduction

Much of the interest in the thermodynamics of clusters has centred on the melting transition, particularly its character as the finite-size analogue of the bulk first-order phase transition. Cluster melting differs from bulk in a number of ways. First, the finite size of clusters causes 'rounding' of thermodynamic properties[124–126]. The cluster melting transition occurs over a temperature range, not a single temperature; heat capacity peaks are not δ-functions, but instead remain finite.

Secondly, phase separation does not occur in most small clusters (potassium chloride clusters may provide an exception[127]), because the energetic cost of the interface is too large. This leads to certain thermodynamic features which are peculiar to clusters. One is that an ensemble of clusters in the melting region is a mixture of solid-like and liquid-like clusters with the ratio fixed by the relative stabilities of the two forms. If one was to observe a single cluster, it would be seen to occasionally change form between solid-like and liquid-like[128,129]. There is a dynamic coexistence of the two states. These phase-like forms have different characteristic properties. For example, the liquid-like state has a higher potential energy, floppier vibrations, a more disordered structure, and a larger diffusion constant[130]. If these differences between states can be quantified using an order parameter, the presence of more than one state will give rise to multimodal probability distributions of that order parameter. Such multimodality can be related to the thermodynamic stability of the states through the concept of Landau functions[131,132], which describe the thermodynamic potential, i.e. the entropy (microcanonical ensemble) or the Helmholtz free energy (canonical ensemble), in terms of an order parameter. The presence of a first-order phase transition is indicated by two stable states of the Landau function, e.g. two minima in the Landau free energy separated by a barrier.

The order parameters that have been most successful in elucidating the nature of cluster melting have taken advantage of the differences in potential energy between the solid-like and liquid-like states[133]. The ability of the order parameter to distinguish between states can sometimes be enhanced by averaging the parameter over short times to reduce the vibrational broadening[112]. The short-time averaged (STA) temperature has proved to be a particular useful microcanonical order parameter[130]. For this time averaging to succeed the length of time the cluster resides in each state needs to be much longer than the time scale for vibrational motion.

Another unusual feature that results from the absence of phase separation for clusters is the possibility of Van der Waals loops (or S-bends) in the microcanonical caloric curve[134]; there can be a range of energy for which the cluster has a negative specific heat capacity[135–137]. The loops are a result of the transition from the high temperature, low potential energy solid-like state to the low temperature, high potential energy liquid-like state. In §3.7 we use an analytical model to investigate the conditions under which they are most likely to occur, examining in particular the effect of system size.

The standard way to calculate the thermodynamic properties of clusters is by some form of simulation, normally based on the Monte Carlo (MC) or molecular dynamics (MD) methods, perhaps augmented by more sophisticated techniques to help achieve ergodicity, such as jump-walking[138] or umbrella sampling[139], or to extract densities of states, such as the multi-histogram methods[140–142]. Such simulations give 'exact' results for the thermodynamics within the statistical errors of the simulation. An alternative route to calculate accurate densities of states is provided by Reinhardt's adiabatic switching method[143]; it has the advantage over histogram MC that it can extract absolute (not relative) values for the densities of states.

However, before such simulations became computationally feasible, considerable attention was given to the calculation of thermodynamic properties of clusters from the PES. Initially, calculations were performed in the harmonic approximation using only knowledge of the vibrational spectrum of a single low energy structure[10,11,144–146]. McGinty and Burton realized that if their results were to have relevance for more than low temperature behaviour, other configurations needed to be included in their partition function[10,145], but without the means to systematically search the PES they were unable to implement this extension of their approach. In particular, if this method is to model the melting transition, the large number of high potential energy minima associated with the liquid-like state need to be taken into account. Hoare and McInnes did obtain a suitable database of minima for small LJ clusters[64,65], and although they outlined the method by which the thermodynamic properties could be calculated from this sample[147], the results were never published. However, with the advent of reliable simulation methods and adequate computer power to carry them out, such calculations were neglected.

Interest in the relationship of the thermodynamics of clusters to the PES was rekindled by the application of Stillinger and Weber's inherent structure approach[148] to clusters. The basic idea is that every configuration of a system can be mapped onto a minimum of the PES (an 'inherent structure'), by a steepest-descent path or 'quench'. This mapping allows one to consider the thermodynamic effects of the energy spectrum of minima separately from thermal motion within the wells, and gives a clearer view of structure, especially for liquids, by removing vibrational noise. In the application of this method to clusters, the thermodynamic and dynamic properties were elucidated by relating them to the qualitative features of the PES, especially the low energy minima and saddle points, thus allowing an intimate connection to be made between structure and thermodynamics[108,130,149–151].

This relationship between cluster thermodynamics and the PES was further developed by Bixon and Jortner[152] who considered the thermodynamics that resulted from different model energy spectra of minima. They showed that a large energy gap between the global minimum and a manifold consisting of a large number of higher energy minima was necessary to produce a significant feature in the caloric curves.

The wheel finally returned to the ideas of Burton, McGinty and Hoare, when Wales[153] and Franke *et al.*[154] independently developed a method to quantitatively determine the thermodynamic properties from the PES. A sample of minima is generated by systematic quenching from a high energy MD run. $\Omega(E)$ is then calculated by summing the harmonic density of states for each minima. This approach has been called the harmonic superposition method, and has been applied to a number of cluster systems to obtain a wide variety of thermodynamic properties[133,155].

The main focus of this chapter is to extend the harmonic superposition method to incorporate anharmonicity (§3.5) and to show how this method can give added physical insights into the thermodynamics by allowing the roles of different regions of the PES to be quantitatively examined (§3.6). First though, we briefly outline the simulation methods that we have used both for LJ_{55} in §3.3 and for the Morse systems studied in Chapter 4. The results for LJ_{55} (§3.3) provide both an example of some of the typical features seen in cluster thermodynamics, and also some of the results necessary for the analysis in §3.5. We then briefly review the harmonic superposition method (§3.4), before addressing the extension of the method to include anharmonicity. Finally, we investigate the effect of size on the possibility of Van der Waals loops appearing in the microcanonical caloric curves (§3.7).

3.2 Simulation Methods

The potential used in this study was the Lennard-Jones form[83],

$$E = 4\,\epsilon \sum_{i<j} \left[\left(\frac{\sigma}{r_{ij}} \right)^{12} - \left(\frac{\sigma}{r_{ij}} \right)^{6} \right], \tag{3.1}$$

where r_{ij} is the distance between atoms i and j. With ϵ, σ and m as the units of energy, distance and mass, respectively, the unit of time is $(m\sigma^2/\epsilon)^{\frac{1}{2}}$. MD simulations of the microcanonical ensemble were conducted using the velocity Verlet algorithm[156]. The initial phase point had zero linear and angular momentum. To prevent evaporation the clusters were placed in a container with walls represented by a LJ type repulsion[153,157]. When an atom hit the wall of the container an equal and opposite force was exerted on the rest of the cluster to prevent linear momentum transfer. As the two forces are collinear, there is also no transfer of angular momentum. The effect of the box is to restrict the phase space considered to bound clusters. The time step used was 0.0465 reduced time units, which is equivalent to 1×10^{-14}s for Ar.

The relative root-mean-square interatomic separation δ was used to assess the degree of melting. It is defined as

$$\delta = \frac{2}{N(N-1)} \sum_{i<j} \frac{\sqrt{\left\langle R_{ij}^2 \right\rangle - \left\langle R_{ij} \right\rangle^2}}{\left\langle R_{ij} \right\rangle}, \tag{3.2}$$

where the angle brackets indicate that an average is taken over the whole trajectory. Lindemann's criterion[158] states that melting is expected when δ becomes greater than about 0.1.

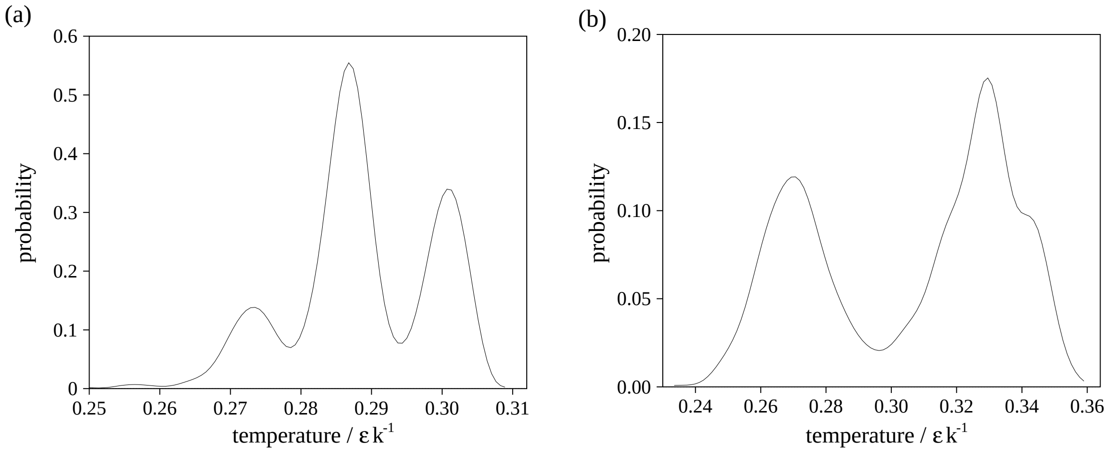

FIGURE 3.1: Probability distributions of STA temperatures for LJ_{55} from MD runs at (a) $54.243\,\epsilon$ and (b) $62.273\,\epsilon$ above the energy of the Mackay icosahedron, $-279.248\,\epsilon$.

The kinetic temperature is calculated from the kinetic energy, E_K, via the generalized equipartition theorem:

$$T_K = \frac{2E_K}{k(3N-6)} \tag{3.3}$$

by taking the mean of T_K over the whole trajectory. This expression is exact in the canonical ensemble, but T_K differs by $\mathcal{O}(N^{-1})$ from the thermodynamic definition of temperature (equation 3.10) in the microcanonical ensemble[159]. STA temperatures were found by averaging T_K over 500 time steps.

3.3 The 55-atom Lennard-Jones Cluster

LJ_{55} has been the focus of much study as an archetype for the melting of small clusters. It exhibits a clear Van der Waals loop and a large peak in the heat capacity[135]. If the potential energy is used as an order parameter, there is a range of energy for which two Landau free energy minima occur corresponding to the solid-like and liquid-like states[133]. If short time averaging is used more structure is revealed in the solid-like branch of the caloric curve. Before melting, atoms can pop out of the surface layer creating a vacancy and a mobile adatom[108,110,111,149]. This defect creation leads to enhanced diffusion in the surface layer, whilst the core of the cluster remains rigid.* Kunz and Berry observed that the cluster would spend a period of time in one region of configuration space, say with a

*Although this behaviour has been referred to as 'surface melting' in some studies[109–111] we prefer not to use this terminology because the behaviour does not evolve with increasing size to the surface melting familiar for bulk surfaces[160].

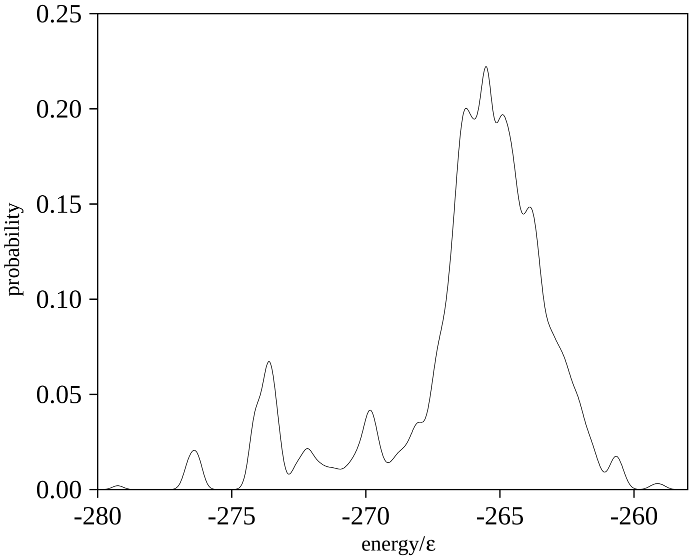

FIGURE 3.2: Probability distribution of the potential energy for a sample of 989 minima of LJ_{55}.

single surface vacancy, and then jump to a region with a different number of vacancies and a different characteristic potential energy. As a result, multimodality is seen in the probability distributions for the microcanonical STA temperature. An example is shown in Figure 3.1a where three coexisting states are seen. As the STA temperature reflects the minimum energy of the wells with which the cluster is associated (high temperatures correspond to low energy minima), we expect that the STA temperature peaks will be related to features in the energy distribution of minima (Figure 3.2).

To test this hypothesis, quenches were performed from configurations generated by an MD run at the energy of Figure 3.1a if they had an STA temperature near to the maxima of any of the three peaks. The resulting minima were then assigned to one of the six energy ranges given in Table 3.1. The results, given in Table 3.2, unequivocally show the correspondence between the STA temperature peaks and the peaks in the potential energy probability distribution for minima. Therefore the STA temperature can be used to elucidate the connection between the observed behaviour and local minima on the PES.

The highest temperature peak corresponds to the Mackay icosahedral global minimum, but to assign sets of structures to the other peaks, some of the minima in energy ranges II and III were examined further. Range II consists of icosahedral-based structures with a vacancy in a five-coordinate vertex site and a single adatom. There are eleven such structures, four with the adatom in the centre of a trian-

Table 3.1: Division of the of LJ_{55} PES into energy ranges based upon the features in the distribution of minima (Figure 3.2). There are no minima with energies between regions I and II, and II and III.

Region	Lower energy bound/ϵ	higher energy bound/ϵ
I	-279.24847	-279.24847
II	-276.60429	-276.19935
III	-274.50000	-273.00000
IV	-273.00000	-271.50000
V	-271.50000	-268.84000
VI	-268.84000	–

Table 3.2: Results of quenching from an MD run for LJ_{55} at an energy of $54.243\,\epsilon$ relative to the icosahedron.

Lower Temperature	Upper Temperature	Number of quenches	I	II	III	IV and V
0.3047	0.3050	110	110	0	0	0
0.2909	0.2912	72	2	70	0	0
0.2756	0.2785	86	1	9	74	2

gular face (Figure 3.3a) and seven with the adatom in an off-centre site (Figure 3.3b). These structures have been reported previously in a study using a more sophisticated potential to represent Ar[108]. Range III consists of structures with two vertex vacancies and two adatoms (Figure 3.3c–f and h–j), and structures with a vacancy in a six-coordinate edge site and a single adatom (Figure 3.3g). For the lower energy structures in this range, the two adatoms form a pair, either on the same face (Figure 3.3c and d) or straddling two faces (Figure 3.3e and f). We also examined some minima corresponding to range IV. We found structures with three adatoms, as well as some with adjacent edge and vertex vacancies and two adatoms (Figure 3.3k) and more complicated distorted icosahedra (Figure 3.3l).

To map out the microcanonical caloric curve MD runs each of 2.5×10^6 time steps were performed at 23 energies around the coexistence region. As expected the resulting curve has a Van der Waals loop. The STA temperature distributions were calculated for each energy. At low energies the distribution is unimodal, because the cluster remains in the Mackay icosahedral well. As it becomes possible

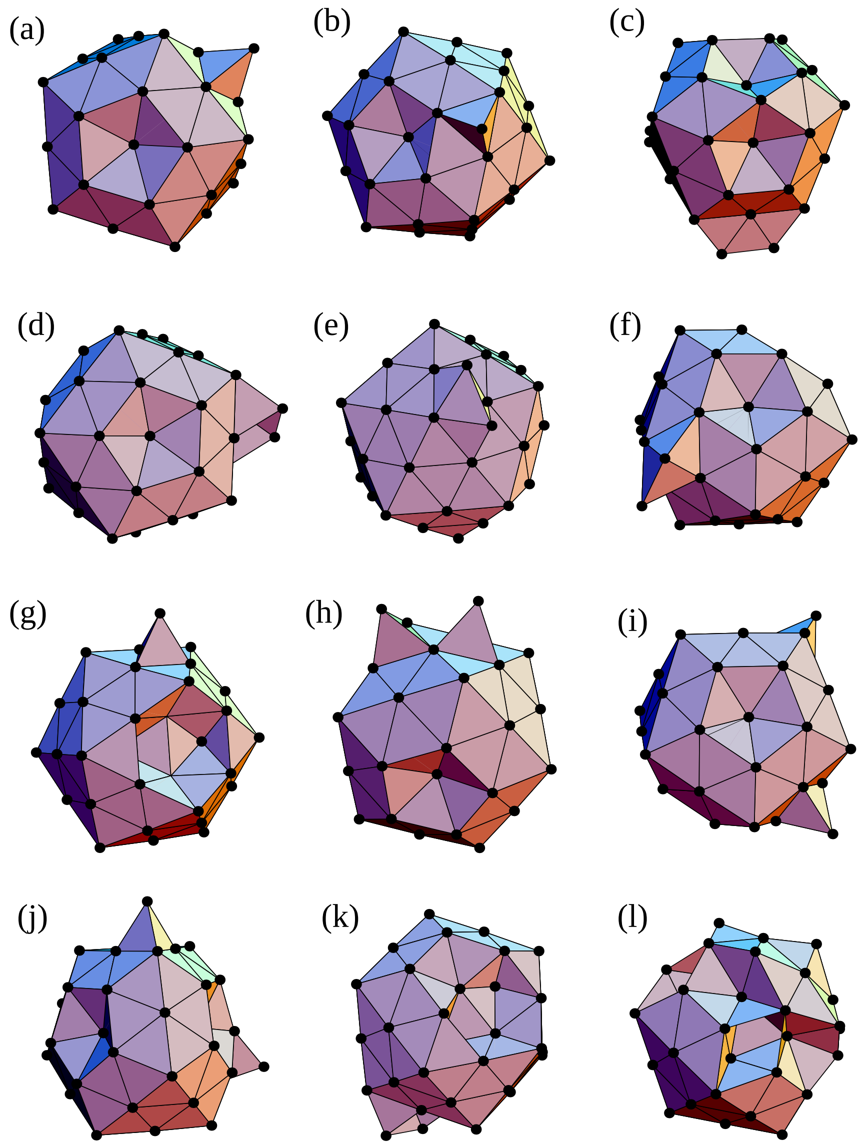

FIGURE 3.3: A selection of representative minima of LJ_{55} from energy ranges II, III and IV. Energies and point groups are given in Table 3.3.

to create surface vacancies, the distributions first become bimodal (at $48.193\,\epsilon$), and then trimodal (at $49.183\,\epsilon$). At $60.238\,\epsilon$ a much broader peak appears at lower temperature. Figure 3.1b shows this bimodal behaviour; it is due to dynamic coexistence between the liquid-like and solid-like states. The shoulders of the high-temperature peak are the remnants of the trimodal behaviour seen at lower energies. The peaks have merged because the greater vibrational energy has

Table 3.3: Energies of the LJ_{55} minima represented in Figure 3.3.

Label	Description	PG	Energy/ϵ
a	vertex vacancy + centred adatom	C_s	-276.59676
b	vertex vacancy + off-centred adatom	C_1	-276.19935
c	2 vertex vacancies + adatom pair	C_s	-274.28136
d	2 vertex vacancies + adatom pair	C_1	-274.25058
e	2 vertex vacancies + adatom pair	C_1	-274.21687
f	2 vertex vacancies + adatom pair	C_1	-274.13672
g	edge vacancy + centred adatom	C_s	-274.08950
h	2 vertex vacancies + 2 adatoms	C_1	-273.83234
i	2 vertex vacancies + 2 adatoms	C_1	-273.62356
j	2 vertex vacancies + 2 adatoms	C_1	-273.21257
k	fused vertex and edge vacancy + adatom pair	C_1	-272.82603
l	distorted icosahedron	C_s	-272.58659

broadened the temperature distributions for each state. The trimodal character of the high temperature peak would reappear if a longer averaging period was used.

The STA temperature distributions were partitioned according to their peaks, and the mean and standard deviation of the temperature were calculated for each, along with the integrated probabilities. This allows the caloric curves for restricted regions of the configuration space to be obtained (Figure 3.4a). Regions II and III have a small effect on the caloric curve; they cause it to bend gradually away from the temperature corresponding to the Mackay icosahedron alone. From the probabilities (Figure 3.4b) it can be seen that, despite their length, some of the MD runs have not achieved ergodicity in the energy range $47-55\,\epsilon$. This is because the free energy barriers between the different states can be large, and so passage between the different states can be infrequent on the time scale of the run.

3.4 The Harmonic Superposition Method

The total energy density of states associated with a single minimum on the PES is in the harmonic approximation[161]

$$\Omega(E) = \frac{(E-E^0)^{\kappa-1}}{\Gamma(\kappa)\prod_{j=1}^{\kappa} h\nu_j}\theta(E-E^0), \tag{3.4}$$

where E^0 is the potential energy of the minimum, θ is the Heaviside step function, and κ, the number of vibrational degrees of freedom, is $3N-6$. (As we will

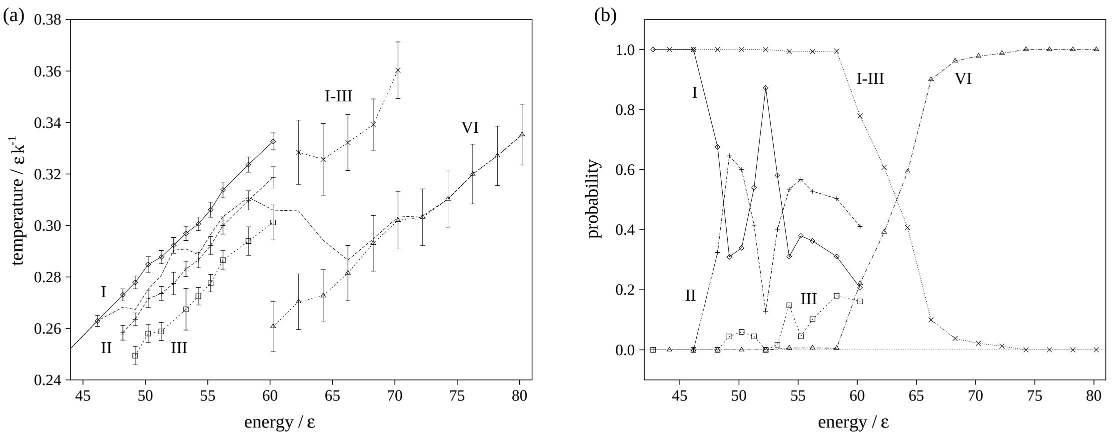

FIGURE 3.4: (a) Plot of the temperature against energy for LJ_{55}. The caloric curve has been split into contributions from regions of configuration space corresponding to peaks in the STA temperature distribution. The overall caloric curve is represented by the dashed line without any error bars. (b) Plot of the probability of LJ_{55} being in regions of phase space I, II, III and VI characterized by their different STA temperatures. Above $60\,\epsilon$ regions I–III were indistinguishable. The energy is measured relative to the energy of the global minimum icosahedron.

be comparing our results to those for stationary, non-rotating clusters, we do not include translational or rotational contributions to the density of states.) To calculate the density of states for the whole system, all the minima on the PES need to be considered. We make a superposition approximation and sum the density of states over all the minima low enough in energy to contribute. This approximation is equivalent to assuming that the phase space hyperellipsoids associated with each minimum do not overlap. This gives

$$\Omega(E) = \sum_{E_s^0 < E} \frac{n_s^*(E - E_s^0)^{\kappa-1}}{\Gamma(\kappa) \prod_{j=1}^{\kappa} h\nu_j^s}, \tag{3.5}$$

where the sum is over all the geometrically distinct minima on the surface; n_s^*, the number of permutational isomers of minimum s, is given by $n_s^* = 2N!/h_s$ where h_s is the order of the point group of s.†

The difficulty with equation 3.5 is that for all but the very smallest clusters this sum involves an impractically large number of minima. Hoare and McInnes[64], and more recently Tsai and Jordan[162] have enumerated lower bounds to the number of geometric isomers for LJ clusters from 6 to 13 atoms. This number rises

†In their formulation of the superposition method Hoare and McInnes missed out the effect of symmetry[147]. This explains why in the brief mention of the results that they obtained, the method predicted that for LJ_{13} the cluster would reside in the icosahedral global minimum up to a reduced temperature of 0.6. (LJ_{13} in fact melts at $\sim$0.29). Without the inclusion of symmetry, the density of the states of the icosahedron is overestimated by 120 times.

exponentially with N. Extrapolating this trend gives for LJ_{55} an estimate of 10^{21} geometric isomers. In such a case, as it is not possible to obtain a complete set of minima, a representative sample is needed. A large set of minima can be obtained by systematic quenching from a high energy MD trajectory. However, this gives a greater proportion of the low energy minima than of the high energy minima. Consequently, if the sample is used in equation 3.5 it is likely to underestimate the density of states due to the high energy minima, and so be inaccurate at high energies.

A method is needed which corrects for the incomplete nature of the sample of minima. This correction can be achieved by weighting the density of states for each known minimum by g_s, the number of minima of energy E_s^0 for which the minimum s is representative. Hence,

$$\Omega(E) = \sum_{E_s^0 < E} \frac{g_s n_s^* (E - E_s^0)^{\kappa - 1}}{\Gamma(\kappa) \prod_{j=1}^{\kappa} h\nu_j^s}, \tag{3.6}$$

where the sum is now over a representative sample of minima. The effect of g_s can be incorporated by using the quench statistics. If the system is ergodic and the MD run is performed at constant energy, the number of quenches to a minimum, γ, is assumed to be proportional to the density of states of the set of g_s minima, i.e. $\gamma(E')_s \propto g_s \Omega(E')_s$. Hence,

$$\Omega(E) \propto \sum_{E_s^0 < E} \gamma\,(E')_s \frac{\Omega(E)_s}{\Omega(E')_s} \tag{3.7}$$

$$\propto \sum_{E_s^0 < E} \gamma\,(E')_s \left(\frac{E - E_s^0}{E' - E_s^0} \right)^{\kappa - 1}, \tag{3.8}$$

where E' is the energy of the MD run. This reweighting technique is analogous to histogram Monte Carlo, but instead of determining the configurational density of states from the canonical potential energy distribution, g, effectively a density of minima, is found from the microcanonical probability distribution for quenching to a minimum.

If all the low energy minima are known, the n^* formula (equation 3.5) will be accurate at low energies. Therefore, the proportionality constant in the above equation can be found by matching it to the low energy form of the n^* formula. For LJ_{13} and LJ_{55}, the term due to the icosahedron is dominant at low energies, and other terms in the sum can be neglected. Comparing the first terms of equations

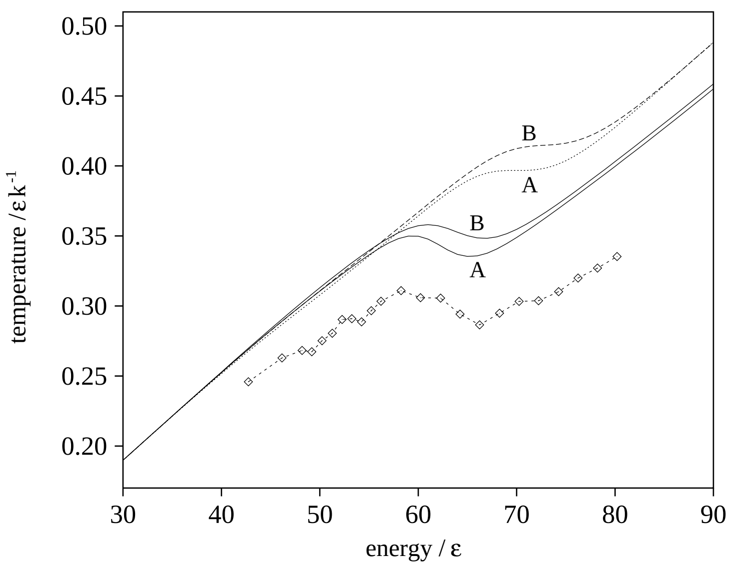

FIGURE 3.5: Microcanonical caloric curves for LJ_{55}. The solid lines were calculated from the γ formula, the dashed lines were calculated from the n^* formula, and the dashed line with diamonds shows the simulation results. The sample of minima used in the calculations is marked on the graph.

3.5 and 3.8 gives for the proportionality constant, c

$$c = \frac{n_0^*(E' - E_0^0)^{\kappa-1}}{\gamma\,(E')_0\,\Gamma(\kappa)\prod_{j=1}^{\kappa} h\nu_j^0}, \tag{3.9}$$

where E_0^0 is the energy of the global minimum.

A critical test of these formulae for $\Omega(E)$ is the predicted microcanonical caloric curve, which for LJ_{55} has a Van der Waals loop[135]. Using the thermodynamic definition of the microcanonical temperature, T_μ,

$$\frac{1}{kT_\mu} = \left(\frac{\partial \ln \Omega}{\partial E}\right)_{N,V} = \frac{1}{\Omega}\left(\frac{\partial \Omega}{\partial E}\right)_{N,V}, \tag{3.10}$$

an expression for T_μ can be derived[153]. For LJ_{55} we have two samples of minima produced by systematic quenching[153], details of which are given in Table 3.4. Sample A is from a MD run at an energy in the upper end of the coexistence region, and B at an energy just into the liquid-like region. The results for samples A and B using the n^* and γ formulations are given in Figure 3.5. It can be seen the n^* formula fails badly, predicting only an inflection in the caloric curve which is too high in energy. This failure is because the contribution to $\Omega(E)$ from the higher energy minima is underestimated. The γ formula is much more successful, reproducing the Van der Waals loop at the observed energy. That the harmonic superposition

Table 3.4: Details of the two samples of minima used for LJ_{55}. E' is measured with respect to the global minimum icosahedron.

	E'/ϵ	Number of minima
A	64.7485	989
B	70.2485	1153

method produces a caloric curve with the correct features shows, as Bixon and Jortner suggested[152], that the distribution of minima is crucial in determining the basic form of the caloric curve. However, the Van der Waals loop is too shallow and lies at too high a temperature. The discrepancy is due to the harmonic approximation. The temperature rises linearly with energy for a single harmonic well. The actual wells of the cluster, however, are flatter than assumed in the harmonic approximation, especially around the transition state regions. Consequently, the cluster spends more time in these high potential energy, low temperature regions of the PES, and so the true temperature is lower than that given by the harmonic approximation.

For smaller clusters it was found that the performance of the n^* formula improved[155]. This improvement occurs because there are fewer minima on the PES of a smaller cluster and so the set of minima obtained from quenching is more complete.

The harmonic superposition method has three main possible sources of error. The first is associated with the statistical accuracy of the quench frequencies. These errors can be mostly eliminated by having a long enough quench run to ensure ergodicity, and by choosing an appropriate energy for the MD run so that the relevant regions of phase space are all significantly sampled. When studying the thermodynamics of melting it is most appropriate to choose E' to lie in the coexistence region, as in the case of sample A, so that quenches to solid-like and liquid-like states are frequent. The second possible source of error is the assumption that the phase space volumes for each minima can be summed independently, i.e. the hyperellipsoids in phase space do not overlap. If overlap occurred $\Omega(E)$ would be overestimated. Of course, above an energy threshold the true phase space volumes of each minimum are interconnected, but this interconnection is normally due to the anharmonic extension of the phase volumes to form necks along the transition state valleys. The third possible source of error is the harmonic approximation. Near the bottom of the well this is a reasonable assumption, but as the energy is increased some parts of the well become increasingly flat. Consequently the harmonic approximation causes $\Omega(E)$ to be underestimated. Comparison of the caloric curves from simulation and the harmonic superposition method (Figure 3.5) shows that the harmonic superposition method does indeed underestimate $\Omega(E)$ and so the harmonic approximation is likely to be the main source of error.

3.5 Anharmonicity

Most attempts to model anharmonicity have concentrated on small systems. As the size of the system increases the difficulty increases greatly. For example, it would be impossible to do the necessary multi-dimensional phase space integrals in the definition of $\Omega(E)$,

$$\Omega(E) = \frac{1}{h^\kappa} \int \int \delta(H - E) dq^\kappa dp^\kappa. \tag{3.11}$$

Most approaches either attempt to calculate the anharmonic element using known information from the PES, such as the third and fourth derivatives of the potential at the minima and the dissociation energies[163] or assume the PES has a certain topology for which the partition function is known[164,165]. A normal mode approximation is often used because the multi-dimensional partition function is then the product of the one-dimensional normal mode partition functions. However, to then obtain the density of states the partition function must be inverse Laplace transformed. This procedure does not necessarily have an analytic solution, and so numerical methods sometimes have to be used[166,167].

The only attempt, that we know of, to evaluate analytically the anharmonic density of states of clusters is due to Chekmarev and Umirzakov[165]. Their expression contained a number of unknown parameters, which they had to estimate. This approximate approach was partly due to their lack of information about the PES of LJ_{13}, the cluster they considered. They showed their form was able to produce the types of feature seen in the LJ_{13} caloric curve, if not to reproduce it accurately. The approach we use here is similar. We are looking for a relatively simple method that will provide an analytical expression for the anharmonic contribution to $\Omega(E)$. We also want to examine how far it is possible to use information extracted from the PES in this task. We will focus on LJ_{55} as a test of the methods developed. For LJ_{55} we have a sample of 3481 transition states which were found from a random selection of 402 of the minima in sample B defined above[90]. We have also calculated the analytical third derivatives for this potential.

3.5.1 The effect of transition state valleys

Transition states are crucial to the dynamics of a system, but how much effect do they have on the thermodynamics? Associated with a transition state is a flat valley on the PES which connects two minima. These transition state valleys will make a contribution to $\Omega(E)$. To consider their effect we need an expression for the density of states of a transition state valley.

We write the partition function for the transition state valley as a product of a vibrational partition function for the $(\kappa - 1)$ modes orthogonal to the transition vector and a translational partition function for motion along the transition state valley. This separation gives

$$Z_{ts} = \frac{L}{h}\sqrt{\frac{2\pi m}{\beta}}\frac{e^{-\beta E_{ts}}}{\prod_{j=1}^{\kappa-1}\beta h\nu_j^{ts}}, \tag{3.12}$$

where L is the length of the transition state valley. Inverse Laplace transforming this expression gives for the density of states of the transition state valley,

$$\Omega(E)_{ts} = \frac{\sqrt{2\pi m}\, L\,(E - E_{ts})^{\kappa-\frac{3}{2}}}{h^\kappa \prod_{j=1}^{\kappa-1}\nu_j^{ts}\,\Gamma(\kappa - \frac{1}{2})}\theta(E - E_{ts}). \tag{3.13}$$

Our expression for the total density of states is then

$$\Omega(E) = \sum_{E_s^0<E}\frac{n_s^*}{h^\kappa}\left(\frac{(E - E_s^0)^{\kappa-1}}{\Gamma(\kappa)\prod_{j=1}^{\kappa}\nu_j^s} + \frac{\sqrt{2\pi m}}{\Gamma(\kappa - \frac{1}{2})}\sum_{E_s^0+\Delta_{s,t}<E}\frac{\sigma_{s,t}L_{s,t}(E - E_s^0 - \Delta_{s,t})^{\kappa-\frac{3}{2}}}{\prod_{j=1}^{\kappa-1}\nu_j^{s,t}}\right), \tag{3.14}$$

where $\Delta_{s,t}$ is the barrier height of transition state t from minimum s, and the reaction path degeneracy $\sigma_{s,t} = h_s/h_t$ or $2h_s/h_t$ for non-degenerate and degenerate rearrangement mechanisms, respectively[168]. A degenerate transition state connects different permutational isomers of the same minimum. In the γ formulation we now have

$$\Omega(E) = \sum_{E_s^0<E}\gamma(E')_s\frac{\frac{(E-E_s^0)^{\kappa-1}}{\Gamma(\kappa)\prod_{j=1}^{\kappa}\nu_j^s} + \frac{\sqrt{2\pi m}}{\Gamma(\kappa-\frac{1}{2})}\sum_{E_s^0+\Delta_{s,t}<E}\frac{\sigma_{s,t}L_{s,t}(E-E_s^0-\Delta_{s,t})^{\kappa-\frac{3}{2}}}{\prod_{j=1}^{\kappa-1}\nu_j^{s,t}}}{\frac{(E'-E_s^0)^{\kappa-1}}{\Gamma(\kappa)\prod_{j=1}^{\kappa}\nu_j^s} + \frac{\sqrt{2\pi m}}{\Gamma(\kappa-\frac{1}{2})}\sum_{E_s^0+\Delta_{s,t}<E'}\frac{\sigma_{s,t}L_{s,t}(E'-E_s^0-\Delta_{s,t})^{\kappa-\frac{3}{2}}}{\prod_{j=1}^{\kappa-1}\nu_j^{s,t}}}. \tag{3.15}$$

Geometrically, the phase volume associated with the transition state valley is an elliptical hypercylinder. There is also a term due to the phase space overlap of this hypercylinder with the hyperellipsoid associated with the minimum. It can be evaluated[169], however it is a small term and so we neglect it, especially as initially we are only trying to determine the magnitude of the effect of the transition state valleys.

The set of transition states previously calculated is not an exhaustive set for the sample of minima. Its incompleteness could cause an underestimation of the density of states arising from the transition state valleys. We therefore performed a more exhaustive search for transition states from 13 minima representing a wide range of energies. This search indicated that a reasonable estimate of the average number of low energy transition states per minimum was 20 (not counting permutational isomers). For each minimum the density of states of the known transition state valleys was multiplied by $20/n_{ts}^s$, where n_{ts}^s is the number of known transition states for minimum s. If the sample of transition states contained none connected to a particular minimum, it was assigned 20 transition states with the average barrier height and average frequency. The length of the transition state valley was estimated using

$$L_{s,t} = D_{s,t} - \frac{1}{2\pi\overline{\nu^s}}\sqrt{\frac{2\Delta}{m}}, \tag{3.16}$$

where $D_{s,t}$ is the displacement in configuration space between minimum s and transition state t, and $\overline{\nu^s}$ is the average normal mode frequency of s. The second term is the average radius of the harmonic well in configuration space at an energy Δ above the minimum.

From the expression for $\Omega(E)$ in equation 3.15 the temperature can be calculated using equation 3.10. It can be seen from the microcanonical caloric curves given in Figure 3.6 that the transition state valleys cause the caloric curve to bend away from the harmonic curve and the Van der Waals loop to be displaced downwards, but these effects are small. Even if the number of transition states connected to a minimum is assumed to be greater than 20 the effects are only slightly increased. The addition of the density of states of the transition state valleys only accounts for a small part of the difference between the harmonic and the true caloric curves. This result occurs not because the contribution of the transition state valleys to the density of states is small compared to that of the minima—in fact the transition state valleys make a larger contribution than the minima above about 55ϵ. Rather it occurs because the density of states for the transition state valleys is not very different from that of the minima; the valleys are modelled as harmonic in all but one dimension. We therefore conclude that a method of modelling the anharmonicity of the wells on the PES is needed to

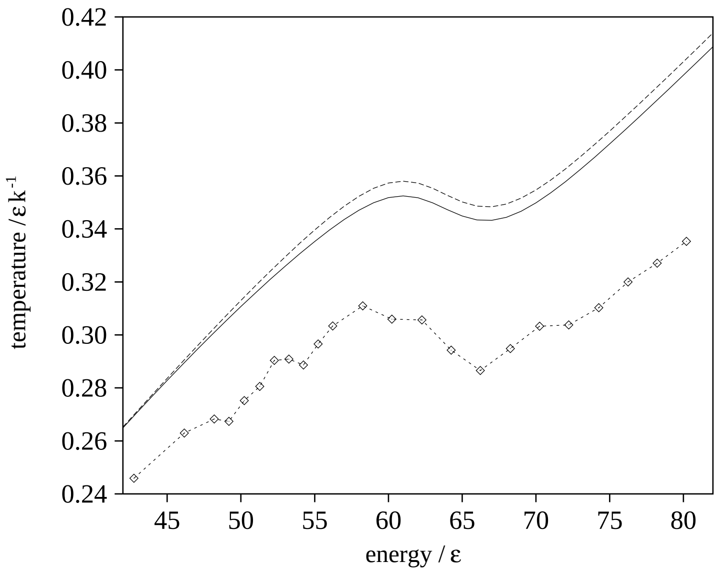

FIGURE 3.6: Microcanonical caloric curves for LJ_{55} using the γ formula with (solid line) and without (dashed line) the contribution from transition state valleys for sample A. The calculated caloric curve is compared to simulation (dashed line with diamonds).

obtain an accurate $\Omega(E)$. This agrees with Stillinger and Stillinger's conclusion that intrawell anharmonicity is dominant for LJ_{55} based on the fact that the caloric curve significantly deviates from the harmonic form at energies where the cluster always resides in the icosahedral well[108].

3.5.2 The effect of well anharmonicity

Here we follow the method of Haarhoff[164,166] to calculate an anharmonic correction term to the density of states. The energy levels for a Morse oscillator are given by

$$E = (n + \frac{1}{2})h\nu - (n + \frac{1}{2})^2 \frac{(h\nu)^2}{4D_e}. \tag{3.17}$$

This quadratic can be solved for n. The root corresponding to a bound state is

$$n + \frac{1}{2} = \frac{2D_e}{h\nu}\left(1 - \sqrt{1 - \frac{E}{D_e}}\right). \tag{3.18}$$

Assuming n is continuous and differentiating with respect to E gives a classical density of states,

$$\begin{aligned} \Omega(E) &= \frac{dn}{dE} = \frac{1}{h\nu\sqrt{1 - \dfrac{E}{D_e}}} \\ &= \frac{1}{h\nu}\left(1 + \frac{E}{2D_e} + \frac{3}{8}\left(\frac{E}{D_e}\right)^2 + \cdots\right), \end{aligned} \tag{3.19}$$

where the square root has been expanded binomially. The expansion is valid if E/D_e is small. The first term in the series is the harmonic term. The full series will diverge as $E \to D_e$. This divergence is the correct behaviour for the Morse oscillator, but for the case of a cluster isomerization $\Omega(E)$ remains finite as $E \to \Delta$ from below, where Δ is the barrier height. As we are seeking a correction term for well anharmonicity, it seems reasonable to truncate equation 3.19 and examine the effect of the first term in this series. Laplace transformation then gives for the partition function

$$z = \frac{1}{h\nu}\left(\frac{1}{\beta} + \frac{1}{2\Delta\beta^2}\right). \tag{3.20}$$

The multi-dimensional partition function is then

$$Z = \prod_{j=1}^{\kappa} \frac{1}{\beta h\nu_j}\left(1 + \frac{1}{2\Delta_j\beta}\right). \tag{3.21}$$

Making the approximation that an average value of $1/\Delta$ can be used then gives

$$Z = \frac{1}{\prod_{j=1}^{\kappa} h\nu_j} \sum_{l=0}^{\kappa} \frac{C_l^\kappa a^l}{\beta^{\kappa+l}}, \tag{3.22}$$

where $a = \langle 1/2\Delta \rangle$ is an anharmonicity parameter and C_l^κ is a binomial coefficient. Inverse Laplace transforming gives

$$\Omega(E) = \frac{1}{\prod_{j=1}^{\kappa} h\nu_j} \sum_{l=0}^{\kappa} \frac{C_l^\kappa a^l E^{\kappa+l-1}}{\Gamma(\kappa+l)}. \tag{3.23}$$

The total density of states is found by summing over all the minima, giving

$$\Omega(E) = \sum_{E_s^0<E} \frac{n_s^*}{\prod_{j=1}^{\kappa} h\nu_j^s} \sum_{l=0}^{\kappa} \frac{C_l^\kappa a_s^l (E-E_s^0)^{\kappa+l-1}}{\Gamma(\kappa+l)}. \tag{3.24}$$

Converting the above equation to the γ formulation using equation 3.7 gives

$$\Omega(E) \propto \sum_{E_s^0<E} \gamma(E')_s \left[\sum_{l=0}^{\kappa} \frac{C_l^\kappa a_s^l (E-E_s^0)^{\kappa+l-1}}{\Gamma(\kappa+l)} \Bigg/ \sum_{l=0}^{\kappa} \frac{C_l^\kappa a_s^l (E'-E_s^0)^{\kappa+l-1}}{\Gamma(\kappa+l)}\right]. \tag{3.25}$$

The temperature follows from equation 3.10

$$T_\mu = \frac{\sum_{E_s^0<E} \gamma(E')_s \left[\sum_{l=0}^{\kappa} \frac{C_l^\kappa a_s^l (E-E_s^0)^{\kappa+l-1}}{\Gamma(\kappa+l)} \Big/ \sum_{l=0}^{\kappa} \frac{C_l^\kappa a_s^l (E'-E_s^0)^{\kappa+l-1}}{\Gamma(\kappa+l)}\right]}{k \sum_{E_s^0<E} \gamma(E')_s \left[\sum_{l=0}^{\kappa} \frac{C_l^\kappa a_s^l (E-E_s^0)^{\kappa+l-2}}{\Gamma(\kappa+l-1)} \Big/ \sum_{l=0}^{\kappa} \frac{C_l^\kappa a_s^l (E'-E_s^0)^{\kappa+l-1}}{\Gamma(\kappa+l)}\right]}. \tag{3.26}$$

This anharmonic correction has a similar form to that used by Chekmarev and Urmirzakov[165] but has been derived in a different way.

We consider two possible ways of calculating a_s from the potential energy surface of LJ_{55}. Firstly, we consider using the third derivatives of the potential. The dissociation energy of a one-dimensional Morse oscillator can be found from the second and third derivatives of the potential by

$$D_e = \frac{(V'')^3}{(V''')^2}. \tag{3.27}$$

If off-diagonal elements in the multidimensional case are ignored, the above equation can be used to calculate the barrier heights associated with each normal mode. Using analytical third derivatives of the LJ potential, the Cartesian third derivatives for the LJ_{55} icosahedron were calculated and transformed to obtain the diagonal elements in the Hessian eigenvector basis. This scheme underestimates the anharmonicity and gives values for a_s which when substituted into equation 3.26 have an insignificant effect on $\Omega(E)$, because the off-diagonal elements, which far outnumber the diagonal elements, should not be neglected. However, there is no obvious way to calculate the effect of the off-diagonal elements and for a system such as LJ_{55} the transformation of the third derivatives into the Hessian eigenvector basis is too computationally expensive for the off-diagonal elements.

The second method considered was to use the barrier heights of our transition state sample. An average barrier height was calculated for each minimum, but for some minima it led to a gross overestimation of the anharmonicity and unphysical caloric curves. The barrier heights are not a good quantitative measure of the anharmonicity of an individual minimum. This method was therefore not considered further.

Therefore, instead of trying to obtain a_s from the PES, we considered how it could be obtained by comparison with the simulation results. If a_s is assumed to be the same for all minima, a value of a can be found which leads to the reproduction of the Van der Waals loop in the caloric curve at the observed temperature and energy, but the temperature difference between the two turning points is still too small. However, one would expect the anharmonicity to depend upon the energy of the minimum: the higher energy minima are likely to have a greater anharmonicity than the solid-like minima.

In §3.3, we saw an example of how the properties of different regions of configuration space could be obtained using suitable order parameters. Indeed, for LJ_{55}, the caloric curves associated with minima in different energy ranges were found. Using the superposition method, it is easy to calculate the properties of

TABLE 3.5: Values of the anharmonicity parameter, a_i, for LJ_{55} in the six energy ranges given in Table 3.1. Values for I, II, III and VI were found by fitting the temperatures for these regions to the simulation results.

Region	a_i/ϵ^{-1}
I	0.50
II	0.51
III	0.53
IV	0.65
V	0.70
VI	0.73

a particular region of configuration space simply by restricting the summation to those minima with suitable values of an order parameter, i.e.

$$\Omega_i = \sum_{E_s^0<E,s\in i} \Omega_s, \tag{3.28}$$

where Ω_i is the densities of states associated with region i. From the definition, $1/kT_i = (\partial \ln \Omega_i/\partial E)_{N,V}$, where T_i is the temperature of region i, it follows that

$$T_i = \frac{\displaystyle\sum_{E_s^0<E,s\in i} \gamma(E')_s \left[\sum_{l=0}^{\kappa} \frac{C_l^\kappa a_s^l (E-E_s^0)^{\kappa+l-1}}{\Gamma(\kappa+l)} \Big/ \sum_{l=0}^{\kappa} \frac{C_l^\kappa a_s^l (E'-E_s^0)^{\kappa+l-1}}{\Gamma(\kappa+l)} \right]}{\displaystyle k \sum_{E_s^0<E,s\in i} \gamma(E')_s \left[\sum_{l=0}^{\kappa} \frac{C_l^\kappa a_s^l (E-E_s^0)^{\kappa+l-2}}{\Gamma(\kappa+l-1)} \Big/ \sum_{l=0}^{\kappa} \frac{C_l^\kappa a_s^l (E'-E_s^0)^{\kappa+l-1}}{\Gamma(\kappa+l)} \right]}. \tag{3.29}$$

We assigned values of the anharmonicity parameter, a_i, to minima in the six different energy ranges (Table 3.1). Values were chosen for regions I, II, III and VI which reproduced the simulation results of Figure 3.4. The caloric curves for each region accurately fitted the simulation curves showing that our anharmonic correction term has an appropriate form. Values of a_i for regions IV and VI were chosen that were intermediate between the values for regions III and VI, but as these regions only make a small contribution to $\Omega(E)$ the exact value chosen will only have a very small effect on the overall caloric curve. The values of a_i are given in Table 3.5. As would be expected the anharmonicity increases with the potential energy of the minima.

The microcanonical caloric curve was calculated using these values of a_i. Figure 3.7 shows that for sample A the calculated curve is in remarkable agreement with the simulation results. The calculated Van der Waals loop now has the correct

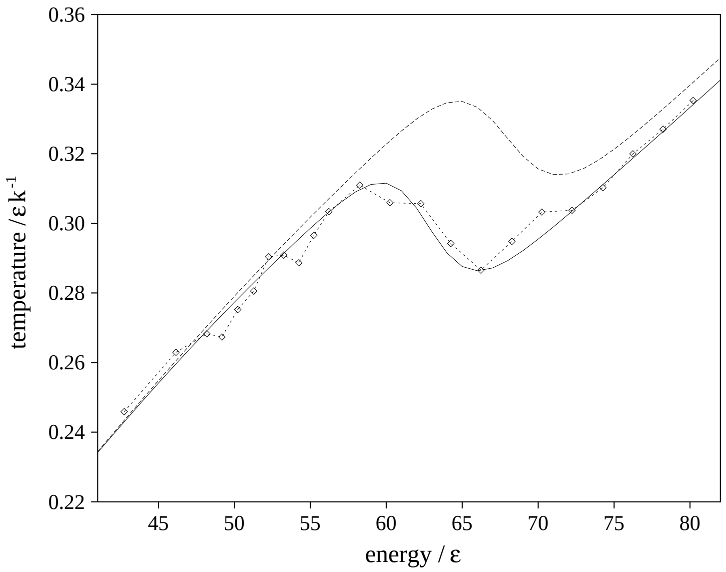

FIGURE 3.7: Microcanonical caloric curves for LJ_{55} using the γ formula including anharmonic terms with minima samples A (solid line) and B (dashed line). The calculated caloric curves are compared to simulation (dashed line with diamonds).

depth, because the effect of the greater anharmonicity of the liquid-like state is to increase the difference in temperature between the two branches of the caloric curve. The success of this method can be understood from the equation

$$\frac{1}{T} = \sum_i \frac{p_i}{T_i}, \tag{3.30}$$

where p_i is the probability that the cluster is in region i. The probabilities at E', $p_i(E')$ are fixed by the quench frequencies,

$$p_i(E') = \frac{\sum_{s \in i} \gamma_s(E')}{\sum_s \gamma_s(E')} \tag{3.31}$$

Furthermore, the p_i calculated from sample A are in good agreement with simulation results over a wide range of energy (see §3.6). The values of a_i have been chosen to reproduce the simulation temperatures, T_i, and so it is unsurprising that the overall temperature, T, is very accurate. Sample B produces worse results because there are fewer quenches to regions I–III, and so the quench frequencies are subject to larger statistical errors than for sample A.

For LJ_{13}, the STA temperature distribution is bimodal. The high temperature peak corresponds to solid-like clusters associated with the icosahedral global minimum, and the low temperature peak to liquid-like clusters. The residence times in the solid-like and liquid-like states are much shorter than for LJ_{55} and so the information provided by short-time averaging for LJ_{13} is less well-resolved. We partitioned the minima distribution into these two regions, and assigned values of a_i to each. The values of a_i were higher than for LJ_{55} and the curvature of the T_i curves differed from the simulation results. The apparently greater anharmonicity can be explained by the larger number of surface atoms for LJ_{13}. The incorrect curvature suggests that the energy dependence of the density of states is inappropriate and so the 2nd-order Morse correction term to the density of states was included. The resulting T_i curves fitted the simulation results much more accurately. The partition function for a single minimum including this term is

$$Z = \prod_{j=1}^{\kappa} \frac{1}{\beta h \nu_j} \left(1 + \frac{a}{\beta} + 3\left(\frac{a}{\beta}\right)^2\right)^{\kappa} \tag{3.32}$$

$$= \frac{1}{\prod_{j=1}^{\kappa} h\nu_j} \sum_{l=0}^{\kappa} \sum_{m=0}^{\kappa-l} D_{l,m}^{\kappa} \frac{3^m a^{l+2m}}{\beta^{\kappa+l+2m}}, \tag{3.33}$$

where

$$D_{l,m}^{\kappa} = \frac{\kappa!}{l!m!(\kappa - l - m)!}. \tag{3.34}$$

Inverse Laplace transforming and summing over all minima gives for the total density of states,

$$\Omega(E) = \sum_{E_s^0 < E} \frac{n_s^*}{\prod_{j=1}^{\kappa} h\nu_j^s} \sum_{l=0}^{\kappa} \sum_{m=0}^{\kappa-l} \frac{D_{l,m}^{\kappa} 3^m a_s^{l+2m} (E - E_s^0)^{\kappa+l+2m-1}}{\Gamma(\kappa + l + 2m)}. \tag{3.35}$$

In an MD simulation one calculates the kinetic temperature, T_K. For LJ_{55} the difference between the thermodynamic and kinetic temperatures is negligible. For LJ_{13} it is still small but not insignificant, and so T_K rather than T_μ is fitted to the simulation results. Bixon and Jortner found both temperatures produced very similar results in their model calculations of the microcanonical caloric curve[152]. T_K has been obtained for the harmonic superposition method by Franke *et al.* using the equipartition theorem[154], however this approach cannot be extended to include anharmonicity. We obtain T_K by a different method. Firstly we note that

$$\langle E_K \rangle = \int_0^E p(E_K) E_K dE_K \tag{3.36}$$

$$= \frac{1}{\Omega(E)} \int_0^E E_K \Omega_c(E - E_K) \Omega_K(E_K) dE_K, \tag{3.37}$$

where $\Omega_K(E_K)$ is the kinetic density of states, $\Omega_c(E_c)$ is the configurational density of states, and the potential energy E_c is given by $E_c = E - E_K$. Deconvoluting $\Omega_K(E_K)$ from $\Omega(E)$ gives

$$\Omega_c(E_c) = \frac{1}{(2\pi m)^{\kappa/2} \prod_{j=1}^{\kappa} \nu_j} \sum_{l=0}^{\kappa} \sum_{m=0}^{\kappa-l} \frac{D_{l,m}^{\kappa} 3^m a_s^{l+2m} (E_c - E_s^0)^{\kappa/2+l+2m-1}}{\Gamma(\kappa/2 + l + 2m)}. \tag{3.38}$$

TABLE 3.6: Details of the two samples of minima for LJ_{13}. E' is measured with respect to the global minimum icosahedron.

	E'/ϵ	Number of minima
C	13.7768	95
D	18.3268	295

TABLE 3.7: Values of the anharmonicity parameter, a_i, for the solid-like (I) and liquid-like (II) regions of the LJ_{13} PES. Region I is the potential well of the icosahedron and region II consists of all other minima.

Region	a_i/ϵ^{-1}
I	0.470
II	0.625

Integrating equation 3.37, summing over all minima and substituting into equation 3.3 gives

$$T_K = \frac{\displaystyle\sum_{E_s^0<E} \frac{n_s^*}{\prod_{j=1}^{\kappa} \nu_j^s} \sum_{l=0}^{\kappa} \sum_{m=0}^{\kappa-l} \frac{D_{l,m}^{\kappa} 3^m a_s^{l+2m} (E-E_s^0)^{\kappa+l+2m}}{\Gamma(\kappa+l+2m+1)}}{\displaystyle k \sum_{E_s^0<E} \frac{n_s^*}{\prod_{j=1}^{\kappa} \nu_j^s} \sum_{l=0}^{\kappa} \sum_{m=0}^{\kappa-l} \frac{D_{l,m}^{\kappa} 3^m a_s^{l+2m} (E-E_s^0)^{\kappa+l+2m-1}}{\Gamma(\kappa+l+2m)}}. \tag{3.39}$$

Sample C (Table 3.6) was used to calculate the caloric curve of LJ_{13} for the γ formulation because it was produced from an MD run in the coexistence region and so should have more accurate quench statistics for the low energy minima, and sample D was used for the n^* formulation because it is from the liquid-like region and so has a larger sample of minima. The values of a_i assigned to solid-like and liquid-like clusters are given in Table 3.7. From Figure 3.8 it can be seen that the caloric curve given by the n^* formulation agrees very well with simulation, because it is possible to obtain a near-complete set of minima for LJ_{13}. (Tsai and Jordan found 1328 minima in a comprehensive search of the LJ_{13} PES[162]. Many of these, though, are too high in energy to be thermodynamically significant.) The γ formulation, however, has too high a transition temperature. This error arises because the probability that the cluster is in the solid-like state derived from quenching is higher than the corresponding probability derived from the STA temperature distributions. In the γ formulation the probabilities, p_i, at E' are

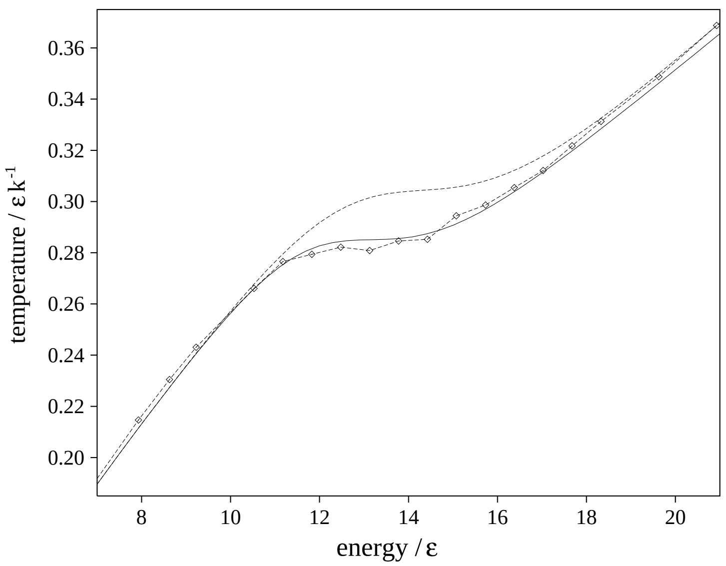

FIGURE 3.8: Microcanonical caloric curves for LJ_{13} using the n^* formula (solid line), the γ formula (dashed line) and from simulation (dashed line with diamonds). Both the n^* and γ formula curves include anharmonic terms.

fixed by the quench statistics (equation 3.31), and so this constraint leads to the higher transition temperature. The difference between the probabilities derived from quenching and the STA temperature distributions may be because there are regions of the PES which are in the basin of attraction of the icosahedron but which have thermodynamic properties similar to a liquid-like well, or because the short-time averaging does not distinguish between the solid-like and liquid-like states with the same resolution as for LJ_{55}. This difference does not stem from the quench method since we obtained similar quench statistics with steepest-descent[170,171], conjugate gradient[87] and eigenvector-following[88] methods.

3.6 Thermodynamic Properties

The accurate expressions for $\Omega(E)$ developed in the previous section can be used to give a wide range of thermodynamic functions, in fact, all except those that depend on derivatives of N or V. The exceptions arise because the thermodynamic properties of small clusters are discontinuously dependent on N and because the volume of a cluster is hard to define[172]. The formulae for the functions illustrated in this section are given in the appendix. They have, for the most part, been derived in previous work within the harmonic approximation[153,133]; the extension to incorporate anharmonicity follows simply from the expressions given in the

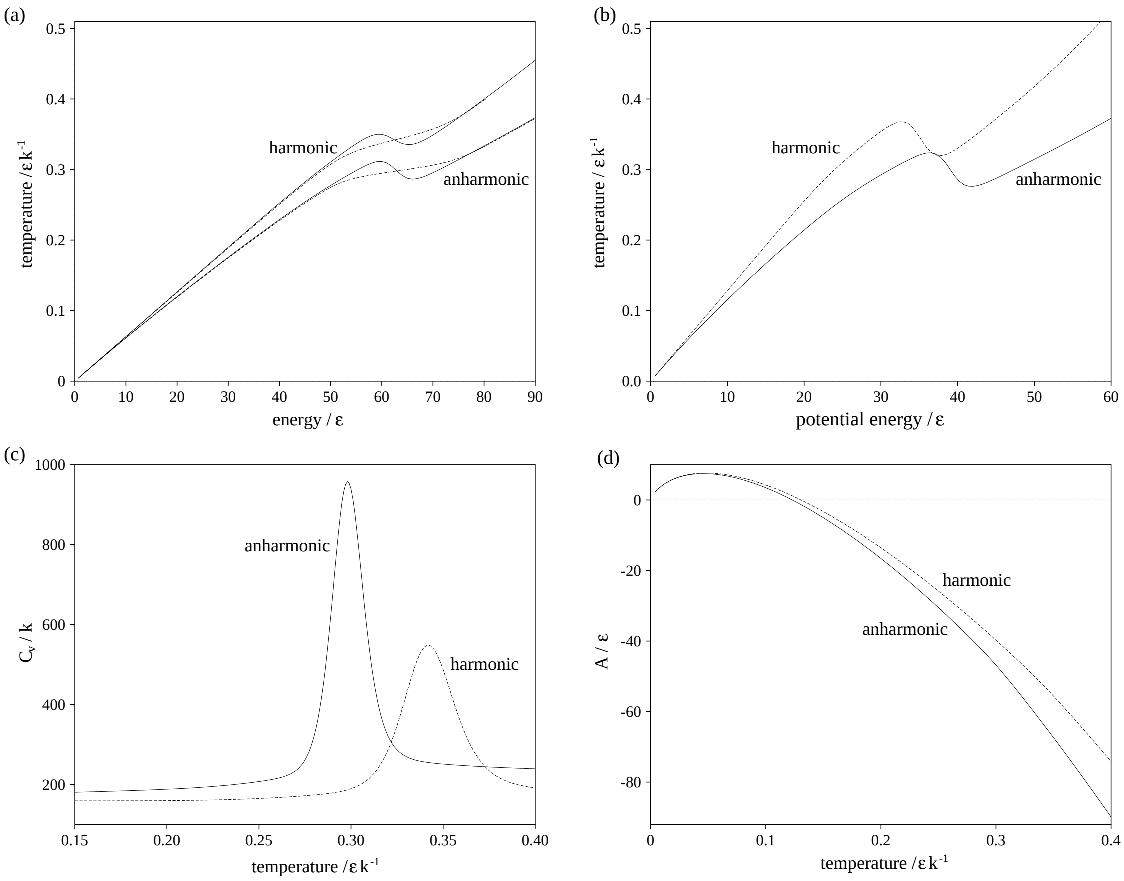

FIGURE 3.9: Comparison of harmonic and anharmonic thermodynamic functions of LJ_{55}: (a) the microcanonical (solid line) and canonical (dashed line) caloric curves, (b) the isopotential caloric curve, (c) $C_v(T)$ and (d) $A(T)$. In all except (a) the anharmonic curve is denoted by a solid line and the harmonic by a dashed line. Energies are measured with respect to the global minimum icosahedron.

previous section. The results are given for the most accurate partition functions: the first-order corrected γ formula for LJ_{55} using sample A and the second-order corrected n^* formula for LJ_{13} using sample D.

Harmonic and anharmonic results for the caloric curves, the heat capacity C_v, the Helmholtz free energy A, the transition temperature $T_{\frac{1}{2}}$ and the latent heat L_m are compared in Figures 3.9 and 3.10 and Table 3.8. We define $T_{\frac{1}{2}}$ as the temperature for which the two states have an equal Landau free energy, $A_L(E_c)$. L_m is the internal energy difference between the two states at $T_{\frac{1}{2}}$ and was obtained by extrapolating the caloric curves for each state to $T_{\frac{1}{2}}$ using equation 3.29. For LJ_{13}, this procedure simply gives $L_m = U_{II} - U_I$, where U_i is the internal energy of region i. For LJ_{55}, we have used $L_m = U_{V-VI} - U_{I-IV}$, where U_{I-IV} is the internal energy for the region of the PES formed from the combination of regions

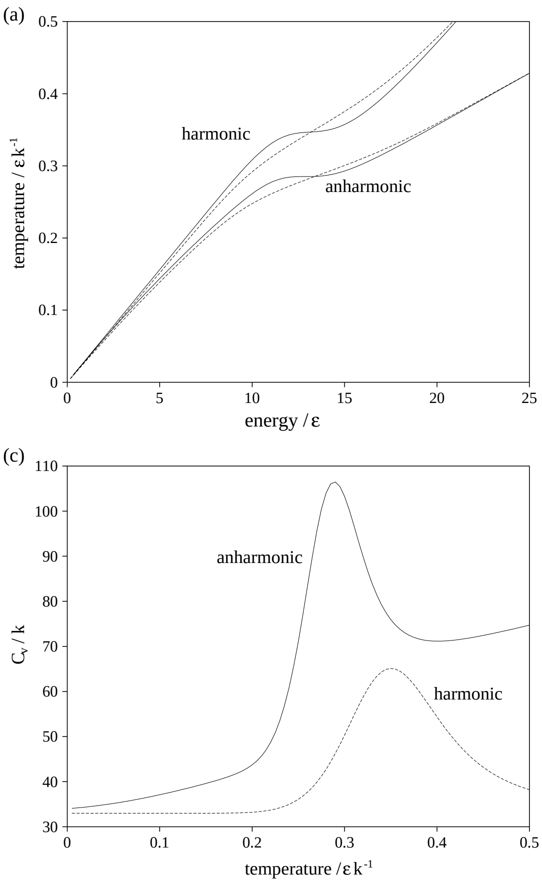

Figure 3.10: Comparison of harmonic and anharmonic thermodynamic functions of LJ_{13}: (a) the microcanonical (solid line) and canonical (dashed line) caloric curves, (b) the isopotential caloric curve, (c) $C_v(T)$ and (d) $A(T)$. In all except (a) the anharmonic curve is denoted by a solid line and the harmonic by a dashed line. Energies are measured with respect to the global minimum icosahedron.

I-IV, and so L_m does not include the latent heat associated with the disordering of the surface that occurs before melting. Just integrating C_v over the transition region would overestimate L_m because it would also include the energy needed to raise the temperature of the cluster.

The anharmonic caloric curves are displaced downward and away from their harmonic equivalents because of the increased densities of states associated with higher potential energy, lower temperature regions of the PES. The anharmonic heat capacity curve of LJ_{55} is in very good agreement with results from the multi-histogram MC[135] and J-walking[173] simulations. The peak in the heat capacity curve is larger and sharper when anharmonicity is included. This change can be understood by considering a two level system, which is a reasonable model to describe the equilibrium between solid-like and liquid-like states of the cluster.

TABLE 3.8: Transition temperatures and latent heats for LJ_{13} and LJ_{55}.

	LJ_{13}	LJ_{55}
$T_{\frac{1}{2}}/\epsilon\, k^{-1}$ (anharmonic)	0.2869	0.2985
$T_{\frac{1}{2}}/\epsilon\, k^{-1}$ (harmonic)	0.3512	0.3427
L_m/ϵ (anharmonic)	3.696	15.821
L_m/ϵ (harmonic)	2.887	12.837

The partition function can be written as $Z = \sum_i Z_i$, where the sum is over the two distinct regions of phase space. It follows that

$$U = -\left(\frac{\partial \ln Z}{\partial \beta}\right)_{N,V} = -\frac{1}{Z}\sum_i \left(\frac{\partial Z_i}{\partial \beta}\right)_{N,V} = \sum_i p_i U_i, \tag{3.40}$$

where $p_i = Z_i/Z$ and $U_i = -(\partial \ln Z_i/\partial\beta)_{N,V}$. Hence,

$$C_v = \left(\frac{\partial U}{\partial T}\right)_{N,V} = \sum_i \left(p_i C_{v,i} + U_i \left(\frac{\partial p_i}{\partial T}\right)_{N,V}\right) \tag{3.41}$$

$$= \frac{1}{2}(C_{v,1} + C_{v,2}) + L_m \left(\frac{\partial p_2}{\partial T}\right)_{N,V} \quad \text{when} \quad p_1 = p_2 = \frac{1}{2}, \tag{3.42}$$

where $L_m = U_2(T_{\frac{1}{2}}) - U_1(T_{\frac{1}{2}})$ and $C_{v,i} = (\partial U_i/\partial T)_{N,V}$. As

$$\left(\frac{\partial p_i}{\partial T}\right)_{N,V} = \frac{1}{kT^2}\left(\frac{Z_i}{Z^2}\left(\frac{\partial Z}{\partial \beta}\right)_{N,V} - \frac{1}{Z}\left(\frac{\partial Z_i}{\partial \beta}\right)_{N,V}\right) = \frac{p_i}{kT^2}(U_i - U), \tag{3.43}$$

$$\left(\frac{\partial p_2}{\partial T}\right)_{N,V} = \frac{p_1 p_2}{kT^2}(U_2 - U_1) \tag{3.44}$$

$$= \frac{L_m}{4kT_{\frac{1}{2}}^2} \quad \text{when} \quad p_1 = p_2 = \frac{1}{2}. \tag{3.45}$$

Substituting this result into equation 3.42 gives

$$C_v = \frac{1}{2}(C_{v,1} + C_{v,2}) + \frac{L_m^2}{4kT_{\frac{1}{2}}^2}. \tag{3.46}$$

The greater anharmonicity of liquid-like minima causes L_m to be larger when anharmonicity is included. This change has two effects: it increases the area under the heat capacity peak, and causes the cluster to change between the two states more rapidly with temperature, decreasing the width of the peak.

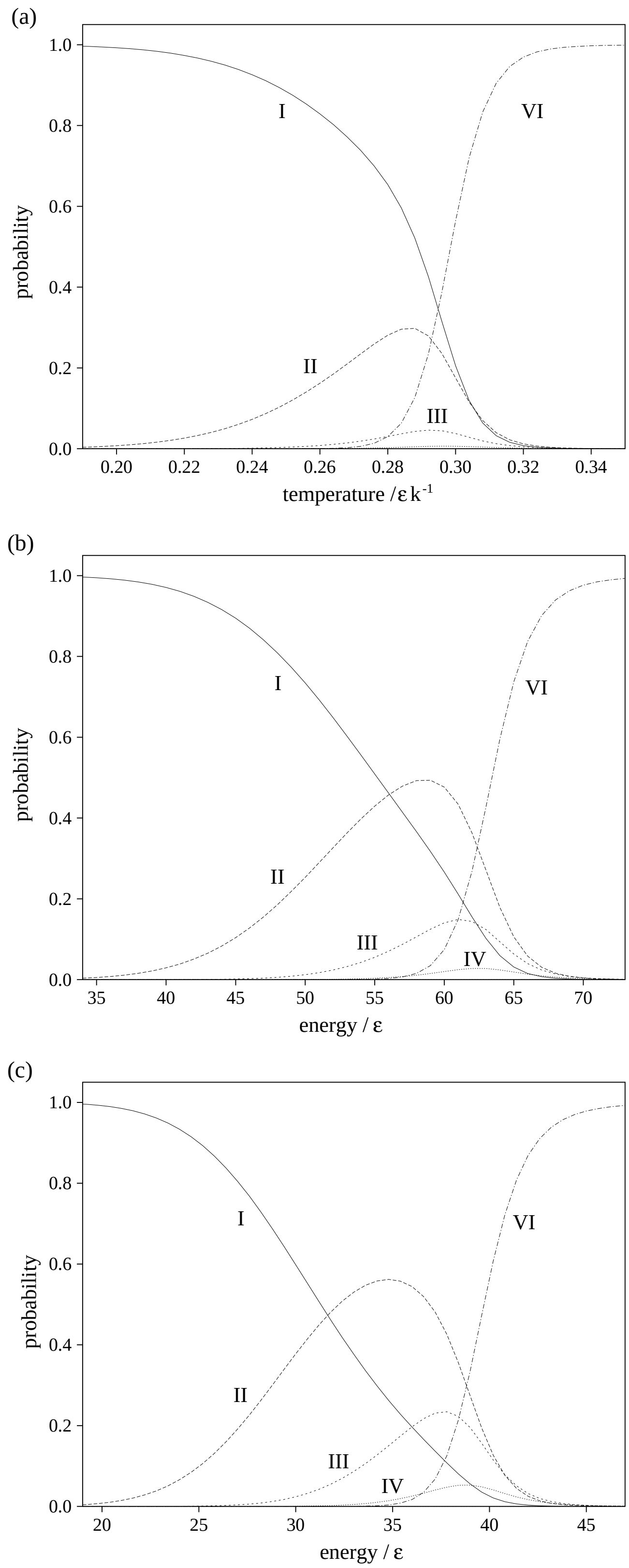

Figure 3.11: Probabilities of LJ_{55} being in regions I, II, III, IV and VI of the PES for (a) canonical, (b) microcanonical and (c) isopotential ensembles.

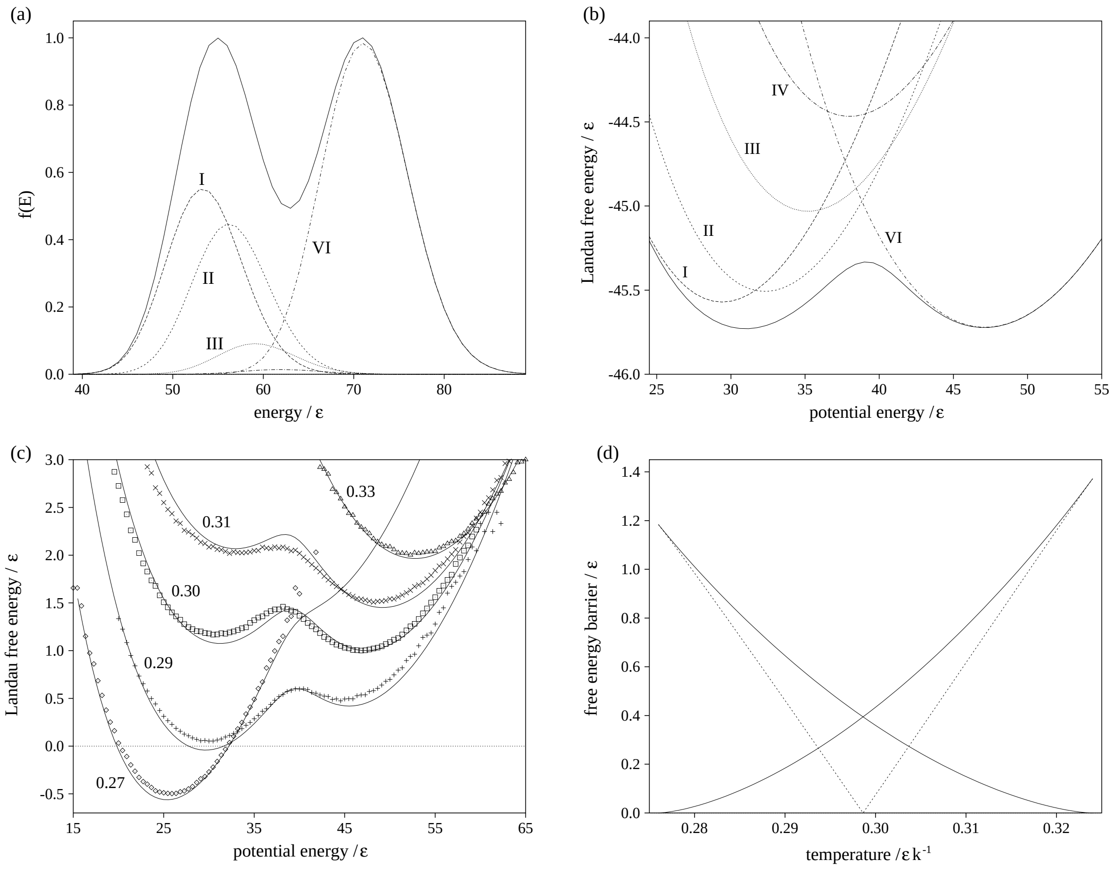

FIGURE 3.12: Plots for LJ_{55} of (a) $\mathcal{P}(E)$ at T=0.2985, (b) $A_L(E_c)$ at T=0.2985 (c) $A_L(E_c)$ at a number of temperatures as labelled and (d) the free energy barrier heights (solid lines) and the free energy difference between solid-like and liquid-like states (dashed line) for $A_L(E_c)$. In (a) and (b) the contributions of the different regions of the PES are also indicated. In (c) the results from our analytic partition function (solid line) are compared to simulation results (data points)[133].

From Figure 3.11 it can be seen that the probability of LJ_{55} being in regions II and III is lowest in the canonical ensemble and highest in the isopotential ensemble. This result is due to the dependence of the partition function on the independent variables, T, E and E_c, of the three ensembles. In the canonical ensemble, Z is exponentially dependent on T, and is the most steeply varying of the three partition functions. In the microcanonical and isopotential ensembles, Ω and Ω_c are dependent on powers of E and E_c, respectively. As the exponent of E_c is lower than that for E, Ω_c is the slowest varying of the partition functions. For LJ_{55} $n_I/n_{II-III} \gg n_{II-III}/n_{VI}$ (Table 3.9), where n_I, n_{II-III} and n_{VI} are the number of minima in regions I, II–III and VI, respectively. Consequently, as the partition function becomes more steeply varying, the defective icosahedra are seen for a

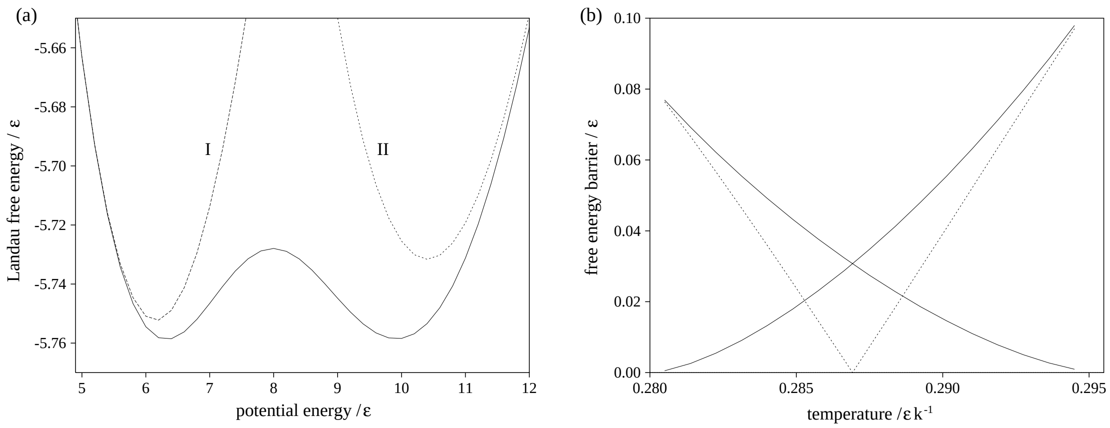

FIGURE 3.13: Plots for LJ_{13} of (a) $A_L(E_c)$ at T=0.2869, and (b) the free energy barrier heights (solid lines) and the free energy difference between solid-like and liquid-like states (dashed line) for $A_L(E_c)$. In (a) the contributions of liquid-like and solid-like states are shown.

narrower range of the independent variable, i.e. the contribution of the liquid-like states overtakes the defective icosahedra at an earlier stage in the generation of surface defects.

The Landau free energy, $A_L(Q)$, is the free energy of a system for a particular value of an order parameter Q. It is defined by

$$A_L(Q) = A - kT \ln p_Q(Q), \tag{3.47}$$

where $p_Q(Q)$ is the canonical probability distribution of the order parameter. The presence of two minima in $A_L(Q)$ indicates that there are two thermodynamically stable states at this temperature. As A is independent of Q, knowledge of $p_Q(Q)$ is sufficient to calculate the Landau free energy barrier. When E_c is used as an order parameter, simulations have shown that LJ_{55} has two Landau free energy minima which correspond to the solid-like and liquid-like states[133]. Bimodality in the canonical energy distribution function, $\mathcal{P}(E)$, implies that there are two Landau free energy minima as a function of the order parameter, E. Figures 3.12 and 3.13 show that both LJ_{13} and LJ_{55} have a range of temperature for which two Landau free energy minima are observed. As can be seen from 3.12c the predicted free energy curves for LJ_{55} are in very good agreement with those from simulation[133], confirming the accuracy of our analytic partition function. The states corresponding to the Mackay icosahedron and the defective icosahedra all contribute to the low potential energy minimum of $A_L(E_c)$, but the free energies of regions IV and V are never low enough to affect the thermodynamics. Although

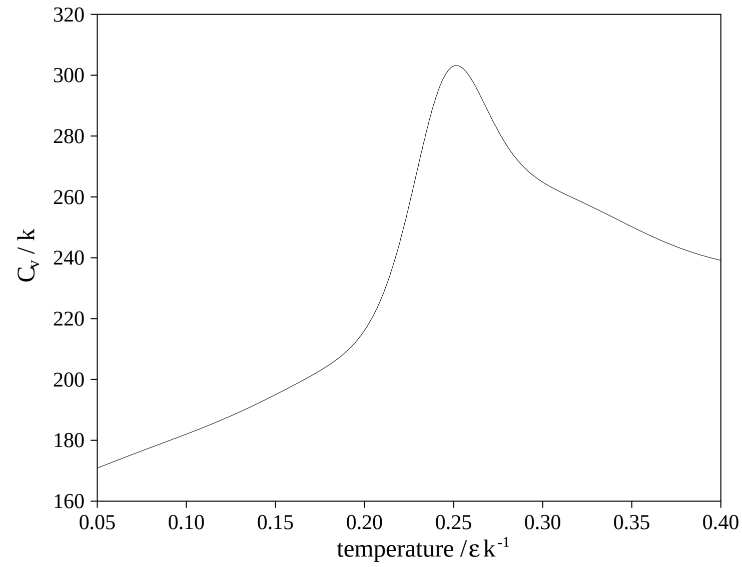

FIGURE 3.14: Heat capacity of LJ_{55} when only regions V and VI are included in the partition function.

the free energy barrier for LJ_{13} is much smaller, it has been observed in some simulations[142,174].

The turning points in $A_L(E_c)$ and $\mathcal{P}(E)$ correspond to points on the isopotential and the microcanonical caloric curves, respectively. This can be demonstrated for $A_L(E_c)$ by solving the equation $(\partial A_L/\partial E_c)_{N,V} = 0$. The solution is $1/kT = (\partial \ln \Omega_c/\partial E_c)_{N,V}$, which is simply the definition of the isopotential temperature. The maxima in $A_L(E_c)$ correspond to the segment of the caloric curve with negative slope, and the minima to segments with positive slope. Therefore the temperature range for which $A_L(E_c)$ has two minima is the same as the depth of the Van der Waals loop in the isopotential caloric curve, as can be seen by comparing Figures 3.9b and 3.12d, and 3.10b and 3.13b.

Comparing the results for LJ_{13} and LJ_{55} the effects of size are apparent. For LJ_{55} the melting transition is much more pronounced: it has a sharper peak in C_v, more pronounced Van der Waals loops in the microcanonical and isopotential caloric curves, a larger Landau free energy barrier, a larger temperature range for which solid-like and liquid-like clusters coexist, a larger latent heat per atom and a higher melting temperature. This behaviour is closer to the first-order phase transition of bulk matter.

One feature of the superposition method is that it allows one to restrict the regions of configuration space considered, and hence to look at thermodynamic properties which would be difficult to obtain by other methods. For example, we

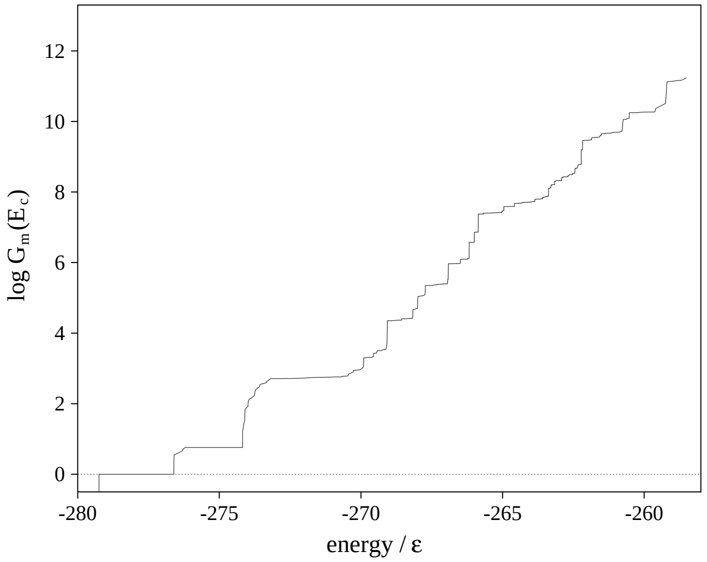

Figure 3.15: Plot of $G_m(E_c)$ for LJ_{55} as a function of the potential energy calculated using sample B.

can study the thermodynamic effects of structural relaxation in the absence of a transition to the solid-like state, thus enabling us to study supercooled liquid-like and perhaps even glass-like clusters. This could not easily be done by simulation since for LJ_{55} the cluster readily passes into the solid-like region of configuration space on cooling. Shown in Figure 3.14 is $C_{v,V-VI}$, the heat capacity when only regions V and VI are included in the partition function. It shows a clear peak at T=0.252 ($0.84T_{\frac{1}{2}}$), which has a height above the background C_v that is about a seventh of that for melting. It resembles the heat capacity peak that is often seen at the bulk glass transition. Such an interpretation should be caveated by the fact that the peak is dependent on where one decides the low energy tail of the liquid-like minima finishes.

Estimates of the number of minima in different regions of the PES can be obtained from the quench frequencies. Using equations 3.6, 3.7 and 3.9 an expression for g_s can be derived:

$$g_s = \frac{\gamma(E')_s h_s \prod_{j=1}^{\kappa} \nu_j^s}{\gamma(E')_0 h_0 \prod_{j=1}^{\kappa} \nu_j^0} \sum_{l=0}^{\kappa} \frac{C_l^\kappa a_0^l (E' - E_0^0)^{\kappa+l-1}}{\Gamma(\kappa+l)} \Big/ \sum_{l=0}^{\kappa} \frac{C_l^\kappa a_s^l (E' - E_s^0)^{\kappa+l-1}}{\Gamma(\kappa+l)}. \quad (3.48)$$

From g_s, the sum of minima, $G_m(E_c)$, can easily be calculated

$$G_m(E_c) = \sum_{E_s^0 < E_c} g_s. \quad (3.49)$$

This approach has been applied to LJ_{55}. From Figure 3.15 it can be seen that above -270ϵ the number of minima rises exponentially with the energy. The total

Table 3.9: Estimated numbers of geometrically distinct minima of LJ_{55} in the six energy ranges given in Table 3.1 calculated using sample A.

Region	number of minima	
	anharmonic	harmonic
I	1	1
II	11.3	6.3
III	994.6	457.9
IV	81.5	2871.2
V	1.26×10^5	1.22×10^6
VI	8.30×10^{11}	3.11×10^{12}

number of minima in the energy range probed by the MD quenching (potential energies up to -259ϵ) is 8.3×10^{11}. This value is much less than the total number of minima predicted by extrapolating Tsai and Jordan's results for small clusters and so suggests that the number of minima will continue to rise exponentially above -259ϵ. The present method has also been used to estimate the number of minima in the energy ranges I-VI (Table 3.9). The number of minima in range II is known[108] to be 11. The results from the quench frequencies agree well with this figure.

The methods developed here should be applicable to other types of clusters, although, as in our examples, the most appropriate form for the anharmonic terms may depend on the type and size of cluster considered. The advantages of the superposition method are that once the partition function is obtained it can be used to calculate a whole gamut of thermodynamic properties analytically, and that it allows one to consider the roles of different regions of configuration space and so gain more physical insight into the system, particularly the relationship between structure and thermodynamics. (If one simply wants $\Omega(E)$ without these extras, one should use a simulation method, such as multi-histogram MC[141].) However, the method currently relies upon there being an energy at which all relevant regions of phase space are sampled. This condition does not hold for larger clusters, such as LJ_{147}. To extend the method to such systems an analogue of the multi-histogram technique would need to be developed, in which the information from quenching at different energies could be combined. The expressions for the density of states could also be used to calculate accurate rate constants using RRKM (Rice-Ramsperger-Kassel-Marcus) theory[166,175], and so aid quantitative elucidation of dynamic properties from a knowledge of the transition states on the PES.

3.7 Van der Waals Loops and Size Dependence

Here, building upon previous work[134], we consider the conditions for a Van der Waals loop to occur in the microcanonical caloric curve using a two state model. By differentiating equation 3.30, we obtain

$$\left(\frac{\partial T}{\partial E}\right)_{N,V} = T^2 \sum_i \left[\frac{p_i}{T_i^2}\left(\frac{\partial T_i}{\partial E}\right)_{N,V} - \frac{1}{T_i}\left(\frac{\partial p_i}{\partial E}\right)_{N,V}\right], \tag{3.50}$$

where the probabilities and their derivatives obey $\sum_i p_i = 1$ and $\sum_i (\partial p_i/\partial E)_{N,V} = 0$. For a two state system, this expression becomes

$$\left(\frac{\partial T}{\partial E}\right)_{N,V} = T^2\left(\frac{\partial p_1}{\partial E}\right)_{N,V}\left(\frac{1}{T_2}-\frac{1}{T_1}\right) + T^2\left(\frac{p_1}{T_1^2}\left(\frac{\partial T_1}{\partial E}\right)_{N,V} + \frac{p_2}{T_2^2}\left(\frac{\partial T_2}{\partial E}\right)_{N,V}\right). \tag{3.51}$$

The first term in this expression is negative and the second positive (assuming region 1 has a lower potential energy than region 2). To exhibit a Van der Waals loop, the caloric curve must have a region of negative slope, and therefore the following inequality must be satisfied for some range of energy,

$$\left(\frac{\partial p_2}{\partial E}\right)_{N,V}\left(\frac{1}{T_2}-\frac{1}{T_1}\right) > \frac{p_1}{T_1^2}\left(\frac{\partial T_1}{\partial E}\right)_{N,V} + \frac{p_2}{T_2^2}\left(\frac{\partial T_2}{\partial E}\right)_{N,V}. \tag{3.52}$$

If we assume both regions behave harmonically, then $T_1 = \alpha E$ and $T_2 = \alpha(E-\Delta)$, where Δ is the potential energy difference between the minima of the two regions. This assumption gives

$$\left(\frac{\partial p_2}{\partial E}\right)_{N,V}\left(\frac{1}{E-\Delta}-\frac{1}{E}\right) > \frac{p_1}{E^2} + \frac{p_2}{(E-\Delta)^2}, \tag{3.53}$$

$$\text{so} \quad \left(\frac{\partial p_2}{\partial E}\right)_{N,V}\Delta > p_1\left(1-\frac{\Delta}{E}\right) + p_2\left(1-\frac{\Delta}{E}\right)^{-1},$$

$$> 1 + \frac{\Delta}{E}(p_2 - p_1) + O\left(\left(\frac{\Delta}{E}\right)^2\right). \tag{3.54}$$

In the middle of the coexistence region where $p_1 = p_2 = 1/2$, neglecting second order terms in (Δ/E) gives

$$\left(\frac{\partial p_2}{\partial E}\right)_{N,V}\Delta > 1. \tag{3.55}$$

This equation was previously derived by Bixon and Jortner[152] for Van der Waals loops in the kinetic temperature. We now continue the analysis, first noting that

$$\left(\frac{\partial p_i}{\partial E}\right)_{N,V} = \frac{1}{\Omega}\left(\frac{\partial \Omega_i}{\partial E}\right)_{N,V} - \frac{\Omega_i}{\Omega^2}\left(\frac{\partial \Omega}{\partial E}\right)_{N,V}, \tag{3.56}$$

$$= \frac{p_i}{k}\left(\frac{1}{T_i} - \frac{1}{T}\right). \tag{3.57}$$

Therefore, using equation 3.30

$$\left(\frac{\partial p_2}{\partial E}\right)_{N,V} = \frac{p_1 p_2}{k}\left(\frac{1}{T_2} - \frac{1}{T_1}\right) = \frac{p_1 p_2}{\alpha k}\frac{\Delta}{E(E-\Delta)}. \tag{3.58}$$

Substituting this result into equation 3.53 and rearranging gives

$$\left(p_1 - \frac{p_1 p_2}{\alpha k}\right)\left(\frac{\Delta}{E}\right)^2 - 2p_1\frac{\Delta}{E} + 1 < 0. \tag{3.59}$$

Taking the middle of the coexistence region, where $p_1 = p_2 = 1/2$ and $E = E_{\frac{1}{2}}$:

$$\left(1 - \frac{1}{2\alpha k}\right)\left(\frac{\Delta}{E_{\frac{1}{2}}}\right)^2 - 2\frac{\Delta}{E_{\frac{1}{2}}} + 2 < 0. \tag{3.60}$$

As this quadratic has negative curvature for all realistic values of α, the above inequality has a physically meaningful solution when $(\Delta/E_{\frac{1}{2}})$ is greater than the larger root of the quadratic. This solution is

$$\frac{\Delta}{E_{\frac{1}{2}}} > \frac{\left(\frac{1}{\alpha k} - 1\right)^{1/2} - 1}{\left(\frac{1}{2\alpha k} - 1\right)}. \tag{3.61}$$

For a single harmonic minimum of an N-atom cluster

$$\frac{1}{\alpha} = \left(\frac{\partial E}{\partial T}\right)_{N,V} = (3N-7)k. \tag{3.62}$$

Hence,

$$\frac{\Delta}{E_{\frac{1}{2}}} > \frac{2((3N-8)^{1/2} - 1)}{(3N-9)} \approx \frac{2}{\sqrt{3N}} \quad \text{for large } N. \tag{3.63}$$

A similar relationship can be derived for the N-dependence of Van der Waals loops in the caloric curve of the isopotential ensemble. In this case

$$\left(\frac{\partial E_c}{\partial T_c}\right)_{N,V} = \left(\frac{3N}{2} - 4\right)k, \tag{3.64}$$

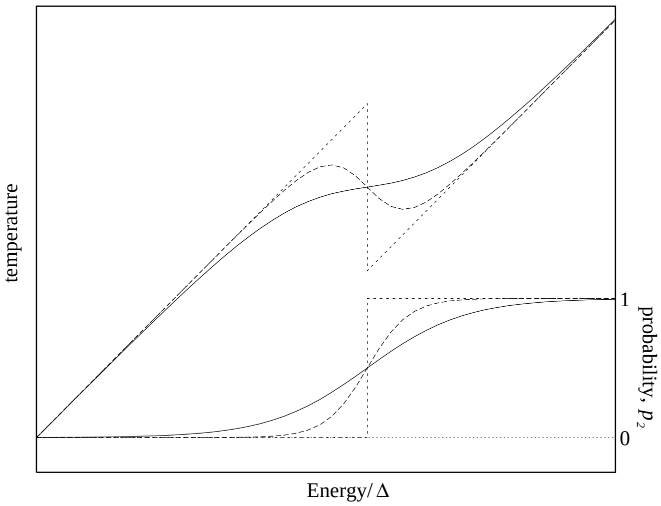

FIGURE 3.16: Plots of temperature (top) and probability, p_2, (bottom) for a two state system. $E_{\frac{1}{2}}/\Delta$ is kept constant as N is varied. The solid line is for small N, long dashed line is for intermediate N and the short dashed line for the bulk limit.

where E_c is the potential energy and T_c is the isopotential temperature. Hence,

$$\frac{\Delta}{E_{c,\frac{1}{2}}} > 2\sqrt{\frac{2}{3N}} \qquad \text{for large } N. \tag{3.65}$$

As $E_{c,\frac{1}{2}} < E_{\frac{1}{2}}/\sqrt{2}$, this confirms that a Van der Waals loop is more likely in the isopotential ensemble than the microcanonical ensemble. As we saw earlier, LJ_{13} has a Van der Waals loop in the isopotential caloric curve but not in the microcanonical curve.

From equation 3.63 it is clear that for a series of structures with similar values of $\Delta/E_{\frac{1}{2}}$, a Van der Waals loop will become more likely as the size increases (Figure 3.16). This result is in good agreement with simulations of icosahedral LJ[135] and cuboctahedral gold clusters[136].

In the bulk limit the above model predicts the caloric curve will be vertical at $E_{\frac{1}{2}}$ (Figure 3.16), which is clearly at variance with the expected behaviour for a bulk first-order phase transition. This discrepancy arises because we have not allowed for the cluster dividing into distinct solid-like and liquid-like regions, which would contribute a term of the form $\Omega_s^{(1-x)}\Omega_l^x$ to the density of states, where x is the fraction of the cluster that is liquid-like. Such phase separation does not occur for small clusters because the energy of the dividing surface makes it unfavourable, but for the bulk the interface is a negligible fraction of the total energy. Recently, an analytical model has been investigated which predicts the size evolution of the microcanonical caloric curve as phase separation becomes possible[176].

Equation 3.63 also shows us that a Van der Waals loop becomes more likely as the quantity $\Delta/E_{\frac{1}{2}}$ increases. We can understand the conditions for this quantity to be large by considering the density of states for each region. For simplicity we do this within the harmonic approximation. We consider region 1 to be made up of n_1 similar geometric isomers (with the same energy, vibrational frequencies and point group), and region 2 of n_2. Each geometric isomer has $2N!/h_i$ permutational isomers. These assumptions yield

$$\Omega_1 = \frac{2n_1 N! E^{\kappa-1}}{h_1 \Gamma(\kappa)(h\overline{\nu}_1)^\kappa} \quad \text{and} \quad \Omega_2 = \frac{2n_2 N! (E-\Delta)^{\kappa-1}}{h_2 \Gamma(\kappa)(h\overline{\nu}_2)^\kappa}, \tag{3.66}$$

where h_i is the order of the point group for states in region i. $\Omega_1 = \Omega_2$ at $E = E_{\frac{1}{2}}$. Hence,

$$\frac{\Delta}{E_{\frac{1}{2}}} = \left(1 - \left(\frac{n_1 h_2 \overline{\nu}_2)^\kappa}{n_2 h_1 \overline{\nu}_1)^\kappa}\right)^{1/(\kappa-1)}\right). \tag{3.67}$$

From this expression we can see that $\Delta/E_{\frac{1}{2}}$ increases, making a Van der Waals loop more likely, as region 1 becomes more solid-like (a few high symmetry, rigid states) and as region 2 becomes more liquid-like (many low symmetry, non-rigid states).

Appendix: Thermodynamic Formulae

In this appendix, the formulae for some of the thermodynamic quantities that can be calculated by the superposition method are given. The thermodynamic functions are derived from the following definitions.

In the isopotential ensemble,

$$p_i(E_c) = \frac{\Omega_{c,i}(E_c)}{\Omega_c(E_c)}, \qquad \frac{1}{kT_c(E_c)} = \left(\frac{\partial \ln \Omega_c}{\partial E_c}\right)_{N,V}.$$

In the microcanonical ensemble,

$$p_i(E) = \frac{\Omega_i(E)}{\Omega(E)}.$$

In the canonical ensemble,

$$p_i(T) = \frac{Z_i}{Z},$$

$$U(T) = -\left(\frac{\partial \ln Z}{\partial \beta}\right)_{N,V} = \frac{1}{Z_{0,0}}(Z_{1,0} + Z_{0,1}),$$

$$\begin{aligned} C_v(T) &= \left(\frac{\partial U}{\partial T}\right)_{N,V}, \\ &= \frac{1}{kT^2}\left(\frac{1}{Z_{0,0}}(Z_{2,0}+2Z_{1,1}+Z_{0,2}) - \left(\frac{Z_{1,0}+Z_{0,1}}{Z_{0,0}}\right)^2\right), \end{aligned}$$

$$A(T) = E_0^0 - kT\ln Z,$$

$$\mathcal{P}(E) = \Omega(E)\exp(-\beta E),$$

$$A_L(E_c) = E_c - kT\ln\Omega_c(E_c),$$

where in $Z_{\alpha,\delta}$ the derivative of the exponential function of β in Z has been taken α times and the derivative of the inverse power of β in Z δ times. Therefore, $Z = Z_{0,0}$.

Below, we give the thermodynamic functions for the γ formulation with a first-order anharmonic correction which was used for LJ_{55}.

$$T_c(E_c) = \frac{\sum_{E_s^0<E_c}\gamma(E')_s \sum_{l=0}^{\kappa}\frac{C_l^\kappa a_s^l(E_c-E_s^0)^{\kappa/2+l-1}}{\Gamma(\kappa/2+l)}\Big/\sum_{l=0}^{\kappa}\frac{C_l^\kappa a_s^l(E'-E_s^0)^{\kappa+l-1}}{\Gamma(\kappa+l)}}{k\sum_{E_s^0<E_c}\gamma(E')_s \sum_{l=0}^{\kappa}\frac{C_l^\kappa a_s^l(E_c-E_s^0)^{\kappa/2+l-2}}{\Gamma(\kappa/2+l-1)}\Big/\sum_{l=0}^{\kappa}\frac{C_l^\kappa a_s^l(E'-E_s^0)^{\kappa+l-1}}{\Gamma(\kappa+l)}}.$$

$$Z_{\alpha,\delta} = c\sum_s \gamma(E')_s(E_s^0)^\alpha e^{-\beta E_s^0}\sum_{l=0}^{\kappa}\frac{\Gamma(\kappa+l+\delta)}{\Gamma(\kappa+l)}\frac{C_l^\kappa a_s^l}{\beta^{\kappa+l+\delta}}\Big/\sum_{l=0}^{\kappa}\frac{C_l^\kappa a_s^l(E'-E_s^0)^{\kappa+l-1}}{\Gamma(\kappa+l)}.$$

$$A_L(E_c) = E_c - \frac{1}{\beta}\ln\frac{c}{\beta^{\kappa/2}}\sum_{E_s^0<E_c}\gamma(E')_s\sum_{l=0}^{\kappa}\frac{C_l^\kappa a_s^l(E_c-E_s^0)^{\kappa/2+l-1}}{\Gamma(\kappa/2+l)}\Big/\sum_{l=0}^{\kappa}\frac{C_l^\kappa a_s^l(E'-E_s^0)^{\kappa+l-1}}{\Gamma(\kappa+l)},$$

where

$$c = \frac{n_0^*}{\gamma(E')_0\prod_{j=1}^{\kappa}h\nu_j^0}\sum_{l=0}^{\kappa}\frac{C_l^\kappa a_0^l(E'-E_0^0)^{\kappa+l-1}}{\Gamma(\kappa+l)}.$$

The harmonic forms can be recovered by taking the $l=0$ term. We obtain the n^* formulation by replacing

$$c\,\gamma(E')_s\Big/\sum_{l=0}^{\kappa}\frac{C_l^\kappa a_s^l(E'-E_s^0)^{\kappa+l-1}}{\Gamma(\kappa+l)} \qquad \text{with} \qquad \frac{n_s^*}{\prod_{j=1}^{\kappa}h\nu_j^s}.$$

Below, we give the thermodynamic functions for the n^* formulation with second-order anharmonic corrections which was used for LJ_{13}.

$$T_c(E_c) = \frac{\sum_{E_s^0<E_c}\frac{n_s^*}{\prod_{j=1}^{\kappa}h\nu_j^s}\sum_{l=0}^{\kappa}\sum_{m=0}^{\kappa-l}\frac{D_{l,m}^\kappa 3^m a_s^{l+2m}(E_c-E_s^0)^{\kappa/2+l+2m-1}}{\Gamma(\kappa/2+l+2m)}}{k\sum_{E_s^0<E_c}\frac{n_s^*}{\prod_{j=1}^{\kappa}h\nu_j^s}\sum_{l=0}^{\kappa}\sum_{m=0}^{\kappa-l}\frac{D_{l,m}^\kappa 3^m a_s^{l+2m}(E_c-E_s^0)^{\kappa/2+l+2m-2}}{\Gamma(\kappa/2+l+2m-1)}},$$

$$Z_{\alpha,\delta} = \sum_s \frac{n_s^* e^{-\beta E_s^0} (E_s^0)^\alpha}{\prod_{j=1}^{\kappa} h\nu_j^s} \sum_{l=0}^{\kappa} \sum_{m=0}^{\kappa-l} \frac{\Gamma(\kappa+l+2m+\delta)}{\Gamma(\kappa+l+2m)} \frac{D_{l,m}^{\kappa} 3^m a_s^{l+2m}}{\beta^{\kappa+l+2m+\delta}},$$

$$A_L(E_c) = E_c - \frac{1}{\beta} \ln \sum_{E_s^0 < E_c} \frac{n_s^*}{\beta^{\kappa/2} \prod_{j=1}^{\kappa} h\nu_j^s} \sum_{l=0}^{\kappa} \sum_{m=0}^{\kappa-l} \frac{D_{l,m}^{\kappa} 3^m a_s^{l+2m} (E_c - E_s^0)^{\kappa/2+l+2m-1}}{\Gamma(\kappa/2+l+2m)}.$$

The harmonic forms can be recovered by taking the $l = 0, m = 0$ term, and the first-order correction forms by taking the $m = 0$ terms. We obtain the γ formulation by replacing

$$\frac{n_s^*}{\prod_{j=1}^{\kappa} h\nu_j^s} \qquad \text{with} \qquad c\,\gamma(E')_s \Big/ \sum_{l=0}^{\kappa} \sum_{m=0}^{\kappa-l} \frac{D_{l,m}^{\kappa} 3^m a_s^{l+2m} (E' - E_s^0)^{\kappa+l+2m-1}}{\Gamma(\kappa+l+2m)},$$

where

$$c = \frac{n_0^*}{\gamma(E')_0 \prod_{j=1}^{\kappa} h\nu_j^0} \sum_{l=0}^{\kappa} \sum_{m=0}^{\kappa-l} \frac{D_{l,m}^{\kappa} 3^m a_0^{l+2m} (E' - E_0^0)^{\kappa+l+2m-1}}{\Gamma(\kappa+l+2m)}.$$

Chapter 4
The Structure and Stability of Simple Liquids

4.1 Introduction

In a recent paper Hagen *et al.* posed the question, 'Does C_{60} have a liquid phase?'[177] A liquid-vapour transition can only occur between the triple point temperature, below which only the solid and vapour are stable, and the critical temperature, above which there is only one fluid phase (Figure 4.1a). So, if the critical temperature is lower than the solid-fluid coexistence temperature at the critical density (Figure 4.1b), the liquid phase is thermodynamically unstable[178]. The answer to Hagen's question, though, has not yet been unequivocally answered: theoretical calculations of the phase diagram predict the liquid phase of bulk C_{60} is either unstable[177] or only marginally stable[179,180] depending on the simulation technique used, whilst experiment seems to suggest that C_{60} molecules are thermally unstable at the relevant temperatures[181].

In contrast to C_{60}, for which the intermolecular potential is very short-ranged with respect to the equilibrium pair separation, the critical temperature for sodium is about seven times larger than the triple point temperature because of the long-ranged interatomic forces. The results for C_{60} have led to a flurry of studies examining the effect of the range of the potential on the phase diagram[182–185]. These investigations have clearly shown that as the range of attraction decreases, the difference between the triple and critical temperatures decreases until the critical temperature drops below the triple point and the liquid phase disappears. Similar effects have previously been noted for mixtures of spherical colloidal particles and non-adsorbing polymer by theory[120], simulation[186] and experiment[121–123]. For such systems, the size of the polymer can be used to vary systematically the range

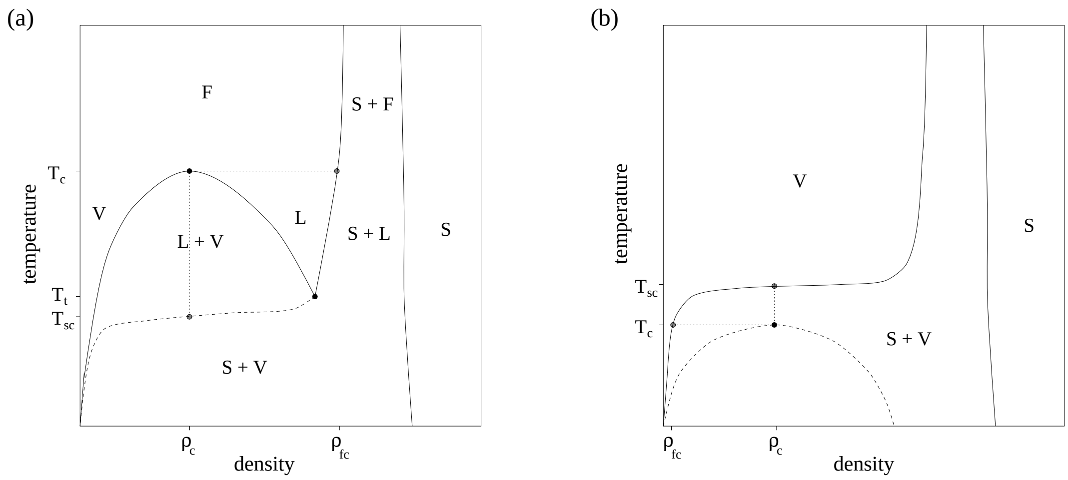

FIGURE 4.1: Temperature/density phase diagrams when (a) there is a stable liquid phase, and (b) the liquid phase is thermodynamically unstable. S, L, V and F stand for solid, liquid, vapour and fluid, respectively. T_c is the critical temperature, T_t is the triple point temperature, T_{sc} is the solid-fluid coexistence temperature at the critical density, ρ_c is the critical density, and ρ_{fc} is the density of the fluid which coexists with the solid at the critical temperature. The dashed lines are in (a) the metastable solid-fluid coexistence line and in (b) the metastable liquid-vapour coexistence line. For (a) $T_c > T_t > T_{sc}$ and $\rho_c < \rho_{fc}$ and for (b) $T_c < T_{sc}$ and $\rho_c > \rho_{fc}$. The latter are the necessary and sufficient conditions for there to be no stable liquid phase. The dotted lines are to guide the eye.

of attraction between the colloidal particles.

Although the phenomenology of the range-dependence of the liquid phase stability is clear, a structural explanation has not been given. In this chapter we provide such a microscopic view by relating the above effects to fundamental changes in the topography of the PES (§4.3) and by making a detailed connection between these changes and liquid structure (§4.4). By studying both clusters and bulk we can address questions concerning the emergence of the phase-like forms of clusters and their evolution to the bulk limit. Detailed simulations of the thermodynamic properties of a 55-atom cluster (§4.5) confirm that our results can explain the range-dependence of the thermodynamics. We can also suggest an explanation for the transition from electronic to geometric magic numbers observed in the mass spectra of sodium clusters[53] (§4.6), showing that the simple approach we describe here can provide insight into a diverse set of phenomena.

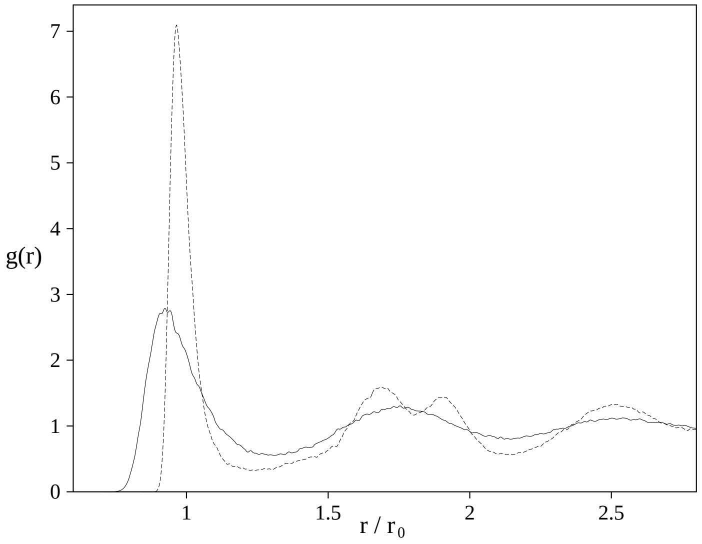

FIGURE 4.2: Bulk liquid radial distribution functions from a set of instantaneous coordinates (solid line) and the resulting minima after quenching (dashed line). The system is a periodically repeated cubic cell containing 256 atoms interacting via a Morse potential with ρ_0=6.

4.2 Methods

The focus of this chapter is to understand the dependence of the global topography (not just the low energy regions as in Chapter 2) of the PES on the range of the potential. To achieve this aim we again use the Morse potential; the analysis of the contributions to the potential energy given in §2.2.1 will be extremely important for understanding the range dependence of the thermodynamics.

In the present examination of the PES we will generally focus upon minima. As we noted in Chapter 3 this 'inherent structure' approach[148] allows one to analyse the thermodynamics in detail by separating the effects of the energetic distribution of local minima from the effects of thermal motion within the minima. Our analysis of the thermodynamics here will be more qualitative, simply concentrating on the distribution of minima. By removing the effects of vibrational noise this approach also allows a much clearer picture of liquid structure. This point is illustrated in Figure 4.2 by a comparison of the radial distribution functions derived from a set of instantaneous configurations of a bulk Morse liquid and the configurations of the corresponding minima. The peaks in the radial distribution function for the minima are much sharper, showing that the structure is much more well-defined. Of particular interest is the split second peak for the minima radial distribution function. This feature only develops in the instantaneous radial distribution function

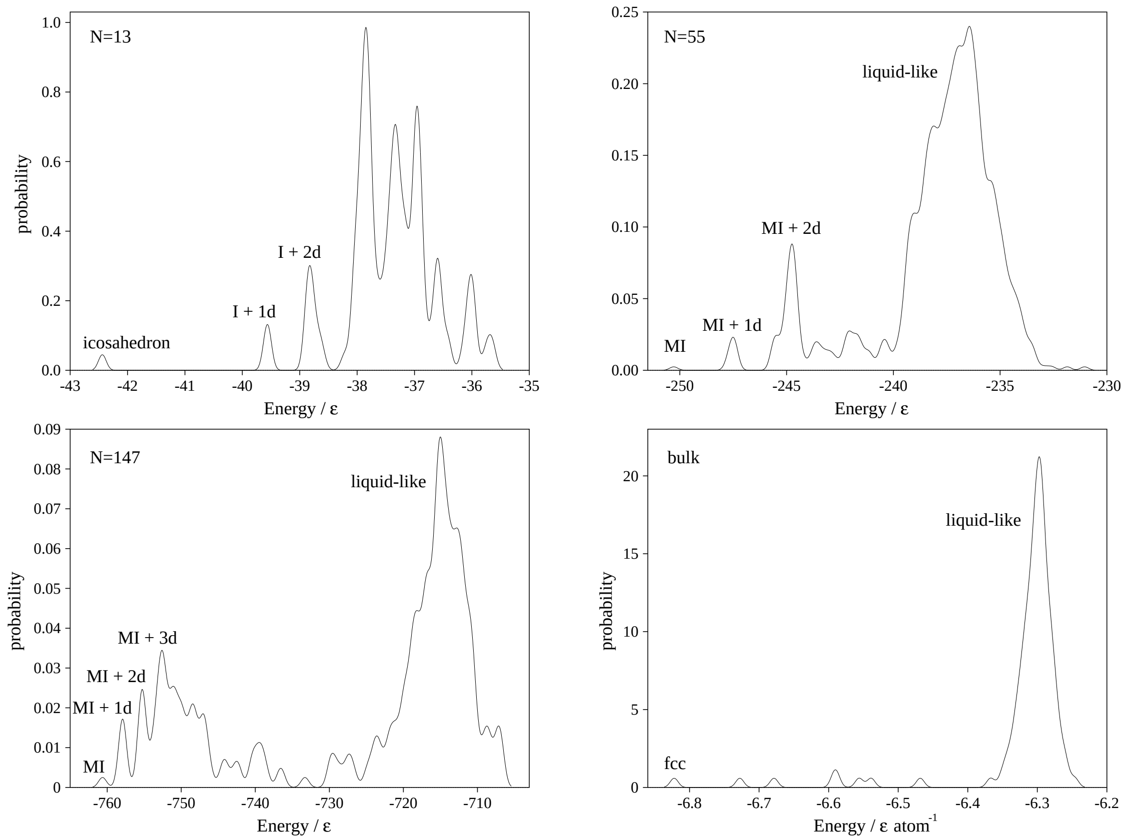

FIGURE 4.3: Probability distributions of the potential energy for samples of minima of M_{13}, M_{55}, M_{147} and bulk material. The samples contain 131, 858, 298 and 117 minima, respectively. Some of the peaks are labelled with the structures they correspond to. I stands for icosahedron, MI for Mackay icosahedron, + nd for a structure with n defects.

for supercooled liquids and glasses[187]. It is not too surprising that minimization and reducing the temperature have similar effects, and this helps to emphasize the structural connection between the liquid and the glass.

4.3 Correlation Diagrams

We employed molecular dynamics and conjugate-gradient techniques to generate between 10^2 and 10^3 local minima for each PES at $\rho_0 = 6$. The simulations of bulk material were performed at constant volume in a cubic box containing 256 atoms at a reduced density of $\sqrt{2}$. The three clusters we studied contained 13, 55 and 147 atoms, and have been chosen because they correspond to sizes for which complete Mackay icosahedra are possible. In the melting region these clusters fluctuate between a solid-like and a liquid-like state as a function of time. Consequently, a simulation at a single energy in this coexistence region was sufficient to sample

Table 4.1: Lowest energy minima found for M_{147}. The format is as for Table 2.2.

	PG	n_{nn}	E_{strain}	$\rho_0 = 3.0$	$\rho_0 = 6$	$\rho_0 = 10$	$\rho_0 = 14$	ρ_{min}	ρ_{max}
147A	C_1	729	97.629	**-1531.499**	-732.549	-637.693	-605.600		3.56
147B	I_h	696	26.896	-1509.272	**-760.631**	-678.171	-644.002	3.56	9.12
147C	C_s	674	1.514		-748.869	**-682.399**	-672.885	9.12	10.91
147D	C_s	674	1.495		-748.598	-682.386	**-672.911**	10.91	18.88
147E	C_{3v}	669	0.084	-1468.423[8]	-744.765	-678.962	-670.708	18.88	

all relevant regions of the PES's of the M_{13} and M_{55} clusters. However, for M_{147} separate simulations were needed to sample the equilibria between the solid and its low energy defective states, and between the high energy defective states of the solid and the liquid.

The four distributions of minima obtained are shown in Figure 4.3. The geometries of the local minima were subsequently reoptimized for ascending and descending integer values of ρ_0. For the bulk material, the box size was scaled at each value of ρ_0 to keep the energy of the fcc minimum at a constant fraction of its zero-pressure energy. On changing ρ_0 a minimum may disappear from the PES. When this occurs, geometry optimization leads to a new minimum and this causes the discontinuities in the correlation diagrams (Figure 4.4). This effect is particularly noticeable for the 13-atom cluster at long range, because the total number of minima on the PES at ρ_0=3 is less than the number of minima in our sample from ρ_0=6 (Table 2.1).

The lowest energy line in each correlation diagram at any given ρ_0 corresponds to the solid phase, since at zero Kelvin this structure must have the lowest free energy. For the bulk material (Figure 4.4), the lowest energy minimum is fcc for all values of ρ_0. However, as we saw in Chapter 2 the structure of the global minimum depends on ρ_0 for clusters. The global minima of M_{147} are illustrated in Figure 4.5, and their energies and the ranges of ρ_0 for which they are the global minima are given in Table 4.1.

In the correlation diagrams the relative slope of two lines is a measure of the difference in strain energies between two minima, a more positive slope implying a larger strain energy. For bulk material, the lowest energy lines above the fcc minimum are either close-packed structures misoriented with respect to the cubic box, or are based on the fcc minimum and contain defects such as vacancy-interstitial

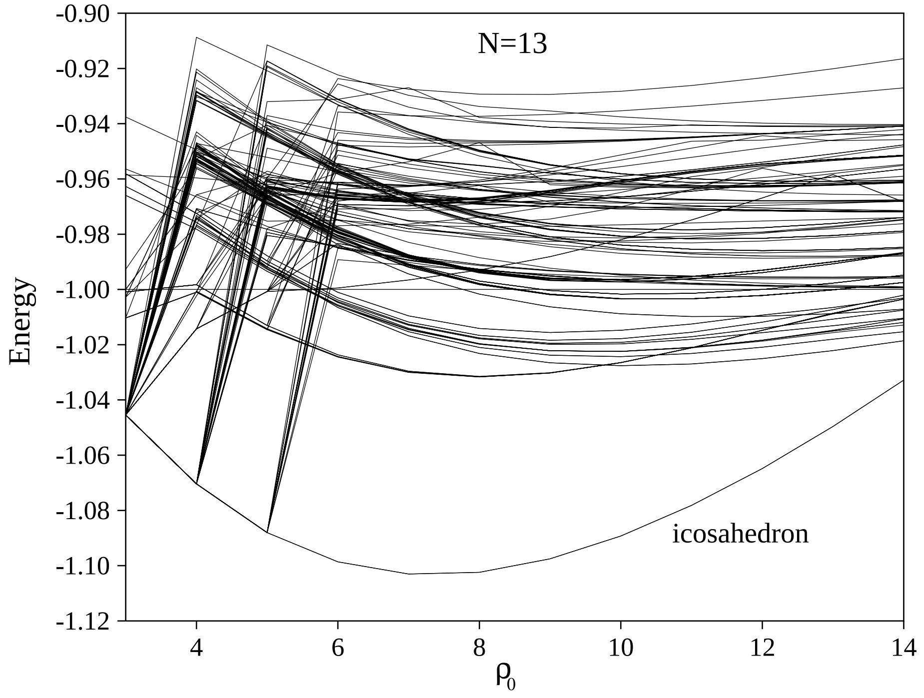

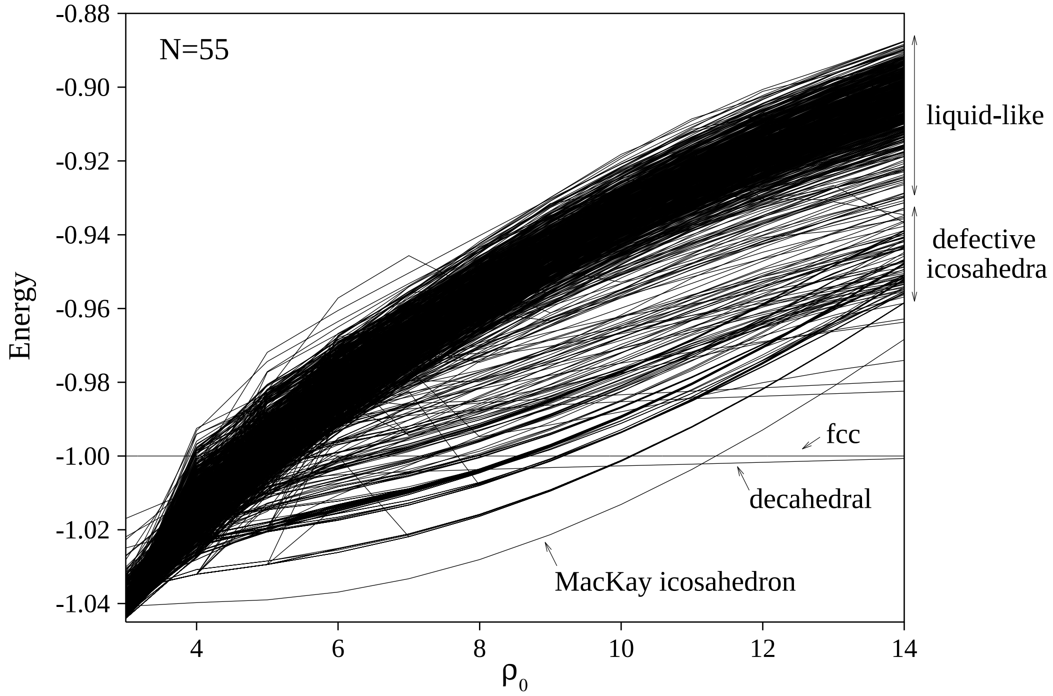

FIGURE 4.4: Correlation diagrams for M_{13}, M_{55}, M_{147} and bulk material. In each case the unit of energy is the binding energy of the lowest energy fcc structure. The samples contain 131, 858, 298 and 117 minima, respectively. Lines due to the decahedral and fcc structures which become the global minimum at large values of ρ_0 for M_{55} and M_{147} and the amorphous structure which is the global minimum of M_{147} at ρ_0=3 have been added.

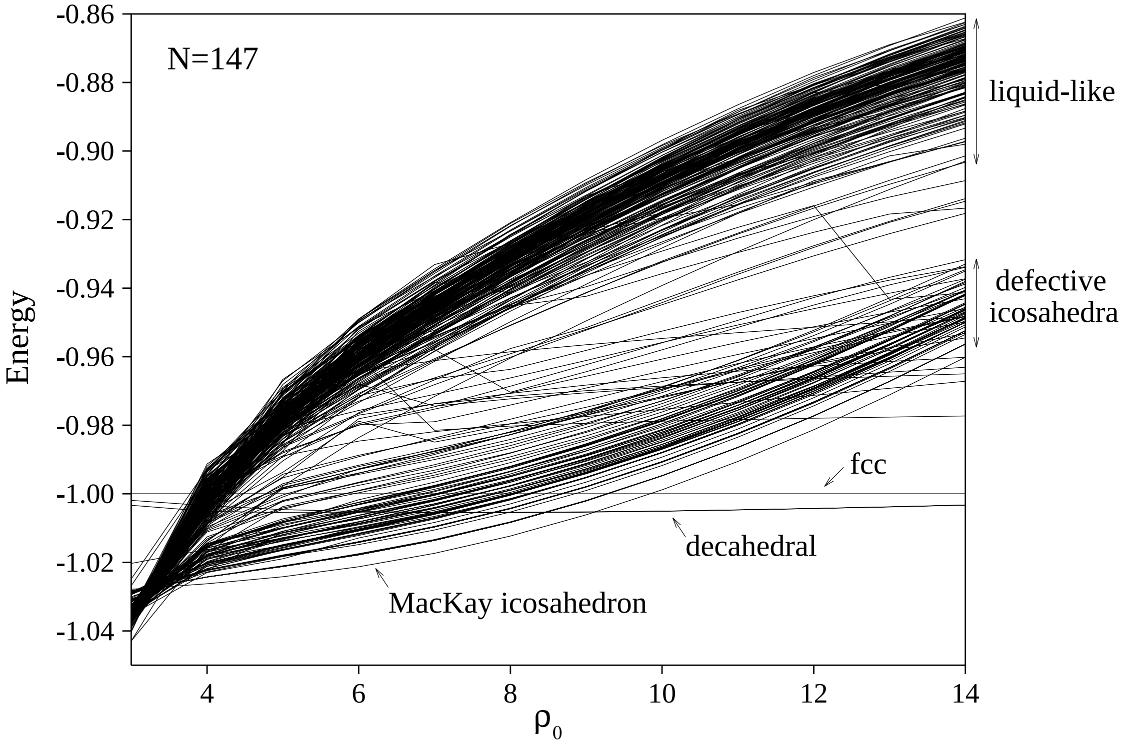

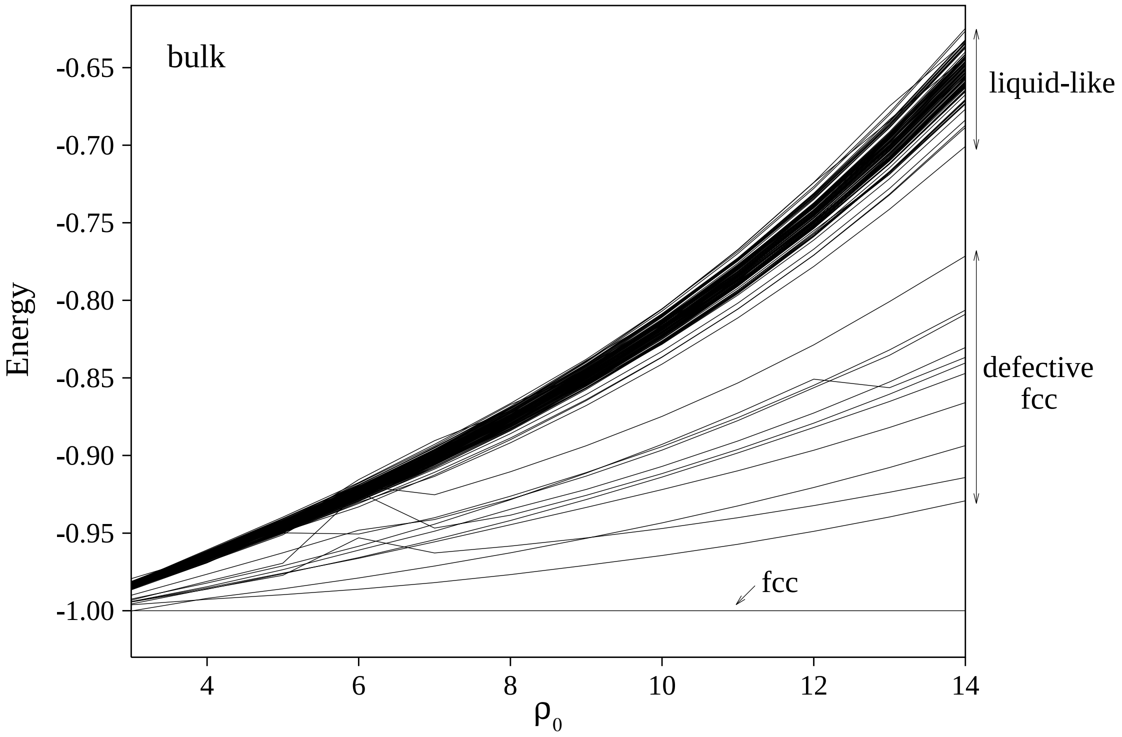

Figure 4.4: continued.

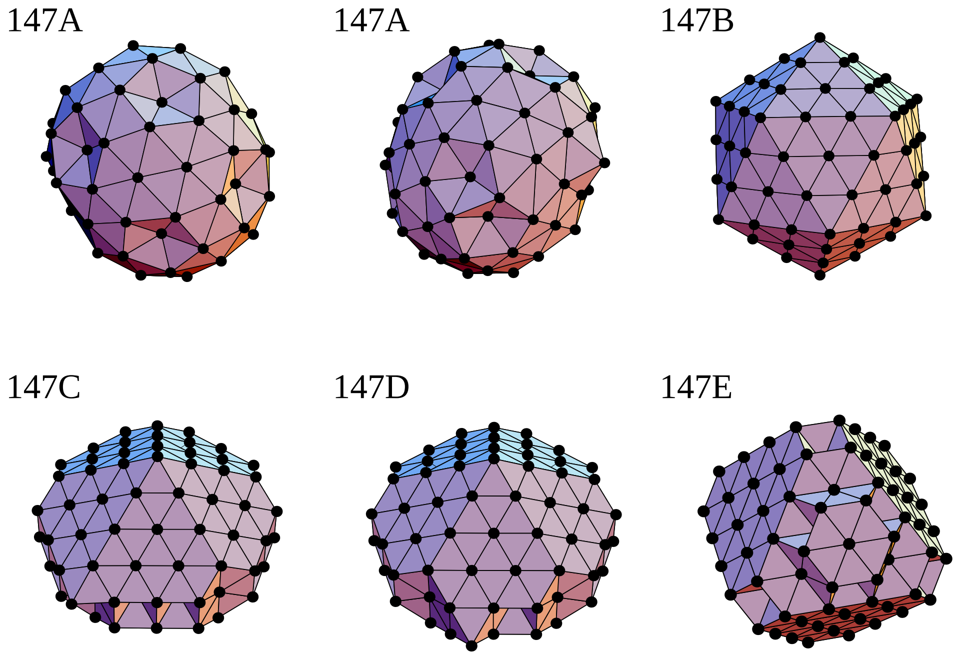

Figure 4.5: Global minima for M_{147}. Each structure is labelled by the symbol given in Table 4.1.

pairs. Both types of structure have a positive slope with respect to the perfect fcc structure, in the first case because the structure has to be sheared in order to fit into the box, and in the latter case because the interstitial defects introduce local strains. Although vacancies could be accommodated without any strain, the constant number and volume constraints used in this study only allow defects to be generated in pairs.

In contrast, the low energy lines in the cluster correlation diagrams run parallel to the line due to the icosahedral global minimum—a sign of their structural similarity. These lines are due to icosahedra with vacancies in the surface layer and adatoms on the surface. These minima give rise to the roughly equally-spaced peaks in the low energy region of the M_{55} and M_{147} probability distributions in Figure 4.3, and correspond to increasing numbers of defects. Rearrangements between these structures occur at energies just below that required for complete melting, leading to enhanced diffusion in the surface layer[110,111].

The thick bands of lines with positive slope in the bulk, M_{55} and M_{147} correlation diagrams along with the corresponding large, high energy peaks in the potential energy distributions (Figure 4.3) are due to minima found by quenching

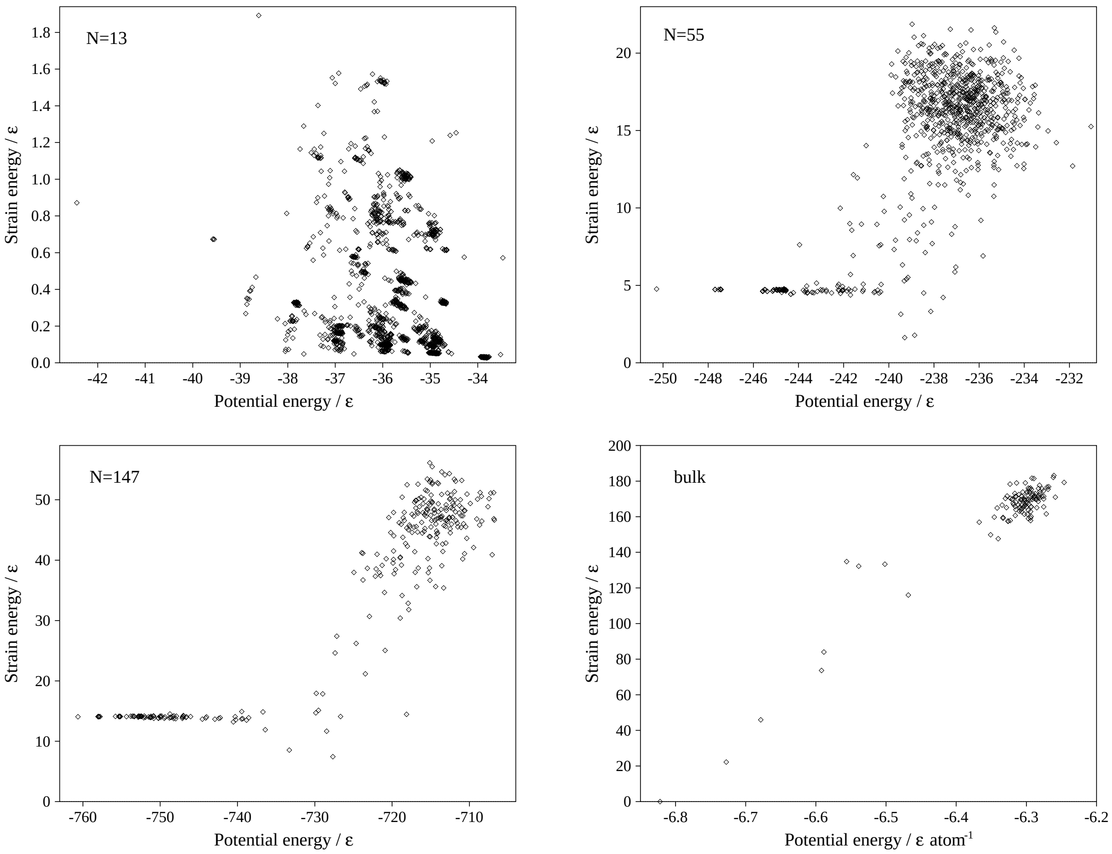

FIGURE 4.6: Plots of the strain energy versus the potential energy for the samples of ρ_0=6 minima for M_{13}, M_{55}, M_{147} and bulk material. The sample of M_{13} minima is larger than that used in Figure 4.4 and contains 1441 minima (Table 2.1).

from the region of phase space corresponding to liquid behaviour. We have sampled only a tiny fraction of all these 'liquid-like' minima; for comparison, the number of minima corresponding to the liquid-like phase space of LJ_{55} has been estimated as 8.3×10^{11} (§3.6). It is because of this large configurational entropy and the greater vibrational entropy that the free energy of the liquid phase usually becomes lower than that of the solid phase as the temperature increases, leading to melting. For the bulk, the energy gap between these 'liquid-like' minima and the fcc minimum clearly increases with ρ_0 (Figure 4.4). Thus, decreasing the range of the potential energetically destabilizes the liquid phase. For the clusters the energy of the 'liquid-like' minima must be compared to the energy of the global minimum. As the decahedral and fcc structures which become global minima at short range were not obtained in the sample of minima at ρ_0=6, the lines due to these structures have been added to the correlation diagrams, although we have not added lines due to the many defective minima based upon them. Hence, a similar result to bulk

TABLE 4.2: Partitioning of the potential energy of the bulk phases into the different contributions of equation 2.1 at different values of ρ_0. The values for the liquid phase are averages over all the 'liquid-like' minima. All energies are given in reduced units per atom. The nearest-neighbour criterion, $x_0 = 0.243$, corresponds to the minimum between the first and second peaks of the radial distribution function.

phase	ρ_0	E	n_{nn}	E_{strain}	E_{nnn}
solid	6	-6.822	6.000	0.000	-0.822
	10	-6.050	6.000	0.034	-0.097
	14	-5.958	6.000	0.042	-0.016
liquid	6	-6.292	6.103	0.657	-0.846
	10	-4.935	5.931	1.134	-0.138
	14	-3.859	5.925	2.100	-0.034

is seen for M_{55} and M_{147}, i.e. the energy gap between the 'liquid-like' minima and the lowest energy solid structure, be it icosahedral or decahedral, clearly increases as the range decreases (Figure 4.4).

The physical basis for this behaviour is simply the greater strain energy of the 'liquid-like' minima, as shown by their positive slope in the correlation diagrams. Figure 4.6 shows clearly the differentiation between the low potential energy, low strain energy minima and the high potential energy, high strain energy 'liquid-like' minima. This greater strain arises from the inherent disorder of the 'liquid-like' minima; they have a range of nearest-neighbour distances, and consequently the first peak in the radial distribution function is broader than for the solid. The strain energy is the energetic penalty for this disorder and it rises rapidly as the range decreases and the potential wells narrow. This view is confirmed by examining the three contributions to the energy for the two bulk phases at different values of ρ_0 (Table 4.2). The main contribution to the energy gap is found to be the larger strain energy of the liquid minima. This greater strain energy will be related to the liquid structure in more detail in §4.4.

The energetic destabilization of the liquid phase seen for bulk and the two larger clusters gives rise to a term in the free energy difference between the solid and liquid phases which increases rapidly with ρ_0. Since the energetics of the vapour phase can be assumed to be relatively unaffected by the range of the potential, the rise in energy of the 'liquid-like' minima with ρ_0 for bulk and the two larger clusters also causes the energy difference between the liquid and vapour to decrease. Thus, the range-dependence of the energetics should have a large effect on the free energy differences both between the solid and liquid phases and between the liquid and vapour phases, in both cases destabilizing the liquid phase. It is significantly harder to determine the range-dependence of the entropic contribution to the free energy in our approach. However, the entropy of the vapour phase should be relatively unaffected by ρ_0 and the entropy of both the solid and the liquid phases decreases as ρ_0 increases due to the narrowing of the potential wells and the attendant loss of accessible configuration space. We have shown that the range-dependence of the energetics is sufficient to account for the known range-dependence of the phase diagram and in particular the decrease of the critical temperature as the potential becomes more short-ranged. Thus, at least part of the destabilization of the liquid phase that has been noted in experiments and simulations of colloids and C_{60} can be traced to the PES in this way.

The situation for M_{13} is rather different because of its small size—this cluster is nearer to the atomic limit. The introduction of defects in the icosahedron involves an increase in the energy of the cluster which is a significant fraction of the total potential energy. The heat capacity peak found for LJ_{13} (it should exhibit very similar behaviour to an M_{13} cluster with $\rho_0 = 6$) is associated with isomerization between the icosahedron and the defective structures based upon it[128], rather than between two phase-like forms that are structurally dissimilar. The nature of the 'melting' transition is therefore significantly different from the larger clusters and from bulk. As the removal of an atom from the vertex of the icosahedron allows relaxation of some of the strain, the gap between the icosahedron and the defective states decreases as the range of the potential decreases.

There is another interesting effect evident in the correlation diagrams of M_{55} and M_{147}: as ρ_0 decreases the gap between the 'liquid-like' band of minima and the Mackay icosahedron decreases until for a sufficiently long-ranged potential the 'liquid-like' band becomes lower in energy than the icosahedron. At $\rho_0 = 3$ for both M_{55} and M_{147}, the lowest energy clusters (55A and 147A) have an amorphous structure typical of the liquid-like state, which as we saw in §2.3.4 can be analysed in terms of disclination lines.

4.4 Liquid Structure

In this section we relate our results to current models of the structure of liquids and glasses and perform further structural analysis on our samples of minima. Our investigations of clusters are particularly helpful in this task since models of liquid structure often make use of results from cluster studies[188–190]. It was Frank who first suggested that the large supercooling of atomic liquids might be due to a local icosahedral ordering in the liquid phase. He justified this suggestion by pointing out that for a 13-atom Lennard-Jones cluster the icosahedron was significantly lower in energy than the fcc cuboctahedron. It has since been demonstrated that the structure of atomic liquids and glasses has significant polytetrahedral character[191], first through the success of the dense random packing of hard spheres[192,193] as a model for metallic glasses[194] and later by computer simulations[195]. In this polytetrahedral model liquid structure is considered to be a tessellation of all space by tetrahedra with atoms at the vertices of the tetrahedra. The 13-atom icosahedral cluster is an example of a finite polytetrahedral structure as it is composed of twenty face-sharing tetrahedra. Local icosahedral arrangements are therefore possible, although not necessary, in bulk polytetrahedral packings.

One reason suggested for the polytetrahedral character of liquids is the fact that the regular tetrahedron represents the densest possible local packing of spheres. However, the regular tetrahedron cannot be used to pack all space. This is illustrated in Figure 2.3; if five regular tetrahedra are packed around a common edge, there remains a small gap of 7.36°, and if twenty regular tetrahedra are packed around a common vertex the gaps amount to a solid angle of 1.54 steradians, which is equivalent to 2.79 additional regular tetrahedra. This incompatibility of the preferred short-range order with a global packing is termed ‘frustration’. As a consequence of this frustration, close packing, which consists of a mixture of regular tetrahedra and octahedra, rather than a polytetrahedral packing, is the densest packing of all space. Furthermore, a polytetrahedral packing of space must involve tetrahedra that are distorted from regularity, leading to local strains and a range of nearest-neighbour distances. Polytetrahedral structure therefore underlies the larger strain energies in the liquid phase and the dependence of liquid stability on the range of the potential.

The radial distribution functions shown in Figure 4.7 provide evidence for the polytetrahedral character of the liquid minima through the absence of a peak at $r = \sqrt{2}$, which is the signature of the octahedra that occur in closed-packed

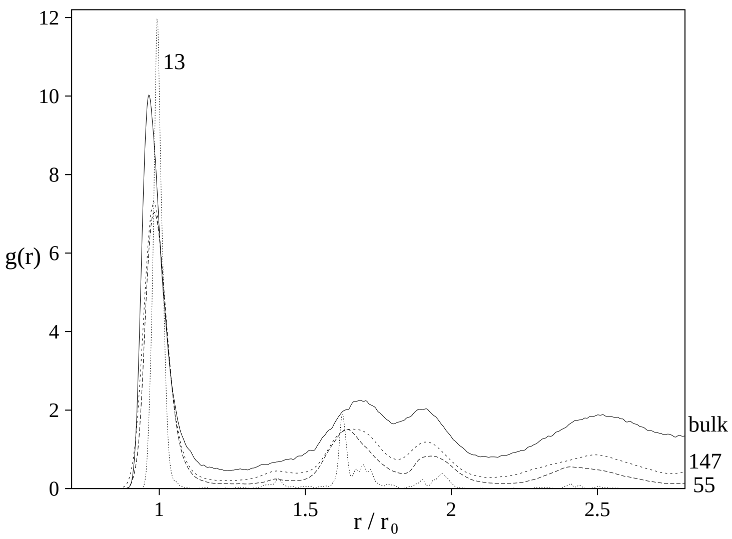

Figure 4.7: Average radial distribution functions, $g(r)$, for the four sets of 'liquid-like' minima at $\rho_0 = 6$. The distribution function has not been normalized with respect to the density since the volume of a cluster is not well-defined.

structures, and the split second peak. The split second peak of the structure factor, which is a common feature of supercooled liquids and glasses, has also been shown to be a consequence of polytetrahedral order[196].

We have also performed a common-neighbour analysis[149,195,197] for our samples of minima. This analysis assigns four indices $ijkl$ to each pair of atoms which have common neighbours, and provides a description of the local environment of the pair. Firstly, those pairs of atoms which are separated by less than a physically reasonable cutoff distance are designated nearest neighbours. We have simply set the cutoff equal to the minimum between the first and second peaks in the liquid radial distribution function. For those pairs of atoms which are nearest neighbours i is assigned the value 1. For those pairs of atoms which are not nearest neighbours but which have common neighbours i is assigned the value 2. The index j specifies the number of neighbours common to both atoms. The index k specifies the number of nearest-neighbour bonds between the common neighbours. The index l specifies the longest continuous chain formed by the k bonds between common neighbours.

This analysis allows differentiation between different types of local order. In particular, 1421, 1422 and 2444 (an octahedron) pairs are associated with close packing; 1555 (a pentagonal bipyramid), and 2333 (a trigonal bipyramid) pairs are associated with polytetrahedral packing. Scatter plots of some of these indices

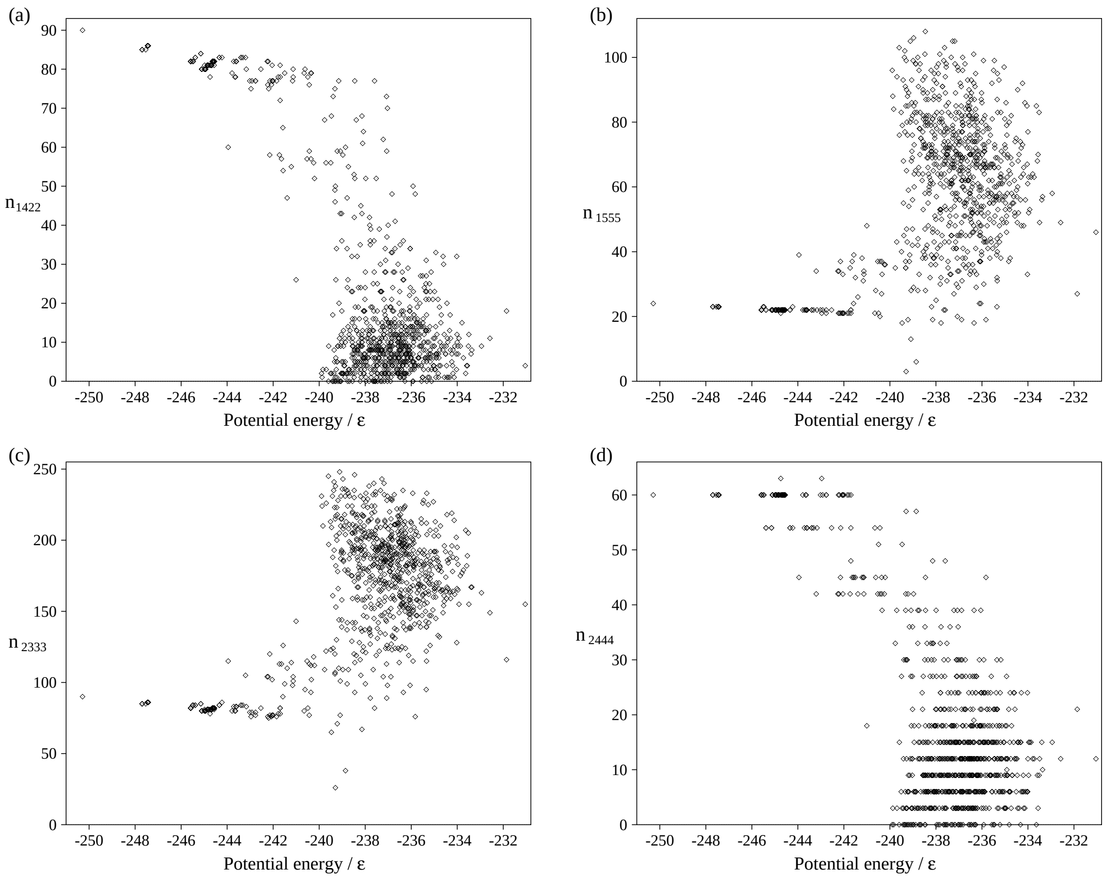

FIGURE 4.8: Scatter plots of the number of (a) 1422, (b) 1555, (c) 2333 and (d) 2444 pairs defined by the common neighbour analysis for the 858 M_{55} $\rho_0 = 6$ minima.

for the M_{55} minima are shown in Figure 4.8. The plots clearly show that the higher energy 'liquid-like' minima have a larger proportion of polytetrahedral pairs and fewer close-packed environments. Furthermore, a common neighbour analysis allows the properties associated with certain local environments to be found. In Figure 4.9, we decompose the second peak of the radial distribution function for M_{55} according to the types of common neighbour pairs. The first subpeak is clearly due to trigonal bipyramids (2333 pairs) and the 2nd subpeak to linear configurations (2100 pairs). The split second peak is therefore an indicator of polytetrahedral order. The effect of 2111 pairs (a pair of atoms at the apices of a rhombus) is smaller than in the case of bulk hard sphere systems[197].

The constraints that lead to the frustration inherent in polytetrahedral packings of 3-dimensional Euclidean space can be altered by introducing curvature into the space. In fact, in a space of appropriate positive curvature a perfect tetrahedral packing can be achieved in which there is no frustration and each atom

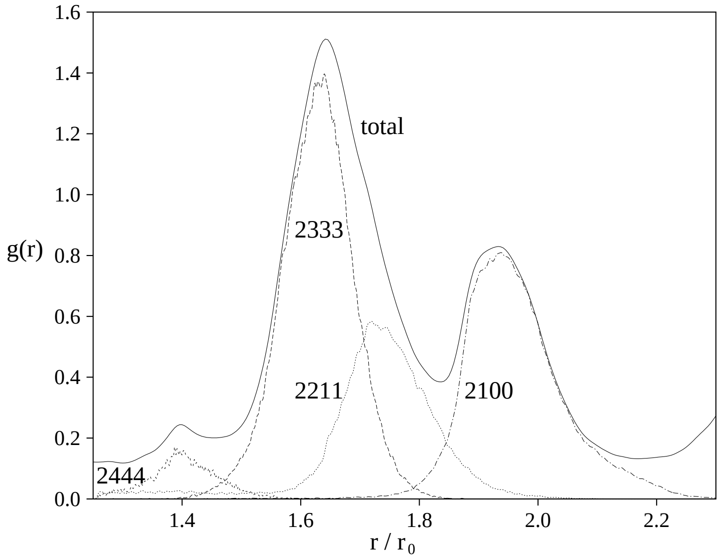

FIGURE 4.9: Decomposition of the second peak of the radial distribution function of M_{55} $\rho_0 = 6$ 'liquid-like' minima by common neighbour analysis. The solid line is the total radial distribution function and the dashed lines are the components due to four types of common neighbour pairs as labelled.

is icosahedrally coordinated. The resulting structure is that of polytope $\{3,3,5\}$ which consists of a regular arrangement of 120 atoms on the 3-dimensional hypersurface of a 4-dimensional hypersphere[198,199]. The effects of this lack of frustration have been well illustrated in work by Straley[200,201] who compared the melting and crystallization of an fcc crystal in flat space, with that of polytope $\{3,3,5\}$. In particular, the kinetics of crystallization from a liquid are much easier on the 4D hypersphere. In line with Frank's original suggestion concerning the supercooling of metallic liquids, this result has been interpreted as showing that the solid and liquid on the 4D hypersphere have the same kind of order, i.e. both are polytetrahedral. Therefore, it provides further evidence for the polytetrahedral nature of the liquid phase.

Nelson has shown that in the transformation of regular polytetrahedral packings from curved to Euclidean space disclination lines must be introduced[198,199]. If these disclination lines are arrayed periodically one obtains crystalline structures called Frank-Kasper phases[202,203]. If the disclination lines have a disordered arrangement it has been suggested that one obtains structures typical of liquids and glasses. The disclination networks for three types of Frank-Kasper phase, termed the A15, C15 and T phases[204], are illustrated in Figure 4.10; the disclinations of the T phase form an interconnected network of dodecahedra. The Frank-Kasper phases

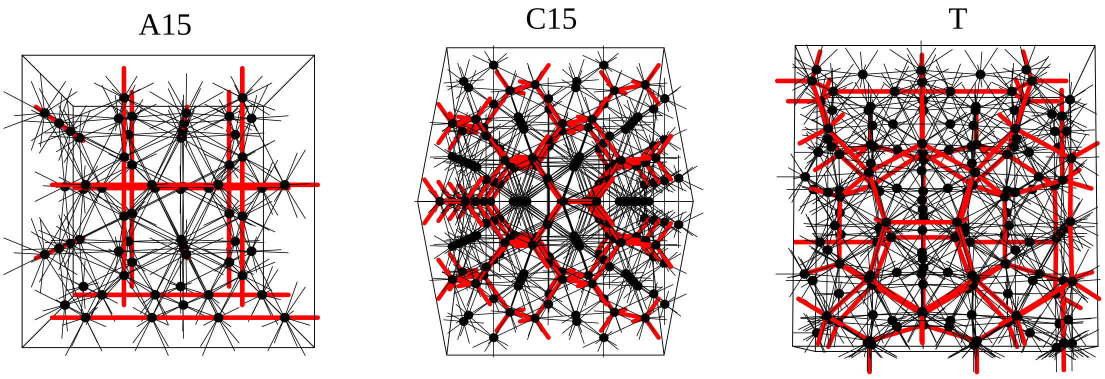

FIGURE 4.10: Some examples of the ordered arrays of disclination lines that occur in Frank-Kasper phases: A15, e.g. β-W, C15, e.g. $MgCu_2$, and T, e.g. $Mg_{32}(Zn,Al)_{49}$. The $-72°$ disclination lines are indicated by thick red lines. Disclination-free nearest-neighbour bonds are indicated by thin black lines.

are sometimes referred to as tetrahedrally close-packed because of their polytetrahedral nature and are closely related to many icosahedral quasicrystals[205]. The known examples are generally alloys where some of the frustration is relieved by the different atomic sizes. It has been suggested that a mixture of different-sized fullerenes might be able to form a Frank-Kasper phase and even quasicrystals[206]. However, this seems unlikely given the short-ranged character of fullerene potentials (§2.2.1)—the structures must still be able to accommodate some strain. Interestingly, the dual of the A15 Frank-Kasper phase (Figure 4.10) has recently been found to divide space into equal cells of minimum surface area[207], overturning Kelvin's proposed optimal structure[208] which stood for over a century.

On the unfrustrated 4D hypersphere there must be an equal number of positive and negative disclinations. However, as a consequence of the residual gap that occurs when five regular tetrahedra share a common edge in Euclidean space (Figure 2.3a), there must be an excess of negative disclinations[198,199]. For example, the Frank-Kasper phases involve only negative disclinations (Figure 4.10). If an atom is 12-coordinate by the Voronoi procedure, it can be free of disclinations. However, atoms that have a different coordination number must have disclinations passing through them. Using Euler's rule and the fact that the coordination polyhedra are deltahedral, one can deduce the coordination polyhedra which involve the minimum number of disclinations. These polyhedra are termed the Kasper polyhedra, and are illustrated in Figure 4.11. (They are denoted by ZN, where N is the coordination number.) For example, apart from icosahedra the A15 Frank-Kasper phase (Figure 4.10) involves only Z14 Kasper polyhedra, and the C15 structure

(Figure 4.10) involves only Z16 Kasper polyhedra.

We can also understand the range-dependence of the energy of the 'liquid-like' minima by considering the energetics of disclination lines. The strains associated with the disclination lines are most easily accommodated in systems bound by long-ranged forces. In fact the clusters which correspond to the Kasper polyhedra Z10, Z13, Z14 and Z15 are the global minima for the Morse potential at $\rho_0 = 3$, and those that correspond to Z11 and Z16 are the second lowest energy stationary points of their size (§2.3.4). As the range of the potential decreases the energetic penalty for the local strains associated with the lines increases, causing destabilization of the liquid phase.

In Nelson's original paper outlining his disordered disclination model for liquid structure, he gives a schematic diagram of such an arrangement[198,199]. The sketch involves only Kasper polyhedra; long disclination lines, mediated by the Z10 and Z14 Kasper polyhedra, thread through the icosahedrally coordinated medium, and the other Kasper polyhedra act as nodes for the disclinations. Surprisingly, no-one, as far as we are aware, has attempted to verify this model by visualization of the disclination network. However, results from the statistical analysis of Voronoi polyhedra indicate that the density of disclinations is higher than this picture would suggest; for example, in Finney's analysis of dense random packings of hard spheres only 40% of the faces of the Voronoi polyhedra are pentagonal, thus indicating that for this system about 60% of bonds involve disclinations including a significant number of 144°-type[209]. In part of Figure 4.12 we show the disclination network for a typical bulk liquid minimum; the disclination density is so high that the result is an unintelligible mass of lines. Typically, for the minima we analysed, only about 10% of the atoms have an icosahedral or Kasper polyhedral coordination shell, in contrast to Nelson's original picture. However, the disclination density is likely to be lower for simple binary liquids where the size of the atoms are chosen to reduce the frustration. It is for such a system that the most striking examples of local icosahedral order have been obtained[195].

As we saw in Chapter 2, the lowest energy structures of clusters at low ρ_0 are polytetrahedral. Furthermore, Figure 4.4 shows that for M_{55} and M_{147} these structures correlate with low energy liquid-like minima. Therefore, Figures 2.10 and 2.18 allow us to see how polytetrahedral packings and liquid structure evolve with size. At small sizes is it possible to accommodate the strain that is associated with the bridging of the 'gaps' that occur in a disclination-free packing of regular tetrahedra (Figure 2.3). Anti-Mackay growth on the 13-atom icosahedron gives

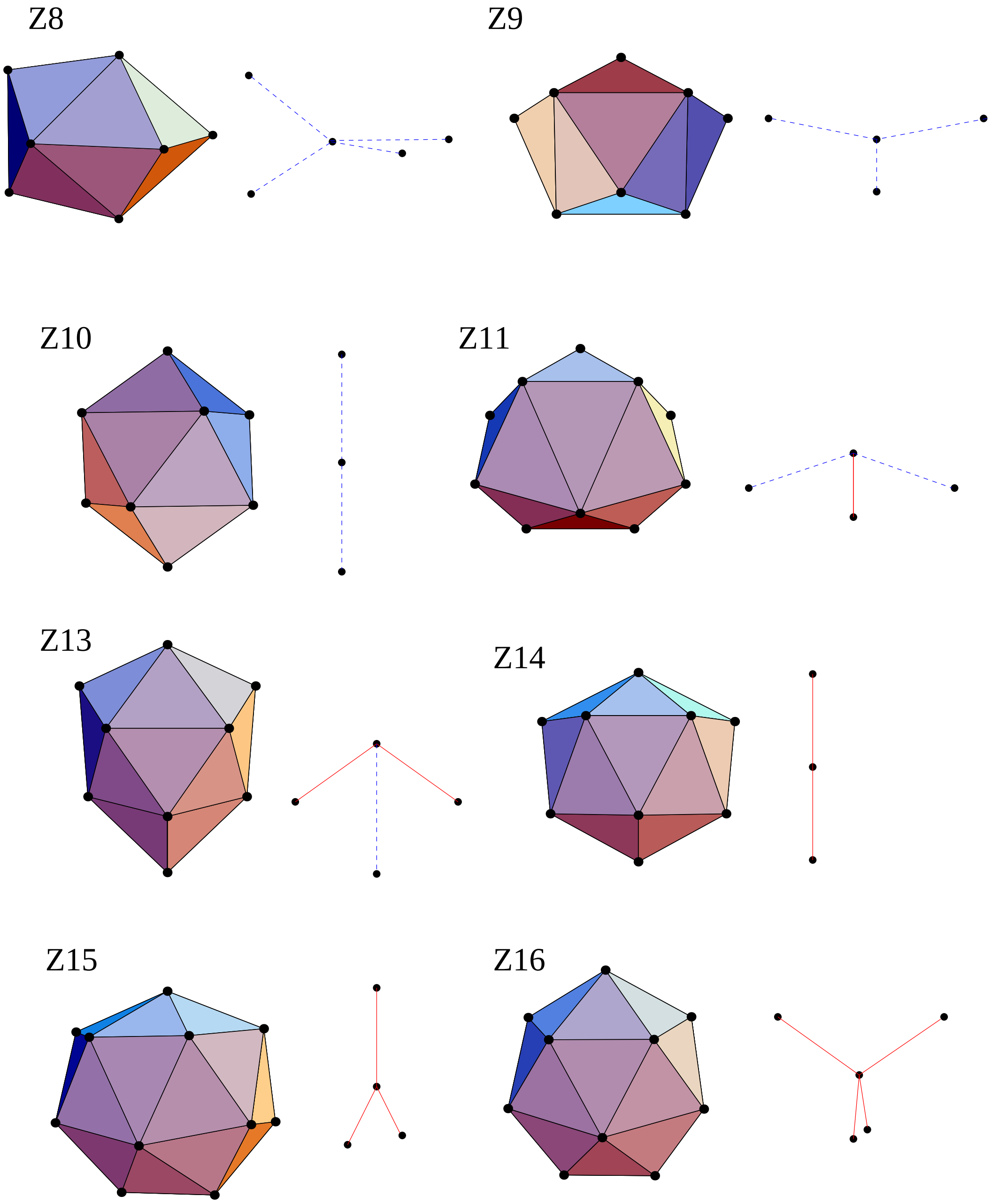

Figure 4.11: Kasper Polyhedra for coordination numbers between 8 and 16 (except for the disclination-free icosahedral coordination shell). Both the coordination polyhedra and the associated disclination lines are shown. Negative disclinations are represented by red lines and positive disclinations by dashed blue lines

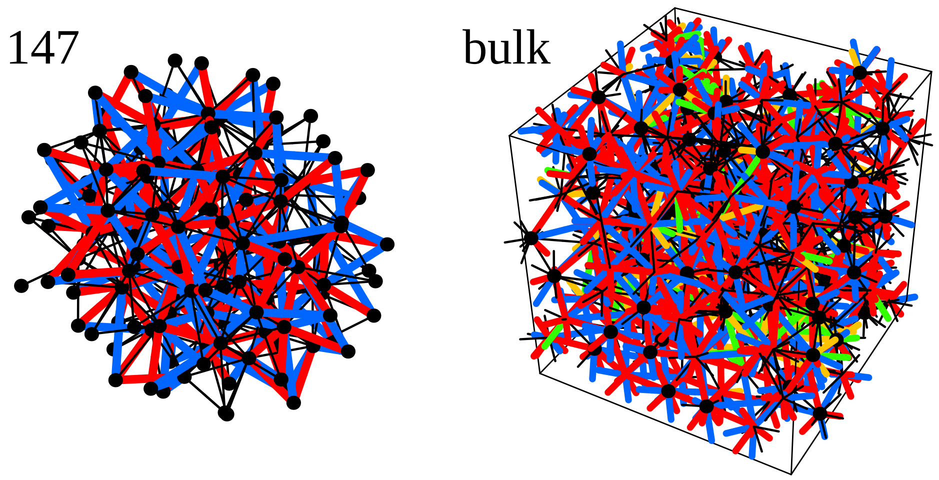

Figure 4.12: Disclination networks for the ρ_0=3 M_{147} global minimum and a bulk Morse liquid minimum. Thin black lines represent nearest-neighbour bonds which are disclination-free, red lines represent $-72°$ disclinations, blue lines $+72°$ disclinations, green lines $-144°$ disclinations, and yellow lines $+144°$ disclinations.

disclination-free polytetrahedral structures up to 45. Above this size disclinations have to be introduced. Whilst the disclination density is still small, ordered arrangements of the disclinations, which are fragments of Frank-Kasper phases, can form at some sizes (N=51–53, 56, 57, 59–61, 70, and 74). However, as the size increases the structures become progressively more disordered. By the time M_{147} is reached the cluster is a mass of interconnected disclinations (Figure 4.12); only 53% of the interior bonds of 147A are disclination-free.

Why should liquids have a polytetrahedral structure though? Why is liquid structure not more like a highly defective version of the solid? Stillinger and Weber have used a model partition function to show that if defects of a body-centred-cubic lattice interact, then a first-order melting transition can occur which is associated with the condensation of a 'gas' of defects[210]. One of the common reasons suggested for the polytetrahedral character of liquids is the energetic favourability of local icosahedral order. This argument dates back to Frank and his comparison of icosahedral and cuboctahedral 13-atom clusters that we mentioned above. However, this argument contains a fallacy. The reason for the lower energy of the icosahedron is primarily a surface effect; each surface atom is six-coordinate for the icosahedron and five-coordinate for the cuboctahedron. The actual energy of the interior atom will be slightly higher for the icosahedron, because the radial nearest-neighbour distance is slightly compressed with respect to the ideal. Furthermore, as has been pointed out by Clarke and Jonsson[197], an energetic argument cannot account for the fact that dense random packings of hard spheres (where all configurations have the same energy) show significant polytetrahedral order. Another observation is the fact that the tetrahedron has the greatest local density. However, if one considers the density of an icosahedron, the distortion required to bridge the gaps of Figure 2.3b leads to a decrease in density to such an extent that a cuboctahedron is denser[211].

What then is the reason for the polytetrahedral structure of liquids? To answer this question one needs to realize that polytetrahedral packings should be compared not to the close-packed solid, but to other states that could possibly mediate a melting transition. The number of ways of arranging disclination lines in a polytetrahedral packing or of introducing disclination lines into polytope $\{3,3,5\}$ to bring the curvature nearer to that of flat space is huge[212]. Consequently, there is a large configurational entropy associated with the set of all polytetrahedral states. Yet they are also fairly dense, and depending on the range of the potential, can be fairly low in energy. It is the combination of these three factors (or the first two in the case of hard spheres) which underlies the favourability of polytetrahedral order.

One of the fundamental questions of cluster science is when and how bulk-like character develops. The answer of course depends on the property considered. For instance, the structure of solid-like clusters only becomes bulk-like at large sizes for many systems, especially for those clusters with a long-ranged potential[213]—sodium clusters are icosahedral up to at least 20 000 atoms[53] even though the bulk structure is body-centred cubic. In contrast, our results show that bulk-like liquid structure can develop at rather small cluster sizes. This is suggested by the similar energetic destabilization of the bulk, M_{55} and M_{147} 'liquid-like' minima and by the clear similarity of their radial distribution functions (Figure 4.7). The only significant difference is the uniformly smaller value of the cluster radial distribution function, and this is simply due to the finite size. The peaks in the M_{13} radial distribution function are at a similar position to the larger clusters but are much sharper because at this size the effects of frustration are small. The similarity of bulk and cluster radial distribution functions can easily be understood within the polytetrahedral model of liquid structure. Given the favourability of polytetrahedral structure for small clusters and the rapid increase in disclination density with size, it is not surprising that bulk-like liquid character is seen at small sizes.

As the size of the Mackay icosahedron increases, the polytetrahedral character decreases and the close-packed character increases. This can explain some of the differences in the correlation diagrams of the two larger clusters (Figure 4.4). For the 55-atom cluster the distinction between the top of the band of defective icosahedral structures and the band of 'liquid-like' minima is unclear because of the greater structural similarity of the solid and the liquid at this small size. The energetic separation of these two bands of minima becomes larger as the number of atoms increases, giving the correlation diagram of M_{147} the two-state character expected for a system that undergoes a first-order phase transition.

Another related effect is the energetic differentiation between the minima found by quenching from a glass or supercooled liquid and from the liquid that occurs for M_{147}. Structure 147A (Figures 4.5 and 4.12), the global minimum at $\rho_0 = 3$, was found from the collapse of one of the 'liquid-like' minima of our sample. It can be seen in Figure 4.4 that at $\rho_0 = 3$ there is an energy gap between this and the next lowest energy minimum that we found. This is not because there are no minima in between. In fact, we found that this gap was an artifact of our sample; 147A is actually at the bottom of a band of minima which is almost continuous in energy. The clue to the nature of structure 147A came when it was reoptimized for ascending values of ρ_0; the resulting line runs parallel to but below the main 'liquid-like' band, indicating that it is of essentially similar structure to the 'liquid-like' minima. This suggested that 147A was one of a set of minima that for a medium-ranged potential comes from a glassy region of phase space; these states are essentially just the low energy continuation of the 'liquid-like' band of minima but are never observed at equilibrium because of their smaller entropy. This hypothesis was confirmed by quenching from a supercooled M_{147} liquid at $\rho_0 = 6$. The resulting minima were lower in energy than the 'liquid-like' band, but as for 147A ran parallel to the 'liquid-like' band in the correlation diagram.

4.5 The 55-atom Morse Cluster

In this section we shall illustrate the effects of the range of the potential on cluster thermodynamics in more detail, by presenting results of simulations of M_{55} at different values of the range parameter, ρ_0. As in §3.3 we use STA temperature distributions (e.g. Figure 4.13) to decompose the caloric curve into contributions from different states. The caloric curves for M_{55} at five different values of ρ_0 are

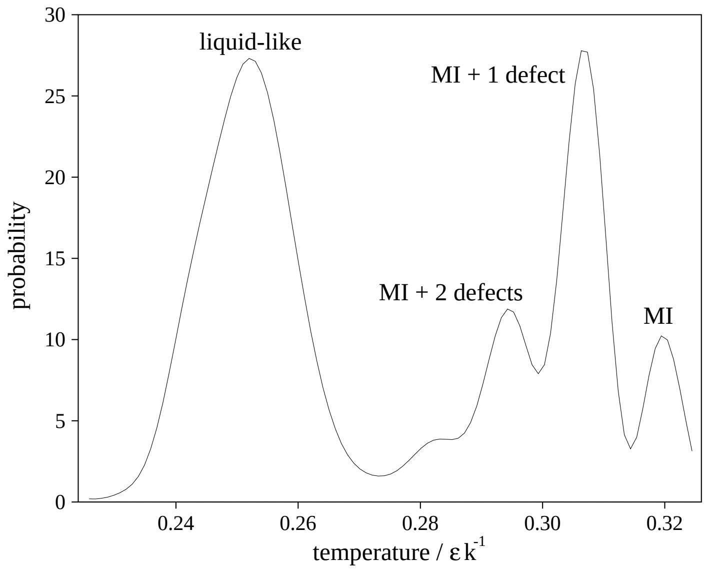

Figure 4.13: An example of a multimodal short time-averaged temperature distribution. It is from an MD run for M_{55} at $\rho_0 = 6$ at an energy of $-3.483\,\epsilon\,\mathrm{atom}^{-1}$. Each temperature peak is labelled with the structure associated with it. MI stands for Mackay icosahedron. The averaging period is 3000 time steps.

shown in Figure 4.14. At ρ_0=6, the melting behaviour is very similar to that seen for LJ_{55} in §3.3. The caloric curve has a Van der Waals loop, and surface defects of the Mackay icosahedron can be generated at energies just below that required for complete melting. In comparison, the ρ_0=9 caloric curve shows a higher melting temperature, a deeper S-bend and a greater role for the defective states. This is a direct result of the increasing energy gap between the Mackay icosahedron and the 'liquid-like' band of minima noted in §4.3. At ρ_0=4, the melting temperature is lower than for ρ_0=6, the latent heat is smaller and defective Mackay icosahedra are not seen. Again this can be related to the correlation diagram Figure 4.4 and is simply a result of the decrease in the energy gap between the Mackay icosahedron and the 'liquid-like' band of minima as ρ_0 is decreased.

The behaviour at ρ_0=3 and 13 is significantly different; in particular the melting transitions are closer to a continuous transition than a two-state transition, i.e. between a liquid and a solid. At $\rho_0 = 3$, the lowest energy minimum that we have found is 55A. This minimum lies at the bottom of the band of 'liquid-like' minima, which is approximately continuous in energy. At low temperatures transitions from 55A to higher energy minima begin to occur, because of the small differences in energy. This leads to the fluxional liquid-like behaviour which is exhibited in the rise in Lindemann's δ (Figure 4.14a). Melting occurs at low temperatures without

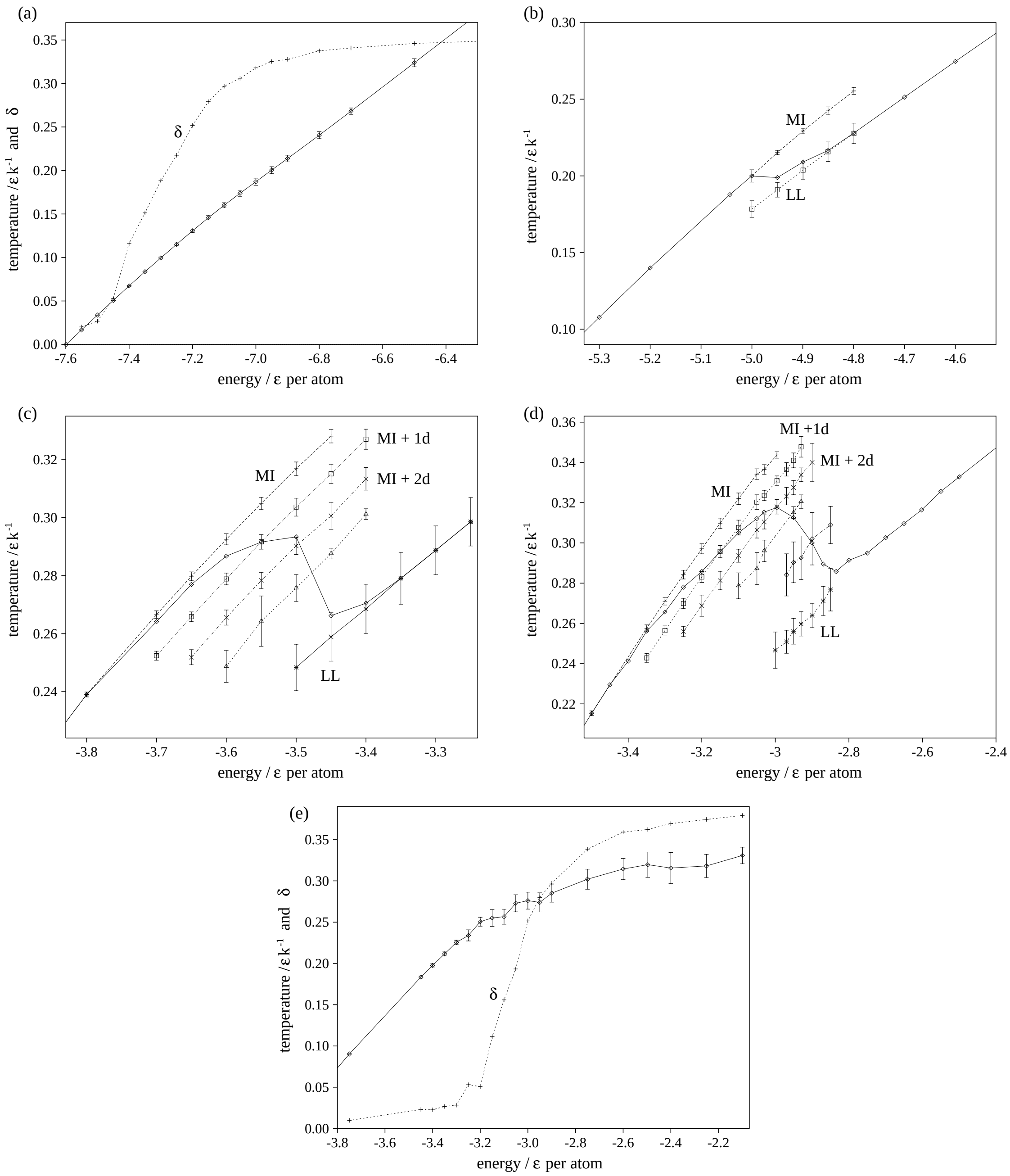

FIGURE 4.14: Caloric curves for M_{55} for ρ_0 = (a) 3, (b) 4, (c) 6, (d) 9 and (e) 13. For ρ_0=3 and 13 Lindemann's δ has also been plotted, so that the melting region can be identified. For ρ_0=4, 6 and 9 the solid line without error bars is the overall caloric curve, and the dashed lines with error bars are the average values of the temperature for the peaks in the STA temperature distribution. The latter lines are labelled with the structures associated with them. MI stands for Mackay icosahedron, + nd for a structure with n defects, and LL for liquid-like.

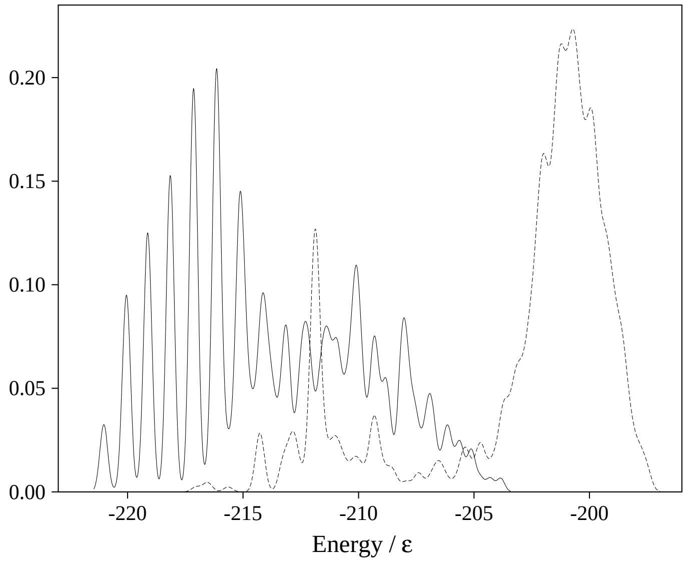

FIGURE 4.15: Probability distributions of the potential energy for samples of minima for M_{55} at ρ_0=13. The solid line is for a sample of 357 minima obtained by quenching from simulations performed for ρ_0 =13 at energies below $-2.7\epsilon\,\text{atom}^{-1}$. The dashed line is for the ρ_0 =6 sample of minima after reoptimization at ρ_0 =13.

producing any noticeable feature in the caloric curve—the latent heat is essentially zero.

For ρ_0=13, on the other hand, the global minimum is the decahedral structure 55C. The difference in energy between this structure and the 'liquid-like' band of minima is now so large that a transition to the latter is only observed at the highest energies ($E \geq -2.4\epsilon\,\text{atom}^{-1}$) probed by our simulation. This transition occurs after δ has risen to a value which indicates that the cluster has already melted, and does not lead to a noticeable feature in the caloric curve. Instead, as energy is added to 55C, the cluster progresses up a ladder of increasingly defective structures (Figure 4.15—the minima bunch into bands that have the same number of nearest neighbours). This climbing up the PES leads to the decreased slope of the caloric curve at higher energies. The melting transition is quasicontinuous and mediated by defect motion. Defective states of 55C are observed at a lower temperature than the defective states of the Mackay icosahedron in the simulations at ρ_0=6 and 9 simply because the energy gap between the icosahedron and its defective states is larger; the first defective state of the icosahedron has three fewer nearest-neighbour contacts whereas the first defective state of 55C has one less contact[71].

The dependence of the thermodynamic behaviour of M_{55} on its energetic distribution of minima agrees very well with that predicted in a seminal paper by Bixon and Jortner[152], which elucidated this relationship for model PES's. In particular, these authors predicted that significant features in the caloric curve, such as an S-bend, would only be seen when there is a large energy gap between the solid and liquid states (e.g. ρ_0=4, 6 and 9), and not when the energetic distribution of minima is quasi-continuous (e.g. ρ_0=3 and 13).

4.6 Electronic vs Geometric Magic Numbers

Magic numbers based on electronic shells were first observed in mass spectra of alkali metal clusters[214]. These features are now well understood in the framework of the self-consistent spherical jellium model, in which the nearly-free valence electrons are assumed to move in a homogeneous spherical ionic background. Further refinements, such as allowing the cluster to deform into an ellipsoidal shape for incomplete electronic shells, improve the agreement with experiment[94].

In experiments on large sodium clusters by Martin *et al.* electronic shell structure was found to persist up to about 1000 atoms and above this size geometric magic numbers were observed[53]. These magic numbers are associated with the completion of shells of the Mackay icosahedron. Further temperature-dependent experiments have shown that for $N > 1000$ the geometric magic numbers disappear as the temperature is increased[215]. This has been attributed to the loss of icosahedral structure on melting (or surface melting) of the cluster and so has been used to examine the size dependence of the melting temperature. At sufficiently high temperatures, electronic magic numbers have been observed up to at least 3000 sodium atoms[216]. Similarly, experiments on large aluminium clusters have shown that as the temperature is increased the observed magic numbers change from geometric (due to octahedra[217]) to electronic[218].

The natural interpretation of these experiments is that geometric magic numbers are associated with solid-like clusters that are based on a regular packing and that electronic magic numbers are associated with liquid-like clusters. However, before this conclusion can be confirmed, another question must be addressed: could a regularly-packed structure also have the observed electronic shell structure? This has been examined in calculations by Mansikka-aho *et al.* which have shown that the electronic shell structure differs from that observed experimentally for all the common cluster shapes except the icosahedron[219,220]. The icosahedron is sufficiently spherical that the electronic shell structure is similar to the experimental up to 1000 atoms. However, Pavloff and Creagh[221] have shown that the electronic supershell structure observed for sodium clusters[216] cannot be explained if the clusters have icosahedral structure, thus confirming that the sodium clusters which exhibit electronic magic numbers are liquid-like.

Our results allow us to explain the transition. For small Morse clusters with a long-ranged potential the lowest energy minimum has an amorphous structure typical of the liquid-like state. At these sizes, the cluster has a very low melting point, as shown in §4.5, because the lowest energy minimum lies at the bottom of a band of minima which are almost continuous in energy. Hence, the cluster can adopt structures that give the most favourable electronic energy without incurring excessive strain energy and the cluster would be expected to exhibit electronic magic numbers at all temperatures. The effect of size on the correlation diagram is to displace the 'liquid-like' band of minima upwards with respect to the line of the Mackay icosahedron until in the bulk limit regular structures are the lowest in energy for all ρ_0. Increasing the size has an effect similar to decreasing the range of the potential—they both destabilize more strained structures. A corollary of this is the well-known increase in cluster melting temperature with size[222] that was first predicted by Pawlow[223]. As a consequence of this effect, for clusters with long-ranged potentials, there must be a critical size at which the Mackay icosahedron becomes lower in energy than the 'liquid-like' minima. Above this size the cluster would be expected to exhibit geometric shell structure at temperatures below the melting point.

One alternative explanation for this transition that has been proposed by Stampfli and Bennemann simply considers the size- and temperature-dependence of the variation in the electronic and geometric effects[224,225]; they show that the latter is likely to dominate at large sizes. However, in their model they do not include the possibility that small clusters may never adopt regular structures.

The jellium-type models can provide a good description of the alkali metals because these elements most closely approximate free electron systems, and understanding the electronic effects becomes more difficult as one goes further from this limit. Our results lead us to expect that for metals with shorter-ranged potentials geometric magic numbers could be seen at much smaller sizes than for sodium. This may provide an explanation for the behaviour of group II metals: barium clusters of less than 50 atoms show magic numbers consistent with an icosahedral growth sequence[99] and magnesium[54] and calcium[55] have magic numbers due to Mackay icosahedra from 147 atoms upwards. However, it is hard to judge the role many-body forces may play in the energetic competition between regular and disordered structures in these systems.

Chapter 5
On Relaxation to the Global Minimum

5.1 Introduction

How difficult is it to go from a random point on a PES to the global minimum? The answer, of course, depends upon the system. Many proteins are able to fold reversibly to the physiologically active native structure from unfolded states. However, a random amino acid sequence is very unlikely to be able to fold to a unique structure. Similarly, in condensed matter physics there are substances for which it is hard to prevent crystallization as the liquid is cooled, and others which instead are likely to form glasses.

The seminal analysis of the global optimization problem in the context of protein folding was made by Levinthal[226]. This author estimated the number of configurations a typical protein could adopt (3^N where N is the number of amino acids) and noted that even if protein configurations could be sampled at a rate of, say, 10^{13} per second, it would take longer than the age of the universe to find the native structure if this sampling was simply random. The result of this simple calculation markedly contradicts the actual properties of proteins, which can generally find the native structure from an unfolded state on time scales of the order of seconds or less. This well-known contradiction has come to be known as Levinthal's paradox. A similar paradox can be formulated for a cluster. For example, the number of geometrically distinct minima on the PES of a 55-atom cluster interacting via the Lennard-Jones potential has been estimated to be of the order of 10^{21}, yet the cluster can rapidly find the Mackay icosahedral global minimum from the liquid-like state[110,111]. The existence of 'magic number' peaks in the mass spectra of rare gas clusters[47,48] indicates that these systems can also locate certain global minima very efficiently.

A more rigorous approach to defining the effort involved in finding the global minimum can be obtained using computational complexity theory[227], which categorizes problems into classes of similar difficulty. The most relevant class is that of NP-hard problems, for which there is no known algorithm that is guaranteed to find the solution within polynomial time, effectively rendering NP-hard problems intractable for large sizes. It has been shown that finding the global minimum of a protein[228,229] or a cluster[93] is NP-hard. Again, there seems to be a paradox between the NP-hardness of protein folding and the actual behaviour of proteins. However, it should be noted that computational complexity theory provides a worst case analysis. First, the proofs apply to general categories of problems and not necessarily to every instance of a problem. Although there may be no efficient method for finding the global minimum of a general heteropolymer, biological proteins may represent a subset whose properties have evolved so that they can fold. Secondly, the criterion for a successful algorithm is very stringent; one must not only find the global minimum, but prove that this it is actually the global minimum. In contrast, proteins do not necessarily have to fold to the global potential energy minimum, but instead must have a high probability of folding to the native structure which probably corresponds to one of the lowest energy minima on the PES. Similarly, the heuristic global optimization methods, such as simulated annealing[107] and genetic algorithms[230,231] are not rigorously guaranteed to find the global minimum. For example, these methods can find the Mackay icosahedron for the 55-atom Lennard-Jones cluster, which is widely accepted to be the global minimum even though this has never been rigorously proved.

Some have tried to resolve Levinthal's paradox by hypothesizing a reduction in the number of states that the protein has to search through. Typically it is argued that the protein first collapses rapidly to a compact conformation and that the subsequent search is through the greatly reduced space of these compact states[232–234]. Although in some cases this might so reduce the number of states that Levinthal's paradox no longer applies, it cannot in general provide a complete answer. For instance, the number of minima corresponding to the liquid-like state of a 55-atom Lennard-Jones cluster is of the order of 10^{12} (§3.6). This is much less than the total number of minima on the PES but the ease with which the global minimum can be found is still incompatible with a random search through this reduced configuration space. In fact, when the cluster has an energy or temperature in the melting region, it can switch back and forth between the Mackay icosahedral global minimum and the liquid-like states on a time scale of the order of nanoseconds (using parameters appropriate for argon)[110,111].

Seeking to resolve Levinthal's paradox by reducing the search space may be unproductive in a more fundamental sense, for it ignores a basic fallacy in Levinthal's paradox: namely the assumption that each point in configuration space is equally likely. Levinthal was effectively assuming that the PES is totally flat. However, the topography of a protein PES is far from flat, involving many 'mountain ranges' and 'valleys', thus making some configurations more likely than others. (In the canonical ensemble the low potential energy configurations have larger Boltzmann weights, and in the microcanonical ensemble they have a larger momentum density of states.) To illustrate this point Zwanzig *et al.* produced a simple model of a protein with an energetic bias towards the native structure which could find the global minimum on physically reasonable time scales[235]. However, this particular model problem belongs[229] to the class of problems P, which are tractable in polynomial time, not to the class NP.

In lattice model studies of proteins, sequences that fold are often compared with those that do not. Some studies have suggested that one of the distinctive characteristics of the folding sequences is a significant energy gap between the global minimum and the next lowest energy structure[233,234,236] and this criterion has been used to design sequences that fold rapidly[237,238]. One particularly comprehensive study of a 27-unit chain led Sali *et al.* to conclude that the necessary and sufficient condition for a folding sequence is that the native state be a pronounced global minimum[233,234]. However, this conclusion has been criticized both because the correlation between the energy gap and folding ability is rather weak and because the criterion concentrates on only a very small part of the PES, whereas folding ability surely depends on the entire energy landscape[239]. Interestingly, Sali *et al.*'s results actually show a stronger correlation between the folding ability and the temperature, T_x, at which the global minimum has an equilibrium probability of 0.8, if only compact states are considered.

There are further problems when trying to apply the energy gap criterion to real proteins, since for a real protein there are many minima on the PES which involve only small perturbations to the native structure and have very similar potential energies[240]. In contrast, for the lattice model considered by Sali *et al.* any change to the native structure involves a much larger perturbation and can give rise to a large increase in the energy. Therefore, when applied to more complex models and real proteins, it is probably best to interpret the energy gap criterion as the energy gap between the native state and the lowest energy structurally distinct non-native state. The higher the energy of the non-native states relative to the global minimum the less likely they are to act as kinetic traps. Support for this reinterpretation has been found from an annealing study of simple off-lattice proteins[241].

Other studies of lattice models have come to very different conclusions from Sali *et al.* In particular, Klimov and Thirumalai report no correlation between the folding time and the energy gap between the two lowest energy states[242]. Instead, they found that the folding time decreased as the ratio of the folding temperature, T_f, (at which the native structure becomes the thermodynamically most stable state) to the collapse transition temperature, T_θ, (at which the protein transforms from an extended to a compact state) increased. The source of the differences between this study and that of Sali *et al.* is not clear since they involved very similar systems.

An alternative approach to understanding protein folding has been put forward by Wolynes and coworkers[243–247]. It is based upon a statistical characterization of the free energy landscape, and has its origin in spin-glass theory. This approach was combined with the idea of a 'folding funnel', a set of convergent pathways which lead to the global minimum, making it kinetically accessible from the ensemble of misfolded states[248]. A protein that can fold would have a single folding funnel, whereas a random heteropolymer is likely to have numerous funnels leading to structurally different low energy states. The theory describes the global properties of the free energy surface in terms of a few parameters: the ruggedness of the surface, the extent of the funnel (the size of the configurational space), and the potential energy gradient towards the native state. A rugged PES has many minima with large barriers between them. For a protein to be able to fold the funnel would need a sufficiently large potential energy gradient to direct the folding protein to the native structure.

In the above model, the slope of the funnel can also be related to the energy gap between the native state and the disordered collapsed structures, (a different energy gap to that used by Sali *et al.*). By maximizing this energy gap the ratio of T_f (defined above) to the glass transition temperature, T_g, (at which the dynamics dramatically slow down because of kinetic barriers to escape local minima on the PES) is maximized. A large ratio T_f/T_g ensures that the native state is the most stable state at temperatures where the dynamics are still fast, allowing the protein to reach the native state rather than becoming trapped in a local minimum. This criterion can also explain the performance of global optimization methods, such as simulated annealing, which attempt to follow the global free energy minimum as a system is cooled. Such methods are likely to fail when the global minimum of the free energy changes at a temperature below T_g. This approach can also help us to understand some aspects of the results for lattice model proteins that we noted earlier. The T_x that was used by Sali *et al.* has a very similar definition to T_f; both are measures of the stability of the native state of the protein. It is, therefore, unsurprising that increasing T_x (and hence T_f/T_g, if T_g is fairly independent of sequence) increases the ability of the protein to reach the native state. Also, Thirumalai has emphasized[249] the relationship between the values of the ratios T_f/T_θ and T_f/T_g.

Another equivalent formulation of the above ideas is in the 'principle of minimal frustration'. Proteins that have a single folding funnel are likely to have a native state in which all the interactions between residues are favourable. In contrast, in compact configurations of a random heteropolymer there are likely to be residues brought together with conflicting interactions—a random heteropolymer is 'frustrated'. Minimizing the frustration leads to a low energy native structure and consequently to a large value for T_f. These ideas not only provide an elegant theoretical understanding of protein folding, but by using experimental information to estimate the characteristic parameters of the energy landscape for real proteins, they allow a connection to be made between real proteins and lattice models[250].

These theories developed in the context of protein folding can also be useful in understanding the dynamics of systems in the realm of condensed matter physics. As we noted in §4.4, simple liquids have been described as frustrated systems: they have significant polytetrahedral character, yet all space cannot be packed with regular tetrahedra. Therefore, close-packed structures, which are packings of both tetrahedra and octahedra, are the densest and lowest energy structures. Frank was the first to suggest that this structural difference between the solid and the liquid was responsible for the large degree of supercooling that could be achieved for liquid metals[188]. The widest funnels on the PES in such systems lead to glassy minima rather than to close-packed structures.

The packing constraints, and hence the degree of frustration, can be changed by introducing positive curvature into space. In fact for a space of appropriate positive curvature, the lowest energy, highest density structure is a perfect polytetrahedral packing[191] called polytope $\{3,3,5\}$. Straley performed a series of simulations which showed that crystallization occurs much more rapidly in this curved space than in Euclidean space, elegantly demonstrating the effect of frustration on the dynamics[200]. For the curved space there is a single funnel on the PES which leads down through the liquid states to the global minimum.

Similarly, for small Lennard-Jones clusters global optimization strategies, such as genetic algorithms, are able to find the global minimum based on icosahedra from the mass of liquid-like structures fairly easily[73] because icosahedral structures have significant polytetrahedral character. However, there are a number of sizes at which small Lennard-Jones clusters do not have an icosahedral global minimum. For example, the global minimum of a 38-atom cluster is the face-centred-cubic truncated octahedron[70,71] and the lowest energy structures for clusters with 75, 76, 77, 102, 103 and 104 atoms are probably decahedral[71,72]. These cases are much harder for a global optimization algorithm to find since the structures have a much greater close-packed character. In fact the decahedral clusters have never been found yet by an unbiased global optimization method*. It is much harder for the cluster to find the funnel associated with the decahedral minima, compared to the wide funnel that leads down to the icosahedral minima.

Interestingly, in a study of small Lennard-Jones clusters (19 atoms and less) which used global optimization methods based upon the simulated annealing of the classical density distribution, the efficiency was found to be correlated with the energy gap between the global minimum and the next lowest energy state[251]. However, it may be dangerous to draw general conclusions from this result. First, the difference in dynamic behaviour between proteins that can and cannot fold is much greater than that between clusters of different sizes; all the clusters considered in the above study can reach the global minimum relatively easy. Secondly, for these very small systems, much of the thermodynamics is determined by the low energy minima on the PES and the energy gap between the two lowest energy structures is likely to correlate with the melting temperature. For example, the 'melting' transition of the 13-atom cluster is associated with transitions between the icosahedron and the set of the defective icosahedral minima which are next lowest in energy[128]. However, for larger clusters melting is associated with a transition between the low energy minima and the numerous high energy amorphous minima, and the melting temperature is now likely to be correlated with the energy gap between the global minimum and this band of 'liquid-like' minima.

The complexity of proteins means that, inevitably, one has to be satisfied with

*The 75-atom Marks decahedron, though, has been found by a global optimization method developed by David Wales where a decahedral seed is introduced at the centre of the cluster.

a coarse-grained picture of the dynamics involved in protein folding. Studies of small clusters, therefore, could offer particularly important insights since their size allows a much more detailed analysis of the PES[252] and the time scale of the transition from the disordered liquid-like states to a unique solid-like structure is short enough to be probed by computer simulation. Initial studies exploring the relationship between the dynamic behaviour of clusters and the PES have already produced interesting results[252–254]. For example, a comparison of potassium chloride and argon clusters has shown that the greater ability of potassium chloride clusters to crystallize into solid-like structures from the liquid is due to the lower energy barriers and the greater potential energy gradient along series of reaction paths which lead to rock-salt type structures[252]. A more quantitative study sought to understand the behaviour of a 19-atom Lennard-Jones cluster based upon large samples of minima and transition states. The dynamical behaviour was found by calculating transition rates between minima, and then constructing and solving a master equation to describe the flow of probability through configuration space[253,254]. The latter results, however, did not include corrections for the fact that the samples represent only a small fraction of the total number of stationary points on the PES.

In this chapter we follow a similar approach, proceeding from a complete description of a model PES in terms of its minima and transition states to the thermodynamic and dynamic behaviour. We concentrate on the ability of the system to find the global minimum and how this is related to the thermodynamics through Landau entropy profiles. This approach allows us to systematically investigate the effects of various topographic features. In §5.2 we describe the basic PES and the methods for calculating the thermodynamic and dynamic behaviour. In §5.3 we present the results for the PES with a single folding funnel, and in §5.4 we consider the results for the modified surfaces. Finally in §5.5, we summarize the main conclusions from this work. Throughout the chapter we attempt to show how our approach can illuminate and provide a framework for understanding the results already known for specific systems, such as proteins, clusters and glasses.

5.2 Methods

A master equation can be used to describe the dynamics on a multi-dimensional PES[254,255], thus giving the time evolution of the probability distribution, $\mathbf{P}(t) = \{P_i(t)\}$, where P_i is the probability of the system being in state i. The master equation has the form

$$\frac{dP_i}{dt} = \sum_j w_{ij} P_j, \tag{5.1}$$

where $w_{ij} = W_{ij} - \delta_{ij} \sum_k W_{ki}$ and W_{ij} is the rate of transition from state j to state i. The diagonal elements of the matrix, w_{ii}, give the total rate of transition out of state i.

If the transition matrix $\mathbf{w}$ is neither decomposable nor splitting, the matrix has a single zero eigenvalue[255], whose eigenvector corresponds to the equilibrium probability distribution, $\mathbf{P}^{eq}$. The master equation describes the evolution of a system from an initial distribution, $\mathbf{P}(0)$, towards $\mathbf{P}^{eq}$; at infinite time the probability distribution must be equal to $\mathbf{P}^{eq}$. The dynamics and thermodynamics must be consistent in this limit.

The transition matrix must satisfy detailed balance to be physically reasonable, i.e. $W_{ij}P_j^{eq} = W_{ji}P_i^{eq}$. As a consequence, the solution of the master equation can be expanded in a complete set of eigenfunctions of the symmetric matrix, $\mathbf{w}'$, defined as $w'_{ij} = \sqrt{P_j^{eq}/P_i^{eq}}\, w_{ij}$. The result is[254]

$$P_i(t) = \sqrt{P_i^{eq}} \sum_{j,k} u_i^j e^{\lambda_j t} u_k^j \frac{P_k(0)}{\sqrt{P_k^{eq}}}, \tag{5.2}$$

where u_i^j is the i^{th} element of the j^{th} eigenvector of $\mathbf{w}'$ and λ_j is the j^{th} eigenvalue of $\mathbf{w}'$. Apart from the zero eigenvalue, the λ_j are all negative. In all our calculations, we have used the above analytical solution. An alternative method of solving the master equation is to integrate equation 5.1 numerically.

The concept of detailed balance also allows us to define when two states come into local equilibrium; i.e. $W_{ij}P_j(t) \approx W_{ji}P_i(t)$. The precise condition that we use is

$$\frac{\left|P_i(t)P_j^{eq} - P_j(t)P_i^{eq}\right|}{\sqrt{P_i(t)P_j(t)P_i^{eq}P_j^{eq}}} \leq 0.01, \tag{5.3}$$

i.e. the two states are within 1% of equilibrium. The equilibration time for two states is then defined as the time at which the above inequality is first satisfied. This allows us to construct equilibration trees mapping out how the system proceeds to the state where the whole system is in equilibrium[256,257].

The standard PES that we consider is depicted in Figure 5.1. It consists of a single funnel in which the number of minima increases rapidly with energy (Figure 5.1b). To simplify the calculations the minima have been grouped into l_{max} levels. The minima in each level are assumed to have identical properties, and to be

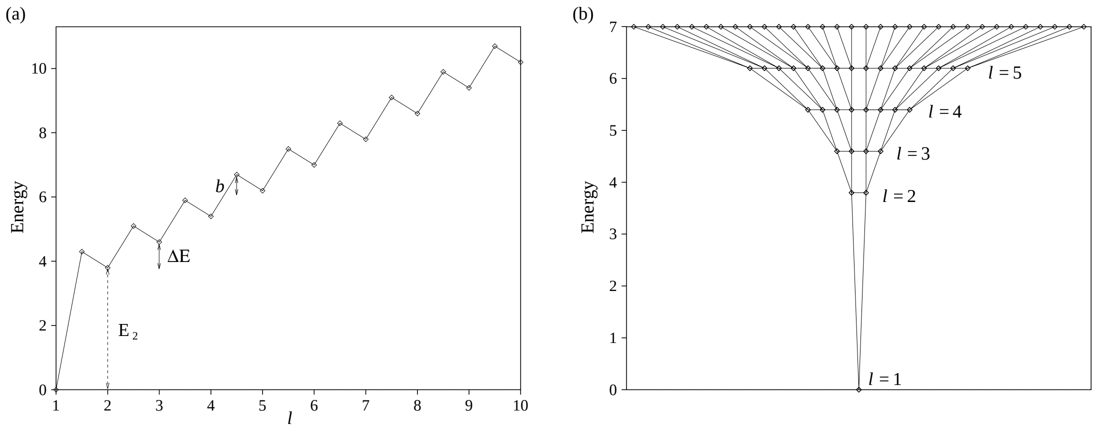

FIGURE 5.1: (a) One-dimensional cross-section through our standard PES showing a reaction pathway from the top of the PES to the global minimum. Integer values of l correspond to minima and half-integer values to transition states. (b) Schematic depiction of a PES with g=2 and l_{max}=6 showing the dramatic increase in the number of minima with energy.

always in equilibrium with each other, thus allowing us to consider each level as a single state in the master equation. This framework is equivalent to assuming that the barriers between minima in the same level are zero. Level $l = 1$ is the global minimum, and the number of minima increases geometrically as the PES is ascended. There are g times more minima in each subsequent level. Therefore the number of minima in level l, n_l, is g^{l-1} and the total number of minima on the PES is $(g^{l_{max}} - 1)/(g - 1)$. We do not consider permutational isomers explicitly since they do not affect the relaxation dynamics. For a real PES, there are $\mathcal{O}(\mathcal{N}!)$ permutational isomers of each minimum. Therefore, there will be many funnels leading down to the different permutational isomers of the global minimum. However, as each funnel is identical they do not need to be considered separately.

We assume that the minima in level l are only connected to minima in levels $l \pm 1$. The transition states connecting minima in adjacent levels are all assumed to lie an energy b above the higher minimum. Each minimum in level l is assumed to be connected to σ minima in level $l-1$ and hence to $g\sigma$ minima in level $l+1$. From this information, and using RRKM theory[166] within the harmonic approximation, the microcanonical rates for transitions between levels are

$$\begin{aligned} W_{l+1,l} &= g\sigma \left(\frac{E - E_{l+1} - b}{E - E_l} \right)^{\kappa-1} \frac{\overline{\nu}_l{}^{\kappa}}{\overline{\nu}_{l+1,l}{}^{\kappa-1}} \quad \text{uphill} \\ W_{l-1,l} &= \sigma \left(\frac{E - E_l - b}{E - E_l} \right)^{\kappa-1} \frac{\overline{\nu}_l{}^{\kappa}}{\overline{\nu}_{l-1,l}{}^{\kappa-1}} \quad \text{downhill,} \end{aligned} \tag{5.4}$$

where E_l is the energy of level l, κ is the number of internal degrees of freedom, and $\overline{\nu}_l$ and $\overline{\nu}_{l,l+1}$ are the geometric mean vibrational frequencies of the minima in level l, and the transition states between levels l and $l+1$, respectively. All other elements of the matrix $\mathbf{W}$ are assumed to be 0 in the present treatment. Similarly, the canonical transition rates are given by

$$\begin{aligned} W_{l+1,l} &= g\sigma\frac{\overline{\nu}_l{}^{\kappa}}{\overline{\nu}_{l+1,l}{}^{\kappa-1}}\exp\left(-\beta(E_{l+1}-E_l+b)\right) \quad \text{uphill} \\ W_{l-1,l} &= \sigma\frac{\overline{\nu}_l{}^{\kappa}}{\overline{\nu}_{l-1,l}{}^{\kappa-1}}\exp\left(-\beta b\right) \qquad\qquad\qquad \text{downhill,} \end{aligned} \tag{5.5}$$

where β is the inverse temperature. We have performed calculations both in the microcanonical and canonical ensembles, but since most of the properties probed show a weak ensemble dependence the majority of the results reported here are microcanonical. The microcanonical ensemble is appropriate to describe an isolated cluster in vacuo, but the canonical ensemble is probably more appropriate for proteins where the solvent can act as a heat bath.

The thermodynamics of the system can be described using a superposition method (Chapter 3), whereby the total energy density of states, $\Omega(E)$, is constructed by summing the density of states for all the energetically accessible minima on the PES. Applying this method to the model PES within the harmonic approximation gives

$$\Omega(E) = \sum_{l=1}^{l_{max}} \frac{n_l(E-E_l)^{\kappa-1}}{\Gamma(\kappa)\overline{\nu}_l{}^{\kappa}}, \tag{5.6}$$

where Γ is the Gamma function. It follows that the microcanonical equilibrium probabilities are given by

$$P_l^{eq}(E) = \frac{n_l(E-E_l)^{\kappa-1}}{\Gamma(\kappa)\overline{\nu}_l{}^{\kappa}\Omega(E)}. \tag{5.7}$$

The canonical partition function and equilibrium probabilities can be constructed in a similar manner:

$$Z(T) = \sum_{l=1}^{l_{max}} \frac{n_l e^{-\beta E_l}}{(\beta h\overline{\nu}_l)^{\kappa}}, \qquad \text{and} \qquad P_l^{eq}(T) = \frac{n_l e^{-\beta E_l}}{(\beta h\overline{\nu}_l)^{\kappa} Z}. \tag{5.8}$$

The global minimum defines the energy zero, i.e. $E_1 = 0$. Beyond $l = 2$ the potential energy is assumed to increase linearly with l. Therefore, $E_l = E_2 + (l-2)\Delta E$ for $l \geq 2$, where ΔE is a measure of the potential energy gradient of the funnel. For a typical cluster PES, the mean vibrational frequency is smaller for minima of higher potential energy[153]—the stabilization of the liquid-like phase at high temperatures is due to both the large number of minima and the greater vibrational entropy. Therefore, we use $\overline{\nu}_l = 1-(l-1)\Delta\nu$. This defines the unit of time as the vibrational period of the global minimum. The mean vibrational frequency of a transition state is assumed to be the geometric mean of the vibrational frequencies of the two minima it connects, i.e. $\overline{\nu}_{l+1,l} = \sqrt{\nu_l\nu_{l+1}}$

5.3 The Standard Potential Energy Surface

The parameters for the standard PES employed in the present study are

$$\kappa = 101 \qquad \sigma = 1 \tag{5.9}$$

$$E_2 = 3.79688 \qquad \Delta E = 0.8 \tag{5.10}$$

$$g = 10 \qquad l_{max} = 10 \tag{5.11}$$

$$\Delta\nu = 0.01 \qquad b = 0.5 \tag{5.12}$$

These values produce a total of 1.11×10^9 minima on the PES. Some of the thermodynamic properties of the system are shown in Figure 5.2. These were calculated using the following definitions: the microcanonical temperature, T, is given by $1/kT = (\partial\ln\Omega/\partial E)_{N,V}$, the canonical internal energy by $U = -(\partial\ln Z/\partial\beta)_{N,V}$, and the canonical heat capacity by $C_v = (\partial U/\partial T)_{N,V}$. In each case analytic derivatives of the appropriate partition functions were employed.

It can be seen from Figure 5.2 that the system shows the finite-size analogue of a first-order phase transition; there are prominent features in the caloric curves and a large peak in the heat capacity. The transition has a two-state character involving the global minimum and minima in the highest energy region of the PES, with intermediate minima never being significantly populated at equilibrium (Figure 5.2c). The energy at which the global minimum has an equilibrium probability of 0.5, E_f, can be used as a definition of the transition energy. For our 'standard' PES, $E_f = 38.2745$.

Also of note is the Van der Waals loop that occurs in the microcanonical caloric curve (Figure 5.2a), which is a feature unique to finite systems[134]. Such loops have been commonly observed for clusters[135,136] and have also been noted in protein simulations[258]. In small clusters the physical cause of this region of negative heat capacity is the absence of phase separation, which is prevented by the relatively high energetic cost of an interface between the solid-like and liquid-like regions[176].

The microcanonical dynamics of the system were examined by initially populating the highest energy state, i.e. setting $P_{10}(0) = 1$, and observing the relaxation

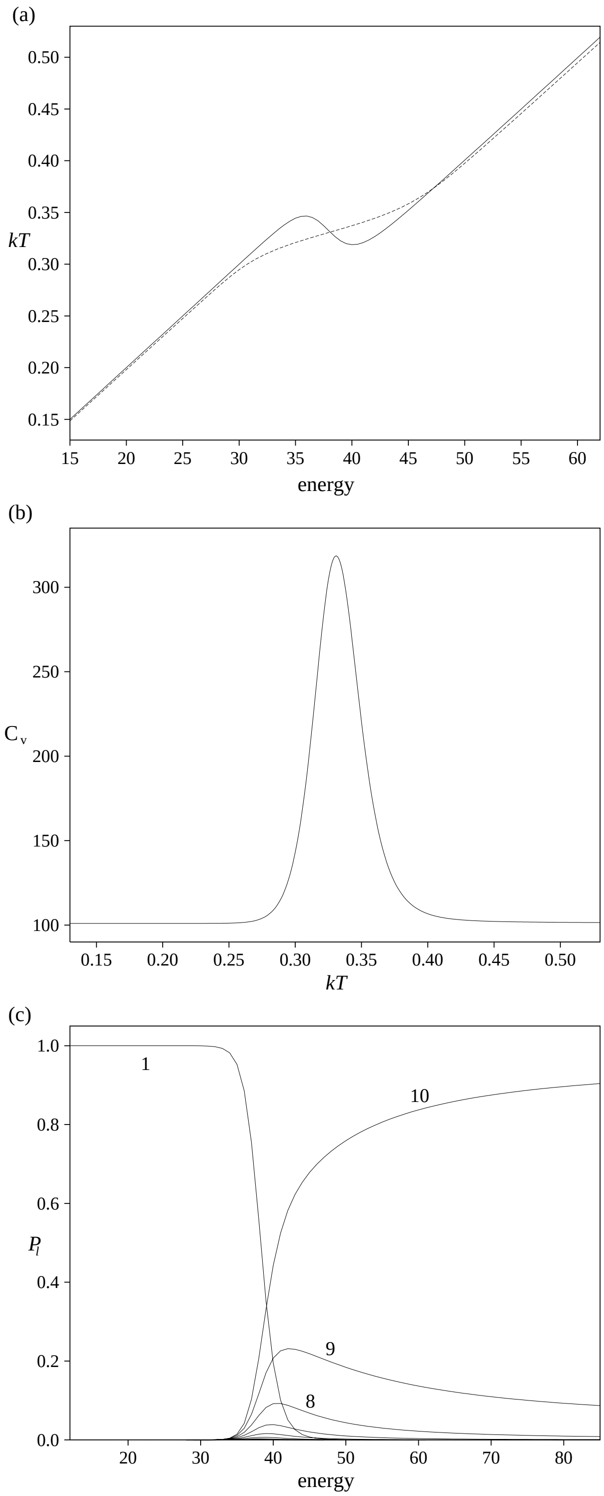

FIGURE 5.2: Thermodynamics of our standard PES: (a) caloric curves for the microcanonical (solid line) and canonical (dashed line) ensembles, (b) canonical heat capacity, and (c) equilibrium probabilities of occupation of level l, P_l^{eq}, for the microcanonical ensemble.

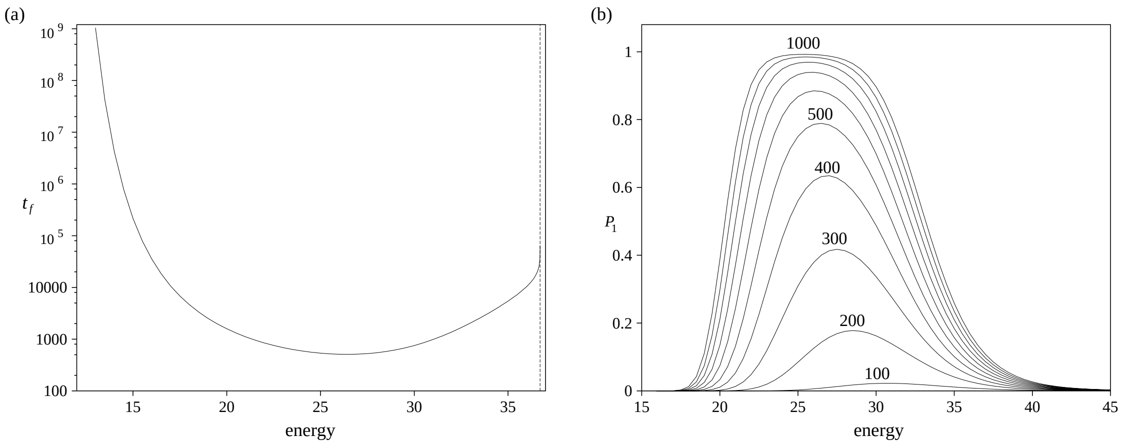

FIGURE 5.3: (a) Variation of the folding time, t_f, with energy for our standard PES. t_f is defined as the time for P_1 to reach 0.8, from an initial state $P_{10}(0) = 1$. The vertical dashed line denotes the energy at which $P_1^{eq} = 0.8$ and so is the upper limit for which t_f is defined. (Above this energy $P_1(t)$ is always less than 0.8). (b) The variation of the probability of being in the global minimum, P_1, as a function of time and energy. The ten lines shown are for $t = 100$ to 1000 in intervals of 100 and are labelled by the appropriate value of t.

towards equilibrium at constant energy. The corresponding canonical results are omitted for brevity. We consider in particular the time required for the global minimum to develop an 80% probability of occupation. By analogy to relaxation in proteins we call this the 'folding' time, t_f; i.e. $P_1(t_f)$=0.8. The dependence of t_f on E for the standard PES is shown in Figure 5.3a. There is a clear minimum in t_f which occurs at an energy, E_{max}, of 26.41 ($= 0.69E_f$). The folding time increases rapidly at low energy because it becomes more difficult to overcome the barriers on the PES, and increases at higher energies because the thermodynamic driving force towards the global minimum is diminished. Similar maxima have been seen in the folding rates of model proteins[247,259–262] in the 'crystallization' rate of a $(KCl)_{32}$ cluster[91], and in the nucleation rate of glasses[263]; these maxima occur for the same reasons as for our model PES. Maxima in the folding rates have also been observed in experiments on proteins which are rapid folders[264–266], but the interpretation of these results is complicated by the fact that real proteins can undergo low temperature denaturation[267].

Another view of the relaxation dynamics is provided by Figure 5.3b which shows the increase in the population of the ground state with time; there is again an energy window for which the global minimum can become significantly populated. It is interesting to note that the energy at which the maximum in the population

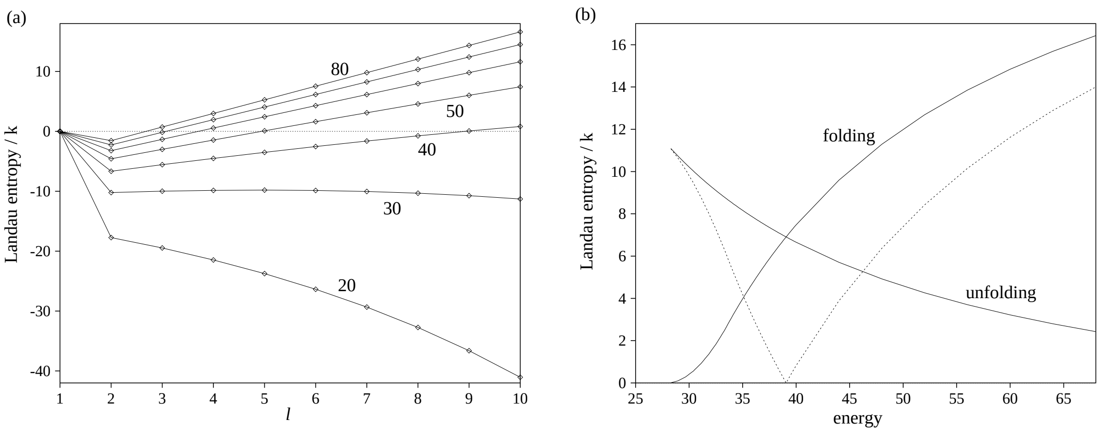

FIGURE 5.4: (a) Landau entropy profiles for our standard PES using the order parameter l. The seven lines shown are for E=20 to 80 in intervals of 10 and are labelled by the appropriate value of E. (b) Depth of the Landau entropy bottleneck relative to the Landau entropy maximum at large values of l ('folding') and relative to the Landau entropy maximum at the global minimum ('unfolding'). The dashed line gives the magnitude of the Landau entropy difference between the two stable states.

of the global minimum occurs decreases somewhat as the time increases. This indicates that to optimize the population of the global minimum one should not quench the system to a low energy and let it evolve, but rather use a cooling schedule whereby the energy is decreased as a function of time, as in constant thermodynamic speed annealing[268].

To further understand the dynamics of the system it is helpful to use Landau functions. In the microcanonical ensemble the presence of a first-order phase transition is indicated by two maxima in the Landau entropy separated by a well. We choose to call the minimum in the Landau entropy an entropy bottleneck, since it represents a constricted region of phase space which has a lower density of states than the regions that it connects. The Landau profiles also enable us to understand the influence of the thermodynamics on the dynamics. If there is one stable state, relaxation to that state is likely to be rapid unless other kinetic factors intervene. If there are two stable states, the rate of transition from the metastable to the stable state decreases as the entropy bottleneck becomes narrower or the free energy barrier increases. The importance of the Landau free energy in understanding protein folding has been recognized by Bryngelson *et al.*, who considered the dynamics expected for a number of different Landau free energy profiles[245].

Application of a Landau-type analysis using a restricted thermodynamic potential depends on finding a suitable order parameter which can differentiate between the states of interest. For many systems this can be a difficult task, but for our model PES l provides a natural order parameter since it is a measure of the distance from the global minimum. The Landau entropy is then defined as $S_L(l) = S(E) + k \ln P_l^{eq}(E)$ and the Landau free energy by $A_L(l) = A(T) - kT \ln P_l^{eq}(T)$. Landau entropy profiles for our standard PES are given in Figure 5.4 for a range of energies. At low energy there is a single maximum corresponding to the global minimum, and relaxation to the global minimum is thermodynamically 'downhill'. Consequently at E_{max}, the probability density 'flows' smoothly down the PES with the intermediate states having significant transient populations (Figure 5.5).

The equilibration trees in Figure 5.5 map out the times at which different levels come in to approximate equilibrium with each other (as defined by equation 5.3). At E_{max} levels 1 and 2 first reach local equilibrium (Figure 5.5e), i.e. equilibrium first occurs between the levels corresponding to the Landau entropy maximum. Next, level 3 reaches equilibrium with levels 1 and 2, and so on to higher values of l: the local equilibrium propagates to higher energy away from the Landau entropy maximum. Similar behaviour occurs at lower energies, except that the barriers on the PES have a larger retarding effect on the dynamics. Therefore, the equilibration tree at E=15 (Figure 5.5c) shows the same structure as at E_{max} except that the time scales are around a thousand times slower. In the microcanonical ensemble the kinetic energy increases as the potential energy decreases. Consequently, at low energies the transition rate over the barriers is much slower at the top of the PES, and the system accelerates as it descends the PES. Therefore, transient populations in the intermediate states are less pronounced at $E = 15$ than at E_{max}. In the canonical ensemble this effect is absent because the kinetic energy is independent of the position in configuration space.

For $E > 28.238$, there are two Landau entropy maxima, which correspond to the global minimum and the high potential energy 'unfolded' states. The entropy bottleneck occurs because at lower potential energy the loss in entropy due to the reduced number of minima is not completely compensated by the greater vibrational entropy that results from the larger kinetic energy. As a result of the entropy bottleneck, the equilibration trees have a qualitatively different form from those at lower energies; equilibration initially occurs within the secondary Landau entropy maximum corresponding to the higher lying levels and then propagates down the PES (Figure 5.5f). It is interesting to note that this change in direction of equilibration appears at approximately the same energy as the Landau entropy bottleneck. For E=36 there is a separation of time scales between equilibration

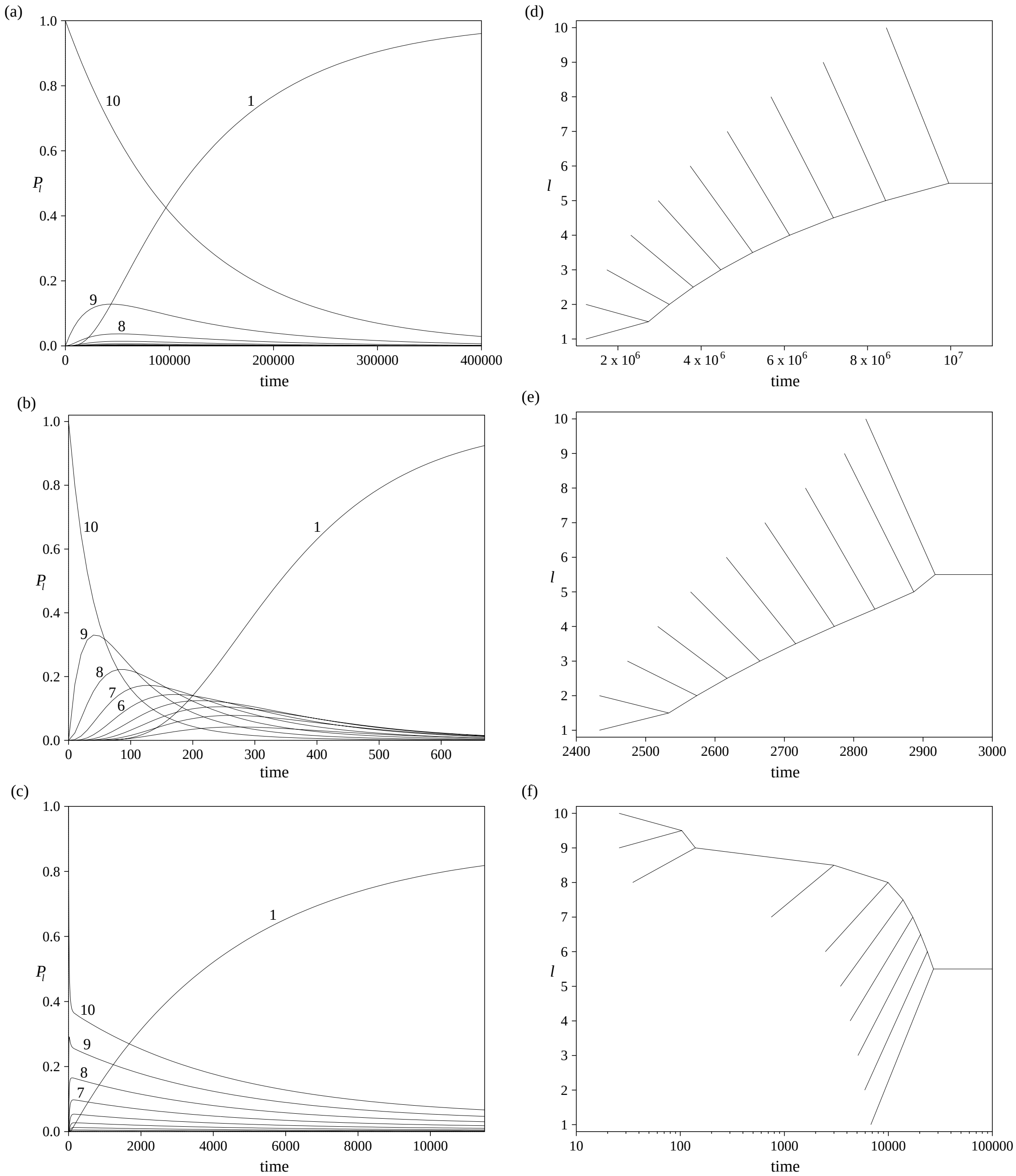

FIGURE 5.5: (a)–(c) Time evolution of the probabilities, P_l, and (d)–(f) equilibration trees for our standard PES at an energy of (a) and (d) 15; (b) and (e) 26.41; and (c) and (f) 36. Initially, P_{10}=1. The energy 26.41 corresponds to the minimum in the 'folding' time of Figure 5.3a. Each line in the equilibration tree represents a single level or a set of levels that are in equilibrium with each other. The lines join at times when states first come into local equilibrium as defined by equation 5.33. The vertical position of these nodes is given by the average value of l for the levels that are in equilibrium with each other. The horizontal positions of the ends of lines on the left-hand side of the graph, which correspond to individual levels, are arbitrary.

within the secondary Landau entropy maximum, and equilibration between the maxima. This is reflected in the time evolution of the probability distribution: the probabilities of occupying higher potential energy levels rapidly attain approximate local equilibrium values which then slowly decay as the global minimum becomes more populated (Figure 5.5c).

Similar behaviour is seen for the Landau free energy in the canonical ensemble. In fact, the temperature at which A_L develops a double well can be derived analytically (assuming that $\Delta\nu$ is small). Two free energy minima are observed if

$$kT > \frac{\Delta E}{\ln g + \kappa \Delta\nu}. \tag{5.13}$$

This corresponds to $kT > 0.242$ for our standard PES. As relaxation to the global minimum is impeded by a free energy barrier, equation 5.13 implies that large ΔE and small g and $\Delta\nu$ assist relaxation to the global minimum. These are the same conditions as those that lead to a large value of T_f.

Landau free energy profiles have previously been calculated for lattice models of proteins[233,234,247,250,258]. They show a similar behaviour to that found for our model PES, with a single minimum at low temperature, and two stable states at higher temperatures corresponding to the folded and unfolded protein[233,234,247]. For clusters there can be a range of temperature around the melting transition for which Landau functions reveal two stable states corresponding to the solid-like and liquid-like states[112,133]. Similarly it has been shown that the nucleation of a crystalline phase from the bulk Lennard-Jones liquid involves a large free energy barrier[269,270].

5.4 Modified Potential Energy Surfaces

The previous section showed that our simplest model PES captured many of the dynamical effects commonly seen in finite systems such as proteins and clusters. Here we seek to modify the standard PES to understand which factors influence a system's ability to find the global minimum. The model PES has too many parameters to allow a systematic study of the whole parameter space. Additional complexity could, of course, be generated by making the parameters functions of l. The effects of varying some of the parameters, though, are fairly obvious. For example, increasing σ would make all the rates σ times faster. Our approach here is to make only changes to the PES that leave the basic thermodynamics

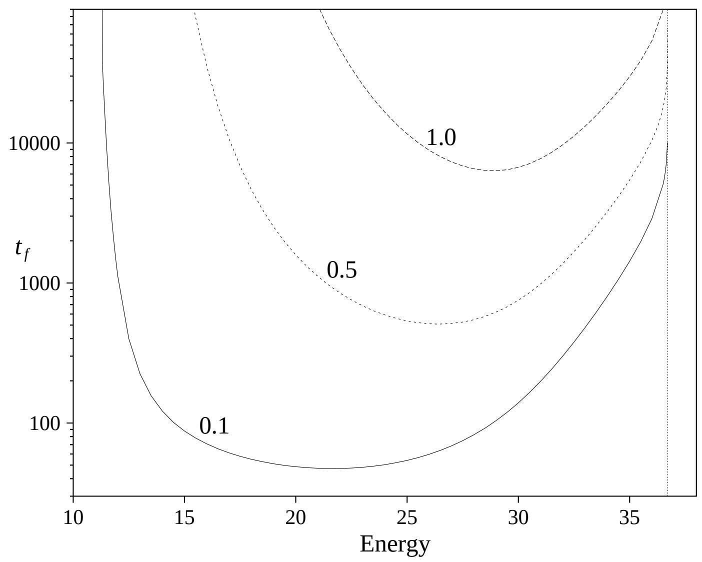

Figure 5.6: The dependence of t_f on the barrier height, b, for our standard PES. t_f is defined by $P_1(t_f)$=0.8. The vertical dotted line denotes the energy at which $P_1^{eq} = 0.8$. Each line is marked by the value of b.

unchanged—i.e. we keep E_f constant—and to concentrate on the factors that could lead to particularly interesting behaviour.

5.4.1 Barrier heights

The first modification that we make is to change the barrier height. Unsurprisingly, increasing b leads to a reduction in the rate of relaxation to the global minimum (Figure 5.6). More interesting is the dependence of this effect upon the energy: increasing the barrier heights leads to a much larger increase in t_f at low energies. This is because a larger fraction of the kinetic energy must be converted to potential energy to overcome the barriers at low energies. The energy at which the maximum 'folding' rate occurs increases as the barrier heights increase. The shape of the minimum in t_f is also dependent on b, becoming broader as the barrier heights are decreased; at $b = 0.01$ there is a larger energy window for which fast relaxation to the global minimum can occur.

Similar behaviour is observed for the canonical ensemble, namely the rate of relaxation to the global minimum has a $\exp(-\beta b)$ dependence on the barrier height. Therefore, at fixed temperature the relaxation rate has a rigorously exponential dependence on b, and changing b has a greater effect on the relaxation rate at low temperature.

These results can easily be understood in the language of Bryngelson and

Wolynes[243–245]: increasing the barrier heights corresponds to increasing T_g without changing T_f, hence decreasing the ratio T_f/T_g and the 'folding' ability. Potassium chloride clusters provide a good example of systems for which relatively small barrier heights produce rapid relaxation down the PES[252].

5.4.2 The slope of the funnel

In the energy landscape model of protein folding, the slope of the funnel (potential energy gradient) is a key parameter[246,250]. Here we analyse the effect of the slope by varying ΔE. To keep E_f constant we must also vary E_2. For the case when ΔE is zero, i.e. a flat surface, $E_l = 10$ for $l \geq 2$. It can be seen from Figure 5.7a that the slope has a dramatic effect on the folding time, and that a sufficiently steep slope is necessary for reasonably rapid relaxation to the global minimum. This behaviour can be explained from the relative rates of uphill and downhill transitions in our model. The barrier for going downhill is b, and for going uphill $\Delta E + b$. Therefore, the downhill transition rate is not significantly affected by the slope, but the uphill rate decreases rapidly as the slope is increased. For the flat PES taking a step to higher l is, ignoring the vibrational contributions to the rate, g times more likely than to lower l, causing the probability distribution to remain concentrated at large values of l. As a slope is introduced into the PES the uphill rate decreases relative to the downhill rate and the folding time begins to decrease rapidly. However, once the PES is sufficiently steep to make the uphill rate small compared to the downhill rate, further increasing the slope only has a limited effect. At large ΔE the folding time even begins to increase again because the level $l = 2$ begins to have a low enough energy for it to have a significant equilibrium population.

An equivalent explanation for the behaviour can be provided in terms of the Landau entropy. In order to keep E_f constant as the slope is decreased the energy of the intermediate levels must be increased. This has the effect of reducing the equilibrium probability for occupation of these levels. Therefore, as ΔE is decreased a Landau entropy bottleneck develops and then increases in depth (Figure 5.7b). The folding time increases rapidly as the bottleneck deepens, but has only a weak dependence on ΔE when there is a single Landau entropy maximum.

The flat PES would correspond to the Levinthal limit where the states are searched randomly, but for the variation of the vibrational frequency with l, which makes the minima in higher levels slightly more probable. For this PES, equili-

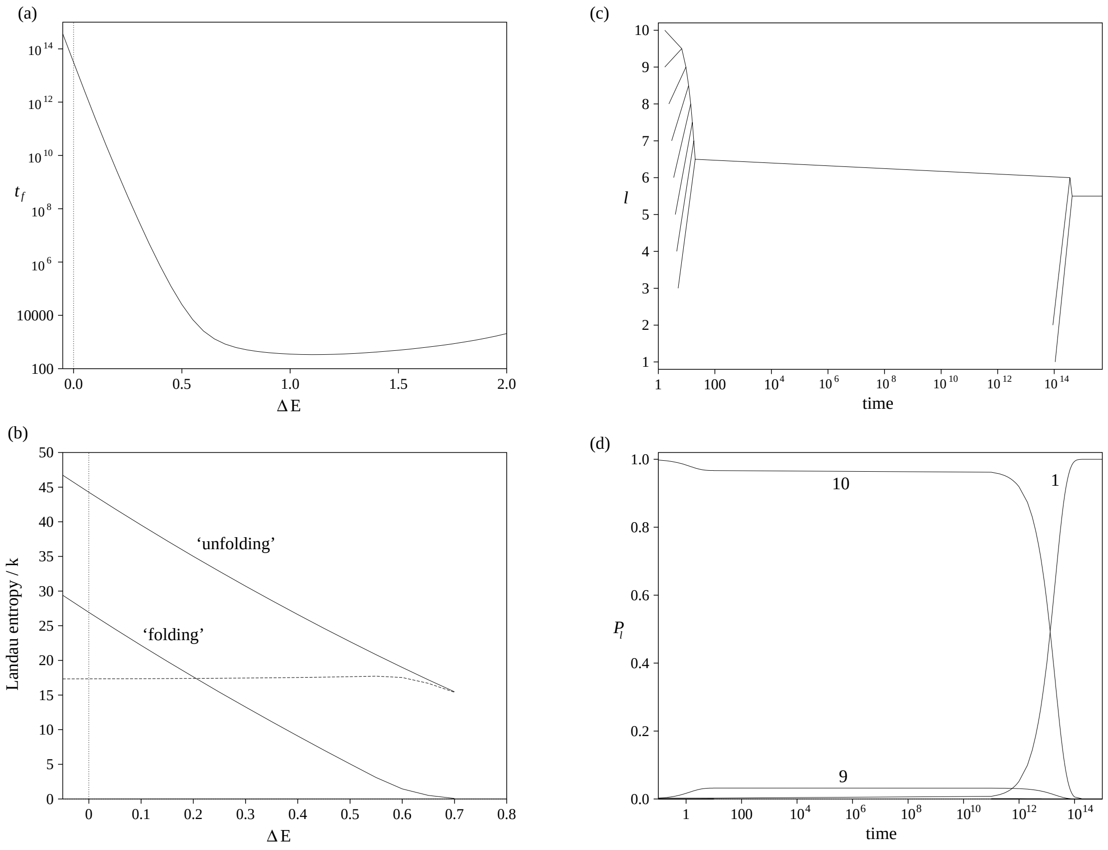

FIGURE 5.7: (a) Variation of t_f with the slope of the PES. (b) Variation of the magnitude of the Landau entropy bottlenecks (solid lines) with ΔE. The dashed line gives the magnitude of the Landau entropy difference between the two stable states. (c) Equilibration tree and (d) time evolution of the probabilities, P_l, for the flat PES (ΔE=0) from an initial distribution P_{10}=1. All results are for E=26.41.

bration occurs initially at large values of l and proceeds away from the Landau entropy maximum. There is a large separation (of the order of 10^{13}) between the time scales for equilibration within the large l entropy maximum and between the entropy maxima (Figure 5.7c), because of the deep Landau entropy bottleneck. This is evidenced by the probability flows across the PES (Figure 5.7d); P_{10} and P_9 rapidly reach local equilibrium values, which then decay away as the ground state is slowly populated.

These results help to explain why potassium chloride clusters are able to relax to the rock-salt structures so rapidly[91]. Reaction pathways leading down to the rock-salt structures generally exhibit[252] $\Delta E \gg b$.

As ΔE is decreased E_2, which is simply the energy gap between the global minimum and the next lowest energy state, has to be increased to maintain E_f. Therefore, the efficiency with which the global minimum is found is reduced as

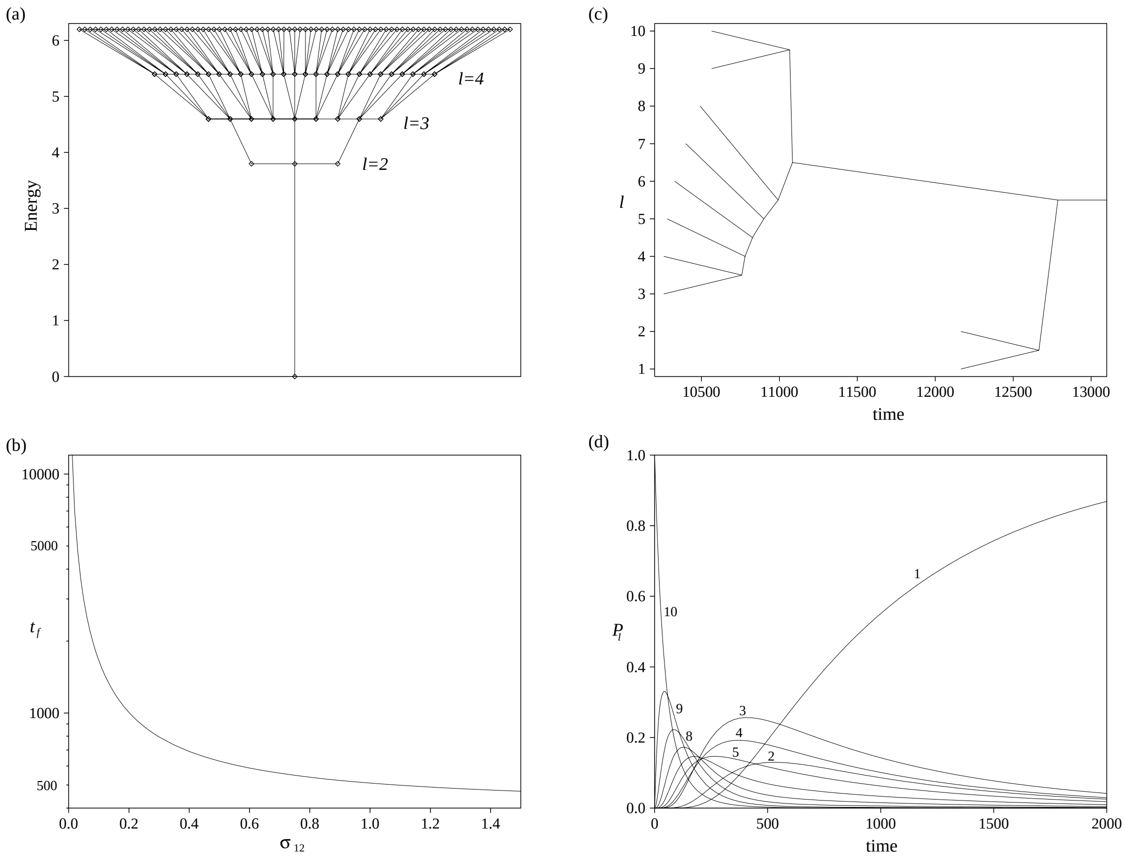

Figure 5.8: (a) Schematic depiction of a PES with a kinetic bottleneck. $g = 3$, and $\sigma = 1$ except for $\sigma_{12} = \sigma_{23} = \frac{1}{3}$. (b) Dependence of t_f on σ_{12}. (c) Equilibration tree and (d) time evolution of the probabilities, P_l, from an initial distribution P_{10}=1 for a PES with $\sigma_{12} = 0.1$. All results are for E=26.41.

E_2 is increased. This result does not necessarily contradict the view of Sali *et al.*, however, since we can decouple factors in our model in a way that may not be possible for real PES's. However, it does show that even if the energy gap view were correct, it would require further explanation; it is not self-evident why an energy gap should guarantee kinetic foldability.

5.4.3 Kinetic bottlenecks

For our standard PES surface σ is independent of l. However, a real PES is unlikely to show such uniformity. For example, it has been suggested that for some proteins the number of available pathways may decrease near to the native state leading to the observation of kinetically-determined intermediates[245].

In this section we investigate the effect of making σ dependent on l. In particular, we reduce the number of connections between l=1 and l=2, and between

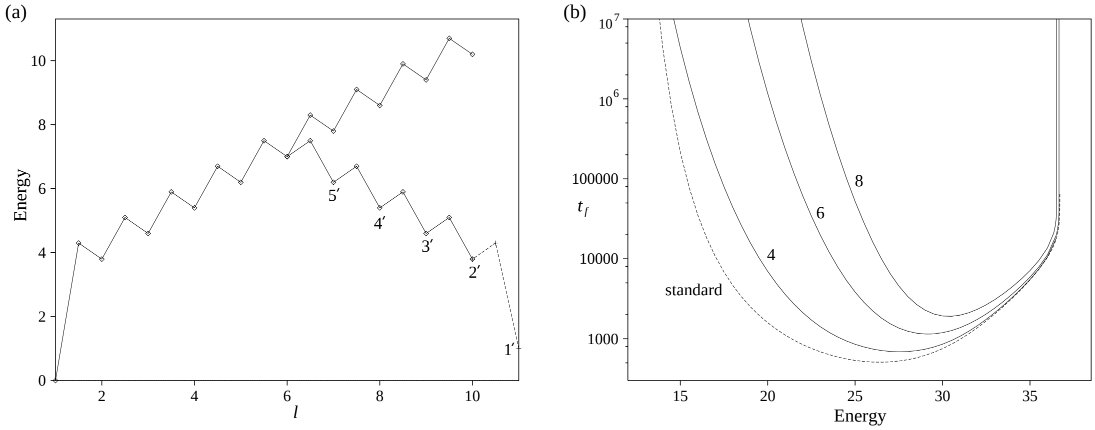

FIGURE 5.9: (a) One-dimensional cross-section through a PES with two funnels where l_{node}=6 The values of l' for the minima in the secondary funnel are as labelled. (b) Dependence of t_f upon the energy and l_{node}. The values of l_{node} are as labelled, and the curve for our standard PES (dashed line) has been added for comparison.

l=2 and l=3. Such a PES is illustrated in Figure 5.8a; it has $\sigma_{12} = \sigma_{23} = \frac{1}{3}$ and so only 1 in 3 of the minima in level 3 are connected to a minimum in level 2. These changes do not affect the thermodynamics in any way (including the Landau entropy) but instead produce a kinetic bottleneck. In Figure 5.8b, the dependence of the folding time for the modified surface upon σ_{12} is shown. t_f increases as the number of connections is reduced, but at the most by only one to two orders of magnitude. The slowing down of the dynamics at the bottleneck leads first to local equilibrium above the bottleneck (Figure 5.8c) and to a build-up of probability in level 3 and to a lesser extent in levels 4 and 5 (Figure 5.8d).

These results show that kinetic bottlenecks may significantly affect the folding rate, but to a smaller extent than other factors, such as the slope of the funnel or the multiple funnels that we shall consider next. Kinetic bottlenecks may be important in rationalizing the detailed dynamic behaviour of a particular system, but are unlikely to represent the difference between, for example, folding and non-folding proteins.

5.4.4 Multiple funnels

In this section, we consider the consequences for the dynamics when the PES has more than one funnel. This allows us to examine Leopold *et al.*'s suggestion that the amino acid sequences which fold to a unique native state are characterized by a single funnel leading to the global minimum, whereas those that do not fold have multiple funnels leading to structurally different minima[248]. The results should also

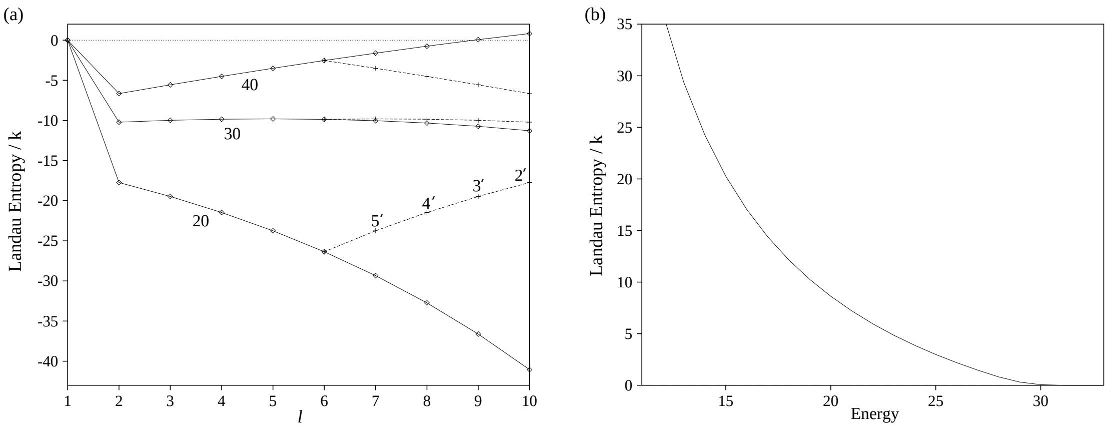

FIGURE 5.10: (a) Landau entropy profiles for a PES with two funnels and l_{node}=6. The lines are labelled by the corresponding values of the energy. The dashed lines are for the secondary funnel and points have been marked by the appropriate value of l'. (b) The energy dependence of the magnitude of the Landau entropy bottleneck for passage from the bottom of the secondary funnel to the primary funnel.

be relevant to other systems where the system has difficulty in reaching the global minimum, such as glasses. It has been suggested that the glassy states are located at the bottom of funnels which are separate from the crystalline funnel[91,271,272].

A schematic picture of the modified PES which we have investigated is shown in Figure 5.9. It has a secondary funnel joined to the primary funnel at $l = l_{node}$. The levels in the secondary funnel are denoted by l' and have the same properties as the corresponding levels for the standard PES. Initially, we consider the case where the secondary funnel ends at $l' = 2'$, since for this case the secondary funnel hardly affects the equilibrium thermodynamics—the $P_{l'}^{eq}$ never have significant magnitudes (see e.g. Figure 5.2c).

The rate of relaxation to the global minimum is not significantly affected by the secondary funnel at energies near to E_f, but as the energy is decreased the rate slows dramatically compared to the standard PES (Figure 5.9b). The latter effect becomes more pronounced at larger values of l_{node}. This behaviour can be explained by examining the Landau entropy (Figure 5.10). At higher energies, the bottom of the secondary funnel is not an entropy maximum, and so the system never gets trapped there. However, below the energy for which relaxation down the primary funnel is thermodynamically favourable, level $l' = 2'$ becomes a Landau entropy maximum and there is a Landau entropy bottleneck which must be overcome in passing from the secondary to the primary funnel (Figure 5.10b). The conditions which are thermodynamically most favourable for folding for the standard PES

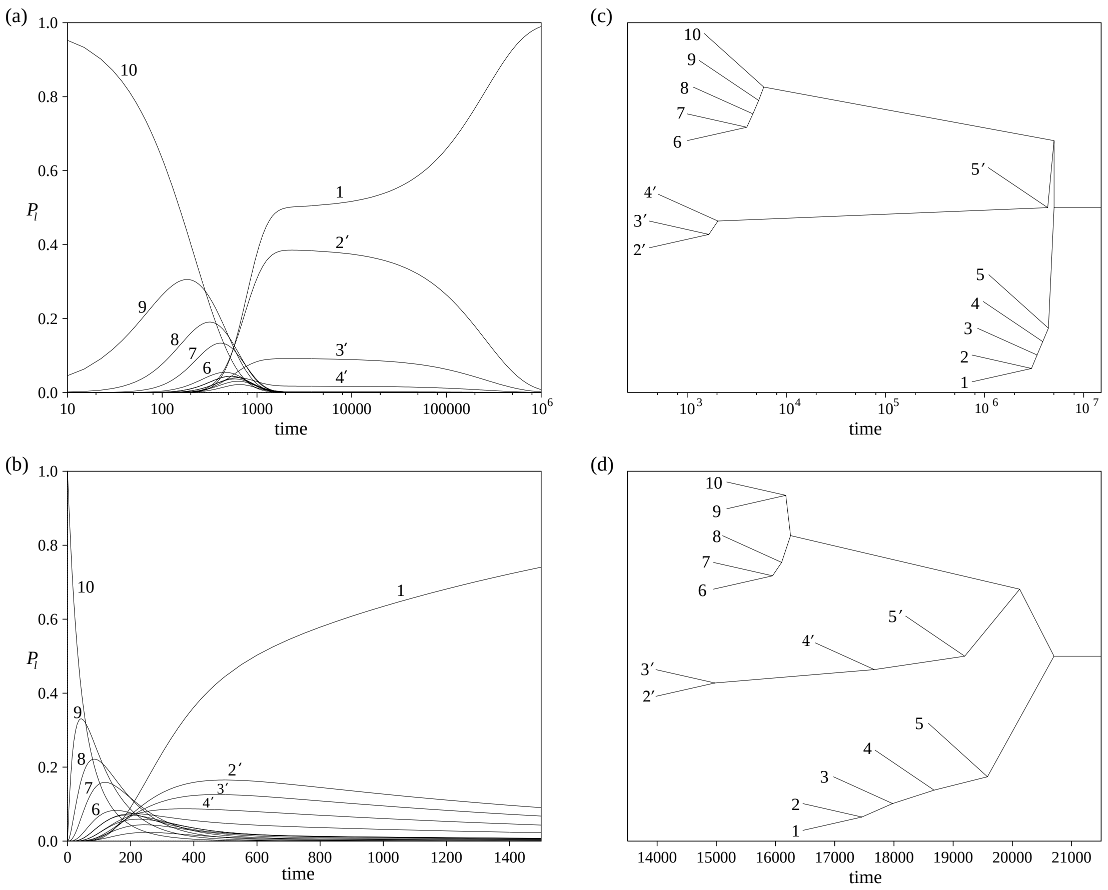

Figure 5.11: (a) and (b) Time evolution of the probabilities, P_l, and (c) and (d) equilibration trees at an energy of (a) and (c) 21; and (b) and (d) 26.41 for a PES with two funnels and l_{node}=6. The secondary funnel ends at l'=2. Initially, P_{10}=1. The lines of the equilibration trees corresponding to individual levels are labelled by the appropriate values of l or l'.

also most favour trapping in the secondary funnel.

The consequences of these changes in the Landau entropy can be seen in the probability flows and the equilibration trees (Figure 5.11). At $E = 26.41$, there is only a small entropy bottleneck associated with exit from the secondary funnel, and the time scale for this process is only about an order of magnitude larger than that for relaxation from high energy minima. At higher energies, where there is no entropy bottleneck, this time scale separation disappears altogether. However, for $E = 21$ there is a much larger entropy bottleneck to be overcome. By $t = 1000$, the system has relaxed down the PES, reaching a state where $P_1 \approx \frac{1}{2}$ and the probability of being in the secondary funnel is also close to a half (Figure 5.11a). In the initial relaxation the system is equally likely to go into either funnel, because both funnels have the same properties around $l = l_{node}$. This situation persists for about two orders of magnitude in time (note the log scale in the figure) until the probability begins to flow from the secondary funnel into the primary. The same basic structure is seen for both equilibration trees in Figure 5.11; equilibration occurs separately above l_{node} and within the bottoms of the two funnels. The tree for $E = 21$ clearly shows the large separation in time scales.

There have been some interesting investigations of the effects of trapping by low energy non-native states in protein folding simulations[262,273]. These show that at low temperatures there is a fast component to the relaxation rate, which corresponds to the protein passing directly into the native structure, and a slower component, where the system becomes trapped in one of the low energy non-native states before reaching the native structure. As for our model PES, this separation of time scales can disappear at higher temperatures[262]. Experimental studies of protein folding often show kinetics with two (or more) time scales present[264,274–278]; there are subpopulations of proteins which fold at different rates. Experiments on hen lysozyme have clearly shown that the faster rate corresponds to direct folding to the native state[276], and it has been inferred that the slower rate is due to trapping in low energy non-native structures. This interpretation has been confirmed for cytochrome c. For this protein, the chain misorganization responsible for trapping is the incorrect ligation of a haem group by a histidine residue. Under refolding conditions which prevent this incorrect contact forming, the protein folds on a time scale of 15ms, but when trapping occurs folding takes longer than 0.3s[278]. The temperature dependence of the two rate constants[264] for cytochrome c agrees well with the behaviour of our model PES. The faster rate constant exhibits a maximum, as would be expected for direct relaxation to the global minimum (Figure 5.3a), whereas the rate constant for the slower process just decreases as the temperature decreases[264], which is what would be expected when the magnitude of the Landau entropy bottleneck for escape from a trap increases with decreasing temperature (Figure 5.10b).

Interestingly, it has been suggested that chaperonins, such as GroEL and GroES, assist protein folding by reducing the effect of trapping[279,280]. The chaperonins bind proteins which are trapped in non-native structures and then release them in a less folded state, thus allowing the protein another opportunity to find the native structure directly. Simulations show that the folding rate of slow-folding proteins increases significantly when this 'iterative annealing' model for chaperonin action is included[281], lending further credence to this proposal.

The trapping properties of the secondary funnel can be increased by adding

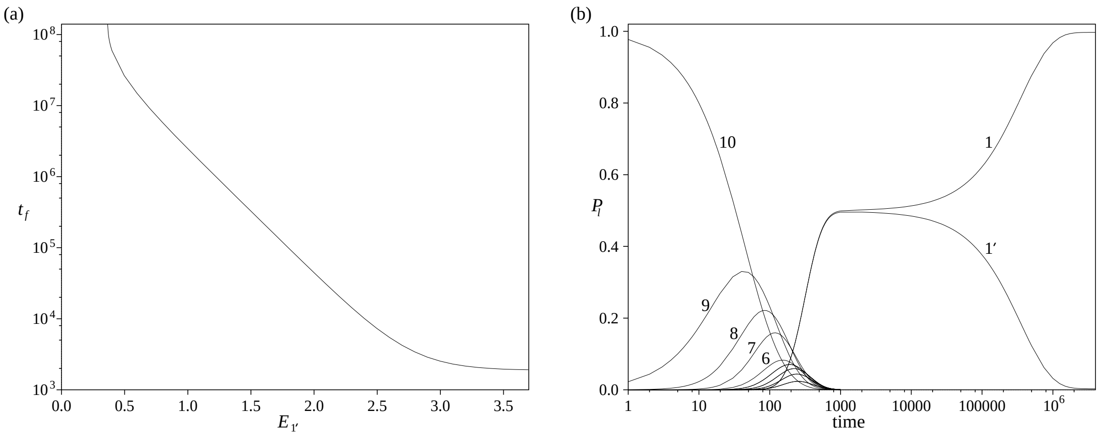

FIGURE 5.12: Dynamic properties of a PES with two funnels and l_{node}=6 at an energy of 26.41. The secondary funnel ends at $l' = 1$. (a) Dependence of t_f upon $E_{1'}$. (b) Time evolution of the probabilities, P_l, for $E_{1'}$=1.5 from an initial distribution P_{10}=1.

a minimum at $l' = 1'$, as shown in Figure 5.12a. t_f increases exponentially as the depth of the secondary funnel is increased. As $E_{1'}$ approaches the value for which $P_{1'}^{eq}$=0.2 ($E_{1'}$=0.364), t_f increases even more rapidly, as expected from our definition of t_f ($P_1(t_f) = 0.8$). At higher energies, the dependence of the relaxation rate on $E_{1'}$ diminishes as $E_{2'}$ is approached. For this system the probability density flows rapidly and equally into the bottoms of both funnels and then begins to trickle very slowly back up the PES from $l' = 1'$ into the primary funnel (Figure 5.12b). This PES provides an example where the energy difference between the two lowest energy minima has a very significant effect on the relaxation rate to the global minimum, and supports our suggestion that this quantity is most important when the two minima equilibrate very slowly because they are structurally dissimilar and well-separated on the PES.

The PES of $(KCl)_{32}$ shows some interesting features. The relaxation down to the low energy rock-salt-like structures from the amorphous states is rapid[91]. However, it is not clear whether the system can then reach the $(4 \times 4 \times 4)$ global minimum from the other rock-salt-like structures, which can have very different shapes from the global minimum, e.g. the second lowest energy minimum has a $(5 \times 4 \times 3)$ shape plus an extra row of four atoms[127]. It might be that these crystal-like structures have separate funnels, the steep slopes of which make interconversion to other rock-salt-like structures difficult. This would give rise to a significant separation between time scales for relaxation down the PES and equilibration between the rock-salt-like structures, similar to that seen for our model PES above.

In the above examples, the properties of both funnels were the same except at $l' = 1'$. As a result, the initial relaxation down the PES was equally likely to take the system into either funnel. However, for materials that easily form glasses the system is more likely to relax into the amorphous glassy minima than into the crystalline minima. A similar effect can be achieved in our model by making the 'width' of the primary funnel narrower than that of the secondary. g determines the number of minima in each level, and consequently also determines the increase in the configurational entropy as the funnel is ascended, i.e. its width. Therefore, if we make the value of g for the primary funnel below l_{node}, g_p, where g_p is smaller than for the rest of the PES, the primary funnel is only connected to $g_p^{l_{node}-1}$ of the $g^{l_{node}-1}$ minima in the level $l = l_{node}$. For the parameters l_{node}=6, g_p=4 and g=10, this corresponds to only 1% of the minima in the level $l = l_{node}$. These changes to the PES affect the rate of transition between levels l_{node} and $l_{node} - 1$, which becomes

$$W_{l_{node}-1,l_{node}} = \sigma \left(\frac{g_p}{g}\right)^{l_{node}-1} \left(\frac{E - E_{l_{node}} - b}{E - E_{l_{node}}}\right)^{\kappa-1} \frac{\overline{\nu}_{l_{node}}{}^{\kappa}}{\overline{\nu}_{l_{node}-1,l_{node}}{}^{\kappa-1}}. \tag{5.14}$$

This PES can mimic some of the effects of frustration. If, as in simple liquids, the high potential energy amorphous minima have a different type of order from the crystalline global minimum, one might expect that the glassy states at the bottom of the liquid-like band of minima maximize the polytetrahedral order as far as is possible. Therefore, the glassy minima are not likely to be connected to the crystalline funnel, but instead reside at the bottom of rugged funnels which descend from the liquid-like regions of configuration space. In contrast, the funnel terminating at the crystalline state is likely to be connected to a small fraction of the higher energy amorphous minima which contain incipient crystal-like nuclei. Consistent with this idea, large Landau free energy barriers have been found in simulations of nucleation of a crystalline phase from a Lennard-Jones liquid[269,270]. This view of the PES topography of glass-formers has many similarities to the ideas put forward by Stillinger for fragile liquids[271,272].

We now choose to end the secondary funnel at $l' = 2'$ since glasses normally have a significantly higher potential energy than the crystalline state. For this PES, the rate of relaxation to the global minimum dramatically slows as the primary funnel is narrowed by decreasing g_p (Figure 5.13a). This occurs because the level l=5 has a lower entropy than $l' = 5'$ and $l_{node} = 6$ (Figure 5.13b). On reaching $l = l_{node}$, the system is much more likely to pass into the secondary funnel, rather than overcome the Landau entropy bottleneck associated with passage into the

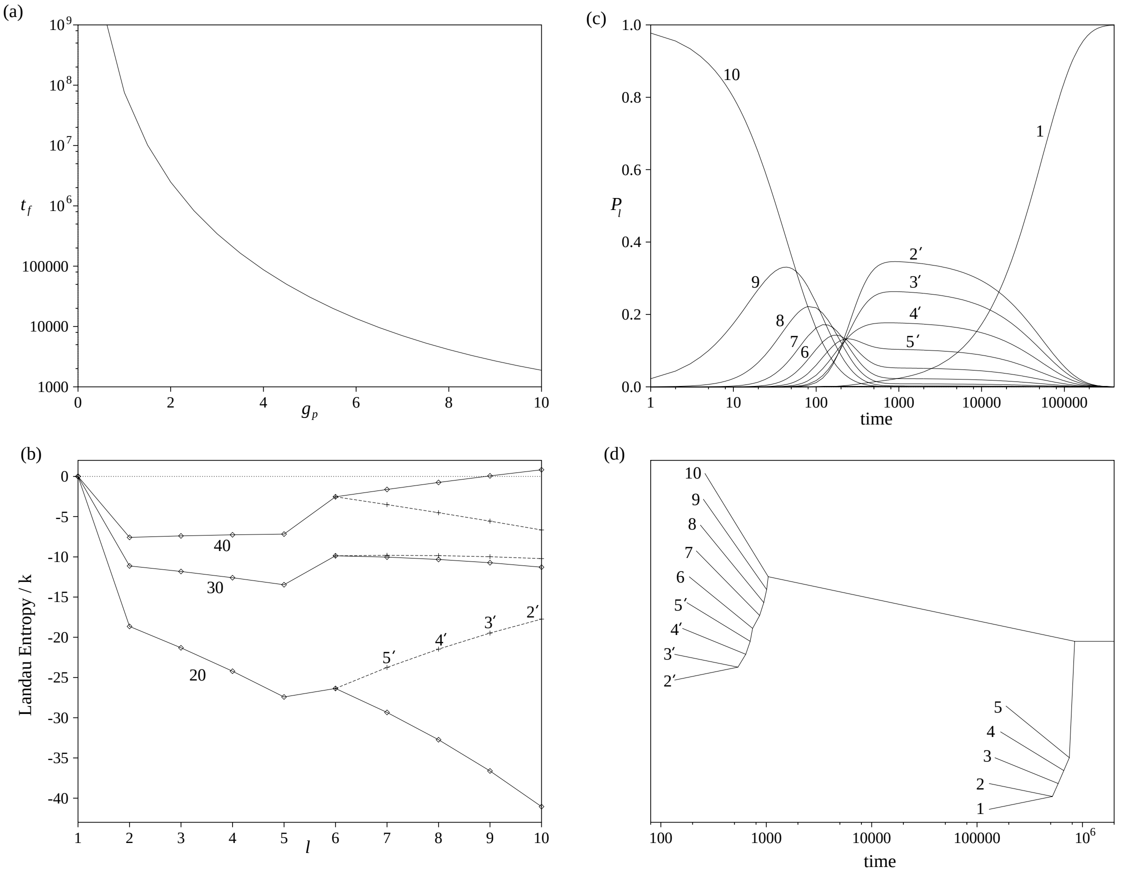

FIGURE 5.13: Dynamic properties of a PES with two funnels and l_{node}=6. For $l < l_{node}$ the primary funnel has a lower value of g than for the rest of the PES. The secondary funnel ends at $l' = 2$. (a) Dependence of t_f upon g_p at an energy of 26.41. (b) Landau entropy profiles when g_p=4 at different values of the energy as labelled. (c) Time evolution of the probabilities, P_l, and (d) Equilibration tree when g_p=4 from an initial distribution P_{10}=1 at an energy of 26.41.

primary funnel. The depth of this bottleneck increases as the width of the primary funnel decreases.

The time evolution of the probabilities when g_p=4 shows that all the probability initially passes into the secondary funnel, and then slowly trickles back through the Landau entropy bottleneck into the global minimum (Figure 5.13c). This results in a large separation of time scales between the time for equilibration within the secondary funnel and between the two funnels (Figure 5.13d).

This example shows that the secondary funnel is a more effective trap when it has a larger width than the primary funnel. Earlier in this section, we showed that a low energy minimum at the bottom of the secondary funnel also increases its trapping efficiency. By combining these two features we can create a PES where

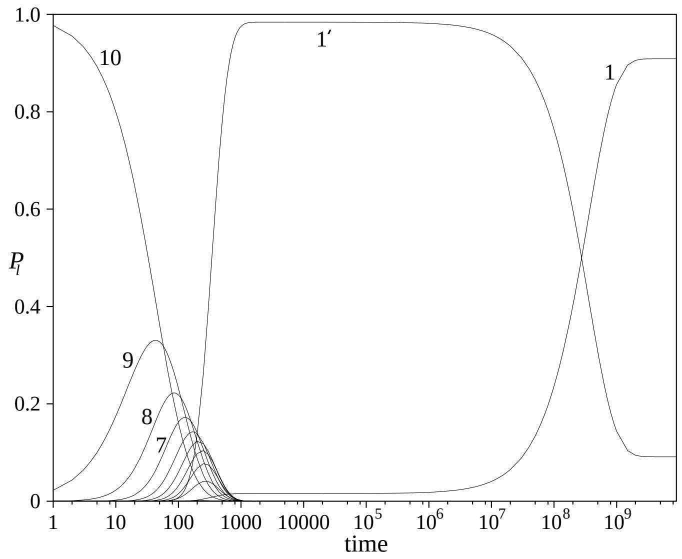

Figure 5.14: Time evolution of the probabilities, P_l, for a PES with two funnels and l_{node}=6 at a total energy of 26.41. For $l < l_{node}$ the primary funnel has g_p=4. The secondary funnel ends at l'=1 at a potential energy $E_{1'}$=0.6. Initially, P_{10}=1.

virtually all the probability flows to the bottom of the secondary funnel, and then remains there for a long time (Figure 5.14). Only on very long time scales does the global minimum start to become significantly populated; t_f for this PES is 7.4×10^8. In the example shown $E_{1'}$=0.6, and so $P_{1'}^{eq}$=0.091, thus preventing complete population of the global minimum at the total energy considered. This PES provides an example of how relaxation to a unique metastable minimum might occur, simply because of its greater kinetic accessibility. A similar behaviour is seen for some proteins from the serpin family of protease inhibitors[282]; the protein plasminogen activator inhibitor-1 first folds to the active state, but then on a time scale of hours can spontaneously transform to an inactive latent form[154,283].

The above PES bears some resemblance to the 38-atom and 75-atom Lennard-Jones clusters, for which the low energy icosahedral minima are reached on relaxation down the PES, rather than the fcc or decahedral global minimum[73,89]. The difficulty in reaching the global minima is associated with the narrowness of the funnels leading down to the global minima. Our results also suggest that it would not be so surprising if it was effectively impossible to reach the global minimum of the 75-atom cluster by a dynamic method without biasing the system towards decahedral minima. These clusters, though, have an additional complication compared to our model PES. The free energy global minimum depends on temperature, and only at low temperatures does it actually correspond to the global potential energy minimum. This is because of the greater configurational entropy of the minima at the bottom of the icosahedral funnel (§2.4).

5.5 Summary

In this chapter we have analysed model PES's of increasing complexity using a master equation approach. The existence of a suitable order parameter for these surfaces has enabled us to identify features which affect the relaxation efficiency to the global minimum by considering Landau entropies and free energies. For a surface with a single funnel relaxation is fastest when the potential energy gradient towards the bottom of the funnel is large and the barrier heights are small.

Our simplest model surface appears to capture many of the most interesting features of the dynamical effects seen in clusters and proteins. Our results are also consistent with previous work framed within the language of spin-glass theory; for example increasing the barrier heights raises the glass temperature, T_g, without changing the folding temperature, T_f, and hence decreases the efficiency of relaxation to the global minimum.

We have also modelled kinetic bottlenecks and surfaces with multiple funnels. Multiple funnels can greatly reduce the relaxation efficiency and produce dynamics with both fast and slow time scales. In contrast the effects of kinetic bottlenecks appear to be more limited.

Our interest in this problem was first stirred by work which stressed the importance of the energy gap between the lowest and the next-lowest energy minima on the folding efficiency of model proteins. There immediately appeared to be an obvious analogy with 'magic number' clusters such as the Mackay icosahedron, which are found in simulations and molecular beam experiments. Indeed, one could push the analogy further and consider magic number clusters as those which have survived a selection procedure in a molecular beam, just as proteins have apparently evolved to possess efficient 'funneling' PES's. However, it now appears that factors other than the lowest energy gap are more important. Nevertheless, the analogies between 'magic number' clusters in molecular beams and rapidly folding proteins are probably still valid and will continue to lead to new insights in the global analysis of PES's in terms of the interplay between structure, function, dynamics and thermodynamics.

Chapter 6
Characterizing the Topography of a Potential Energy Surface

6.1 Introduction

As the dynamical behaviour of a system is determined by the PES, characterization of the topography and topology of the PES is a prerequisite for understanding the dynamics. For example, to apply the master equation approach that we used for our model PES's in the previous chapter, one would need a complete sample of minima and transition states on the PES. Such sampling is only possible for very small clusters (up to $N \approx 13$) because of the exponential increase in the number of minima with size[64,65,162]. For larger clusters one would need some way to statistically characterize the PES in order to compensate for the incompleteness of any sample of stationary points. This would be akin to the method we used in §3.4 to reproduce the thermodynamics from an incomplete sample of minima.

Here we use the eigenvector-following method to obtain a comprehensive characterization of the M_{13} PES and its dependence on the range parameter, ρ_0 (§6.3), and to provide some typical downhill pathways for LJ clusters (§6.4). These surveys of the PES allow qualitative predictions of the effects of the range on the dynamics, and insight into the known relaxation behaviour of LJ clusters. Quantitative predictions await the application of the master equation method.

6.2 Traversing the Potential Energy Surface

The eigenvector-following technique[88] can find transition states on a PES by maximizing the energy along a chosen eigenvector of the Hessian whilst simultaneously minimizing the energy along all other eigenvectors. Once a transition state is located, the minima it connects can be found by taking small initial steps away from the stationary point along the eigenvector of the Hessian corresponding to the unique negative eigenvalue (in both the positive and negative directions) and then performing minimizations.

The technique we use to comprehensively search the PES is simple. From a starting minimum we search for transition states along the n_{ev} eigenvectors with the lowest eigenvalues in both positive and negative directions, and add the new minima that are connected by these transition states to our set of minima. We then repeat this process for all minima until until no new minima are found. The larger the value of n_{ev} (maximum $3N-6$), the more comprehensive the search will be. However, even using the maximum value of n_{ev} there is no guarantee that this approach will find all the minima on the PES. The method has been previously used to generate large samples of minima and transition states for small LJ clusters[162].

The second method we use involves a Monte Carlo walk between connected minima. First, from a starting minimum we randomly choose an eigenvector along which to search for a transition state; this choice is weighted towards those with lower eigenvalues, because a search along an eigenvector with a low eigenvalue generally converges to a transition state more rapidly. Once a transition state is found, we identify the minima it connects. Eigenvector-following occasionally finds a transition state unconnected to the original minimum, and so we check that the original minimum is at one end of the rearrangement pathway.

Having found a connected minimum, a decision whether to accept the step must then be taken. Here, we choose a Metropolis step criterion, which accepts moves with a probability of $\min[1, \exp(-\Delta E/kT)]$, where ΔE is the change in energy associated with the step[284]. There are many other possible step criteria that could be used. For example, the probability of acceptance could be related to the transition rate as calculated using RRKM theory, and so could be used to simulate the dynamics of the real cluster (assuming the density of states of the minimum and transition state could be calculated accurately). Once the decision to accept the step has been made the whole process is repeated, and a new transition state search is started. A record is kept of each transition state search, so that if the same step is attempted the search does not need to be repeated.

Techniques that search the PES by taking steps in configuration or phase space are hindered at low temperatures by the time scale separation between interwell and intrawell motion; this leads to trapping in local minima. Our method avoids this problem by removing the vibrational motion altogether.

To analyse the behaviour of our method further, the concept of a basin introduced by Kunz and Berry is useful[253,254]. These authors defined a basin as a set of connected minima that belong to sequences of minima which are monotonically decreasing in energy and which lead down to the lowest energy minimum in the basin. (This definition overlaps somewhat with the concept of a funnel that is used in the protein folding literature and which we discussed in Chapter 4.) The global minimum is at the bottom of the primary basin. Basins have a similar role in this 'minima space' to that played by minima in configuration space. However, there are far fewer basins than minima on the PES. The time scale for interbasin flow is likely to be slower than for intrabasin flow between minima[253,254]. Therefore, sufficiently deep secondary basins (basins that do not end at the global minimum) can act as traps (§5.4.4).

If a Monte Carlo walk in the minima space is performed at zero temperature, the system is 'quenched' to the bottom of a basin. If the number of basins on the PES is not too large, we might expect that a quench from a random configuration might lead to the global minimum, especially as it is likely that the primary basin would have the largest catchment area. This suggests that these quenches may be a useful global optimization tool. If a low rather than a zero temperature is used, the method would be able to escape from shallow basins, whilst not significantly compromising the favourability of downhill moves.

6.3 The PES of the 13-atom Morse Cluster

As we have noted in our consideration of Morse clusters in earlier chapters, decreasing the range of the potential increases the ruggedness of the PES. This effect is particularly noticeable in the number of stationary points on the PES (Table 2.1). Here we hope to quantify these ideas further by analysing the topologies of the M_{13} PES in detail. Given the ubiquity of rugged energy landscapes in a diverse range of fields—spin glasses, superconductors, protein folding and optimization problems such as the infamous travelling salesman problem—the results may be of wide interest[285].

The samples of M_{13} stationary points were produced by the method described in the previous section. For ρ_0=3, 4, 6, 10 and 14 we used as our values of n_{ev} 15, 15, 6, 3 and 2, respectively. The decreasing number of eigenvectors searched at shorter range was necessary because of the escalating requirements for computer time and disk space to generate and store the data for such large samples of stationary points. Consequently, the incompleteness of the samples is likely to increase with

TABLE 6.1: Some average properties of the M_{13} stationary point samples at ρ_0=3, 4, 6, 10 and 14. $\overline{\nu}$ is the geometric mean frequency, n_{ts} is the number of geometrically distinct transition states connected to a minimum, n_{gm} is the number of steps in minima space along the shortest path to the global minimum, S_{gm} is the total length in configuration space of the shortest pathway to the global minimum, ω is the magnitude of the imaginary frequency of a transition state, S is the length of a single rearrangement pathway, D is the displacement in configuration space between two connected minima, γ is the moment ratio of displacement, b_d is the smaller (downhill) barrier height, b_u is the larger (uphill) barrier height, ΔE is the difference in energy between two connected minima ($b_u = b_d + \Delta E$), and n_{basin} is the number of basins on the PES. $\overline{\nu}$, n_{ts}, n_{gm} and S_{gm} are averages over all minima; ω, S, D and γ, are averages over all transition states; and b_d, b_u and ΔE are averages over all non-degenerate transition states.

	$\rho_0 = 3$	$\rho_0 = 4$	$\rho_0 = 6$	$\rho_0 = 10$	$\rho_0 = 14$
$h\overline{\nu}/\epsilon$	0.216	0.340	0.682	1.843	3.680
n_{ts}	4.89	8.26	11.54	8.04	8.52
n_{gm}	1.00	1.38	2.40	3.65	3.70
S_{gm}/r_0	2.597	3.079	3.884	3.952	3.770
$h\omega/\epsilon$	0.184	0.262	0.469	1.051	1.450
S/r_0	3.012	2.905	1.874	1.119	1.083
D/r_0	1.607	1.477	1.169	0.842	0.819
b_d/ϵ	0.114	0.483	0.545	0.585	0.786
b_u/ϵ	4.512	3.693	2.087	1.473	1.540
$\Delta E/\epsilon$	4.398	3.210	1.542	0.888	0.786
$13/\gamma$	7.161	5.269	4.748	5.051	4.889
n_{basin}	1	1	3	54	262

ρ_0 and be greater for the transition states than minima. The size of the samples is given in Table 2.1 and some of the average properties are catalogued in Table 6.1. Some properties have a fairly simple dependence on ρ_0. For example, the increase in the mean vibrational frequency as the range decreases correlates with the increased curvature of the pair potential at its minimum (Figure 2.2).

More interesting are those properties that give insight into the global topography of the PES. As can be seen from Figure 4.4 the energy gap between the global minimum, the 13-atom icosahedron, and the other low-lying minima decreases as ρ_0 is increased. This flattening of the surface is also apparent in the average values of ΔE, the difference in energy between two connected minima; ΔE is effectively

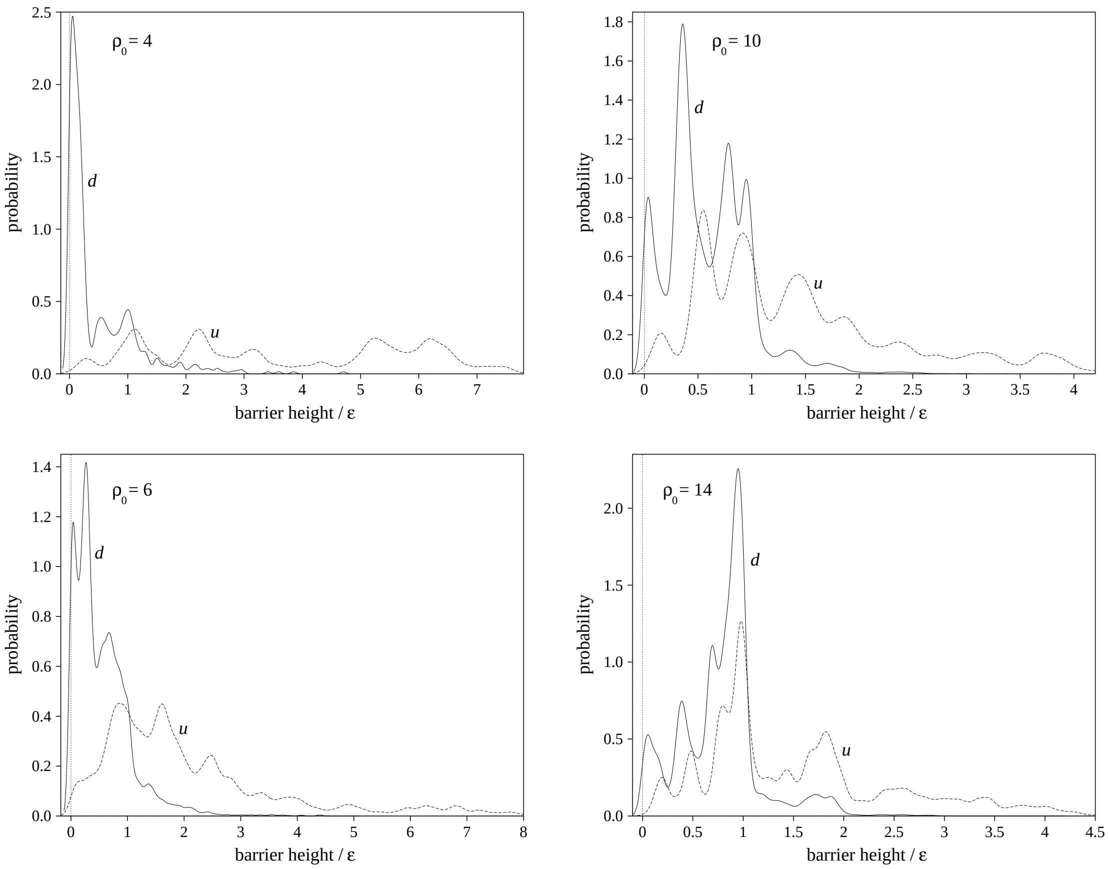

FIGURE 6.1: Probability distributions of the barrier heights of uphill (dashed line) and downhill (solid line) rearrangements for M_{13} at ρ_0=4, 6, 10 and 14, as marked. Transition states mediating degenerate rearrangements have been excluded from the samples.

a local measure of the slope of the PES.* The averages of the barrier heights show that the barrier to go downhill (b_d) increases with ρ_0. At ρ_0=4, the probability distribution of b_d is dominated by the low barrier peak (Figure 6.1), but as ρ_0 increases the magnitude of this peak diminishes. The greater similarity between the distributions for b_d and b_u at larger ρ_0 is a reflection of the smaller value of ΔE. We expect, based on the results of Chapter 5, that the combined effect of the larger downhill barriers and the flatter PES will be to make relaxation to the global minimum more difficult at shorter range.

In a comparison of the topographies of Lennard-Jones and potassium chloride clusters, it was noted that the rearrangements for potassium chloride clusters were

*For the distributions and averages of b_d, b_u and ΔE the degenerate rearrangements (that join permutational isomers of the same minimum) are excluded from the sample because they contain no information about structural relaxation, and simply obscure the changes to the topology of the PES. The fraction of transition states that mediate degenerate rearrangements varies from 38% for ρ_0=3 to 1% for ρ_0=14.

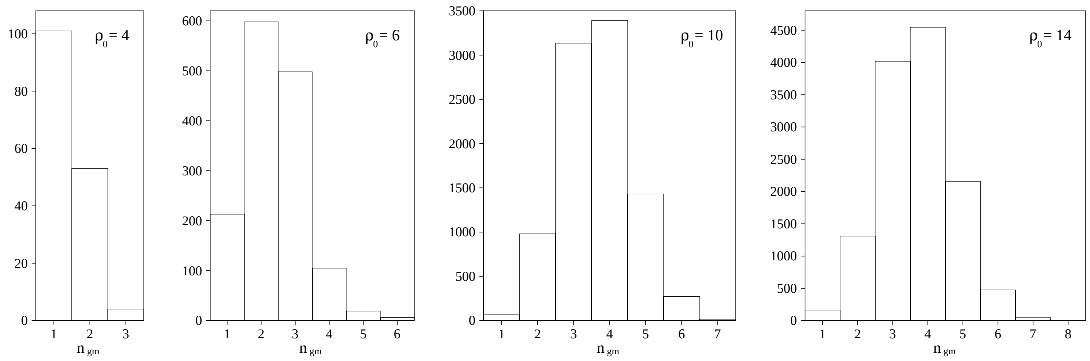

FIGURE 6.2: Histograms of n_{gm}, the number of steps a minimum is away from the global minimum, for M_{13} at ρ_0=4, 6, 10 and 14, as marked.

much more cooperative[252]. It was suggested that this might have been one of the reasons for the greater ease with which the potassium chloride clusters could reach the global minimum. The moment ratio of displacement, γ, can be used to measure the cooperativity of a rearrangement. It is defined by[286]

$$\gamma = \frac{N \sum_i \left[Q_i(s) - Q_i(t)\right]^4}{\left(\sum_i \left[Q_i(s) - Q_i(t)\right]^2\right)^2}, \tag{6.1}$$

where $Q_i(s)$ is the value of the nuclear Cartesian coordinate Q_i for minimum s, etc. γ was evaluated using the relative positions of the two minima at the end-points. If only a single atom moves then $\gamma = N$ and the rearrangement is strongly localized, while if all atoms move through the same distance then $\gamma = 1$ and the process is completely cooperative. N/γ therefore can be interpreted as the number of atoms involved in the rearrangement. Somewhat surprisingly, apart from the greater cooperativity at ρ_0=3, γ does not depend significantly on the range of the potential (Table 6.1). This is in contrast to a study which compared rearrangements of LJ_{55} and $(C_{60})_{55}$ clusters, which found that cooperative rearrangements were much less likely for $(C_{60})_{55}$ clusters[90]. This difference may reflect the fact that the structure of small clusters is less dependent on the range than for larger clusters.

The shortest reaction pathway to the global minimum was calculated for each minimum on the PES. If we look at n_{gm}, the number of steps between minima along one of these pathways, it is clear that n_{gm} increases as the range decreases (Figure 6.2). At ρ_0=3 all the minima are directly connected to the global minimum, yet at ρ_0=14, a minimum can be as far as eight steps away. The n_{gm} histograms also show that the connectivity patterns for the M_{13} PES are quite different from the standard model PES that we considered in Chapter 5 for which the number of minima increased exponentially with the number of steps away from

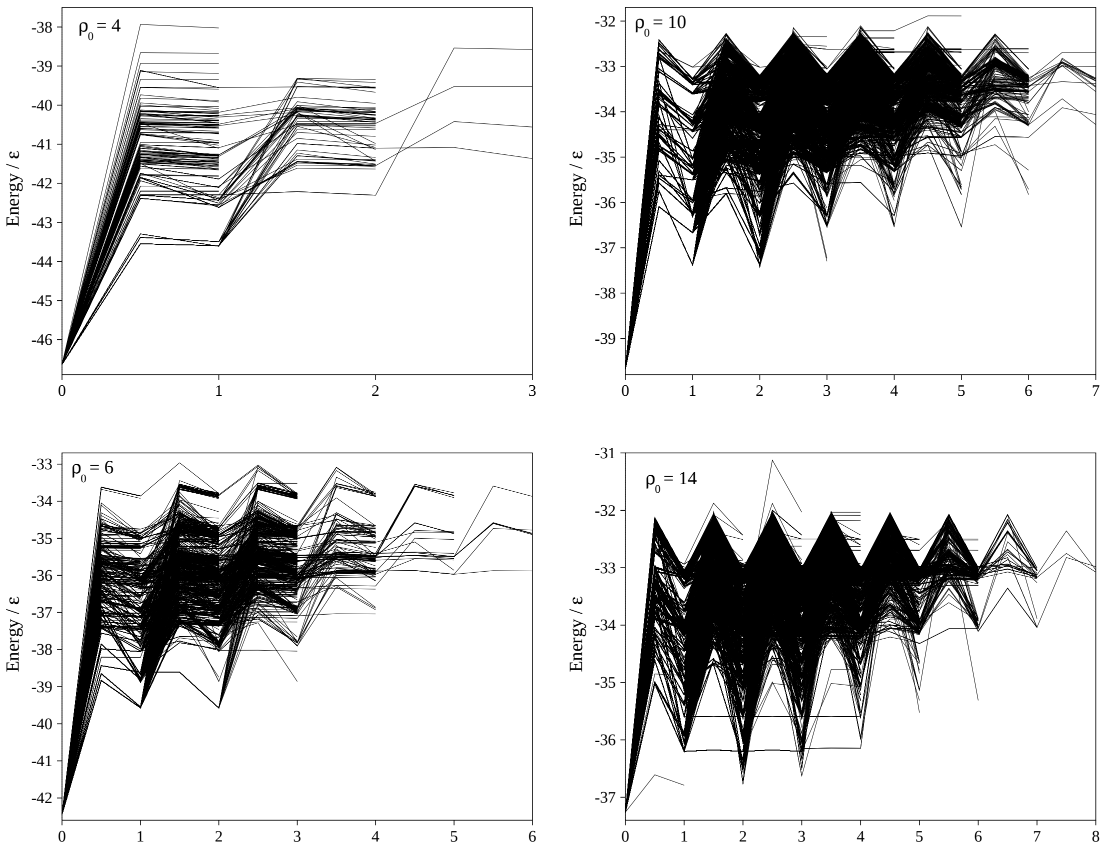

FIGURE 6.3: Shortest pathways to the global minimum for each minimum of M_{13} at ρ_0=4, 6, 10 and 14 as marked. The reaction coordinate is the number of steps away from the global minimum. Half integer values correspond to transition states.

the global minimum. It is also interesting to note the large number of minima that are directly connected to the global minimum. For example, at ρ_0=6 we found 568 geometrically distinct transition states which connect the icosahedron to 213 geometrically distinct minima. If one takes into account the reaction path degeneracy, the number of transition states surrounding a single permutational isomer of the icosahedron is at least 67 836.

In Figure 6.3, we show the shortest reaction path to the global minimum for each minimum. Again the larger barrier heights and the increased flatness of the PES are apparent at short range. At ρ_0=14 there are clearly some pathways for which the minima do not monotonically decrease in energy as the global minimum is approached. This will be considered further when we examine the basin structure of the PES.

Although n_{gm} increases with ρ_0 the average total length of the reaction paths in configuration space (S_{gm}) is relatively constant for $\rho_0 \geq 6$, and for smaller ρ_0

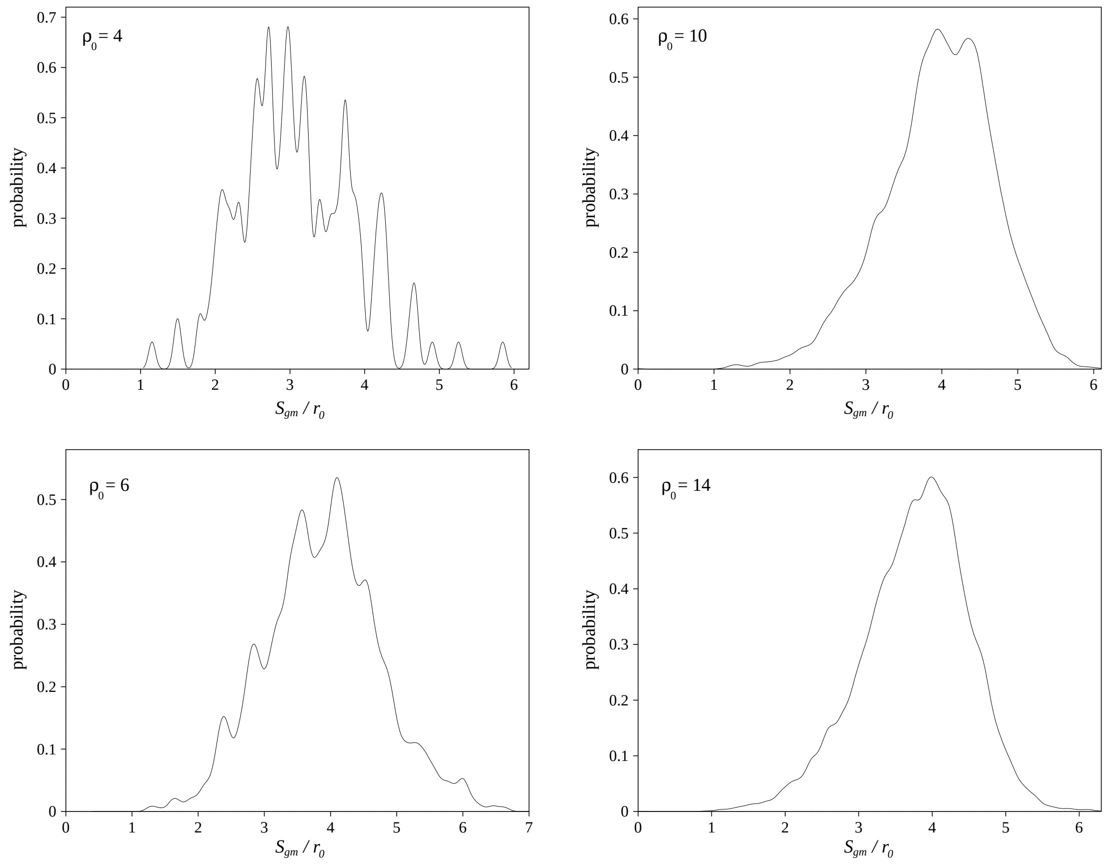

FIGURE 6.4: Probability distributions of S_{gm}, the length of the shortest pathway from a minimum to the global minimum, for M_{13} at ρ_0=4, 6, 10 and 14 as marked.

shows a much weaker dependence on the range than n_{gm} (Table 6.1 and Figure 6.4). This is not too surprising if we consider the dependence of the path length for a single rearrangement on ρ_0: this length decreases significantly as the range is reduced (Figure 6.5). The pathways simply become more rugged rather than longer: more transition states must be crossed.

The topology of the surface was further analysed in terms of the structure of the basins on the PES. For ρ_0=3 and 4, every minimum lies on a sequence of minima which are monotonically decreasing in energy and lead down to the global minimum; the PES consists of a single basin. For ρ_0=6 all but two of the minima lie on such monotonic sequences. By Kunz and Berry's definition these two minima also represent basin bottoms, albeit very shallow; only one step needs to be taken to reach a minimum in the basin surrounding the icosahedron. For ρ_0=10 and 14 many more shallow basins appear on the PES (Table 6.1). Despite this increase in the number of basins, 96.8% of the minima located are in the icosahedral basin for ρ_0=14 (Figure 6.6e).

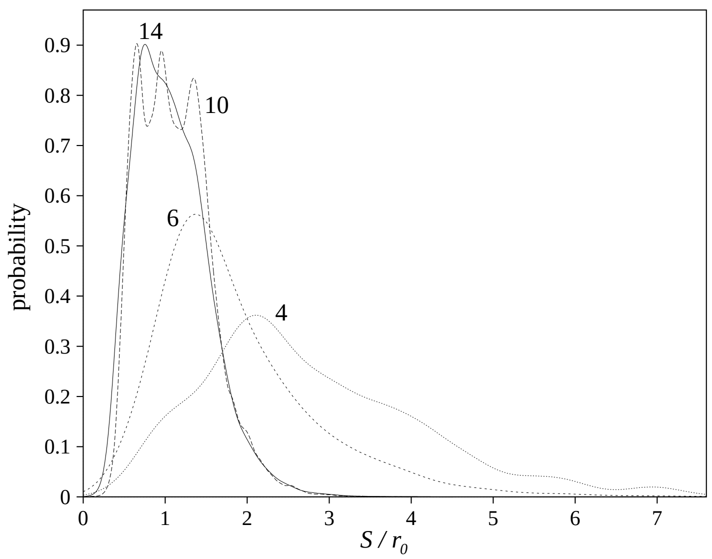

FIGURE 6.5: Probability distributions of S, the length of a single rearrangement pathway, for the transition states of M_{13} at ρ_0=4, 6, 10 and 14 as marked.

One consequence of the definition of a basin is that it is possible for a minimum to lie on monotonic sequences which lead down to the bottom of different basins. Indeed high energy minima may lie in numerous basins (Figure 6.6f). In this regard the division of minima space into basins differs from the division of configuration space into wells surrounding minima, since there is no equivalent of the steepest descent path which uniquely maps each point in configuration space to a minimum. Instead the division of minima space is more like a Venn diagram where overlap can occur between regions.

One method to analyse this basin structure is with ‘tree’ diagrams (Figure 6.6); these are in some ways similar to the equilibration trees considered in Chapter 5. Two basins are considered to become ‘connected’ and to form a new metabasin when the energy is that of the lowest energy minimum which lies in both basins. Each point in the tree diagram represents a basin or the creation of a new metabasin, and the nodes occurs at the energies at which the basins or metabasins become connected. The tree diagrams, therefore, follow the pattern of connections that occurs between basins and metabasins as the energy is increased.

It is noticeable that in the tree diagrams virtually all the basins are directly connected to the line corresponding to the metabasin of the global minimum, i.e. the basin which requires least energy to enter is the metabasin of the global minimum. The basin surrounding the global minimum is clearly the dominant feature even on the more rugged PES’s for ρ_0=10 and 14. Furthermore, many of

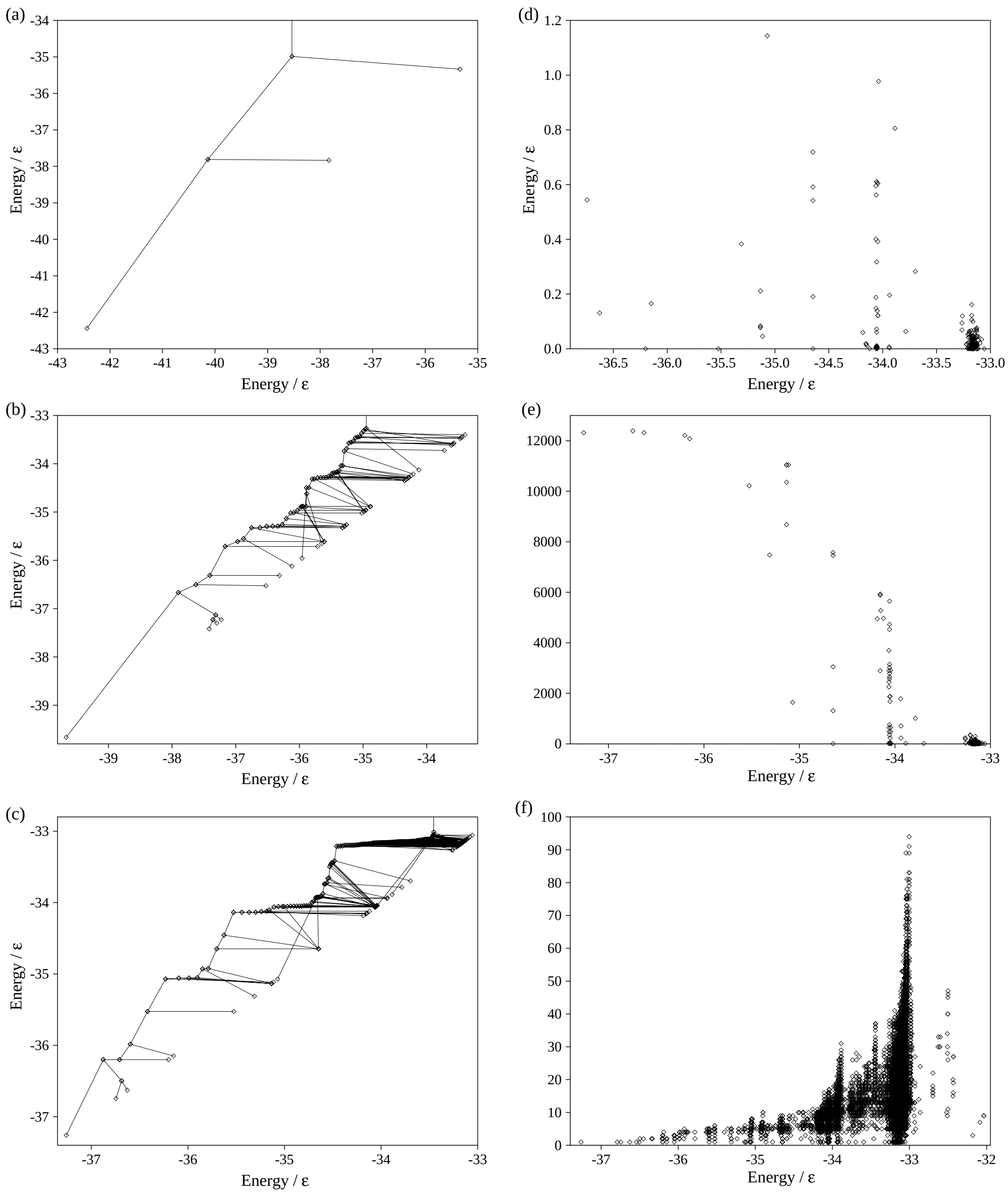

FIGURE 6.6: 'Tree' diagrams showing the basin structure for M_{13} at (a) ρ_0=6, (b) ρ_0=10, and (c) ρ_0=14. The endpoints are at the energies of the minima at the bottoms of the basin. Nodes occur when two basins or metabasins become connected; The y coordinate of the node corresponds to the energy of the lowest energy minimum which lies in both (meta)basins, and the x coordinate to the average energy of the all the basin bottoms in the resulting metabasin. Scatter plots of (d) the energy (relative to the bottom of a basin) of the lowest energy minimum which is in both the basin concerned and a lower energy basin against the basin energy, (e) the number of minima in a basin against the basin energy and (f) the number of basins a minimum belongs to against the energy of the minimum for M_{13} at ρ_0=14

the lines joining a basin to the icosahedral basin are virtually horizontal implying that the depth of most basins (measured in terms of the energy, relative to the basin bottom, of the lowest energy minimum that is also in another basin) is small (Figure 6.6d). The average depths for ρ_0=10 and 14 are 0.237 and 0.067 ϵ, respectively. Most of the basins are not sufficiently deep to act as effective traps. The lower average depth for ρ_0=14 results from the large number of very shallow basins at high energy; 163 of the 262 basins lie above $-33.5\,\epsilon$.

Although the PES's at ρ_0=10 and 14 involve a large number of basins, these PES's do not equate with the multiple funnel scenarios outlined in §5.4 since the basins are too shallow for them to be categorized as separate funnels. However, their roughness is still likely to hinder relaxation to the global minimum, even if not to as large an extent as multiple funnels.

6.4 Pathways for Lennard-Jones Clusters

Our second method for surveying the PES has been applied to LJ_{13}, LJ_{38} and LJ_{55}. For the 13- and 55-atom clusters the global minima are Mackay icosahedra. We also chose to study LJ_{38} because, unusually for small clusters, it does not have an icosahedral global minimum but instead an fcc truncated octahedron (structure 38D of Chapter 2) is lowest in energy[70,71]. This cluster therefore represents a relatively difficult test for a global optimization method.

The energy profiles for typical low temperature quenches in minima space performed from random starting configurations are shown in Figure 6.7 for the three clusters. The quenches for the 13-atom cluster typically find the icosahedral global minimum in three or four accepted steps. This is not surprising given the relative simplicity of the PES; the number of minima on the surface[162] is probably of the order of 1500 and none of the minima are more than four steps away from the global minimum.[†]

The quenches for LJ_{55} also find the global minimum, although the pathway and the number of steps is inevitably larger because of the increased system size. Still it is a remarkable feature of this PES that the global minimum is so easy to find considering there are probably of the order of 10^{21} minima on the PES. In the last part of the pathway shown in Figure 6.7c the cluster finds the Mackay icosahedron in two steps from a low energy liquid-like minimum, rather than by

[†]This result is based upon an analysis of the LJ_{13} PES similar to that performed for M_{13} in §6.3. Using n_{ev}=15, 1467 minima and 12 435 transition states were found.

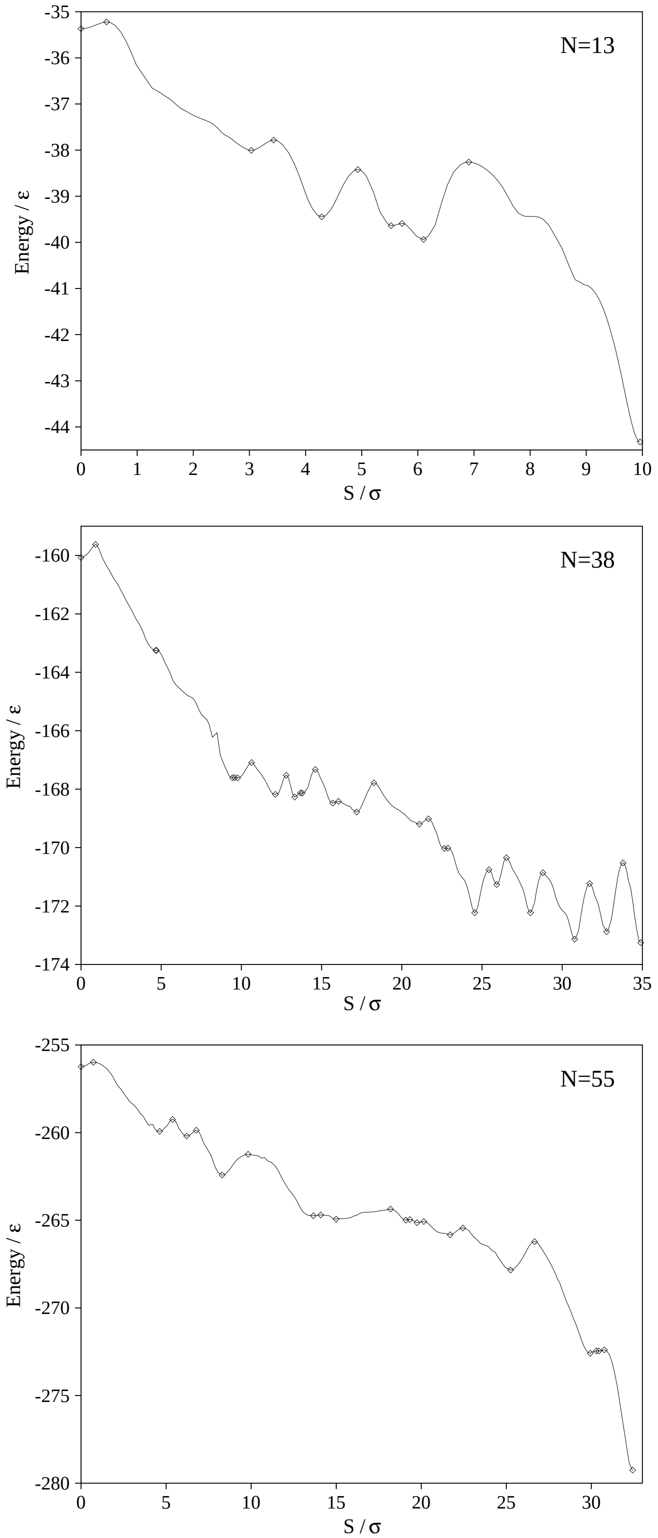

Figure 6.7: Reaction profiles of typical downhill pathways from a random minimum to the lowest energy icosahedral minimum for LJ_{13}, LJ_{38} and LJ_{55}. Stationary points are denoted by diamonds. S is the integrated path length along the reaction pathway[90]

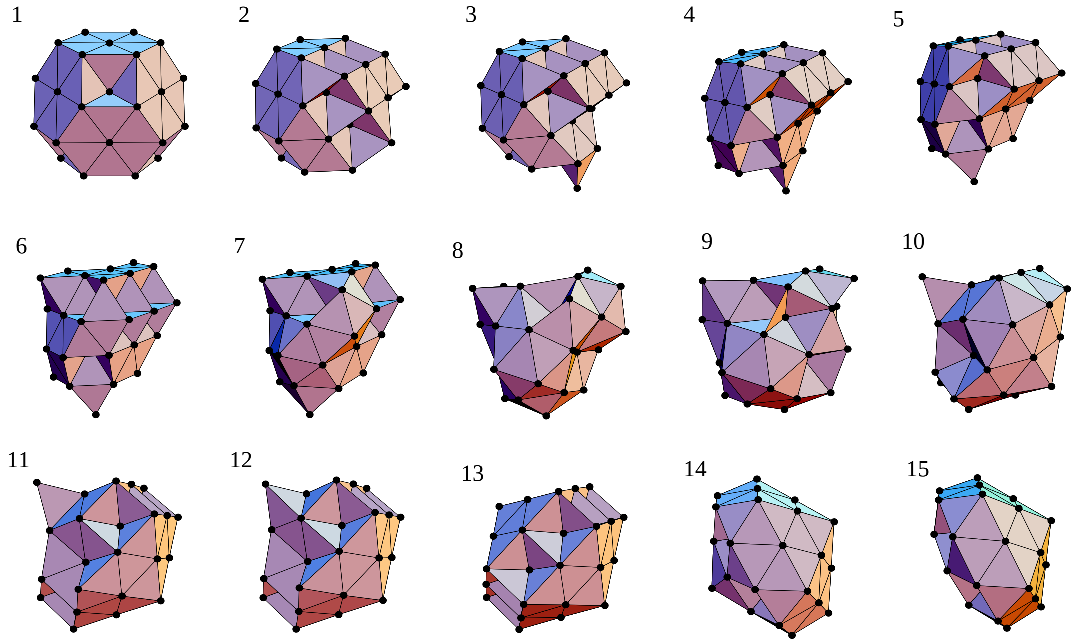

FIGURE 6.8: Minima on the LJ_{38} pathway from the truncated octahedron to the lowest energy icosahedral minimum. The minima are numbered by their position along the pathway

passing through defective Mackay icosahedra as was observed for some of the other pathways.

For LJ_{38} the system never finds the fcc global minimum but instead the quenches always lead into the basin of icosahedral minima and down to the lowest energy icosahedral minimum (structure 38E of Chapter 2). Although this represents a failure of the method as a global optimization tool, it provides us with some interesting information about the topography of the PES. It seems that the basin containing the icosahedral minima is much more easily accessed from higher energy minima than the basin leading down to the fcc minima. This is probably a result of the greater structural similarity between the icosahedral structures and the liquid that we discussed in §4.4.

One difference between the quench pathway for LJ_{38} and that of the other two clusters is that in the last stages of the pathway the system has to search through the low energy icosahedral isomers. The bottom of the icosahedral basin is flatter than for LJ_{13} and LJ_{55}, both of which have global minima that are significantly lower in energy than the next lowest energy minimum, making the last stages of global optimization easier. For comparison, the energy gaps between the lowest energy icosahedral minima are $2.644\,\epsilon$, $0.118\,\epsilon$ and $2.855\,\epsilon$ for LJ_{13}, LJ_{38} and LJ_{55},

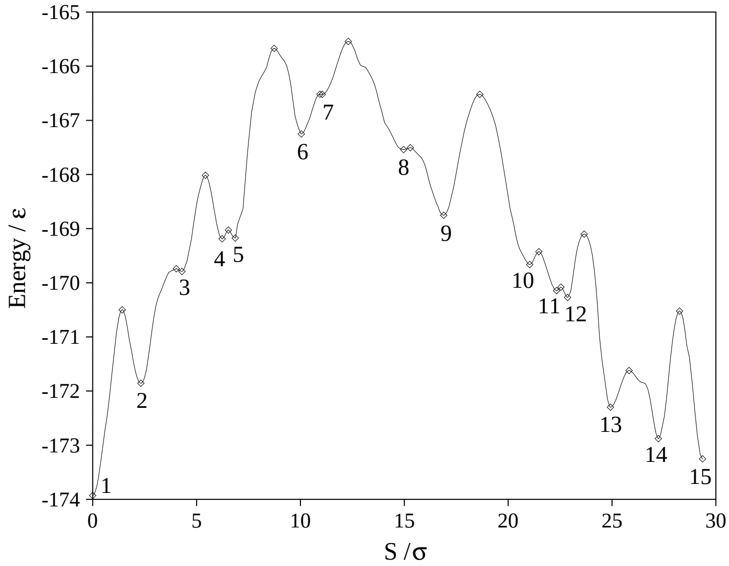

FIGURE 6.9: Reaction profile of a pathway on the LJ_{38} PES from the truncated octahedron to the lowest energy icosahedral minimum. Stationary points are denoted by diamonds. The minima are numbered by their position along the pathway

respectively.

As for M_{75} at ρ_0=6 (§2.4), it may be that the 38-atom truncated octahedron is the free energy global minimum only at low temperature. If this is the case, we would expect a high temperature Monte Carlo walk in minima space starting from the truncated octahedron to escape from the fcc basin and pass into the icosahedral basin, and this is indeed what we observed. The length of the initial pathway between the two lowest energy structures produced by this method was about $100\,\sigma$. However, by performing quenches on either side of the barrier, the pathway was significantly shortened. The resulting pathway is illustrated in Figures 6.8 and 6.9. The LJ_{38} PES clearly has similarities to some of the multiple funnels scenarios considered in §5.4.4. From the cross-section (Figure 6.9) it does appear that the basin surrounding the truncated octahedron is narrower than the icosahedral basin, which is what would be expected given the propensity for LJ_{38} to go into the icosahedral basin on relaxation.

In the structural transformation the truncated octahedron initially undergoes a series of rearrangements that take it to the high energy hexagonal close-packed minimum 6. This structure then collapses to a polytetrahedral structure typical of the liquid-like state, which becomes more and more ordered until it reaches the decahedral structure 11. After two localized rearrangements, the decahedral minimum 13 is then converted to an icosahedral minimum by a multiple square-diamond process in which one half of the structure is rotated by $\pi/5$ about the decahedral axis.

In electron microscopy studies of metal clusters supported on a surface, transformations are often observed between icosahedral, decahedral and fcc structures[1]. The pathway we have found here, although for a cluster much smaller than those observed experimentally, is probably fairly typical of the complex series of rearrangements and high energy barriers that need to be overcome to move between ordered structures with different morphologies.

Chapter 7
Conclusions

In this thesis I have attempted to relate the structural, thermodynamic and dynamic behaviour of simple atomic clusters to the underlying PES and the form of the potential. This has led to the following accomplishments:

- I have created a comprehensive structural database cataloguing the effects of the range of the potential. It should provide candidate structures for comparison with the indirect structural information available from experimental studies of clusters in molecular beams, and for theoretical studies using computationally expensive methods for which comprehensive searches of the PES are not feasible.* It is also an ideal system to benchmark global optimization methods.

- I have developed a statistical method which can accurately reproduce the thermodynamic properties of clusters from a sample of minima, and which provides insight into the respective roles of different regions of configuration space.

- I have provided a microscopic understanding for the destabilization of the liquid phase that occurs for short-ranged potentials.

- I have shown that the structure of the liquid-like state of small clusters has many of the characteristics of the bulk liquid, and that this structure evolves through a rapid increase in the disclination density with size.

- I have suggested an explanation for the transition from electronic to geometric magic numbers observed in mass spectroscopic studies of sodium clusters.

*For this purpose, the points files of all the global minima will soon be made available on the world wide web at URL <http://brian.ch.cam.ac.uk/ jon/jon.html>

- I have characterized some of the features of a model PES which play key roles in aiding or hindering relaxation to the global minimum.

The work presented here also suggests a considerable number of applications, extensions and fresh challenges. As is often the case, the more we know the more we realize our ignorance.

- The predictions for the structure of neutral clusters of C_{60} molecules presents both a challenge to experiment to probe the neutrals through techniques, such as electron diffraction, and a challenge to theory to quantitatively understand the differences between neutral and charged clusters.

- The range of applicability of the superposition method could be extended by incorporating a 'multi-histogram' approach to combine the information from samples of minima produced by systematic quenching at different energies.

- There are many possible extensions to the work relating the dynamics to the PES, since this field is, in many ways, still in its infancy. There is the application of the master equation method to the M_{13} data that we have obtained, and the development of statistical methods to accurately model the dynamics when only an incomplete sample of stationary points is available, as is inevitable for all but the smallest sizes. In this thesis, the aspect of the dynamics upon which I have focussed most attention is relaxation to the global minimum, but there are many other possible research avenues. One area of particular promise is the dynamical properties of supercooled liquids[287,288], including such topics as self-diffusion and the structural origins of the α and β mechanisms of relaxation[272,289].

- The unusual structural (Chapter 2), thermodynamic (§2.4) and dynamic (§6.4) properties of LJ_{38} and LJ_{75} make them particularly attractive cases for more detailed study. Such an investigation could provide insights into why global optimization methods can fail, and possibly even suggest improvements to these methods to help circumvent such difficulties.

Although this thesis has concentrated on the properties of clusters, the ubiquity of PES's means that some of the ideas contained here are relevant to a much wider domain. For example, in Chapter 5, I attempted to make detailed connections between the behaviour of clusters, proteins and glasses. Furthermore, I hope the allusions and asides to seemingly unrelated subjects, such as polytopes in 4D space, the optimal shapes of the bubbles in an idealized head of beer and the heptagonal barrel-shaped chaperones that assist the folding of proteins, have illustrated the rich and interdisciplinary nature of research into clusters. Moreover, I hope this thesis has shown the utility of simple models that capture aspects of the essential physics in providing a framework for understanding a diverse range of behaviour. Indeed, the complexity that emerges from these simple models is quite remarkable. Do complex systems, such as these, herald, as some have suggested, the dawn of a post-reductionist science? Certainly, a cluster is much more than just a collection of atoms.

References

[1] L. D. Marks, Rep. Prog. Phys. **57**, 603 (1994).

[2] G. Schmid, V. Maihack, F. Lantermann and S. Peschel, J. Chem. Soc., Dalton Trans. 589 (1996).

[3] G. M. Francis, I. M. Goldby, L. Kuipers, B. von Issendorf and R. E. Palmer, J. Chem. Soc., Dalton Trans. 665 (1996).

[4] M. Faraday, Phil. Trans. R. Soc. Lond. **147**, 145 (1857).

[5] G. Schmid, Chem. Rev. **92**, 1709 (1992).

[6] T. S. Ahmadi, Z. L. Wang, T. C. Green, A. Henglein and M. A. El-Sayed, Science **272**, 1924 (1996).

[7] R. L. Whetten, J. T. Khoury, M. M. Alvarez, S. Murty, I. Vezmar, Z. L. Wang, P. W. Stephens, C. L. Cleveland, W. D. Luedtke and U. Landman, Adv. Mater. **8**, 428 (1996).

[8] J. Jortner, Z. Phys. D **24**, 247 (1992).

[9] J. Frenkel, *Kinetic Theory of Liquids*, Dover (1955).

[10] D. J. McGinty, J. Chem. Phys. **55**, 580 (1971).

[11] J. J. Burton, J. Chem. Soc., Faraday Trans. **69**, 540 (1973).

[12] J. K. Lee, J. A. Barker and F. F. Abraham, J. Chem. Phys. **58**, 3166 (1973).

[13] L. S. Bartell, J. Phys. Chem. **99**, 1080 (1995).

[14] S. H. Tolber and A. P. Alivisatos, Annu. Rev. Phys. Chem. **46**, 595 (1995).

[15] M. Boudart, Nature **372**, 320 (1994).

[16] Z. Xu, F.-S. Xiao, S. K. Purnell, O. Alexeev, S. Kawi, S. E. Deutsch and B. C. Gates, Nature **372**, 346 (1994).

[17] K. Liu, J. D. Cruzan and R. J. Saykally, Science **271**, 929 (1996).

[18] K. Liu, M. G. Brown, C. Carter, R. J. Saykally, J. K. Gregory and D. C. Clary, Nature **381**, 6582 (1996).

[19] D. J. Wales, J. Am. Chem. Soc. **115**, 11180 (1993).

[20] Z. Bačić and R. E. Miller, J. Phys. Chem. **100**, 12945 (1996).

[21] C. Guillame, J. Le Calvé, I. Dimicoli and M. Mons, J. Phys. Chem. **98**, 13443 (1994).

[22] Q. Liu, J.-K. Wang and A. H. Zewail, Nature **364**, 427 (1993).

[23] S. K. Kim, J. J. Breen, D. M. Willberg, L. W. Peng, A. Heikal, J. A. Syage and A. H. Zewail, J. Phys. Chem. **99**, 7421 (1995).

[24] A. A. Heikal, S. H. Chong, J. S. Baskin and A. H. Zewail, Chem. Phys. Lett. **242**, 380 (1995).

[25] M. Hartmann, R. E. Miller, J. P. Toennies and A. F. Vilesov, Phys. Rev. Lett. **75**, 1566 (1995).

[26] M. Hartmann, R. E. Miller, J. P. Toennies and A. F. Vilesov, Science **272**, 1631 (1996).

[27] C. L. Cleveland and U. Landman, Science **257**, 355 (1992).

[28] T. Raz and R. D. Levine, J. Am. Chem. Soc. **116**, 11167 (1994).

[29] T. Raz and R. D. Levine, Chem. Phys. Lett. **246**, 405 (1995).

[30] W. D. Luedtke and U. Landman, Phys. Rev. Lett. **73**, 569 (1994).

[31] H. Haberland, Z. Insepov and M. Moseler, Phys. Rev. B **51**, 11061 (1995).

[32] R. F. Service, Science **271**, 920 (1996).

[33] H.-P. Cheng and U. Landman, Science **260**, 1304 (1993).

[34] A. P. Alivisatos, Science **271**, 933 (1996).

[35] A. P. Alivisatos, J. Phys. Chem. **100**, 13226 (1996).

[36] S. A. Harfenist, Z. L. Wang, M. M. Alvarez, I. Vezmar and R. L. Whetten, J. Phys. Chem. **100**, 13904 (1996).

[37] C. A. Mirkin, R. L. Letsinger, R. C. Mucic and J. J. Storhoff, Nature **382**, 607 (1996).

[38] A. P. Alivisatos, K. P. Johnsson, X. Peng, T. E. Wilson, C. J. Loweth, M. P. Bruchez and P. G. Schultz, Nature **382**, 609 (1996).

[39] S. J. Riley, in *Clusters of atoms and molecules II*, edited by H. Haberland, p. 221, Springer-Verlag, Berlin (1994).

[40] S. E. Apsel, J. W. Emmert, J. Deng and L. A. Bloomfield, Phys. Rev. Lett. **76**, 1441 (1996).

[41] M. R. Hoare and P. Pal, Nature (Physical Science) **236**, 35 (1972).

[42] A. L. Mackay, Acta Cryst. **15**, 916 (1962).

[43] J. Farges, M. F. de Feraudy, B. Raoult and G. Torchet, J. Chem. Phys. **78**, 506 (1983).

[44] J. Farges, M. F. de Feraudy, B. Raoult and G. Torchet, J. Chem. Phys. **84**, 3491 (1986).

[45] J. Farges, M. F. de Feraudy, B. Raoult and G. Torchet, Adv. Chem. Phys. **70**, 45 (1988).

[46] J. W. Lee and G. D. Stein, J. Phys. Chem. **91**, 2450 (1987).

[47] O. Echt, K. Sattler and E. Recknagel, Phys. Rev. Lett. **47**, 1121 (1981).

[48] I. A. Harris, R. S. Kidwell and J. A. Northby, Phys. Rev. Lett. **53**, 2390 (1984).

[49] I. A. Harris, K. A. Norman, R. V. Mulkern and J. A. Northby, Chem. Phys. Lett. **130**, 316 (1986).

[50] J. A. Northby, J. Chem. Phys. **87**, 6166 (1987).

[51] T. D. Klots, B. J. Winter, E. K. Parks and S. J. Riley, J. Chem. Phys. **92**, 2110 (1990).

[52] T. D. Klots, B. J. Winter, E. K. Parks and S. J. Riley, J. Chem. Phys. **95**, 8919 (1991).

[53] T. P. Martin, T. Bergmann, H. Göhlich and T. Lange, Chem. Phys. Lett. **172**, 209 (1990).

[54] T. P. Martin, T. Bergmann, H. Göhlich and T. Lange, Chem. Phys. Lett. **176**, 343 (1991).

[55] T. P. Martin, U. Näher, T. Bergmann, H. Göhlich and T. Lange, Chem. Phys. Lett. **183**, 119 (1991).

[56] M. Pellarin, B. Baguenard, J. L. Vialle, J. Lermé, M. Broyer, J. Miller and A. Perez, Chem. Phys. Lett. **217**, 349 (1994).

[57] O. Echt, O. Kandler, T. Leisner, W. Miehle and E. Recknagel, J. Chem. Soc., Faraday Trans. **86**, 2411 (1990).

[58] T. P. Martin, U. Näher, H. Schaber and U. Zimmermann, Phys. Rev. Lett. **70**, 3079 (1993).

[59] P. A. Braier, R. S. Berry and D. J. Wales, J. Chem. Phys. **93**, 8745 (1990).

[60] I. Bytheway and D. L. Kepert, J. Math. Chem. **9**, 161 (1992).

[61] D. T. Mainz and R. S. Berry, Mol. Phys. **88**, 709 (1996).

[62] D. J. Wales, J. Chem. Soc., Faraday Trans. **86**, 3505 (1990).

[63] J. P. K. Doye and D. J. Wales, J. Chem. Soc., Faraday Trans. **88**, 3295 (1992).

[64] M. R. Hoare and J. McInnes, J. Chem. Soc., Faraday Discuss. **61**, 12 (1976).

[65] M. R. Hoare and J. McInnes, Adv. Phys. **32**, 791 (1983).

[66] E. K. Parks, L. Zhu, J. Ho and S. J. Riley, J. Chem. Phys. **100**, 7206 (1994).

[67] E. K. Parks and S. J. Riley, Z. Phys. D **33**, 59 (1995).

[68] E. K. Parks, L. Zhu, J. Ho and S. J. Riley, J. Chem. Phys. **102**, 7377 (1995).

[69] T. Coleman and D. Shalloway, J. Global Optimization **4**, 171 (1994).

[70] J. Pillardy and L. Piela, J. Phys. Chem. **99**, 11805 (1995).

[71] J. P. K. Doye, D. J. Wales and R. S. Berry, J. Chem. Phys. **103**, 4234 (1995).

[72] J. P. K. Doye and D. J. Wales, Chem. Phys. Lett. **247**, 339 (1995).

[73] D. M. Deaven, N. Tit, J. R. Morris and K. M. Ho, Chem. Phys. Lett. **256**, 195 (1996).

[74] B. W. van de Waal, J. Chem. Phys. **90**, 3407 (1989).

[75] J. Xie, J. A. Northby, D. L. Freeman and J. D. Doll, J. Chem. Phys. **91**, 612 (1989).

[76] B. Raoult, J. Farges, M. F. de Feraudy and G. Torchet, Phil. Mag. B **60**, 881 (1989).

[77] P. M. Morse, Phys. Rev. **34**, 57 (1929).

[78] D. J. Wales, L. J. Munro and J. P. K. Doye, J. Chem. Soc., Dalton Trans. 611 (1996).

[79] L. A. Girifalco, J. Phys. Chem. **96**, 858 (1992).

[80] D. J. Wales and J. Uppenbrink, Phys. Rev. B **50**, 12342 (1994).

[81] L. A. Girifalco and V. G. Weizer, Phys. Rev. **114**, 687 (1959).

[82] M. S. Stave and A. E. DePristo, J. Chem. Phys. **97**, 3386 (1992).

[83] J. E. Jones and A. E. Ingham, Proc. R. Soc. A **107**, 636 (1925).

[84] T. Kihara and S. Koba, J. Phys. Soc. Jpn. **7**, 348 (1952).

[85] L. D. Marks, Phil. Mag. A **49**, 81 (1984).

[86] C. L. Cleveland and U. Landman, J. Chem. Phys. **94**, 7376 (1991).

[87] W. H. Press, B. P. Flannery, Teukolsky, S. A. and W. T. Vetterling, *Numerical Recipes*, Cambridge University Press, Cambridge (1986).

[88] C. J. Cerjan and W. H. Miller, J. Chem. Phys. **75**, 2800 (1981).

[89] J. P. K. Doye and D. J. Wales, Z. Phys. D in press (1996).

[90] D. J. Wales, J. Chem. Phys. **101**, 3750 (1994).

[91] J. Rose and R. S. Berry, J. Chem. Phys. **98**, 3262 (1993).

[92] F. H. Stillinger and D. K. Stillinger, J. Chem. Phys. **93**, 6106 (1990).

[93] L. T. Wille and J. Vennik, J. Phys. A **18**, L419 (1985).

[94] K. Clemenger, Phys. Rev. B **32**, 1359 (1985).

[95] J. P. K. Doye and D. J. Wales, Chem. Phys. Lett. in press (1996).

[96] U. Zimmermann, N. Milinowski, U. Näher, S. Frank and T. P. Martin, Phys. Rev. Lett. **72**, 3542 (1994).

[97] M. Sung, R. Kawai and J. H. Weare, Phys. Rev. Lett. **73**, 3552 (1994).

[98] R. Poteau and F. Spiegelmann, J. Chem. Phys. **98**, 6540 (1993).

[99] D. Rayane, P. Melinon, B. Cabaud, A. Horeau, B. Tribolet and M. Broyer, Phys. Rev. A **39**, 6056 (1989).

[100] W. N. Lipscomb, Science **153**, 373 (1966).

[101] A. Pinto, A. R. Pennisi, G. Faraci, G. D'Agostino, S. Mobilo and F. Boscherini, Phys. Rev. B **51**, 5315 (1995).

[102] J. Uppenbrink and D. J. Wales, J. Chem. Phys. **96**, 8520 (1992).

[103] Q. Wang, M. D. Glossman, M. P. Iniguez and J. A. Alonso, Phil. Mag. B **69**, 1045 (1994).

[104] H. S. Lim, C. K. Ong and F. Ercolessi, Surf. Sci. **269/270**, 1109 (1992).

[105] M. F. Ashby, F. Spaepen and S. Williams, Acta Metall. **20**, 1647 (1978).

[106] M. D. Glossman, J. A. Alonso and M. P. Iñiguez, Phys. Rev. B **47**, 4747 (1993).

[107] S. Kirkpatrick, C. D. Gelatt and M. P. Vecchi, Science **220**, 671 (1983).

[108] F. H. Stillinger and D. K. Stillinger, J. Chem. Phys. **93**, 6013 (1990).

[109] H.-P. Cheng and R. S. Berry, Phys. Rev. A **45**, 7969 (1992).

[110] R. E. Kunz and R. S. Berry, Phys. Rev. Lett. **71**, 3987 (1993).

[111] R. E. Kunz and R. S. Berry, Phys. Rev. E **49**, 1895 (1994).

[112] J. P. K. Doye and D. J. Wales, J. Chem. Phys. **102**, 9673 (1995).

[113] B. W. van de Waal, Phys. Rev. Lett. **67**, 3263 (1991).

[114] B. W. van de Waal, J. Chem. Phys. **98**, 4909 (1993).

[115] B. W. van de Waal, J. Cryst. Growth **158**, 153 (1996).

[116] B. W. van de Waal, Phys. Rev. Lett. **76**, 1083 (1996).

[117] W. Krätschmer, L. D. Lamb, K. Fostiropoulos and D. R. Huffman, Nature **347**, 354 (1990).

[118] J. P. K. Doye, A. Dullweber and D. J. Wales, unpublished.

[119] X.-Y. Chang and R. S. Berry, J. Chem. Phys. **97**, 3573 (1992).

[120] A. P. Gast, C. K. Hall and W. B. Russel, J. Colloid Interface Sci. **96**, 251 (1983).

[121] F. Leal Calderon, J. Bibette and J. Biais, Europhys. Lett. **23**, 653 (1993).

[122] P. N. Pusey, W. C. K. Poon, S. M. Ilett and P. Bartlett, J. Phys.: Condens. Matter **6**, A29 (1994).

[123] S. M. Ilett, A. Orrock, W. C. K. Poon and P. N. Pusey, Phys. Rev. E **51**, 1344 (1995).

[124] T. L. Hill, *The Thermodynamics of Small Systems Part I and II*, Benjamin, New York (1963–4).

[125] Y. Imry, Phys. Rev. B **21**, 2042 (1980).

[126] M. E. Fisher and A. N. Berker, Phys. Rev. B **26**, 2507 (1982).

[127] J. Rose and R. S. Berry, J. Chem. Phys. **98**, 3246 (1993).

[128] J. Jellinek, T. L. Beck and R. S. Berry, J. Chem. Phys. **84**, 2783 (1986).

[129] T. L. Beck, J. Jellinek and R. S. Berry, J. Chem. Phys. **87**, 545 (1987).

[130] R. S. Berry, T. L. Beck, H. L. Davis and J. Jellinek, Adv. Chem. Phys. **70**, 75 (1988).

[131] L. D. Landau and E. M. Lifshitz, *Statistical Physics*, Pergamon Press, Oxford (1980).

[132] R. M. Lynden-Bell, Mol. Phys. **86**, 1353 (1995).

[133] R. M. Lynden-Bell and D. J. Wales, J. Chem. Phys. **101**, 1460 (1994).

[134] D. J. Wales and R. S. Berry, Phys. Rev. Lett. **73**, 2875 (1994).

[135] P. Labastie and R. L. Whetten, Phys. Rev. Lett. **65**, 1567 (1990).

[136] F. Ercolessi, W. Andreoni and E. Tosatti, Phys. Rev. Lett. **66**, 911 (1991).

[137] O. H. Nielsen, J. P. Sethna, P. Stoltze, K. W. Jacobsen and J. K. Nørskov, Europhys. Lett. **26**, 51 (1994).

[138] D. D. Frantz, D. L. Freeman and J. D. Doll, J. Chem. Phys. **93**, 2769 (1990).

[139] G. M. Torrie and J. P. Valleau, Chem. Phys. Lett. **28**, 578 (1974).

[140] I. R. McDonald and K. Singer, J. Chem. Soc. and Faraday Discuss. **43**, 40 (1967).

[141] A. M. Ferrenberg and R. H. Swendsen, Phys. Rev. Lett. **63**, 1195 (1989).

[142] F. Calvo and P. Labastie, Chem. Phys. Lett. **247**, 395 (1995).

[143] M. Watanabe and W. P. Reinhardt, Phys. Rev. Lett. **65**, 3301 (1990).

[144] J. J. Burton, J. Chem. Phys. **52**, 345 (1970).

[145] J. J. Burton, J. Chem. Phys. **56**, 3123 (1972).

[146] W. G. Hoover, A. C. Hindmarsh and B. L. Holian, J. Chem. Phys. **57**, 1980 (1972).

[147] M. R. Hoare, Adv. Chem. Phys. **40**, 49 (1979).

[148] F. H. Stillinger and T. A. Weber, Science **225**, 983 (1984).

[149] J. D. Honeycutt and H. C. Andersen, J. Phys. Chem. **91**, 4590 (1987).

[150] D. J. Wales and R. S. Berry, J. Chem. Phys. **92**, 4283 (1990).

[151] J. P. Rose and R. S. Berry, J. Chem. Phys. **96**, 517 (1991).

[152] M. Bixon and J. Jortner, J. Chem. Phys. **91**, 1631 (1989).

[153] D. J. Wales, Mol. Phys. **78**, 151 (1993).

[154] G. Franke, E. R. Hilf and P. Borrmann, J. Chem. Phys. **98**, 3496 (1993).

[155] D. J. Wales and I. Ohmine, J. Chem. Phys. **98**, 7245 (1993).

[156] L. Verlet, Phys. Rev. **159**, 98 (1967).

[157] S. M. Thompson, K. E. Gubbins, J. P. R. B. Walton, R. A. R. Chantry and J. S. Rowlinson, J. Chem. Phys. **81**, 530 (1984).

[158] F. A. Lindemann, Phys. Zeitschr. **11**, 609 (1910).

[159] M. P. Allen and D. J. Tildesley, *The Computer Simulation of Liquids*, Clarendon Press, Oxford (1987).

[160] J. P. K. Doye and D. J. Wales, Z. Phys. D in press (1996).

[161] F. G. Amar and R. S. Berry, J. Chem. Phys. **85**, 5943 (1986).

[162] C. J. Tsai and K. D. Jordan, J. Phys. Chem. **97**, 11227 (1993).

[163] A. D. Isaacson and D. G. Truhlar, J. Chem. Phys. **80**, 2888 (1984).

[164] P. C. Haarhoff, Mol. Phys. **7**, 101 (1963).

[165] S. F. Chekmarev and I. H. Umirzakov, Z. Phys. D **26**, 373 (1993).

[166] W. Forst, *Theory of Unimolecular Reactions*, Academic Press, New York (1973).

[167] D. Romanini and K. K. Lehmann, J. Chem. Phys. **98**, 6437 (1993).

[168] A. J. Karas, R. G. Gilbert and M. A. Collins, Chem. Phys. Lett. **193**, 181 (1992).

[169] J. P. K. Doye, *CPGS thesis*, University of Cambridge (1994).

[170] M. Page and J. W. McIver, J. Chem. Phys. **88**, 922 (1988).

[171] M. Page, C. Doubleday and J. W. McIver, J. Chem. Phys. **93**, 5634 (1990).

[172] H.-P. Cheng, X. Li, R. L. Whetten and R. S. Berry, Phys. Rev. A **46**, 791 (1992).

[173] G. E. Lopez, J. Chem. Phys. **104**, 6650 (1996).

[174] D. D. Frantz, J. Chem. Phys. **102**, 3747 (1995).

[175] G. H. Peslherbe and W. L. Hase, J. Chem. Phys. **105**, in press (1996).

[176] D. J. Wales and J. P. K. Doye, J. Chem. Phys. **103**, 3061 (1995).

[177] M. H. J. Hagen, E. J. Meijer, G. C. A. M. Mooij, D. Frenkel and H. N. W. Lekkerkerker, Nature **365**, 425 (1993).

[178] T. Coussaert and M. Baus, Phys. Rev. E **52**, 862 (1995).

[179] A. Cheng, M. L. Klein and C. Caccamo, Phys. Rev. Lett. **71**, 1200 (1993).

[180] C. Caccamo, Phys. Rev. B **51**, 3387 (1995).

[181] S. D. Leifer, D. G. Goodwin, M. S. Anderson and J. R. Anderson, Phys. Rev. B **51**, 9973 (1995).

[182] M. H. J. Hagen and D. Frenkel, J. Chem. Phys. **101**, 4093 (1994).

[183] E. Lomba and N. G. Almarza, J. Chem. Phys. **100**, 8367 (1994).

[184] L. Mederos and G. Navascues, J. Chem. Phys. **101**, 9841 (1994).

[185] K. Shukla and R. Rajagopalan, J. Chem. Phys. **101**, 11077 (1994).

[186] E. J. Meijer and D. Frenkel, J. Chem. Phys. **100**, 6873 (1994).

[187] A. Rahman, M. J. Mandell and J. P. McTague, J. Chem. Phys. **64**, 1564 (1976).

[188] F. C. Frank, Proc. Royal Soc. London A **215**, 43 (1952).

[189] M. R. Hoare, Ann. N. Y. Acad. Sci. **279**, 186 (1976).

[190] J. A. Barker, J. de Physique **C2**, 37 (1977).

[191] D. R. Nelson and F. Spaepen, Solid State Phys. **42**, 1 (1989).

[192] J. D. Bernal, Nature **185**, 68 (1960).

[193] J. D. Bernal, Proc. Royal Soc. A **280**, 299 (1964).

[194] G. S. Cargill, Solid State Phys. **30**, 227 (1975).

[195] H. Jonsson and H. C. Andersen, Phys. Rev. Lett. **60**, 2295 (1988).

[196] B. W. van de Waal, J. Non-Cryst. Solids **189**, 118 (1995).

[197] A. S. Clarke and H. Jonsson, Phys. Rev. E **47**, 3975 (1993).

[198] D. R. Nelson, Phys. Rev. Lett. **50**, 982 (1983).

[199] D. R. Nelson, Phys. Rev. B **28**, 5515 (1983).

[200] J. P. Straley, Phys. Rev. B **30**, 6592 (1984).

[201] J. P. Straley, Phys. Rev. B **34**, 405 (1986).

[202] F. C. Frank and J. S. Kasper, Acta Cryst. **11**, 184 (1958).

[203] F. C. Frank and J. S. Kasper, Acta Cryst. **12**, 483 (1959).

[204] D. P. Shoemaker and C. B. Shoemaker, in *Introduction to Quasicrystals*, edited by M. V. Jaric, pp. 1–57, Academic Press, London (1988).

[205] C. L. Henley and V. Elser, Phil. Mag. B **53**, L59 (1986).

[206] H. Terrones, M. Terrones and W. K. Hsu, Chem. Soc. Rev. 341 (1995).

[207] D. Weaire and R. Phelan, Phil. Mag. Lett. **69**, 107 (1994).

[208] W. Thomson, Phil. Mag. **25**, 503 (1887).

[209] J. L. Finney, Proc. Roy. Soc. A **319**, 497 (1970).

[210] F. H. Stillinger and T. A. Weber, J. Chem. Phys. **81**, 5095 (1984).

[211] J. Jäckel, Rev. Mod. Phys. **49**, 171 (1986).

[212] J. F. Sadoc and N. Rivier, Phil. Mag. B **55**, 537 (1987).

[213] D. J. Wales and J. P. K. Doye, in *Large Clusters of Atoms and Molecules*, edited by T. P. Martin, vol. E 313 of *NATO ASI*, pp. 241–279, Kluwer Academic, Dordrecht (1996).

[214] W. D. Knight, K. Clemenger, W. A. de Heer, W. A. Saunders, M. Y. Chou and M. L. Cohen, Phys. Rev. Lett. **52**, 2141 (1984).

[215] T. P. Martin, U. Näher, H. Schaber and U. Zimmermann, J. Chem. Phys. **100**, 2322 (1994).

[216] J. Pedersen, S. Bjørnholm, J. Borggreen, K. Hansen, T. P. Martin and H. D. Rasmussen, Nature **353**, 733 (1991).

[217] T. P. Martin, U. Näher and H. Schaber, Chem. Phys. Lett. **199**, 470 (1992).

[218] B. Baguenard, M. Pellarin, J. Lermé, J. L. Vialle and M. Broyer, J. Chem. Phys. **100**, 754 (1994).

[219] J. Mansikka-aho, M. Manninen and E. Hammeren, Z. Phys. D **21**, 271 (1991).

[220] J. Mansikka-aho, M. Manninen and E. Hammeren, Z. Phys. D **31**, 253 (1994).

[221] N. Pavloff and S. C. Creagh, Phys. Rev. B **48**, 18164 (1993).

[222] S. L. Lai, J. Y. Guo, V. Petrova, G. Ramanath and L. H. Allen, Phys. Rev. Lett. **77**, 99 (1996).

[223] P. Pawlow, Z. phys. Chem. **65**, 545 (1909).

[224] P. Stampfli and K. H. Bennemann, Phys. Rev. Lett. **69**, 3471 (1992).

[225] P. Stampfli and K. H. Bennemann, Z. Phys. D **25**, 87 (1992).

[226] C. Levinthal, in *Mössbauer Spectroscopy in Biological Systems, Proceedings of a Meeting Held at Allerton House, Monticello, Illinois*, edited by J. T. P. DeBrunner and E. Munck, pp. 22–24, University of Illinois Press, Illinois (1969).

[227] M. R. Garey and D. S. Johnson, *Computers and Intractability: A Guide to the Theory of NP-Completeness*, WH Freeman, San Francisco (1979).

[228] J. T. Ngo and J. Marks, Protein Engineering **5**, 313 (1992).

[229] J. T. Ngo, J. Marks and M. Karplus, in *The Protein Folding Problem and Tertiary Structure Prediction*, edited by K. Merz and S. L. Grand, pp. 433–506, Birkhäuser, Boston (1994).

[230] D. M. Deaven and K. M. Ho, Phys. Rev. Lett. **75**, 288 (1995).

[231] S. K. Gregurick, M. H. Alexander and B. Hartke, J. Chem. Phys. **104**, 2684 (1996).

[232] C. J. Camacho and D. Thirumalai, Phys. Rev. Lett. **71**, 2505 (1993).

[233] A. Sali, E. Shakhnovich and M. Karplus, Nature **369**, 248 (1994).

[234] A. Sali, E. Shakhnovich and M. Karplus, J. Mol. Biol. **235**, 1614 (1994).

[235] R. Zwanzig, A. Szabo and B. Bagchi, Proc. Natl. Acad. Sci. USA **89**, 20 (1992).

[236] H. S. Chan and K. A. Dill, J. Chem. Phys. **100**, 9238 (1994).

[237] E. I. Shakhnovich and A. M. Gutin, Proc. Natl. Acad. Sci. USA **90**, 7195 (1994).

[238] E. I. Shakhnovich, Phys. Rev. Lett. **72**, 3907 (1994).

[239] H. S. Chan, Nature **373**, 665 (1995).

[240] H. Frauenfelder, F. Parak and R. D. Young, Ann. Rev. Biophys. Biophys. Chem. **17**, 451 (1988).

[241] P. Amara and J. E. Straub, J. Phys. Chem. **99**, 14840 (1995).

[242] D. K. Klimov and D. Thirumalai, Phys. Rev. Lett. **76**, 4070 (1996).

[243] J. D. Bryngelson and P. G. Wolynes, Proc. Natl. Acad. Sci. USA **84**, 7524 (1987).

[244] J. D. Bryngelson and P. G. Wolynes, J. Phys. Chem. **93**, 6902 (1989).

[245] J. D. Bryngelson, J. N. Onuchic, N. D. Socci and P. G. Wolynes, Proteins: Structure, Function and Genetics **21**, 167 (1995).

[246] P. G. Wolynes, J. N. Onuchic and D. Thirumalai, Science **267**, 1619 (1995).

[247] N. D. Socci, J. N. Onuchic and P. G. Wolynes, J. Chem. Phys. **104**, 5860 (1996).

[248] P. E. Leopold, M. Montal and J. N. Onuchic, Proc. Natl. Acad. Sci. USA **89**, 8271 (1992).

[249] D. Thirumalai, J. Phys. I **1995**, 5 (1457).

[250] J. N. Onuchic, P. G. Wolynes, Z. Luthey-Schulten and N. D. Socci, Proc. Natl. Acad. Sci. USA **92**, 3626 (1995).

[251] J. Ma and J. E. Straub, J. Chem. Phys. **101**, 533 (1994).

[252] K. D. Ball, R. S. Berry, R. E. Kunz, F.-Y. Li, A. Proykova and D. J. Wales, Science **271**, 963 (1996).

[253] R. S. Berry and R. E. Breitengraser-Kunz, Phys. Rev. Lett. **74**, 3951 (1995).

[254] R. E. Kunz and R. S. Berry, J. Chem. Phys. **103**, 1904 (1995).

[255] N. G. V. Kampen, *Stochastic Processes in Physics and Chemistry*, North Holland, Amsterdam (1992).

[256] P. Sibani, J. C. Schön, P. Salamon and J.-O. Andersson, Europhys. Lett. **22**, 479 (1993).

[257] J. C. Schön, H. Putz and M. Jansen, J. Phys.: Condens. Matter **8**, 143 (1996).

[258] M.-H. Hao and H. A. Scheraga, J. Phys. Chem. **98**, 4940 (1994).

[259] J. G. Saven, J. Wang and P. G. Wolynes, J. Chem. Phys. **101**, 11037 (1994).

[260] M. R. Betancourt and J. N. Onuchic, J. Chem. Phys. **103**, 774 (1995).

[261] N. D. Socci and J. N. Onuchic, J. Chem. Phys. **103**, 4732 (1995).

[262] V. I. Abkevich, A. M. Gutin and E. I. Shakhnovich, J. Chem. Phys. **101**, 6052 (1994).

[263] K. F. Kelton, Solid State Phys. **45**, 75 (1991).

[264] S. Kato, N. Shimamoto and H. Utiyama, Biochemistry **21**, 38 (1982).

[265] B. Chen, W. A. Baase and J. A. Schellman, Biochemistry **28**, 691 (1989).

[266] P. Alexander, J. Orban and P. Bryan, Biochemistry **31**, 7243 (1992).

[267] B. Chen and J. A. Schellman, Biochemistry **28**, 685 (1989).

[268] J. D. Nulton and P. Salamon, Phys. Rev. A **37**, 1351 (1995).

[269] P. R. ten Wolde, M. J. Ruiz-Montero and D. Frenkel, Phys. Rev. Lett. **75**, 2714 (1995).

[270] P. R. ten Wolde, M. J. Ruiz-Montero and D. Frenkel, J. Chem. Phys. **104**, 9932 (1996).

[271] F. H. Stillinger, J. Chem. Phys. **88**, 7818 (1988).

[272] F. H. Stillinger, Science **267**, 1935 (1995).

[273] Z. Guo and D. Thirumalai, Biopolymers **36**, 83 (1995).

[274] S. E. Radford, C. M. Dobson and P. A. Evans, Nature **358**, 302 (1992).

[275] A. Miranker, C. V. Robinson, S. E. Radford, R. T. Aplin and C. M. Dobson, Science **262**, 896 (1993).

[276] T. Kiefhaber, Proc. Natl. Acad. Sci. USA **92**, 9029 (1995).

[277] M. S. Briggs and H. Roder, Proc. Natl. Acad. Sci. USA **89**, 2017 (1992).

[278] T. R. Sosnick, L. Mayne, R. Hiller and S. W. Englander, Nature struct. Biol. **1**, 149 (1994).

[279] M. J. Todd, P. V. Viitanen and G. H. Lorimer, Science **265**, 659 (1994).

[280] M. J. Todd, G. H. Lorimer and D. Thirumalai, Proc. Natl. Acad. Sci. USA **93**, 4030 (1996).

[281] C. D. Sfatos, A. M. Gutin, V. I. Abkevich and E. I. Shakhnovich, Biochemistry **35**, 334 (1996).

[282] D. Baker and D. A. Agard, Biochemistry **33**, 7505 (1994).

[283] R. W. Carrell, D. L. Evans and P. E. Stein, Nature **353**, 576 (1991).

[284] N. Metropolis, A. W. Rosenbluth, M. N. Rosenbluth, A. H. Teller and E. Teller, J. Chem. Phys. **21**, 1087 (1953).

[285] M. Buchanan, Nature **382**, 302 (1996).

[286] F. H. Stillinger and T. A. Weber, Phys. Rev. A **23**, 2408 (1983).

[287] U. Mohanty, Adv. Chem. Phys. **89**, 89 (1995).

[288] M. D. Ediger, C. A. Angell and S. R. Nagel, J. Phys. Chem. **100**, 13200 (1996).

[289] U. Mohanty, Science **266**, 425 (1994).

Publications

Some of the work contained in this thesis has been published in the following papers.

1. Calculation of thermodynamic properties of small Lennard-Jones clusters incorporating anharmonicity, J. P. K. Doye and D. J. Wales, J. Chem. Phys. **102**, 9659–9672 (1995).
2. An order parameter approach to coexistence in atomic clusters, J. P. K. Doye and D. J. Wales, J. Chem. Phys. **102**, 9673–9688 (1995).
3. The effect of the range of the potential on the structures of clusters, J. P. K. Doye, D. J. Wales and R. S. Berry, J. Chem. Phys. **103**, 4234–4249 (1995).
4. Theoretical predictions of structure and thermodynamics in the large cluster regime, D. J. Wales and J. P. K. Doye, in *Large Clusters of Atoms and Molecules (NATO ASI Series E: Vol. 313),* ed. T. P. Martin (Kluwer Academic, Dordrecht, 1996), pp. 241–279.
5. What can calculations employing empirical potentials teach us about bare transition metal clusters?, D. J. Wales, L. J. Munro and J. P. K. Doye, J. Chem. Soc., Dalton Trans. 611–623 (1996).
6. The structure and stability of atomic liquids: from clusters to bulk, J. P. K. Doye and D. J. Wales, Science **271**, 484–487 (1996).
7. The effect of the range of the potential on the structure and stability of simple liquids: from clusters to bulk, from sodium to C_{60}, J. P. K. Doye and D. J. Wales, J. Phys. B **29**, in press (1996). (Invited Review)
8. On potential energy surfaces and relaxation to the global minimum, J. P. K. Doye and D. J. Wales, J. Chem. Phys. **105**, in press (1996).
9. Traversing the potential energy surface by eigenvector-following: applications to global optimisation and the structural transformations of clusters, J. P. K. Doye and D. J. Wales, Z. Phys. D in press.

I have also published the following papers during my PhD.

1. Coexistence and phase separation in clusters: From the small to the not-so-small regime, D. J. Wales and J. P. K. Doye, J. Chem. Phys. **103**, 3061–3070 (1995).
2. Magic numbers and growth sequences of small face-centred-cubic and decahedral clusters, J. P. K. Doye and D. J. Wales, Chem. Phys. Lett. **247**, 339–347 (1995).

3. The structure of $(C_{60})_N$ clusters, J. P. K. Doye and D. J. Wales, Chem. Phys. Lett. in press (1996).
4. Thermally-induced surface reconstructions of Mackay icosahedra, J. P. K. Doye and D. J. Wales, Z. Phys. D in press.